Study of the diffusion, rheology and microrheology of complex mixtures of bacteria and particles under flow confined in thin channels.

Gaston L. Miño

DOCTORAL THESIS

UNIVERSITE PIERRE ET MARIE CURIE

Speciality: Physique

Doctoral School: "ED P2MC 389"

made in

École supérieure de physique et de chimie industrielles

Physique et Mécanique des Milieux Hétérogènes

presented by

Gastón Leonardo MIÑO

to obtain the degree of

DOCTOR FROM PIERRE AND MARIE CURIE UNIVERSITY

title of the thesis

Study of the diffusion, rheology and microrheology of complex mixtures of bacteria and particles under flow confined in thin channels.

Presented 10 February 2012, Paris.

jury composed by:

Pr.	Wilson Poon	Referee
Pr.	Hartmut Löwen	Referee
Pr.	Jean-Francois Joanny	Examiner
Pr.	Philippe Peyla	Examiner
Pr.	Eric Clément	Advisor

Résumé

Pour ma thèse, j'ai étudié trois problèmes autour des propriétés de transport des suspensions actives. J'ai utilisé principalement des suspensions de bactéries *Escherichia Coli* mais aussi des systèmes de nageurs artificiels auto-propulsés.

En premier lieu, j'ai étudié l'activation du mouvement Brownien de particules passives dans une suspension de bactéries, près d'une surface. En utilisant diverses solutions et diverses conditions expérimentales permettant de changer les conditions de nage des bactéries et le confinement, j'ai montré que la diffusivité des traceurs passifs augmente linéairement avec ce que j'ai défini comme le flux actif de la suspension; c'est à dire la concentration de nageurs actifs multipliée par leur vitesse moyenne de nage. De manière générale, le confinement entre deux parois ou par rapprochement d'une paroi, montre un meilleur transfert de la quantité de mouvement qui a pour conséquence une augmentation du facteur de couplage entre diffusivité et fluide actif. Le remplacement des bactéries par des nageurs artificiels comme des bâtonnets bi-métalliques en condition réductrice produit des résultats identiques.

Deuxièmement, j'ai étudie la modification de la viscosité d'un fluide produite par la présence d'entités autopropulsées. Il a été montré théoriquement que la présence de nageurs du type "pousseurs" comme les bactéries, réduit la viscosité de la suspension à une valeur inférieure de celle du fluide porteur. Le manque de résultats expérimentaux qui mettent en évidence cet effet au sein d'une suspension (cela été montré pour des films liquides minces), nous a poussé à fabriquer un rhéomètre microfluidique en forme d'Y permettant d'étudier la réponse rhéologique d'une suspension d'*E. Coli*. Des résultats préliminaires révèlent un comportement non Newtonien de la suspension active avec une baisse de viscosité du liquide aux faibles taux de cisaillement et aux faibles fractions volumiques.

Troisièmement, j'ai propose d'étudier les effets de dispersion et de transport de solutions *E. Coli* dans un micro canal rectangulaire possédant une constriction en

son centre. Dans un tel milieu confiné, les interactions avec les parois ainsi que la géométrie du canal jouent un rôle essentiel sur les propriétés de transport. Mes résultats, de façon inattendue, montrent que l'écoulement dans un canal produit une re-concentration en bactéries après la constriction et que cet effet est contrôlé par l'écoulement même.

Abstract

In my thesis, I studied three problems involving *E. Coli* bacterial suspensions.

Firstly, I focused on the Brownian motion of passive tracers in this particular active suspension close to a surface. Buoyancy and non-buoyancy swimming solutions were tested, revealing a linear increase of the passive tracer diffusion with the "active flux", obtained by the active concentration of bacteria multiplied by the mean velocity. Boundary confinements were also explored in buoyancy conditions, showing a better momentum transfer of the active bacteria as the height of the confinement gets smaller. The use of artificial swimmers instead of bacteria also leads to similar results in the enhancement of the diffusion.

Secondly, I considered the modification of the fluid viscosity caused by the presence of these self-propelling entities. It is known that for pusher swimmers as bacteria the viscosity can even be smaller than that of the suspending fluid viscosity. The lack of experimental result showing this effect in the bulk inspired us to build a Y shape micro-fluidic channel in order to study the rheology of wild type *E. Coli* suspension. Preliminary results show a non-Newtonian behavior of active solution with a decrease of the liquid viscosity at low volume fractions and low shear rates.

Thirdly, I proposed to address the question of dispersion and transport of *E. Coli* suspensions flowing in a micro-channel with a constriction. Here, in a confined environment , the interactions with the boundaries and the geometry of the channels play an essential role. Surprisingly, my results show that the flow in a channel can produce a re-concentration of bacteria after passing through the constriction and this can be controlled by the flow.

Acknowledgement

It took me three years to reach this point in my life and to achieve this goal. Several persons have been involved in this process.

First and foremost, I owe a lot to my supervisor Eric Clément who has given me the opportunity to work with him. I thank him for his stimulating suggestions and encouragement. He has helped me immensely during the research for and the writing of this thesis. I also would like to express my gratitude to Dr Annie Rousselet and thank her for sharing her knowledge and for supervising my work. Without her guidance and help this work would not have been possible. I would like to thank Dr José Eduardo Wesfreid for being the "bridge" that brought me to PMMH.

I also want to thank Mr. Jérémie Gachelin, Ing. Thierry Darnige, Dr. Mauricio Hoyos , Hélène Berthet, and Dr. Anke Lindner. These PMMH co-workers have had an active participation during these three years, have helped me and I have had enriching discussions with them. I would like to thank the staff of PMMH and all my colleagues for making my stay comfortable and for making me feel welcome.

Gracias Ms Jocelyn Dunstan and Pr Rodrigo Soto from the Chile University for all the scientific discussions, support and also for the warm welcome received every time that I visited their lab in Chile. Gracias to Pr. Ernesto Altshuler from the University of Havana for working with me and for sharing many hours of discussion and laboratory work. I would like to thank Pr Thomas Mallouk from Penn State who helped me during his sabbatical at the École Normale Supérieure in 2009-2010 with the realization of part of my work presented in this thesis.

This thesis would not have been possible without the financial support of Foundation Pierre-Gilles de Gennes.

I want to express my profound gratitude to a college and very good friend, Dr Veronica Raspa. I thank her for being at my side, for encouraging and supporting me, especially at the last stages of this thesis.

Because they are with me for each step that I take, they support me and are by my side no matter the distance, I want to express my gratitude and love to my Family and Friends in Paraná, Argentina.

Finally, I want to thank someone very important to me and on whom I can count whenever I need to: Thank you Jochen.

Contents

List of Figures

1

Introduction

An active suspension is a fluid containing autonomous swimmers such a bacteria, algae or artificial selfpropelled entities. When a microscopic cell swims in a fluid, usually viscous forces dominates the inertial terms. The comparison between this two magnitudes is made by the Reynolds number *Re*:

$$Re = \frac{\rho V L}{\eta} \tag{1.1}$$

where V is a typical velocity, L a typical length, ρ and η are the density and the dynamic viscosity of the fluid, respectively. Swimmers with a typical length of $1\mu m$, and a propulsion velocity $V = 30\mu m$ swimming in water ($\rho = 1g/cm^3$ and $\eta = 10^{-2}g/cm$), leads to a Reynolds number in the order of 10^{-5} (Purcell, 1977).

Under this conditions, autonomic propulsion is assured only if the time reversibility is broken during the motion (Purcell, 1977; and Golestanian *et al.* 2008). In nature, different way of motions in viscous fluid can be mentioned such as spermatozoid (Gaffney *et al.*, 2011; Gray and Hancok, 1955), bacteria (Dombrowski *et al.*, 2004; and Chen *et al.*, 2007) or algae (Ringo, 1967; Leptos *et al.*, 2009; and Rafaï *et al.*, 2010).

Escherichia Coli (Berg, 2004) represent a good example of self-propelled swimmer. This widely studied bacteria will represent the main active component in the solution studied in this thesis. *E. Coli* is a ellipsoidal-shape cell with 1 μm diameter and 2 μm length. The motion is the consequence of the rotation of several helicoidal flagella.

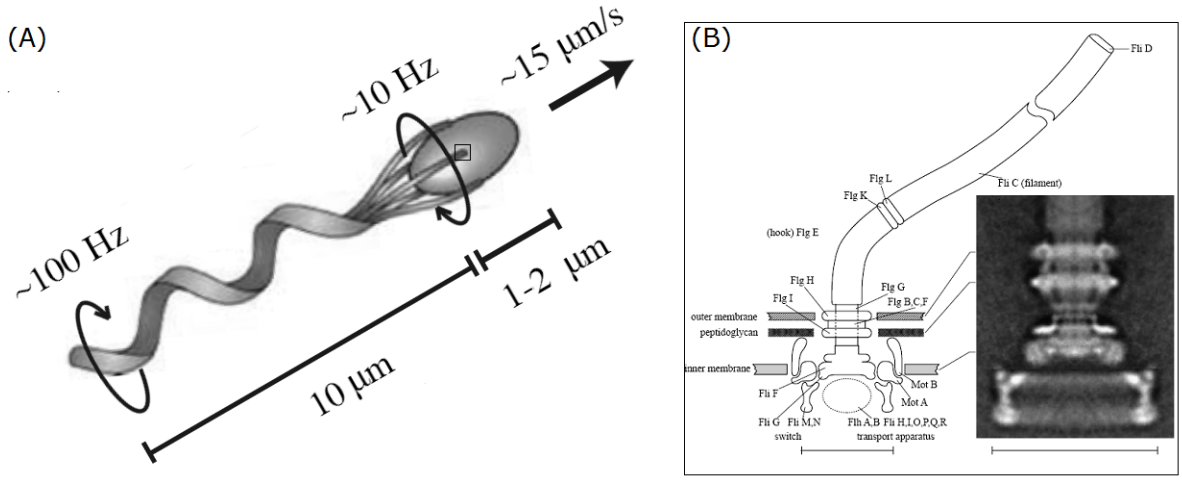

Figure 1.1: A) *Eschericha Coli* diagram (adapted from Eisenbach, 2001). Bacterial sizes, rotating frequencies and a typical swimming velocity near a surface, are also indicated. B) Flagellar motor scheme in comparison with electron microscope image (from Berg, 2003).

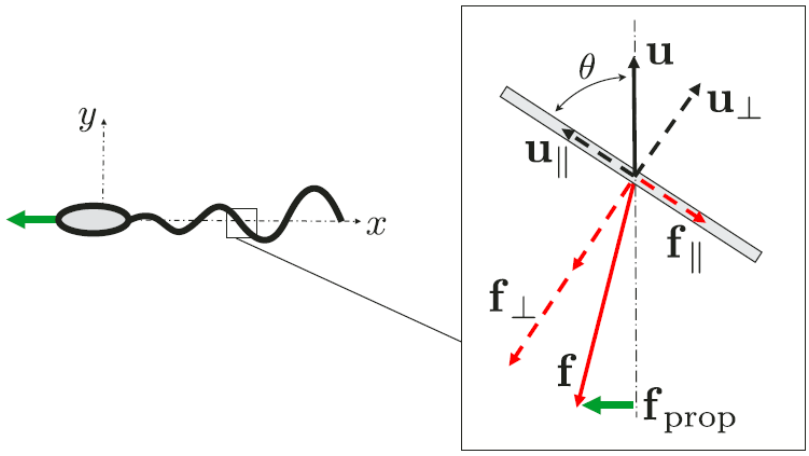

Figure 1.2: Physics of drag-based thrust acting under a segment of flagella (Lauga and Powers, 2009). The drag anisotropy for slender filaments provides a means to generate forces perpendicular $\vec{f}_{prop}$ to the direction of the local velocity $\vec{u}$.

Each flagellum is linked to the cell membrane by a nanoscale motor (Fig. 1.1). When all the motors turn in a counterclockwise (CCW) direction, the flagella rotates in a bundle and this pushes the cell steadily forward (what is called "run"). When the motor rotation switches to clockwise (CW), the cell can change direction (known as a "tumble" process). The mean run interval is typically 1 s, whereas the mean tumble interval is around 0.1 s (Berg, 2000). The ratio between tumble and run depends upon the chemotaxis signals and also the molecular machinery that modulates the rotation direction.

The rotation of helicoidal flagella allows the motion of the *E. Coli* at low Reynolds number and it is caused by the drag anisotropy (Lauga and Powers, 2009). If we consider the motion of a flagella segment, a propulsion force will appears in the direction perpendicular to the rotating velocity (See fig. 1.2).

Since the swimming motion is autonomous at large distances, no external force or torque can be exerted on the fluid. Therefore, the leading long range hydrodynamics should be governed at most by a dipole force. As a consequence, depending on the dipole polarity, many micro-organisms can be classified under two categories: "pushers" and "pullers" (Hernandez-Ortiz, 2005; Saintillan, 2007; Baskaran and Marchetti, 2009). From this point of view, *Escherichia Coli* or *Bacillus Subtilis* can be classified as pushers, algae such as *Chlamydomonas Reinhardtii* as pullers (See fig. 1.3). From an experimental point of view, the presence of active cells or swimmers in the solution

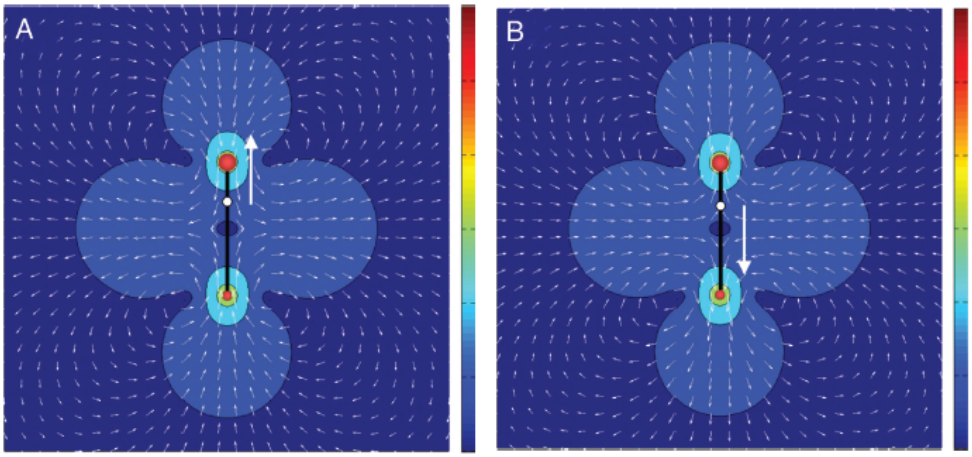

Figure 1.3: Flow patterns induced by a two spheres model acting as active swimmers. A) Represent the active forces that a single puller exerts on the surrounding fluid. B) shows the pusher effect. The colors denote the amplitude of the flow that decreases at large distances. The arrows indicate the direction of the flow. From Baskaran and Marchetti, 2009.

offers a wide scenario to be explored. Here the coupling between the micro to macro scale remains unclear and it reveals the necessity of new studies in order to better understand the problem. Note that, these two categories do not fully cover all the possibilities of propulsion at low Reynolds numbers. Finally, in recent years, progresses have been made on the synthesis of colloids (using Janus-like reactive properties at their surface), that move autonomously. For this artificial system, the classification in terms of long range hydrodynamics is not clearly established (Dreyfus *et al.*, 2005; Wang *et al.*, 2006; Palacci *et al.*, 2010; and Wheat *et al.*, 2010).

In general, the presence of active swimmers changes the mechanical picture usually considered for passive suspension problems. When an organism swims, it interacts with the surrounding medium (i. e., the suspending fluid, other swimmers in the fluid and, also the boundaries of the system). Consequently, balances of momentum and energy as well the constitutive transport properties, are deeply modified by the momentum sources distributed in the bulk.

Active Diffusion

The seminal work addressing the effect of active suspension on the enhancement of passive tracers Brownian diffusivity, was presented by Wu and Libschaber in 2000. They conducted an interesting experiment, wild-type *E. Coli* as well as 4.5 and 10 μm

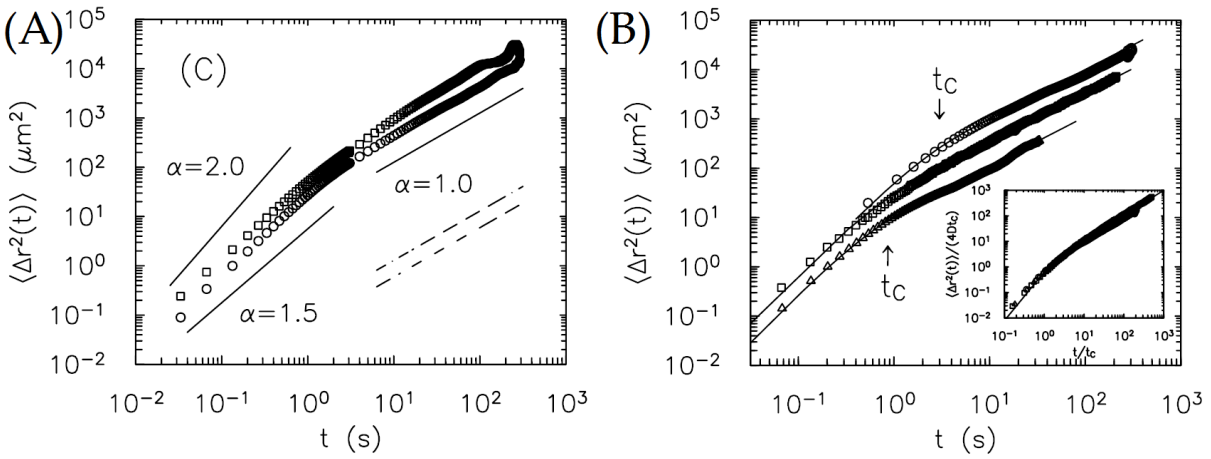

Figure 1.4: (A) Means Square Displacement for 4.5 (squares) and 10 (cirles) μm diameter beads, followed during 3 min. α represents the time exponent. (B) Means Square Displacement of 10 μm diameter particles at different bacterial concentration. From Wu and Libchaber (2000).

diameter particles were trapped in a thin film. They showed the diffusion effect of these two different particles caused by a given bacterial concentration in the film (see fig.1.4). They found the presence of super-diffusion for $t < t_c$ and normal diffusion for $t > t_c$, where t_c is a characteristic time representing the lifetime of coherent structures in the sample. They also studied the influence of the bacterial concentration in the diffusion of 10 μm diameter particles, showing the diffusion of these particles increases linearly with the bacterial concentration. They suggested that this effect could be related to the spontaneous formation of swirls in the bacterial bath.

In 2009, Leptos *et al.* studied the enhancement of the tracer diffusion into an aqueous medium, for a puller puller type. They used *Chlamydomonas Reinhardtii* as the active component of the solution, and 2 μm diameter beads as passive tracers. Their observation was performed far from the wall and they show a linear increase of the tracers diffusion with the volume fraction ϕ. They defined an effective diffusivity D_{eff} for the passive tracers: $D_{eff} = D_B + \alpha\phi$, where D_B is the Brownian diffusion value in the bulk (without swimmers) and, α can be defined (from dimensional analysis) as $\alpha = U^2\tau = Ul$ (where U, τ and l represent a characteristic advective velocity, encounter time, and advective length, respectively). In a recent work presented by Wilson *et al.* (2011), Differential Dynamic Microscopy (DDM) was applied to characterized the bacterial motion in *E. Coli* suspensions. They show that the diffusion of non-motile

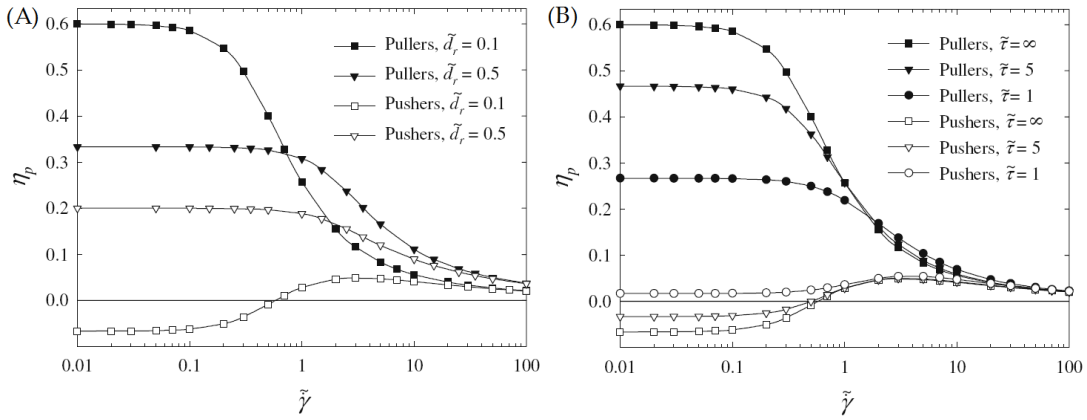

Figure 1.5: (A) Rheology of a suspension of smooth slender swimmers (no tumbling). (B) Effect of tumbling on the rheology of slender swimmers. From Saintillan (2010).

bacteria enhances with the active fraction, given by the proportion of active swimmers, also establishing a linear relationship between these two quantities.

Active viscosity

Active suspensions can also collectively acquire original constitutive properties. Recently, Saintillan (2010) studied theoretically and numerically the rheology of a suspension of autonomous swimmers using a simple kinetic model for diluted active suspension. He found that active suspensions display a non-newtonian behavior with a posible negative contribution on the viscosity for the "pusher" case (see fig.1.5). Also, Ryan *et al.* (2011) investigated the effect on the viscosity of the pusher-like swimming

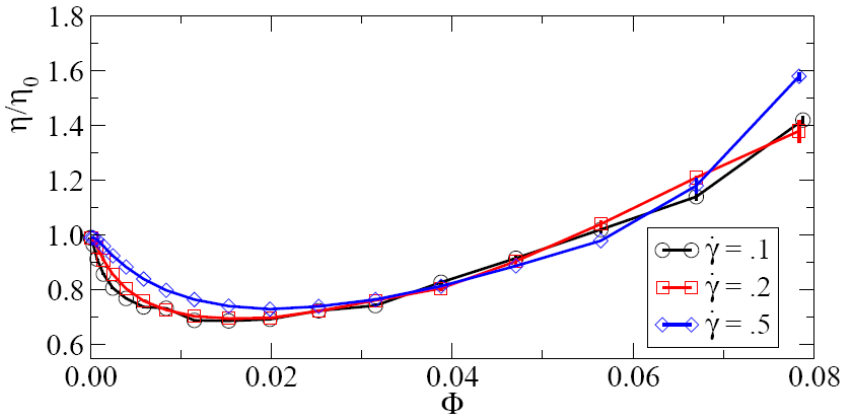

Figure 1.6: Relative Viscosity as function of the volume fraction Φ at different strain rates $\dot{\gamma}$ for a "pusher" model. From Ryan *et al.* (2011).

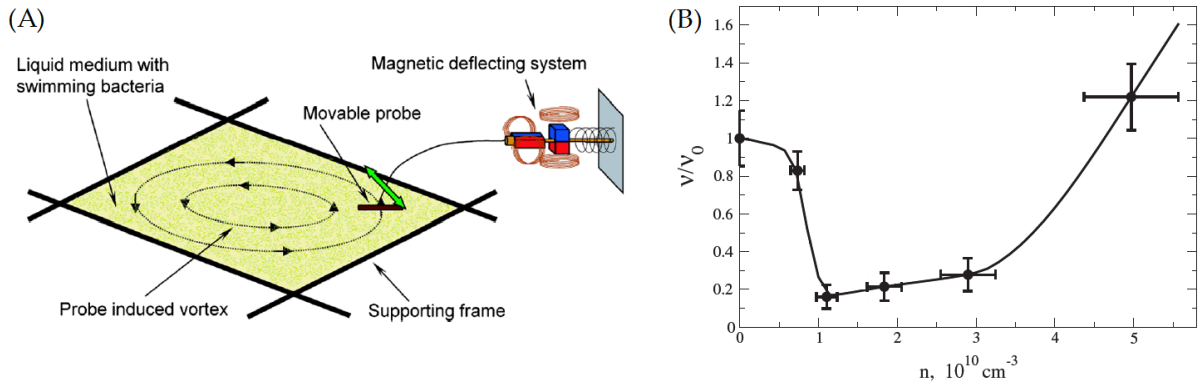

Figure 1.7: (A) Experimental setup of Sokolov and Aranson (2009), using a thin liquid film of bacteria suspension between four movable fibers. (B) Relative viscosity for 6 different concentrations.

bacteria suspension both analytically and numerically (see fig.1.6). They studied the influence of the hydrodynamic interactions on the effective viscosity, showing that this interaction produces an viscosity reduction and, also, that no tumbling is needed to obtain this effect.

From an experimental point of view, there are few studies on viscosity of active suspensions. In 2007, Chen *et al.* studied nonequilibrium properties of *E. Coli* bacterial

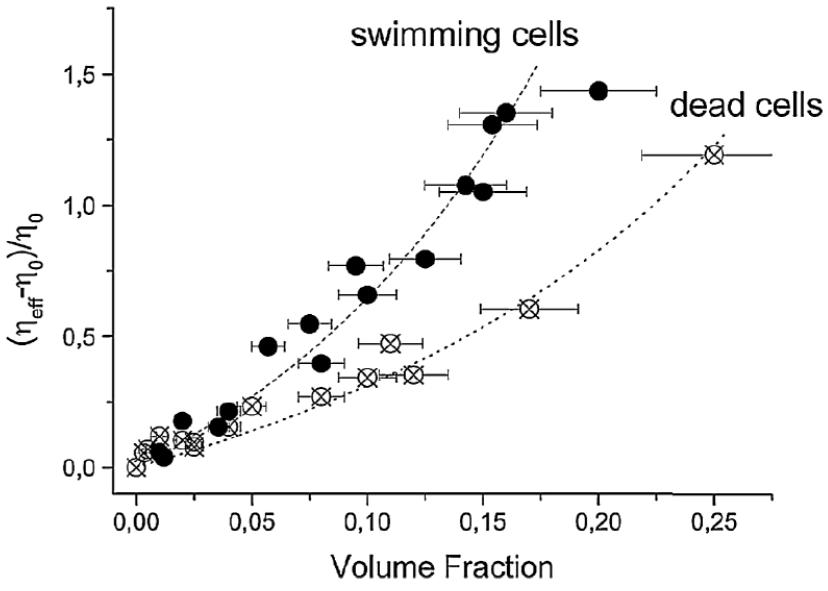

Figure 1.8: Relative viscosity as function of the *Chlamydomonas Reinhardtii* concentration for a shear rate of 5 s^{-1}. Rafaï *et al.* (2010).

bath through measurements of correlations of passive tracer particles. Sokolov and Aranson in 2009 studied effective viscosity of *Bacilus Subtilis* ("pusher" type) suspensions. The study was performed in a film where a controlled vortex is applied and the viscosity is measured through the relaxation characteristic time (see fig.1.7). They showed a strong reduction of the viscosity (up to 7 times) for concentrations ranging between 1 to $3 \times 10^{10} Bacteria/cm^3$). In 2010, Rafaï *et al.* studied the viscosity variation on *Chlamydomonas Reinhardtii* algae suspensions. They showed an increase of the viscosity with the volume fraction. This effect was stronger for living algae than for the dead ones (see fig.1.8).

Collective behavior

Moreover, in the case of dense suspension, the presence of living entities offers the possibility to move collectively, organized and synchronized at a mesoscopic level (Koch, 2011). These collective effects can have two origins; either from short range interactions and dipolar orientation such as in flocks and herds models (Gregoire, 2004) or, via long range hydrodynamic coupling as in semi-diluted particulate fluids (Saintillan, 2007). A primary consequence of this organization will be to yield anomalous statistical behavior either in the spatial distribution of swimmers or in their velocity correlations. These mesoscopic organization properties will have a strong influence on the macroscopic constitutive relations and can be at the origin of complex dynamical patterns. The situation of long range hydrodynamic coupling is certainly the least studied theoretically, essentially due to the difficulty to solve the full N-body

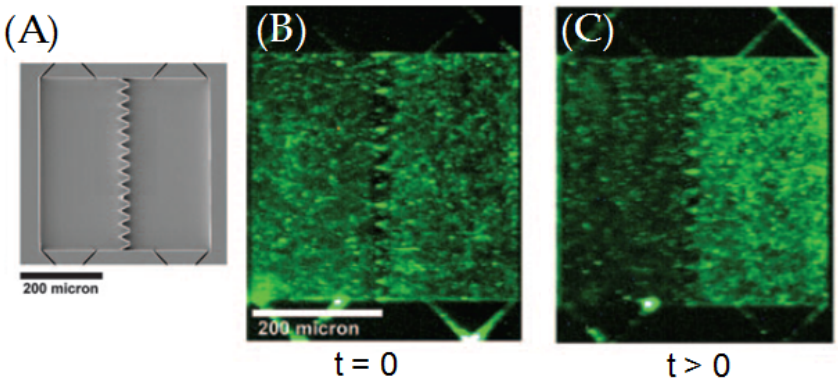

Figure 1.9: (A) Scanning electron micrograph of the device for the interaction of bacteria with the suitable wall. (B) Uniform distribution after injection. (C) Steady-state distribution after 80 min. (Galadja *et al.*, 2007).

hydrodynamic interactions; a question that remains timely also in the case of passive suspensions.

Active density control

It was shown recently that *E. Coli* bacteria show very singular spatial distributions when they are confined in specific geometries. If the volume is split in two by setting a wall of suitable design, the concentration at both sides of this boundary will be different due to the interaction of bacteria with the wall. In 2007 Galajda *et al.* presented a chamber with a splitting microfabricated wall of funnel-shaped openings that traps alive bacteria (see fig.1.9). Hulme *et al.* (2008) presented a channel of suitable shape that directs the motion of *E. Coli* due to their interaction with walls. No external flow is involved and bacteria moves in a very confined system (1.5 μm height) made by PDMS lateral and top walls and a bottom wall made of Agar (see fig.1.10). These

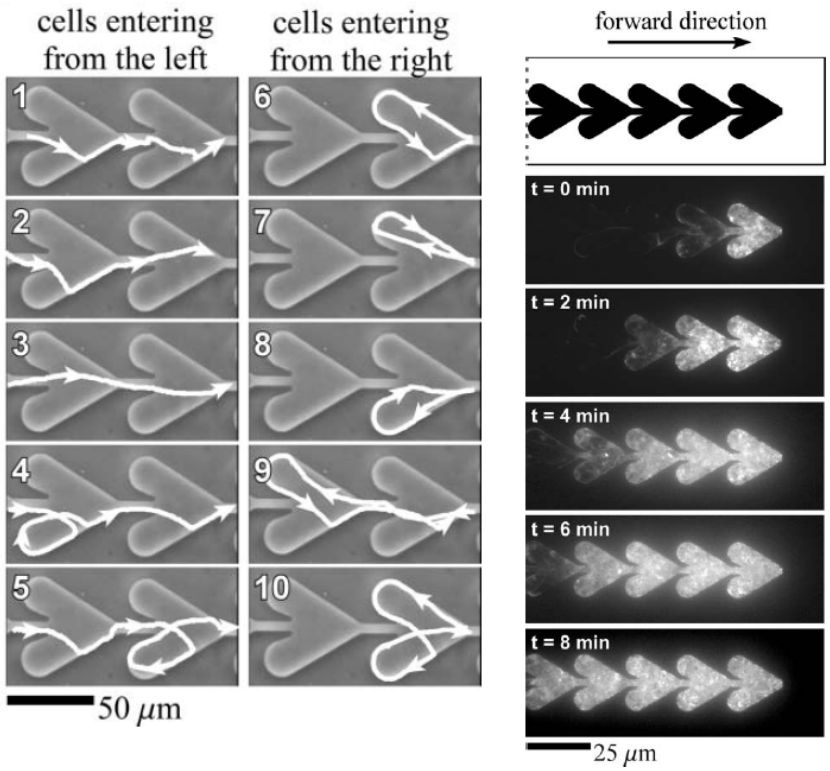

Figure 1.10: Ratchets were design in order to direct the motion of the bacteria. Several trajectories are shown after the cell in the left side of the channel (from 1 to 5) and how the cell is reoriented when it gets in in the "wrong side" (from 6 to 10). Bacteria re-concentration after passing by successive ratchets. The arrow indicates the direction in which the ratchet guided cells. (Hulme *et al.*, 2008).

results open the possibility to play with the geometrical shape to controlled and sort the population of active swimmers.

In this thesis, the protocoles and large parte of the practical study using *E. Coli* were defined in close interaction with Dr Annie Rousselet, biologist at the PMMH.

In the first part of the thesis I investigate the Brownian motion of passive tracers activated by different active suspension conditions. The Brownian diffusivity was monitored in different environments changing the buoyancy of the suspension as well as the wall confinement. This Part also contains a simple model of the bacteria interacting with a wall, developed in collaboration with J. Dunstan and R. Soto from University of Chile. Furthermore we explored a different type of swimmer using synthetic micro-rods in collaboration with Pr Thomas Mallouk from Penn-State University.

The second part includes two experiments on bacteria in a flow. We investigate both: the active viscosity of active suspensions and the anomalous dispersion of a confined bacterial flow. The first topic was addressed in colaboration with Jérémie Gachelin in the framework of his Master's thesis. From the design by Guillot (2006), we developed, tested and used a viscometer suitable for W wild type *E. Coli* suspensions in the dilute and semi-dilute limits. In Chapter II.2, I conducted experiments in collaboration with Pr Ernesto Altshuler from the University of La Havana at the occasion of his sabbatical at the PMMH in 2010-2011. Bacterial suspensions of *E. Coli* were transported through an specially designed micro-fluidic channel. The design includes a constriction placed at the middle of the device, called hereafter, the funnel. The influence of geometry and confinement on both the dispersion and transport properties of a bacterial flow, was studied using this simple but archetypal configuration.

Part I

Active Brownian motion

I.1

Methodology and Protocol

From the perspective of providing a fully consistent treatment of active hydrodynamics, with important applications in clarifying bacterial transfer in biological micro-vessels, microfluidic devices or the formation of bio-films, a reliable description of fluid activity in the vicinity of a solid surface is strongly needed. As described in the introductory chapter for bacteria such as *E. Coli*, in the presence of a solid boundary due to the head contra-rotation in lubrication interaction with the solid boundary, most trajectories are circle-like and the run time increases significantly. To tackle this open and timely question, I studied the effect of enhanced diffusion produced by a wild type *E. Coli* on a passive tracer, close to a solid surface. This study follows the pioneering work of Wu and Libchaber (2000), who provide evidence of an activated Brownian motion for bacteria suspensions trapped in a thin film. This is in fact a measurement of the fluid activity. In the experiments presented in this part of my thesis, the activated Brownian motion was monitored in various confined environments, changing the buoyancy (distance to the bottom wall) and exploring another boundary condition (approach of a top surface). In addition, to investigate the influence of a swimming mode significantly different from a biological one, we also compare to the results of an artificial self-propelling system.

I.1.1 Experimental Setup

The setups used in all the experiments presented in this thesis, have several elements in common. Each chapter will be provided with specific setup details, however generally to conduct the observations on the bacterial suspension, I used a *Z1* inverted microscope from *Zeiss-Observer*. Images and videos were captured using a *Pixelink PL-A741-E* CCD digital camera, connected to and controlled by a computer which stores the images that will be post-processed. The CCD chip has a maximum resolution of 1024×1280 $pixels^2$ and can run at 10 $frames/s$ full frame. However to gain speed of acquisition, I usually reduced the visualization field to work at 600×800 at a rate of 20 $frames/s$.

For the experiments on activated Brownian motion, the principle is to follow the motion of passive particles in a bacterial suspension, in the vicinity of a solid boundary. These tracers are *Beckman-Coulter* latex beads (see Appendix A for details) with a size of either 1 or 2 μm. A 10 μl drop of the following containing the W wild-type *E.*

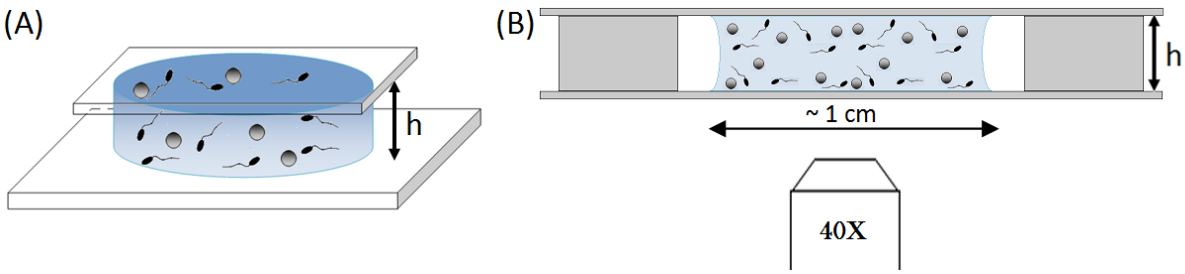

Figure I.1.1: (A) Sketch showing a general view of the chamber used in the experiments. (B) shows a lateral view of the chamber observed on the microscope. For these experiments a 40X objective (Aperture number AN 0.65) was used, given a visualization field of 96×128 μm^2. Observation are performed in the center of the drop far away from the drop border.

Coli bacteria (see Archer *et al.*,2011) and the tracer latex beads, are placed in a transparent chamber on the visualization stage of the microscope. A sketch of the chamber is shown in fig. I.1.1. The chamber is made of two cover-slips separated by a typical distance h of 110 μm (achieved by using two cover-slips $N°0$ as spacers).

The choice of the ambient medium is always a difficult issue as it may modify strongly the bacteria behaviour in terms of chemotaxis, ambient fluid viscosity or response to pH. In the literature, several preparation protocols were designed to be able to achieve different goals. For example, for *E. Coli*, Berg and Brown (1972) defined an specific protocol to study the chemotaxic effects of amino-acids in the bacterial response. A different protocol was chosen by Lowe *et al.* (1987) as they seeked to change the viscosity of the suspending medium to study the rotation of flagella bundles with *Streptococcus*. Note that in general, the biological conditions impose a very narrow window of parameters and in practice it is always difficult to conduct experiments that change one parameter at a time as soon as a set of working conditions is established. In the present study, to change buoyancy and swimming speed, I will consider two different solutions as a swimming medium: (i) a Minimal Motility Medium (MMA) alone and (ii) a (1 vol/1 vol) mixture of MMA and Percoll (a nanoparticles suspension see Laurent *et a.l*, 1980) which achieve non-buoyant conditions (see Appendix A).

- The use of MMA as swimming solution has several advantages. First, it contains a sufficient amount of nutritional elements to preserve the bacteria metabolism (essentially lactose), but cell division is strongly reduced, thus allowing to control density of the bacterial population and limiting the influence of chemotaxis. Second,

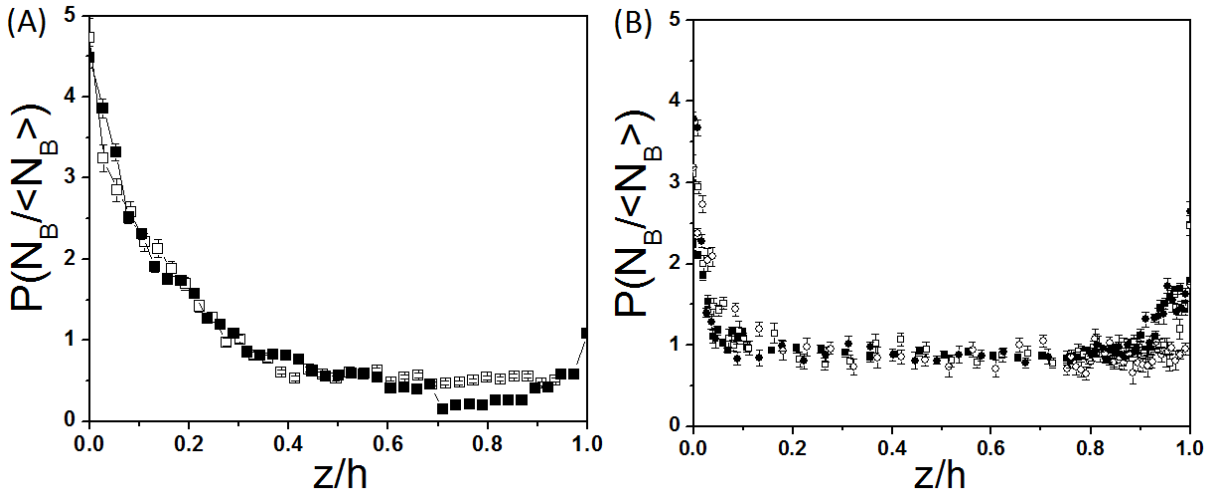

Figure I.1.2: (A) Distribution profile as function of height in buoyancy solution (Minimal Motility Medium at pH 7) for two bacterial concentration n ($4.5 \times 10^8 bact/ml$ and $7 \times 10^8 bact/ml$) corresponding to optical densities OD 0.7 and 1, respectively. (B) Same experiment non-buoyant solution for four bacterial concentration n ranging from $3.8 \times 10^8 bact/ml$ (OD=0.4) to $7 \times 10^8 bact/ml$ (OD=1) (mixture of MMA-Percoll at pH 6.9) . $z/h = 0$ and $z/h = 1$ correspond to the bottom and top glass walls of the chamber, respectively.

this medium allows to change the bacteria velocity by modifying the pH of the solution, thus acting directly on the molecular proton motor that activates the flagella rotation (see Minamino *et al.*, 2003). A third advantage is that for different values of pH, the MMA solution keeps physical properties similar to water as far a density and viscosity are concerned (See appendix A).

- The MMA-Percoll mixture gives optimal condition to work at different buoyancy. The use of a nanoparticle suspension has a decisive advantage to suppress the risk of a cellular osmotic shock. The bacteria and the latex particles are slightly denser than the MMA solution. Regarding the bacteria density, literature does not provide specific values but it is usually larger than MMA. For the beads, the data-sheet by the manufacturer specifies a value of $\rho = 1.027 g/ml$. In order to reach a density similar of the one of the latex beads I chose to mix in equal proportion these two solutions, obtaining a relative density matching of about 1 % at 25 °C for the tracers. However, contrary to MMA as such, this solution has the disadvantage that pH modifies the mixture viscosity (a factor 2 for pH varying from 6 to 8). For this specific reason, I decided to perform the experiments in quasi isodense conditions at a fixed pH value of 6.9 that provides optimal swimming conditions for the bacteria (for details see

appendix A).

In all these experiments, special attention was given to avoid the adhesion of latex beads and bacteria on the surface. This was achieved by adding 0.005 % in volume of Polyvinylpyrrolidone (PVP 40 from Sigma Aldrich) to the solution, a protocol used by Berke *et al.* (2008). Note that glass surfaces were also coated with PVP. Protocol details can also be found in appendix A.

Given this specific preparation protocol, once the chamber is placed under the microscope, a steady distribution of bacteria in the z direction is reached very rapidly. I checked explicitly for the isodense suspension, that in less than 1 minute the bacteria concentration at the center of the chamber reached a steady value. The measurements typically starts a few minutes after the chamber is placed under the microscope. Note that for experiments with MMA alone one has to wait few minutes more in order to let the latex beads sediment. On figures I.1.2.(A) and (B), I display bacteria concentration profiles in the vertical direction for the two types of solutions used (i.e. MMA in (A) and MMA+percoll in (B)) at different mean concentrations.

In the first case (MMA alone), due to buoyancy, there is as accumulation of bacteria at the bottom wall ($z/h = 0$). This is in contrast with the second case (MMA-Percoll), where the bacterial concentration is constant in the center of the chamber and increases when it gets close to the walls (within 10 μm ($z/h \sim 0.1$) distance). Note that due to a slight residual density mismatch, one still observes a small sedimentation effect for the MMA-Percoll experiments visualized as an asymmetry in concentration at the wall (see figure I.1.2.(B)). The attraction effect is due to the fact that from the hydrodynamic point of view the surfaces act as traps for the bacterial motion. We discuss this important point in the next section.

Note that in order to monitor the global concentration of bacteria in our preparation procedures, we use a spectrophotometer *Hitachi U-2000*, which provides the absorption of the suspension at a wavelength of 595 nm. From the optical density (OD) a calibration curve was established to obtain mean bacteria concentrations up to 1.3×10^9 bact/ml (OD=1.5).

The mean density of bacteria was adjusted to reach densities at the surface that could be described as a “dilute regime" i.e. corresponding to figure I.1.3.(A) ($OD <$

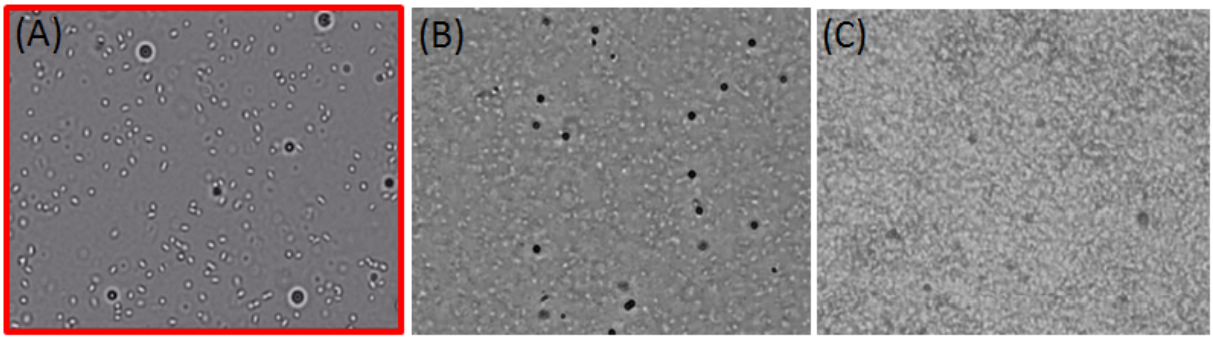

Figure I.1.3: A) Dilute Bacterial suspensions. B) Semi-Dilute Bacterial suspensions C) Concentrated Bacterial Suspension. Biofilm formation.

1.5). The central figure, I.1.3.(B), could correspond to a semi-dilute regime ($1.5 < OD < 2$). At higher concentrations a bio-film would be formed rapidly. The main focus of this thesis is on the first regime.

I.1.1.1 Hydrodynamic trapping at the walls

The accumulation of bacteria like *E.Coli* (pusher swimmers) at a solid surface was reported and measured quantitatively by Berke *et al.* (2008). A qualitative explanation was given by the same authors, and involves the attractive character of a force dipole in hydrodynamic interaction with its image. Actually this effect should exist in principle but should be very small indeed unless the dipole comes very close to the surface. It is then very likely that in this case, other forces will play an important role such as lubrication forces and also the effects of body and flagellar rotations. All these complications in the hydrodynamic interactions will keep the bacteria very close to the wall. This is why it is possibly preferable to describe the phenomenon like a trapping effect rather than an attraction effect.

From a theoretical and simulation point of view, many authors have been concerned about the problem of swimming cells interacting with boundaries. The first numerical work dealing with this subject was presented by Ramia *et al.* (1993). A bacterium is modelled as a sphere with an helical filament, and the velocity field generated by the swimmer in presence of a wall was computed using a boundary element method. They considered a distribution of punctual forces applied on the surface of the object. The magnitude of the forces was obtained by solving an integral

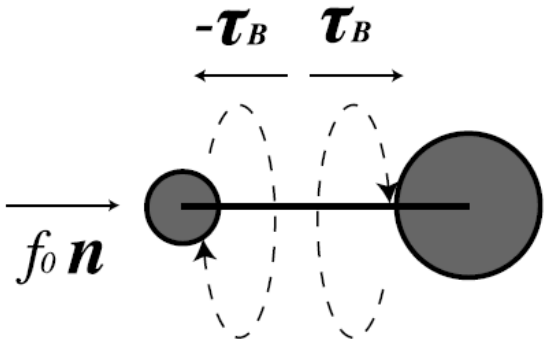

Figure I.1.4: Two spheres of different radii connected by a dragless rod, which exerts equal and opposite torques $\pm\tau_B$. Over the T-sphere, a propulsion force $f_0\mathbf{n}$ is applied by the fluid to mimic the effect of the rotating flagella.

equation for the distribution. The simulation revealed that bacteria swim close to the surface in circles with a radius of the order of the cell length ($10\mu m$). The circular motion is clockwise when viewed from the top as observed experimentally. Lauga *et al.* (2006) approached this problem differently. The same model of swimmers was considered (sphere and helical tail), but the interaction with the wall was taken into account through a resistance matrix which relates the angular and linear velocities with the torques and forces acting on the bacterium. The distance between the swimmer and the wall is an adjustable parameter of the model and was fixed in the matrix. The effect of the bacterium approaching the wall and the azimuthal stability were not explored. Di Leonardo *et al.* (2011) studied the interaction between swimming cells (modeled as rod-shaped bodies with an helical flagellum) and a liquid-air interface. They considered hydrodynamic interactions of a bacterium with its own mirror image swimming on the opposite side of a perfect-slip boundary. They found that, contrary to solid boundary conditions, the circular rotation is in the other direction (counter-clockwise).

In 2010, Gyrya *et al.* presented a simplified model of *E. Coli* introduced by Hernandez-Ortiz *et al.* in 2005, consisting of two spheres and a punctual force connected by a dragless rod. The interaction between swimmers was investigated.

In collaboration with Rodrigo Soto's group from the University of Chile and for the master's thesis of Jocelyn Dunstan, we developed a two sphere *E. Coli* model interacting with a non-slip surface, inspired by the work of Gyrya *et al.* (see Fig. I.1.4). Our aim was to investigate the dynamics of swimmers approaching the wall and also

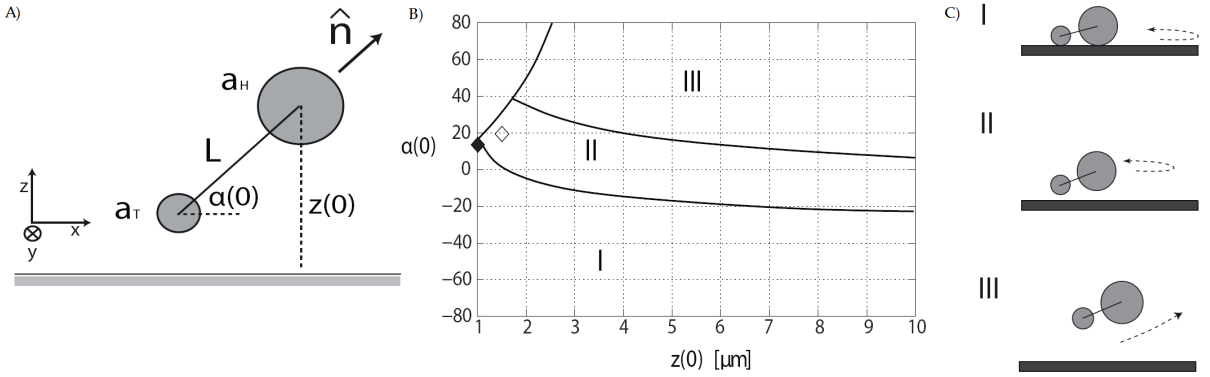

Figure I.1.5: A) Initial condition for the swimmer: the orientational angle with respect to the surface is $\alpha(0)$, and the position of the center of sphere H is $z(0)$. The geometrical parameters are $a_H = 1\mu m$, $a_T = 0.5\mu m$, $L = 2\mu m$, and the gap size is set to $\epsilon = 0.01\mu m$. B) Phase diagram of the initial conditions. Three situations are observed: (I) swimming in circles in contact with the wall, (II) swimming parallel to the wall at a finite distance, and (III) swimming away from the wall. The upper left corner is forbidden by the condition that the T sphere must be above the surface. C) Sketch of the three final regimes.

the hydrodynamic possibilities of escapism of the swimmers far from the wall. Both spheres have a different diameter and they are linked by a dragless rod. In figure I.1.4, the model is sketched. The bigger sphere is considered to be the head and the smaller one the tail on which a propulsion force was imposed in order to mimic the effect of flagella. Opposite torques exerted by the rod over the spheres were introduced to consider the axial rotation of the cell. The hydrodynamic forces and torques on each sphere are computed by taking into account the full interaction with the wall surface using the complete resistance matrix. The hydrodynamic interactions between the spheres was computed by superposing the effect that both spheres have on each other. The details of the calculations are presented at the end of the manuscript, in the paper Dunstan *et al.* (2012) accepted to be published in Physics of fluids.

We investigated for a given geometry of the bacterium, the final trajectories undertaken by the swimmer, by means of two control parameters: the initial distance to the wall $z(0)$ and $\alpha(0)$, the initial angle between the bacterium director and the surface (see fig. I.1.5.A). We chose the model parameters to match the experimental observations of *E.Coli* swimming. Considering only hydrodynamic interactions and an initial condition where the swimmer starts to move with it's head pointing towards to the surface, we found a family of trajectories for which the swimmer stops its motion

after reaching the wall.

To remove this singularity, we had to introduce a gap size ϵ (smaller than the bacterium scale), which cuts off the hydrodynamic forces and would account for the reality of surface roughness or any other physical-chemical interaction (like Derjaguin-Landau-Verwey-Overbeek (DLVO) potential) that could overcome at some distance, the hydrodynamic forces. Experiments using the TIRF technique have shown for a *Caulobacter Crescentus* bacterium, that the minimal distance of approach can be 10 nm (Li *et al.*, 2008). We found three different behaviours, depending on the initial conditions. These results are summarized on Fig. I.1.5.(B). If the motion starts with an angle pointing significantly towards the surface, the swimmer will approach the wall until contact with both spheres. Once the system reaches this state, the swimmer starts a circular motion at constant speed and with a radius of curvature in the range of 8-50 μm, depending upon the value used to regularize the resistances (consistently with experimental data). In the framework of the present model, the swimmer remains in this state forever (domain I on Fig. I.1.5.(B)). A second regime can be reached for intermediate range of height and angle (domain II). In this case it approaches the surface without touching it, swimming parallel to it, keeping a gap of approximately half a micron. The trajectory is also circular and the radius is similar, but it swims faster. At last, if the swimmer is initially placed far enough from the wall, and pointing upwards, it will be able to escape from the surface. Details can be seen in Dunstan *et al.* (2010 and 2012).

In the previous picture, the dwelling time of a bacterium at a surface when it reaches it is infinite, which makes it a perfect trap. However, it is expected that surface accidents, thermal noise, velocity agitations or the tumbling mechanism can allow the swimmer to exit the region near the wall. In a recent contribution Drescher *et al.* (2011) investigated in detail this issue from an experimental, a theoretical and a numerical point of views. They measured for *E.Coli* a dwelling time at a surface that can be as large as a minute. They argued that this dwelling time in this imperfect hydrodynamic trap is indeed sensitive to the rotation diffusion in the azimuthal direction.

As a consequence, in the perspective of developing a reliable hydrodynamic model for bacterial fluids there is a big interest to understand in great details the role of surfaces as boundary conditions and in particular to measure consequences of the

hydrodynamic fluctuations caused by autonomous swimmers present at a surface. This is the purpose of the next sections.

I.1.2 Experimental characterization of bacteria trajectories at the walls

Now I studied the motion of bacteria and passive tracers close to the wall. The following sections will describe the procedure used to monitor their motion. I will start presenting the method used to recognize and characterize the bacterial population in terms of motion at the surface. Then I will continue with the explanation of the procedure used to compute the diffusion of passive tracers.

I.1.2.1 Bacteria Detection

For all experiments described in the following section, I used a 40X magnification objective (NA =0.65) using a direct illumination. I positioned the focal plane at a constant and reproducible height of about 2.5±0.5 μm above the surface to identify the bacteria below the focal plane as a bright spot.

Figure I.1.6 displays a sequence of images for two kinds of bacteria stuck at the solid surface, taken every 1 μm (for the microscope Z-stage position). Note that in

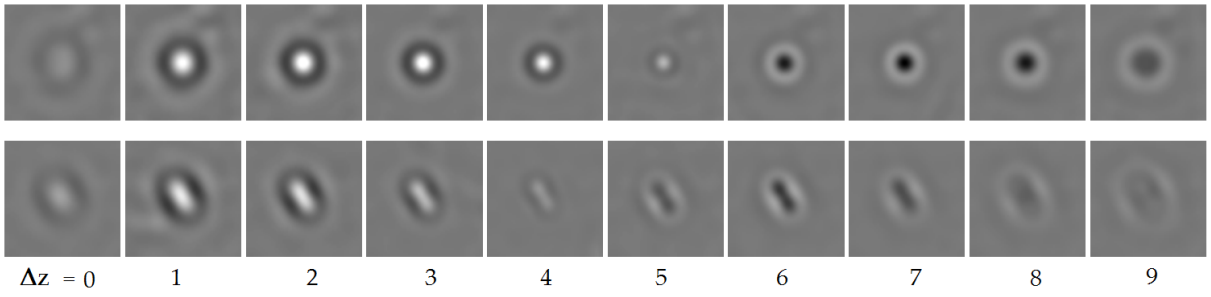

Figure I.1.6: Two different bacterium stuck to the surface are shown at different height from the bacteria focal plane. When a bacterium is in focus, a dark body with a halo appears in the image. The first image (left one) was taken far above the focal plane. Each images was taken with a Δz equal to 1 μm.

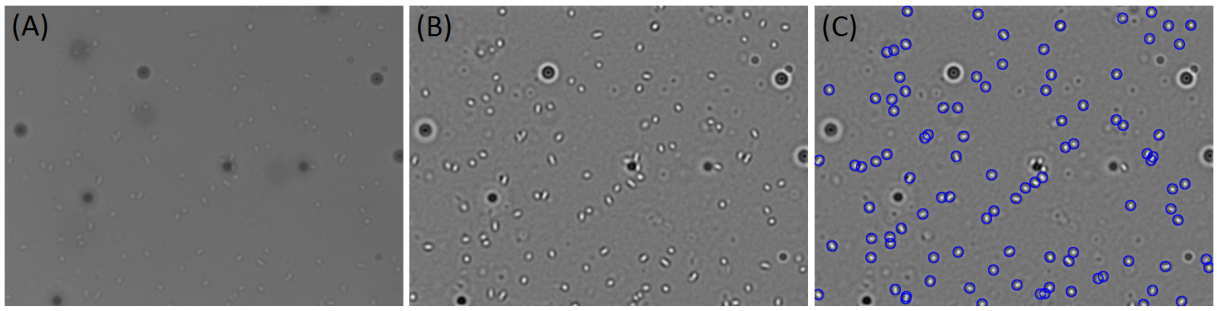

Figure I.1.7: (A) Unprocessed image of *E. Coli* solution containing passive tracers close to the bottom surface. Bacteria appear as a bright object and it is difficult to distinguish. (B) Same image after the analysis processing. It can be notice that the contrast has been increased. (C) The blue circles represent the position of the bacteria, drawing using a 10 pixels diameter circle.

order to get the actual position in the fluid, one has to multiply by the index of refraction $n \approx 1.3$. We see indeed that the bacteria below the focal plane display a bright core surrounded by a dark ring. I always managed to identify a bacterium close to the surface (there is a small fraction of them stuck on the glass slide) and adjust the vertical position in an intermediate position that corresponding typically to $\Delta z = 2$ on fig. I.1.6. Note also that we have then an observation field (in the fluid) of approximately 5 μm. This value will be important to calculate the concentration close to the surface.

Interestingly, note that on this picture I displayed two cells with different shapes. They actually correspond to cells at different stages of the division cycle. The top one is quite circular and is a bacterium emerging from the fission. We call it a “baby cell" and in the literature it is currently referred as a 1N bacterium. The one on the second line is more elongated and it corresponds to a bacterium at a later stage that has duplicated its DNA, it is called a 2N bacterium.

To identify the bacteria, videos of 20 seconds were recorded at 20 frames per second (sequences of 400 images). Each image stored in Tiff format, was post-processed using a macro program developed on *ImageJ*. Figure I.1.7.(A) shows for a typical experiment, an image of the bacteria and the particles at the bottom surface. It can be noticed that bacteria and latex beads appear in the image as bright and dark bodies, respectively. The main idea of the image processing is to distinguish automatically bacteria from passive tracers and to determine their positions. Generally speaking,

each image was processed using 3 kinds of filters (Fourier low pass band, Gaussian and Unsharp Mask) and then the maximal levels of gray were searched using quadratic fits in order to find the particle positions. For details on how images are processed, refer to appendix B. Figure I.1.7.(B) shows the corresponding post processed image, after the filtering. Fig. I.1.7.(C) illustrates the bacteria detected by the macro program.

I.1.2.2 Bacteria Tracking and Trajectory Analysis

Once the particles positions are found, the individual trajectories are reconstructed using a tracking program developed in C++. This program was developed by Thierry Darnige at PMMH lab (see Appendix B). This program provides a collection of tracks starting when a bacterium is detected until it disappears. Note that a problem may occur when eventually two bacteria come in close contact, the tracking program can either confuse the individuals of loose track. This is an issue which may create systematic detection problems of the paths at higher density. We operated in densities

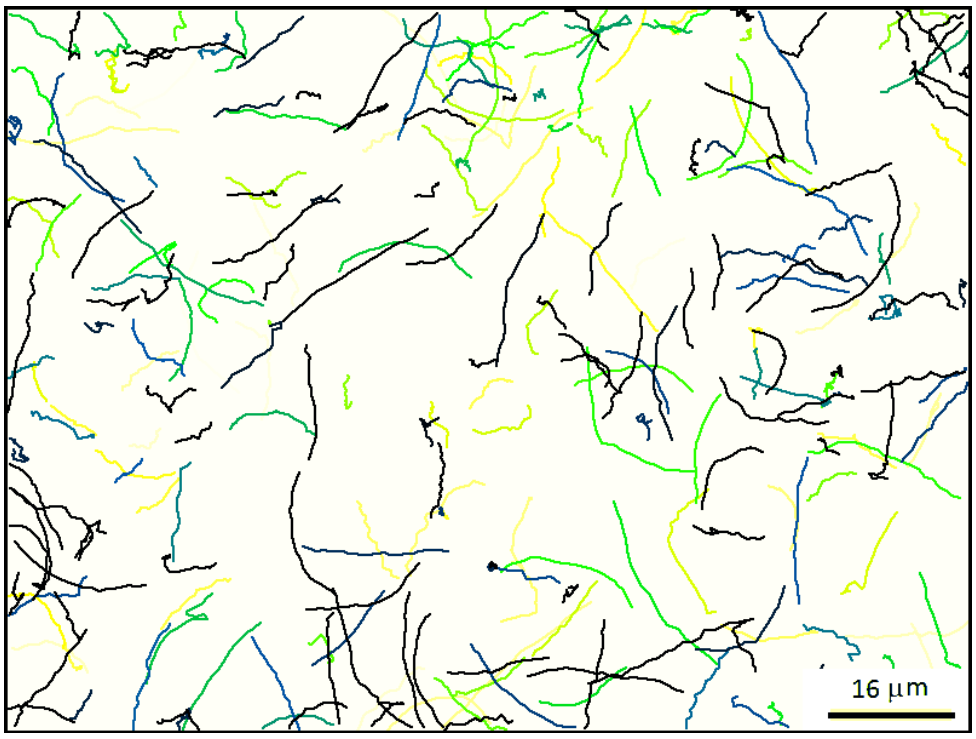

Figure I.1.8: Different bacterial trajectories. Each color represents a different bacterium and the duration of the trajectories displayed is 1.5 seconds.

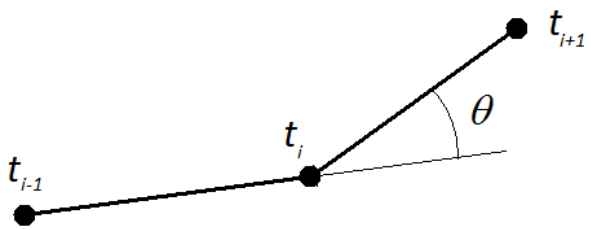

Figure I.1.9: Definition of θ that will give the mean persistence angle $| < \theta > |$ for the trajectory.

low enough so that the track persistence is high and the bacteria can still be followed for more than 10 s.

For the wild-type bacteria, we actually noticed that two different kinds of motion can be observed close to the wall. The first one corresponds to smooth trajectories such as circles or lines. The second type looks more like a random motion (different from a run and tumble motion usually found in the literature (Fig. I.1.8)). This is why I developed a program suited to clearly distinguish these two types of “populations" which may have a different influence on the fluid activity. Actually, I do not exactly know if the diffusive bacteria are with broken flagella or temporally inactive but for a given preparation, I was usually left with a ratio of them which was for a large part unpredictable (in spite of many attempts to do so). For each experiment, the images were processed to extract all the possible bacteria tracks. From each trajectory, I measured two structural parameters: the mean persistence angle ($| < \theta > |$) of the walk and the N_c ratio representing the track "compactness".

- The persistence angle is defined based upon the positions of a bacterium taken at three successive images (see fig. I.1.9). The average is performed over all the steps

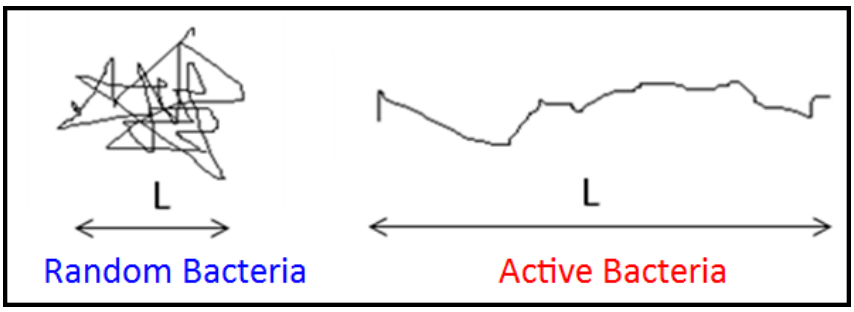

Figure I.1.10: Definition of L for both type of motion.

in the trajectory. Note as an illustration that for a random walk and a linear trajectory one would obtain respectively the values:

$$|<\theta>| \to \pi/2 \text{ (random walk)}$$
$$|<\theta>| \to 0 \text{ (straight line)}$$

- The N_c ratio represents the ratio between the maximal exploration distance of the track L (see figure I.1.10 for an illustration) and the total length of the line. Its definition is:

$$N_c = \frac{L/T}{< dr > /\delta t} \tag{I.1.1}$$

were L is maximal exploration distance of the track, T is the trajectory duration, $< dr >$ is the mean absolute value of the displacement and δt, the acquisition time (1/20 s).

With this definition when the trajectory is a straight line N_C tends to 1. In this case the value L/T and $< dr > /dt$ can be interpreted as the mean and the instantaneous velocity, respectively. For a diffusive process N_C tends to 0 for large trajectory durations.

Therefore, each track is associated with these two numbers (N_c, $< \theta >$), defining a point in a 2D space of parameters. On figure I.1.11, I display the map of the probability density obtained for 1000 bacterial tracks extracted from 4 experiments at the same mean concentration and obtained in similar conditions. The color map goes from blue (vanishing probability) to red (maximum probability). The four experiments were chosen as they seemed to show different behaviour in terms of the type of motion that bacteria may undergo. And indeed, one observes two distinct clusters in the (N_c, $< \theta >$) space, that can be identified as a clear separation between what we will call from now : "active swimmers" and "random swimmers". Since this method does not predict the swimming behaviour for short or interrupted trajectories, tracks shorter than 10 steps were systematically discarded. In practice I chose to separate the behaviour by the line represented on the figure (line of equation : $y = 2.44x$).

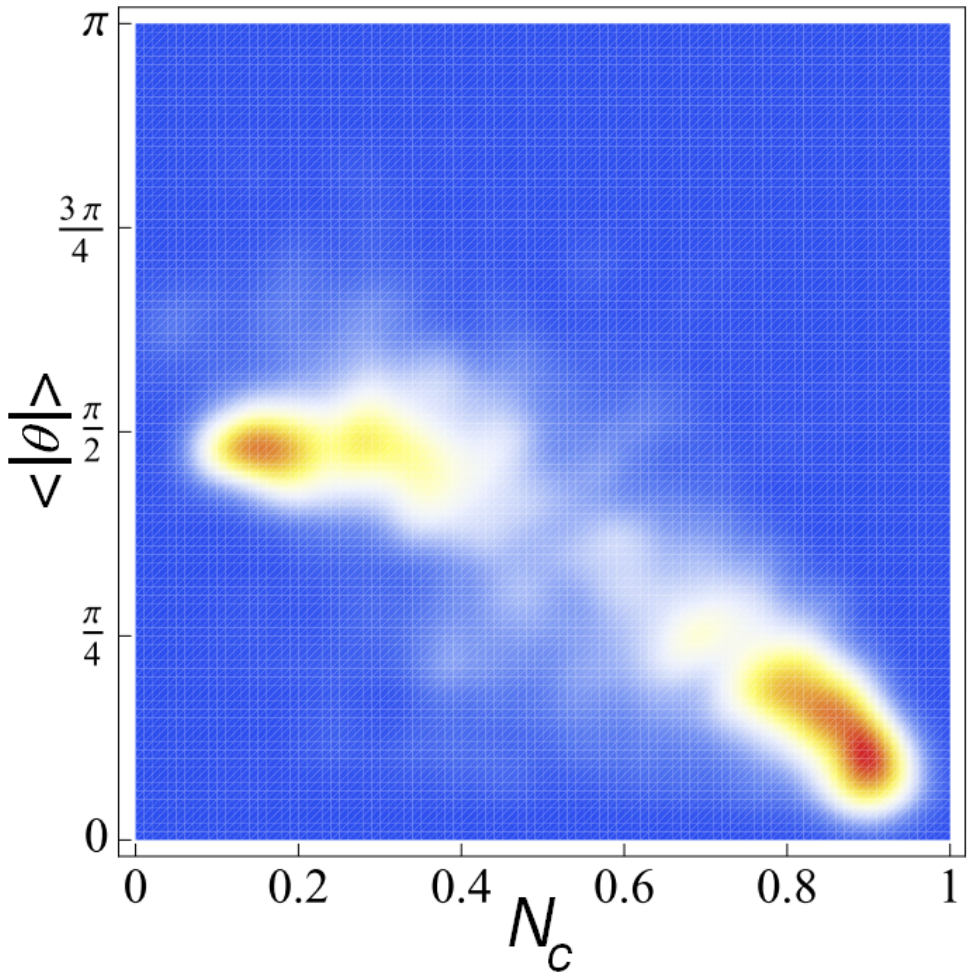

Figure I.1.11: Density probability of the observed bacterial tracks in the (Nc, $|<\theta>|$) space. The color map goes from blue for vanishing probability to red for high probability. Two clusters are identified, centred at (0.9, 0.3) and (0.17; /2), corresponding, respectively, to the active and random swimmers.

Therefore, now we are able to classify the motions into two major groups and to define at each time, a number of active swimmers $N_A(t)$. The mean fraction of active bacteria ϕ_A is then defined as the mean number of active bacteria (time averaged) divided by the mean number of bacteria (time averaged). Fig. I.1.12 shows two examples of bacterial populations that differs in ϕ_A but have about the same bacterial concentration. Active trajectories are colored in red and the random ones, in blue.

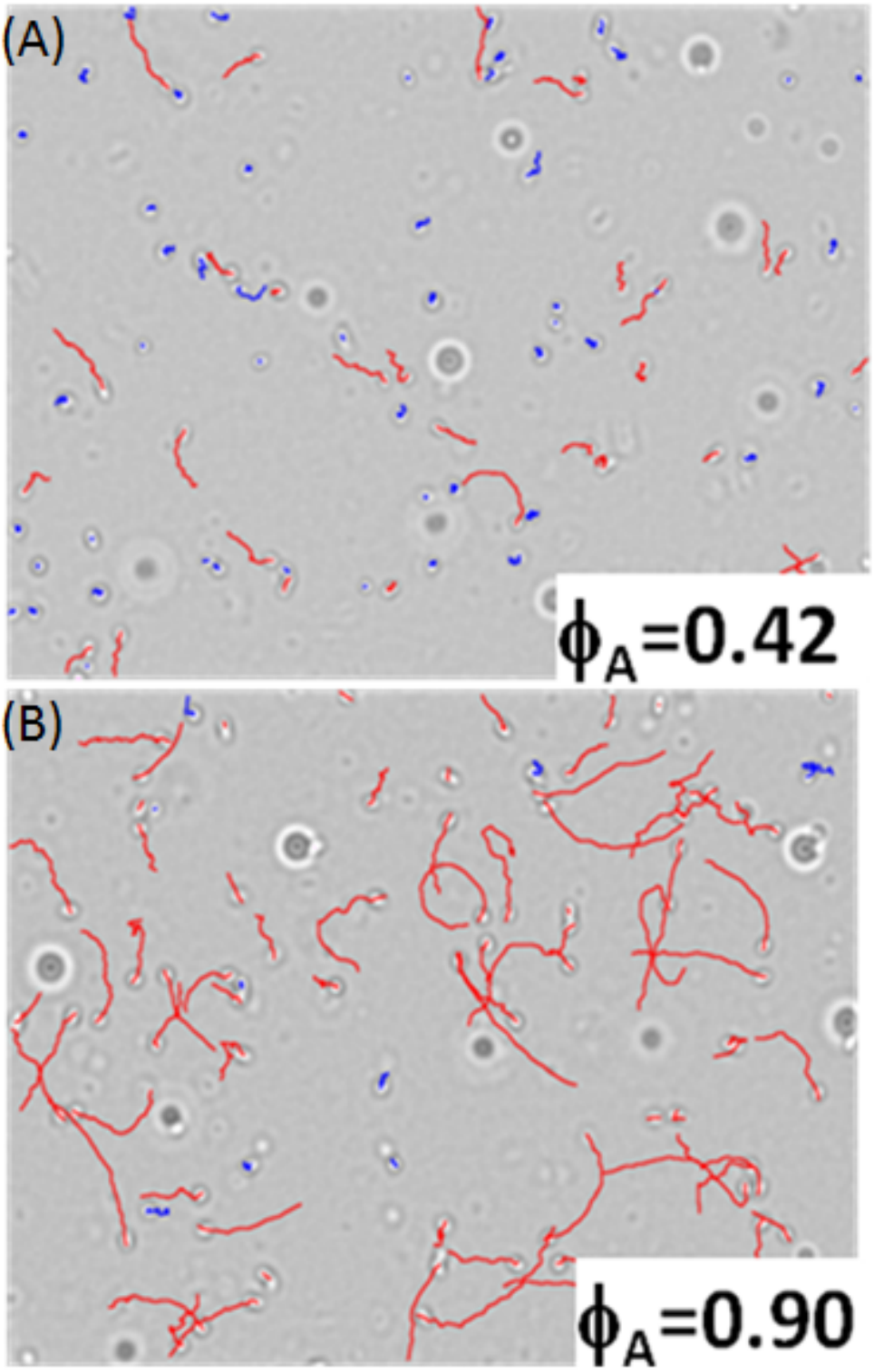

Figure I.1.12: Identification of the swimmer populations by tracking active swimmers (red tracks) and random swimmers (blue tracks), ϕ_A is the corresponding fraction of active swimmers.

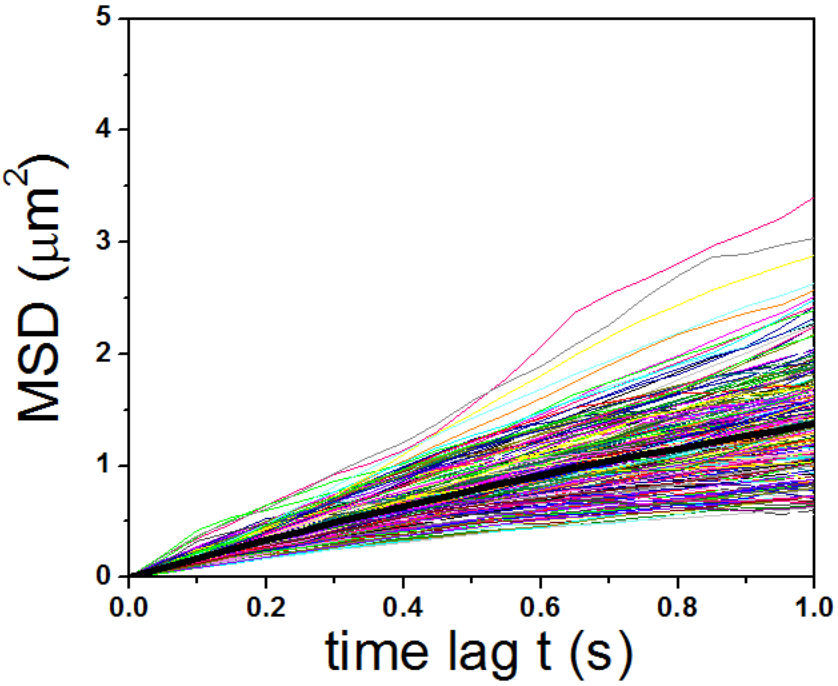

Figure I.1.13: Mean Square Displacement computed with the trajectories of bacteria that are classified as random swimmers in isodense conditions. Thick black line corresponds to the average curve. $4D_R$ represents the slope of the curve, and from the linear fitting, $D_R = 0.34\mu m/s$.

I.1.2.3 Population Motility Characterization

For a specific experiment, once the populations are classified, their motion on the surface can be characterized separately.

Random Swimmers

The random motion can be characterized by the mean square displacement MSD calculated as a function of the time lag τ, as illustrated in fig. I.1.13. The slope is $4D_R$, where D_R is the diffusion coefficient. In the case of the so called random bacteria, it can be noted that not all the analysed trajectories have a diffusive behaviour (i. e. no linear relation between MSD and the time lag), but the average of all the curves has (thick black line in fig. I.1.13). From here we can estimate a mean value of $D_R = 0.34\mu m/s$. Furthermore, for an experiment, the mean value D_R can be computed also by averaging all the tracks. For the experiment presented in fig I.1.13), this calculation

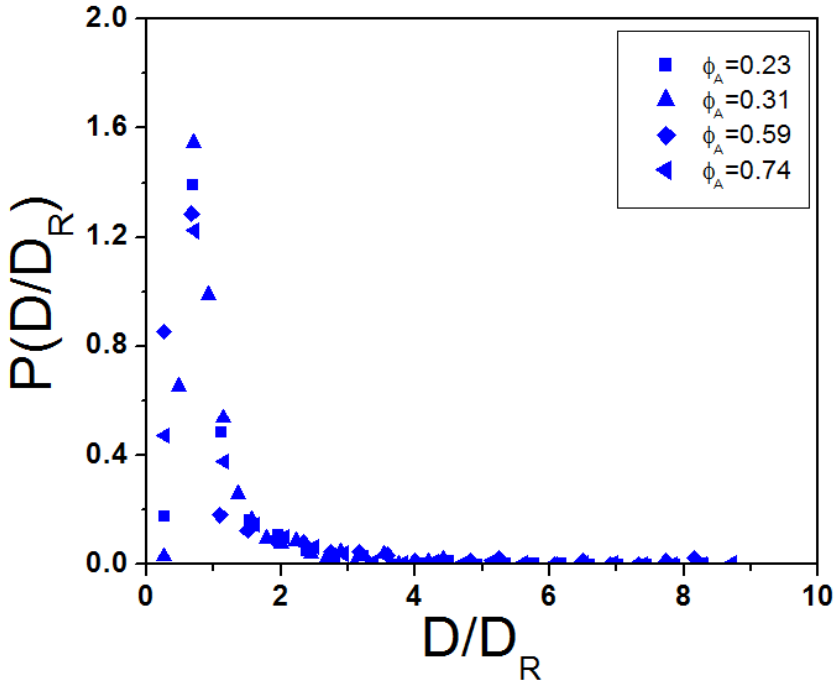

Figure I.1.14: Bacterial diffusion distribution for different ϕ_A. D_R represents the mean diffusion of the random population. D_R represents the mean diffusion of the random population. Experiments shown in this graph were performed in isodense condition. Half heigth width range from 0.6 to 0.62

gives a value of $D_R = 0.32\mu m/s$. On Fig.I.1.14, I display the normalized distribution for different fractions of active bacteria and different concentrations. It seems that the distribution shape does not vary too much. I will discuss the variations of the mean diffusivity D_R in the next chapter.

Active Swimmers

In the case of active bacteria, for each track I defined the mean track velocity V, which is the trajectory length divided by the total time. The mean velocity V_A is the average of this velocity over all the detected tracks. Note that I also checked an alternative definition of the mean velocity by weighting the mean by the track length but it did not change anything. On Fig. I.1.15, I displayed the normalized velocity distribution for different values of the active ϕ_A at two different bacteria densities, for the isodense suspension. These distributions do not seem to vary very much.

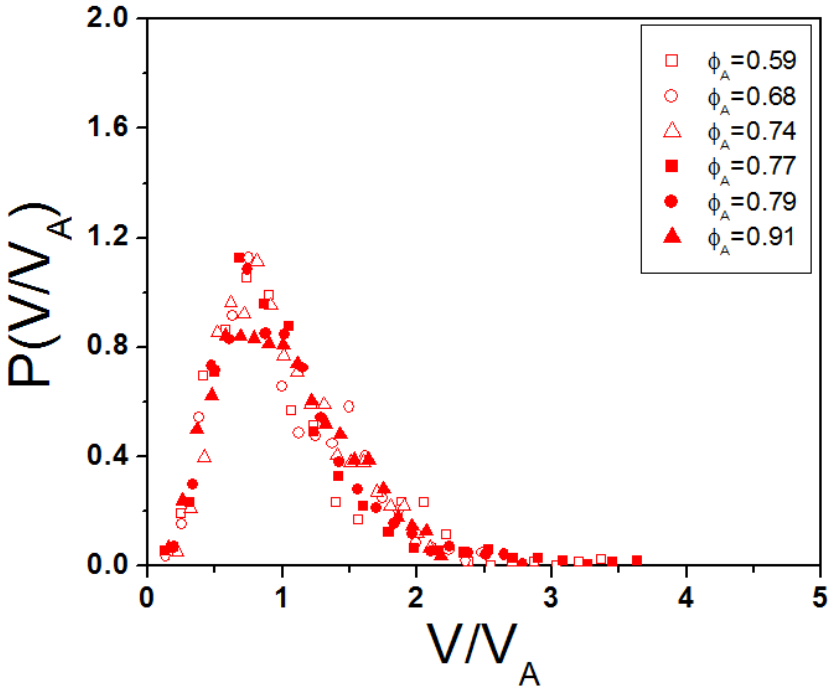

Figure I.1.15: Velocity distribution for different experiments in isodense condition. Each symbol represents different active fractions ϕ_A. V_A represents the mean velocity of the active population. Empty and filled symbols distinguish between a mean number of bacteria $< N >$=100 and $< N >$=200 in the visualization field, respectively. Half heigth width range from 0.90 to 0.95

On Fig I.1.16, I display the velocities of active swimmers (V_A) as a function of the active fraction (ϕ_A), for different experiments. Several synchronization protocols were tested in order to select bacteria at different stages of the cell cycle, which could display different swimming characteristics. We were able to produce "baby-bacteria" populations (1N short cells, 1,12 μm long) with a fraction ϕ_A much larger than the one expected for more mature bacteria populations (2N long cells, 2,5 μm long) (see fig. I.1.6). We took advantage of this difference to analyze the influence a fraction of active swimmers ϕ_A on the mean velocity V_A. Each color stands for a same population of *E. Coli*. The number of bacteria in the visualization field is distinguished, by the labels 1 and 2 corresponding respectively to $< N >$=100 and $< N >$=200. On this figure we did not see any clear dependency of the mean velocity when doubling the concentration and changing the active fraction. These results in conjunction with the invariant distribution shape of Fig. I.1.15 are in favor of a low density limit where collective effects play a marginal role.

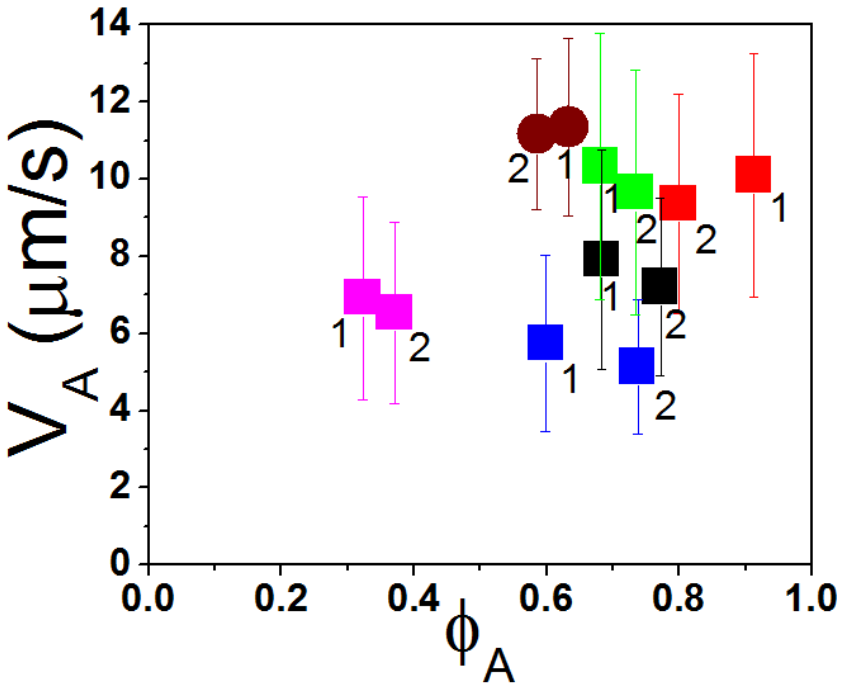

Figure I.1.16: Relation between the active swimmer's mean velocity V_A and ϕ_A. Colors represent 6 independent experiments with E. coli: 1N cells (brown, red, and green), mixture of 1N and 2N cells (black), and 2N cells (pink, blue). Labels (1) and (2) are for $< N >= 100$ and $< N >= 200$ cells in the observation field, respectively.

As mentioned before, several authors have observed that bacteria move in circular trajectories when they swim close to a solid surface(DiLuzio *et al.*, 2005; and Lauga *et al.*, 2006) and the dispersion in the radii had been related with the cell dimension. Following these observations, I was interested in the characterization of this circular motion using "baby cell" experiments, where the aspect ratios of the cells are in an narrow windows close to 1. The analysis of each trajectory was performed by circular fitting using the least square method to compute the radius. Fig. I.1.17 shows a trajectory example close to the wall and the circle obtained through the fit.

This fitting procedure is performed for all the trajectories of the experiment and from here, the distribution of radii can be computed. Fig. I.1.18 presents the normalized distribution of radii, measured in our setup for populations of different numbers of bacteria in the visualization field and high ϕ_A. In the same way, the normalized distributions do not seem to vary much with the concentration variations.

When the mean velocity V_A is plotted as a function of the mean radius $< R >$ (see

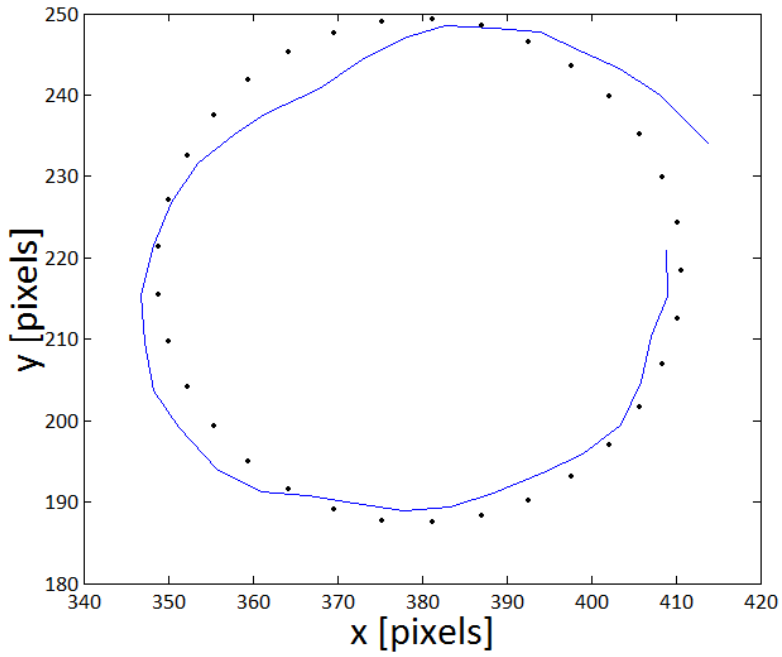

Figure I.1.17: Example of a circular trajectory fitted with a circle of 31.2 pixel radius. Scale: 1 pixel=0.16 μm.

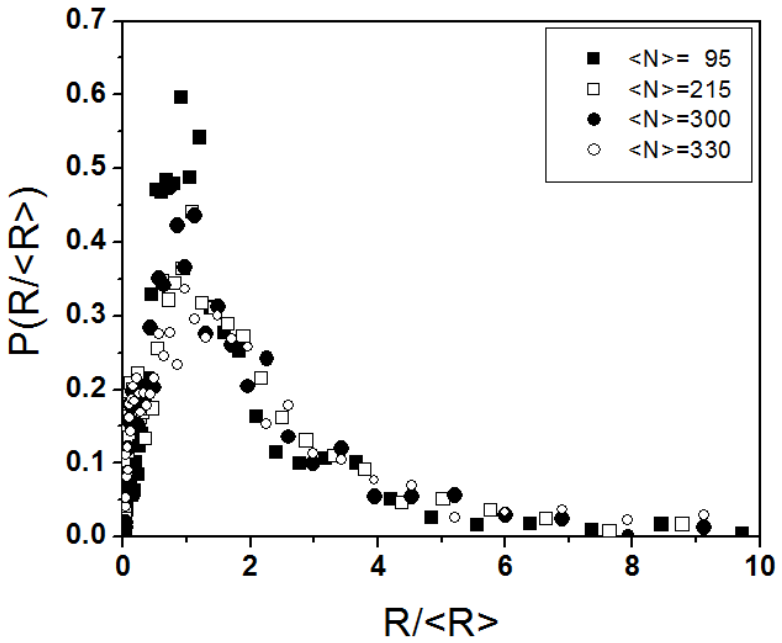

Figure I.1.18: Four normalized distributions are displayed, corresponding to experiments with constant active fraction at different bacterial concentration in isodense conditions. Each distributions was obtained by fitting all the trajectories in the experiment with circles.

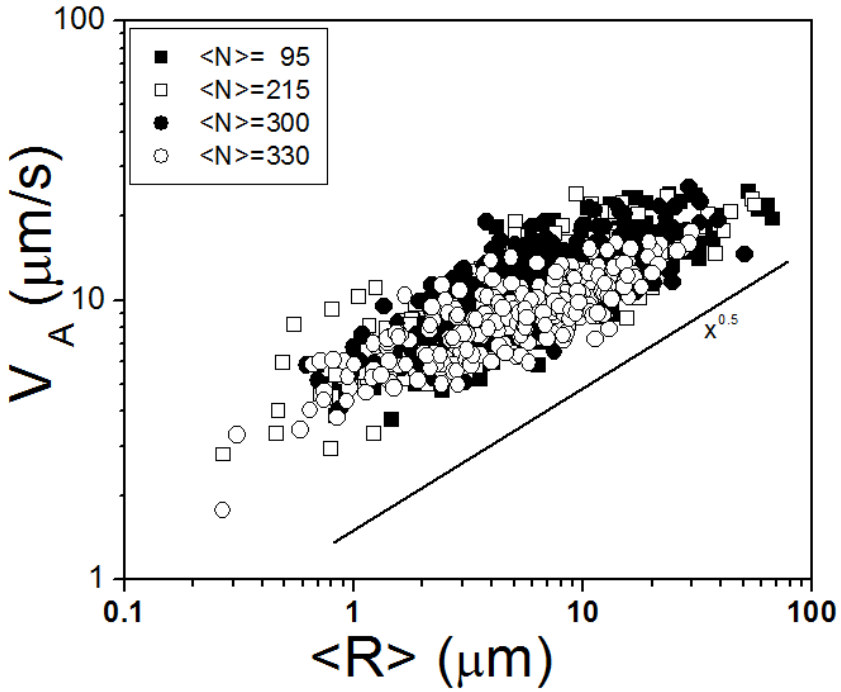

Figure I.1.19: Representation of the pair ($< R >$, V_A) for the different experiment presented in the previous graph.

fig. I.1.19) in spite of a significant data scatter, we observe a relation that seems to be increasing. Note that this relation might not be linear as witnessed by the effective power law presented as guide to the eyes. Importantly, we used in this experiment essentially "baby runner cells" within a synchronization protocol producing bacteria of about the same size and shape. We argue that this relation could be a consequence of a distribution of approaches to the surface and not a consequence of the variability in shape as argued by other authors Lauga *et al.*, 2006.

I.1.3 Motion of Passive Tracers

As noticed previously, the latex tracers always appear as dark objects (see Fig. I.1.20). This facilitates their detection when they are close to the surface. To follow them, sequences of 300 images are registered at 1 frame per second (representing a total observation time of 5 minutes). Following a similar image analysis and a tracking procedure as the one described for the bacterial motion, their trajectories are identified (See Appendix B).

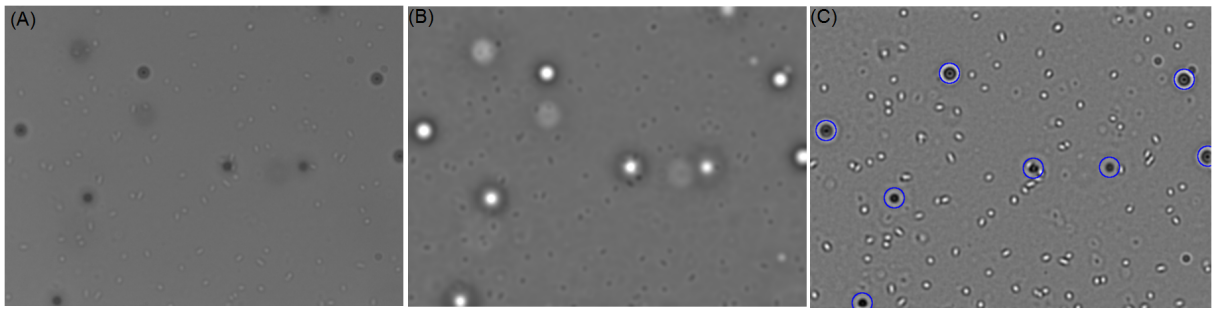

Figure I.1.20: A). Unprocessed image of *E. Coli* solution containing passive tracers close to the bottom of the chamber. The passive tracers or beads appear as dark spots and *E. Coli* as bright objects. (B). Same image after processing. Beads become bright and contrast with the background. (C). The blue circles for visualization of beads position, using a circle of 20 pixels diameter centered in the position detected by the macro, were drawn.

Figure I.1.20.(A) shows the original image. This image is processed by the macro, resulting in an inverted image where beads appear as bright objects (Fig. I.1.20.(B)). The same program recognizes the local maximal intensity, then the positions of the beads are identified (Fig. I.1.20.(C)).

After the beads trajectories are obtained (Fig. I.1.21), the mean square displacement (MSD) is calculated for each particle as a function of the time lag τ. For each trajectory of the tracer i, the MSD for a time lag τ , is computed as:

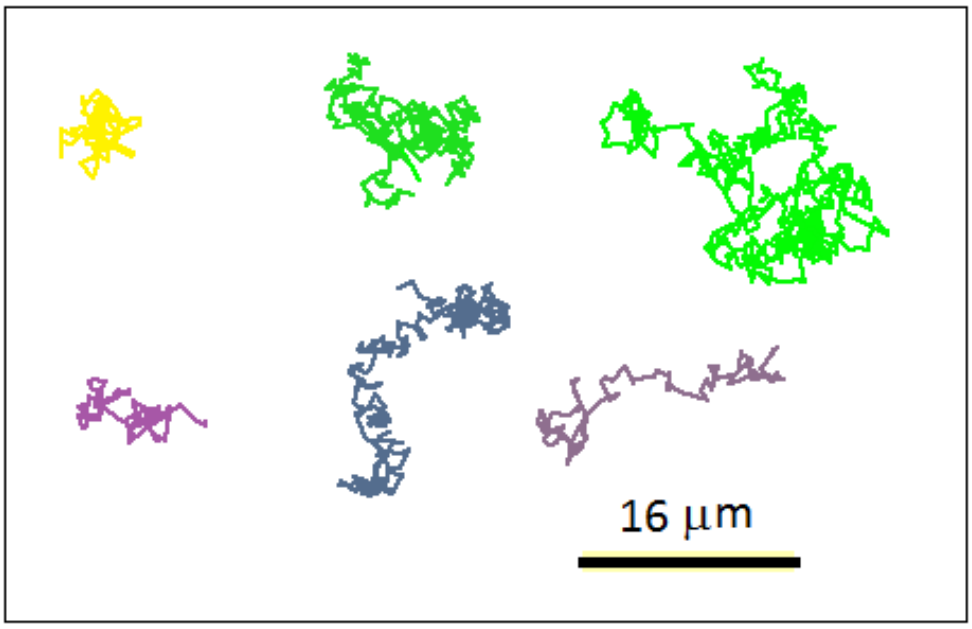

Figure I.1.21: Bead trajectories obtained by tracking the particles.

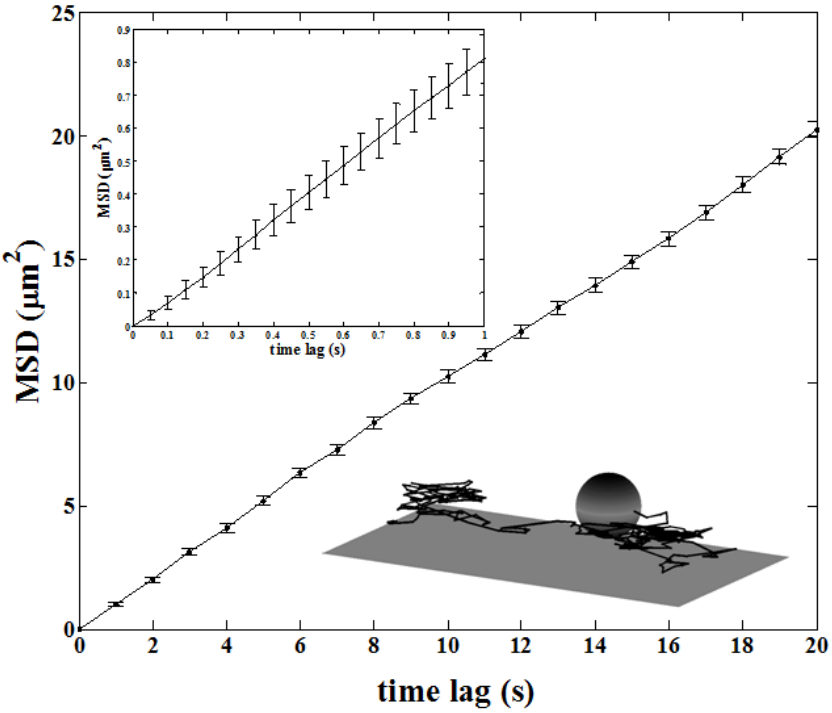

Figure I.1.22: Means Square Displacement (MSD) of a passive particle for an observation time of 20 seconds. Left-top inset: same quantity as a function of time smaller than 1 second. Right-bottom inset: illustration of a bead moving close to the wall.

$$< \Delta r^2(\tau) >_i = < [\vec{r}_i(\tau + t) - \vec{r}_i(t)]^2 >_\tau \tag{I.1.2}$$

where $\vec{r}_i$ represents the position of the *i-th* particle. The average is taken over time t. Figure I.1.22 shows an example of the MSD ($< \Delta r^2(\tau) >$) as a function of the time lag (error bars represent standard deviations) for one particle. We see a linear relationship, probing a diffusive motion, the slope being four times the diffusion constant:

$$< \Delta r^2(\tau) > = 4 D_P \tau \tag{I.1.3}$$

In the superior inset, times smaller than 1 second are explored. As we still see a linear relationship, it means that we have reached the diffusive limit for time larger than 0.1. Note that for bacteria trapped in a film, Wu and Libchaber (2000) pointed out an anomalous diffusion which could be observed for times shorter than 1 second actually it does not seem to happen in our situation. In any case, in all the following

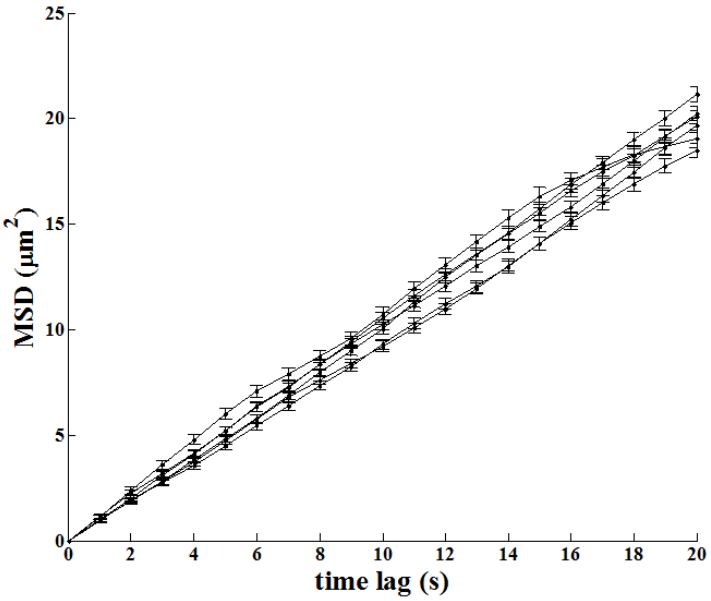

Figure I.1.23: Mean square displacement for passive particles corresponding to one experiment. The number of beads varies from one experiment to other (from 6 to 12).

measurements we used a time resolution of 1 s and 5 minutes measurements. The picture in the right-bottom illustrates a bead trajectory close to the wall.

For each experiment, 6 to 12 beads were tracked and trajectories were obtained. Fig. I.1.23 shows the MSD's obtained for one experiment in which 6 tracers were tracked. The error bars represent the standard deviation of the MSD computed at the corresponding time. We see that we have some dispersion of the diffusion constant. We define the mean diffusion constant by averaging the data points for all beads at a given time-lag and fit the slope by a linear relation. The error bar on the mean diffusion coefficient is computed using the standard deviation from the fit.

In the previously presented case, the trajectories of the tracers did not display any mean drift . This is generally the case, however some times, we noticed the presence of a net flux on the beads (typically few tenths of micron/s, see in fig. I.1.24)). We do not know exactly the reasons for this. It could be a flux of liquid caused by evaporation. However, it could be another effect caused by the activity of bacteria. In any case, we verified that during the measurements the concentration in bacteria did not change significantly. We developed several post-processing procedures to remove these drifts. The data points on mean diffusion extracted by any of these methods were consistent with the other data points when no drift is observed (see I.1.25). The

6 different methods described in the following:

Method 1: Here each MSD curve is fit with a linear function like the equation I.1.3, where the slope of the fitting represents the factor 4D. This method can predict a wrong value if there is a residual drift in the experiment. In case this happens a second method is proposed in order to correct this problem.

Method 2: In this procedure, the fitting function has the form:

$$< \Delta r^2(\tau) >= 4D\tau + V_d^2 t^2 \tag{I.1.4}$$

where V_d represents the eventual drift. The linear term correspond to the diffusive ones and the quadratic term the convective one.

Method 3: here the derivation of MSD is performed and the diffusion term can be obtained from the independent term if we fit the curve with a linear function.

Method 4: Until this stage the determination of the diffusivity uses the MSD after tracking. Here the correction is performed before the computation of the mean square displacement. Each coordinate (x and y) is adjusted by subtracting the convective part.

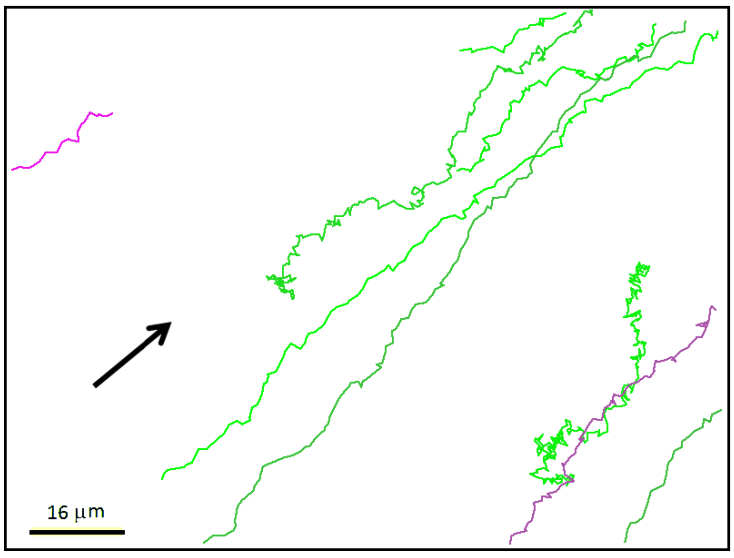

Figure I.1.24: Passive Tracer trajectories under a drift during 5 min of experiment. The arrow, represents the direction of the flow.

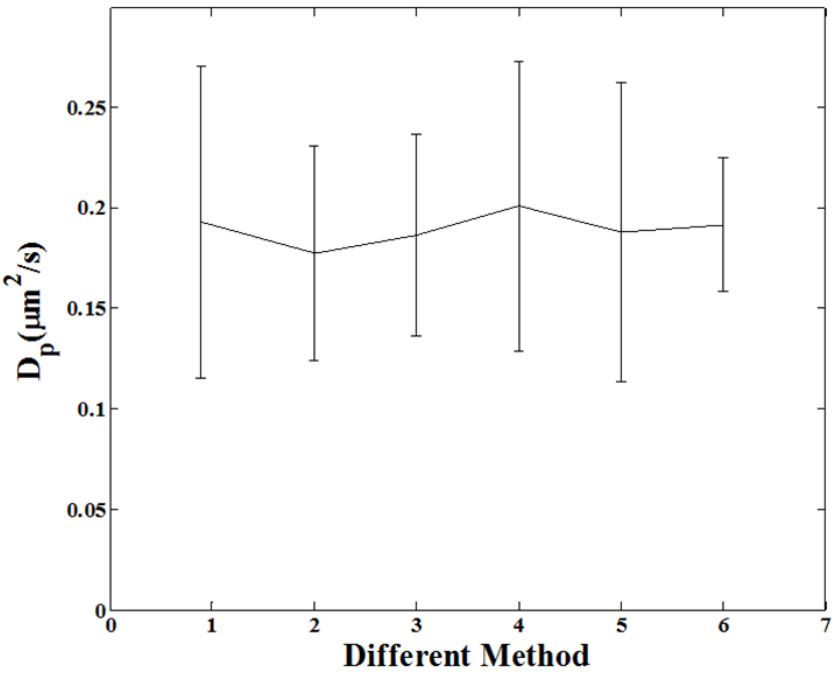

Figure I.1.25: Passive Tracer Diffusivity computed using the six different methods described in the text.

So the x or y displacement is fitted by a linear function and then the drift is eliminated. Then the MSD is computed and a procedure similar to method 1 is followed.

Method 5: Here, the same procedure as method 3 is applied but in this case the MSD calculated in the previous method is differentiated and the diffusion is calculated.

Method 6: So far, one particle displacement was taken into account. In this method, an inter-particles correlation is used to compute the mean square displacement. Two particles MSD calculation is computed following the equation:

$$< \Delta r^2(\tau) >_{ij} = < [\vec{r}_j(\tau + t) - \vec{r}_i(\tau + t)] - [\vec{r}_j(t) - \vec{r}_i(t)]^2 >_\tau \qquad \text{(I.1.5)}$$

where $\vec{r}_j$ and $\vec{r}_i$ represent the position of the particle i and j, respectively. This definition follows the one presented by Cheung *et al* (1996).

Fig. I.1.25 shows the results obtained from the different methods for one experiment. It can be noted that all the methods give similar values, and that one and two particles MSD have a particularly good agreement.

For the measurements presented from here, the values of diffusivity are systematically taken from method 1.

I.2

Diffusion enhancement

In this chapter, I will present an experimental investigation of the Brownian motion activation of passive particles in relation to the activity of swimmers close to a solid wall. I will investigate four different situations. Three related to the presence of *E. Coli* using different swimming media and chamber geometries, I will investigate the effects of confinement and swimming velocities. The last situation is concerned with self-propelled artificial swimmers and it is made in collaboration with Pr. Thomas Mallouk from Penn-State University. These microscopic bimetallic rods were synthesized in his laboratory.

I.2.1 Diffusion enhancement in non-buoyant condition

We will consider in this section results obtained for the non-buoyant suspensions (mixture MMA/percoll see I.1.1). We seek to connect the motion of active bacteria at the surface as described in the previous section with the diffusion coefficient of the passive tracer. Following the previously described protocols, for each experiment, we prepare bacterial suspensions yielding a density of bacteria at the surface $n = \frac{<N>}{V_T}$, where $< N >$ is the mean number of bacteria in the visualization field and V_T the corresponding volume ($96x128x5\mu m^3$). As described previously, from the different populations sorted according to their motion, one can define a fraction of active swimmers ϕ_A, and a mean velocity V_A of these active swimmers. To characterize the activity at the surface I define the "active flux" J_A as :

$$J_A = n_A V_A \tag{I.2.1}$$

were n_A is the active concentration given by,

$$n_A = \frac{\phi_A < N >}{V_T} = \phi_A n \tag{I.2.2}$$

Systematic experiments varying the bacteria concentration were done for two tracer sizes and in each case the mean diffusion of the passive tracer D_P was obtained.

On Fig. I.2.1, I plot the diffusion of the beads D_P as function of the "active flux" J_A. The results are displayed for the 1 and 2 μm particles. Here the circles represent

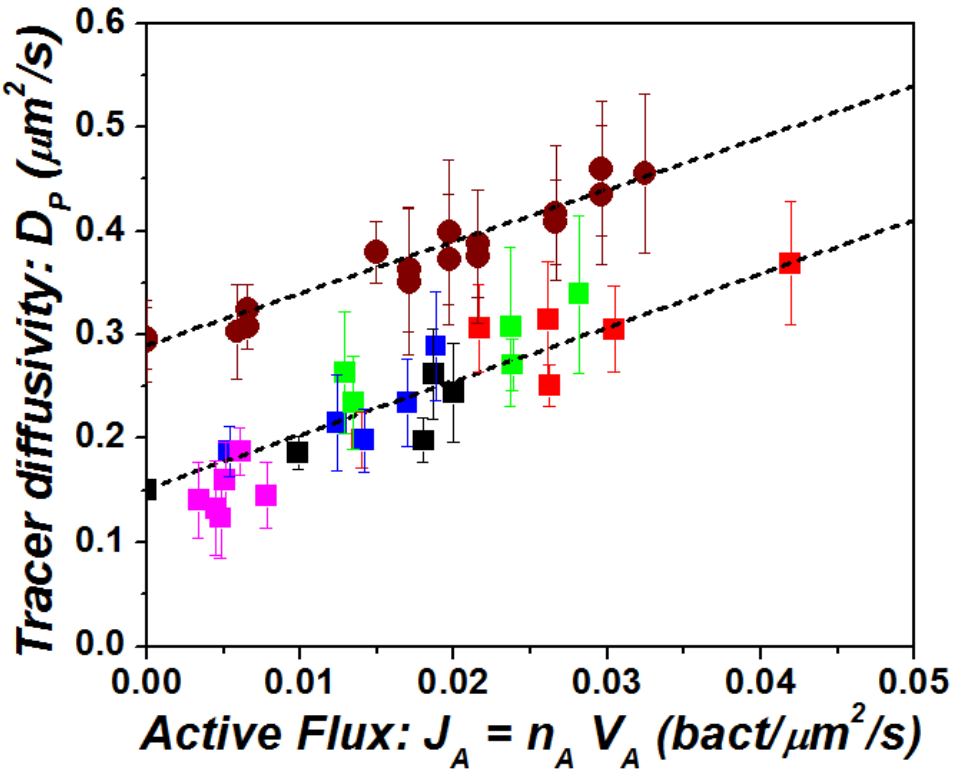

Figure I.2.1: Enhanced diffusivity D_P of passive tracers as a function of J_A in non-buoyancy conditions. Squares and circles represent tracers of 2 and 1 μm diameters, respectively. Each color represents an experiment performed over a range of bacterial dilution. In the graph, 6 independent experiments are shown. Colors represent experiments with 1N cell (brown, read, and green), 2N cell (pink and blue) and a mixture of both (black).

experiments performed with 1 μm beads and the squares show the results with 2 μm beads. Note that in this graph, we have for the 2 μm beads, the results on *E. Coli* corresponding to the 1N and 2N types as described in I.1.2.1. Interestingly all data seem to group on a straight line of the type :

$$D_P = D_P^B + \beta J_A \tag{I.2.3}$$

where D_P^B is the ordinate at the origin which depends on the tracer size and would correspond to the Brownian motion close the wall in the absence of bacteria. Its value is given by the relation:

$$D_P^B = \alpha D_B = \frac{\alpha k_b T}{3\pi\eta d} \tag{I.2.4}$$

here, D_B is the thermal diffusion in the bulk, k_B is the Boltzmann constant, T is the absolute temperature, η the viscosity of the liquid and d the diameter of the particle.

- The value α appears as a consequence of the interactions of the particles with the wall due to the lubrication force and the surface potentials. In a pure hydrodynamic framework, it is often called the hydrodynamic screening factor. This parameter depends on the bead distance to the surface (Brenner, 1967; Goldman and Brenner, 1967; Holmqvist *et at.*, 2006; and Huang and Breuer, 2007), vanishing at contact and going asymptotically to 1 at large distances (recovering the Brownian value in the bulk). In reality the density matching is not perfect which could explain the fact that the value of α for $d = 1\mu m$ ($\alpha = 0.64 \pm 0.08$) is slightly different than the value found for $d = 2\mu m$ ($\alpha = 0.74 \pm 0.03$).

- The other parameter β represents the slope that can be determined experimentally by a linear fit. A dimensional analysis of the equation I.2.3 yields that this pre-factor is a length to the power 4. For both types of bead, it seems that β is of the same value: $\beta = 5 \pm 0.4$. This would correspond to $\beta = \Lambda^4 = (1.5\mu m)^4$. So this characteristic size $\Lambda = 1.5\mu m$ is of the order of the typical size of a bacterium.

I.2.2 Diffusion enhancement in buoyant condition

Now we present a series of experiments done with MMA only. As discussed previously (chapter see I.1.1 for protocol described in Appendix A), the aim is to be able, by changing the pH, to vary the rotation velocity of the molecular motor and then the swimming velocity of the bacteria. However, the price we pay is that we cannot achieve a density matching between the solution and both the beads and the bacteria. We actually tested that the MMA-Percoll mixture changes strongly its viscosity with pH and forms a gel at low pH. It is important to note that for MMA only, pH variation does not affect the viscosity of the fluid (see Appendix A).

In the previous series of experiments under buoyant conditions, we only succeeded, in changing the maturity of the cells, to vary the mean swimming velocity by a factor of two. To test more extensively the empirical relation (I.2.3), I performed the same type of experiment under pH varying from 5.2 to 9. In this context, the latex particles will sediment and they will stay close to the bottom wall and so will the bacteria. Then, I present series of experiments where I fix the pH at a value of 6.9 and then change the confinement by approaching the upper wall.

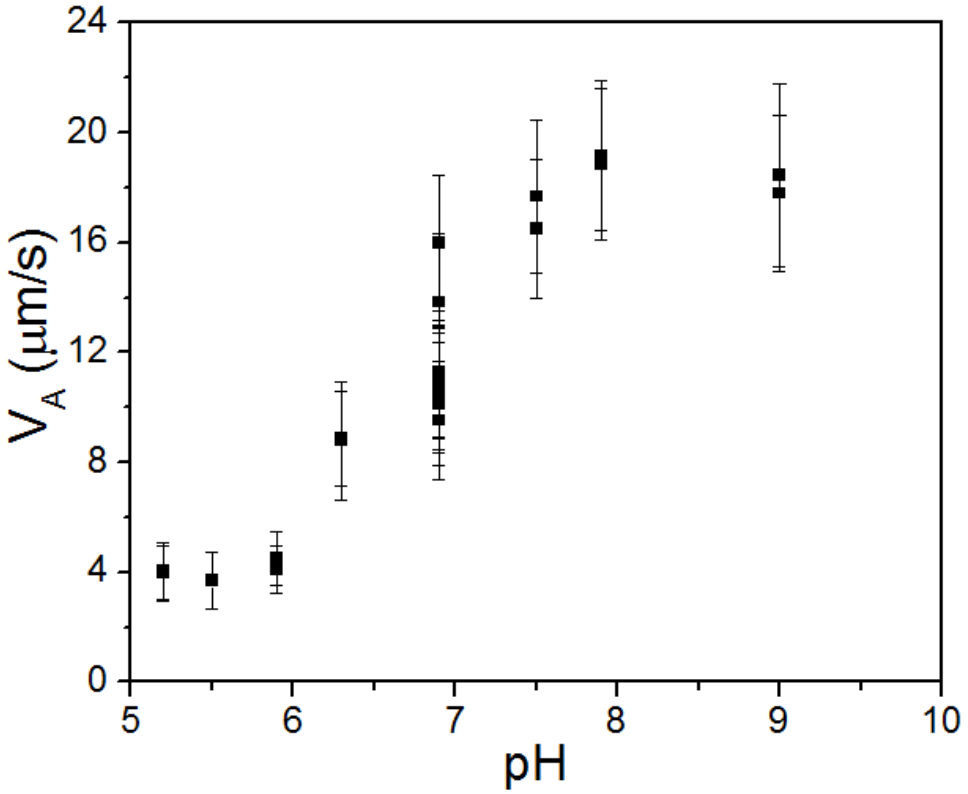

Figure I.2.2: Effect of the pH in mean velocity V_A of the active population using MMA solution.

I.2.2.1 Varying the swimmer velocity

Minamino *et al.* (2003) studied the effect of pH on *E. Coli* and *Salmonela* motility. They varied the pH between 5 and 7.8, showing that in the presence of potassium acetate, there is a significant variation of the swimming speed reaching a maximum at pH equal 7. Inspired by this result, I used a similar protocol (see Appendix A) to vary the velocity of the bacteria and I performed the same kind of experiment as shown in the previous section, varying the bacteria concentration and the pH.

The analysis of the active bacteria motion at the surface shows that for suspensions with a pH varying from 5.2 up to 9, the swimming velocity can increase with factor 5 (see Fig.I.2.2).

In this context I measured the diffusivity of a 2 μm diameter passive tracers and the corresponding activity of the active swimmers. Fig. I.2.3 shows the relation between passive tracer diffusion D_P and the active flux J_A. Different colors represent different values of pH. Again the data seem to collapse on a straight line that can be represented

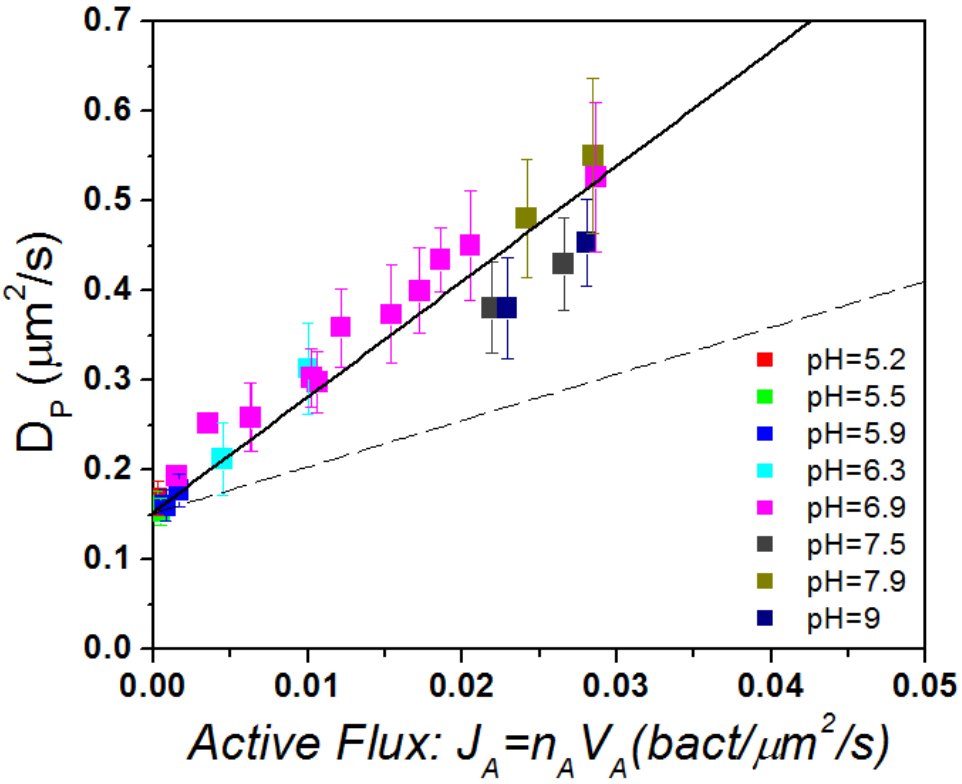

Figure I.2.3: Enhanced diffusivity D_P of passive tracers as a function of J_A in buoyancy conditions. Squares represent tracer of 2 μm diameters. Each color represents an experiment performed with different pH.The black line represents the linear fit and the dash line represents the result obtained under isodense condition for a passive tracer of 2 μm diameters (See fig. I.2.1).

by equation I.2.3. In this case, the value of α gives 0.8 ± 0.08 and the value of β is $13 \pm 0.73 \mu m^4$ corresponding to $\Lambda = 1.89 \mu m$, a value significantly higher than the one found for non-buoyant conditions.

I.2.2.2 Varying the wall confinement

In this section, the influence of the confinement due to the presence of a top wall will be discussed. First, I performed series of experiments to study the Brownian motion, of $2 \mu m$ diameter latex particles in the presence of two walls in pure MMA at pH=6.9. The different gaps between the walls were obtained by sicking by evaporation particles with bigger diameter h, upon drying they distributed as a big circle, on the bottom coverslip, hereafter the suspension containing bacteria and the passive tracers

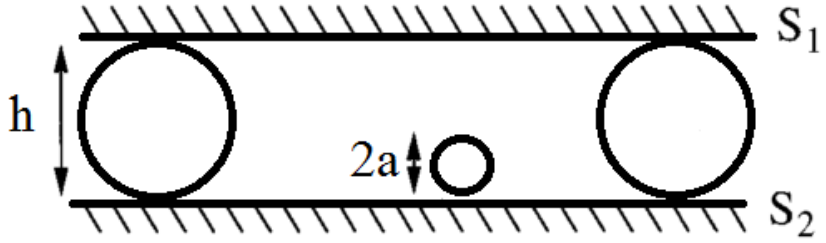

Figure I.2.4: Schematic of the chamber used to vary the distance between bottom and top walls. Beads of diameter h are used as spacers.

was dropped inside that circle and the upper coverslip was put on top of the big particles creating the chamber. In order to avoid evaporation, the drop was sealed by a layer of paraffin oil. Fig. I.2.4 shows the setup of the experiments. Minimal media at pH 6.9 was used, as mentioned before.

Fig. I.2.5 shows the diffusion of 2 μm diameter particles in function of the chamber height. The graph shows that the diffusion decreases when the constriction increases. The graph also includes two previous experimental results obtained by (Feistosa and

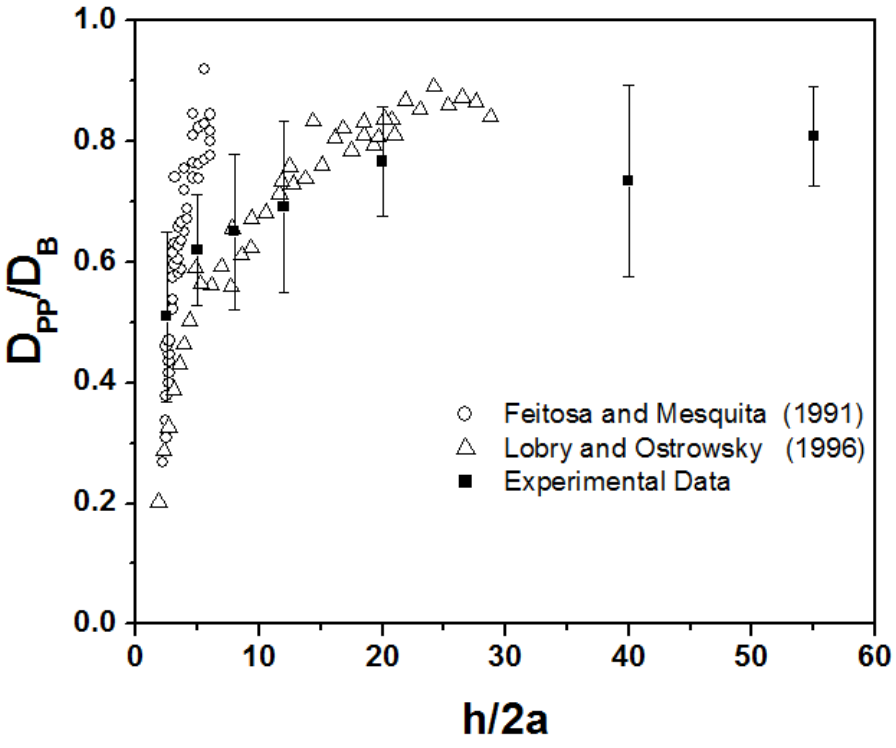

Figure I.2.5: Effect of confinement on the Brownian diffusion of passive tracers (without bacteria). Comparison with previous studies.

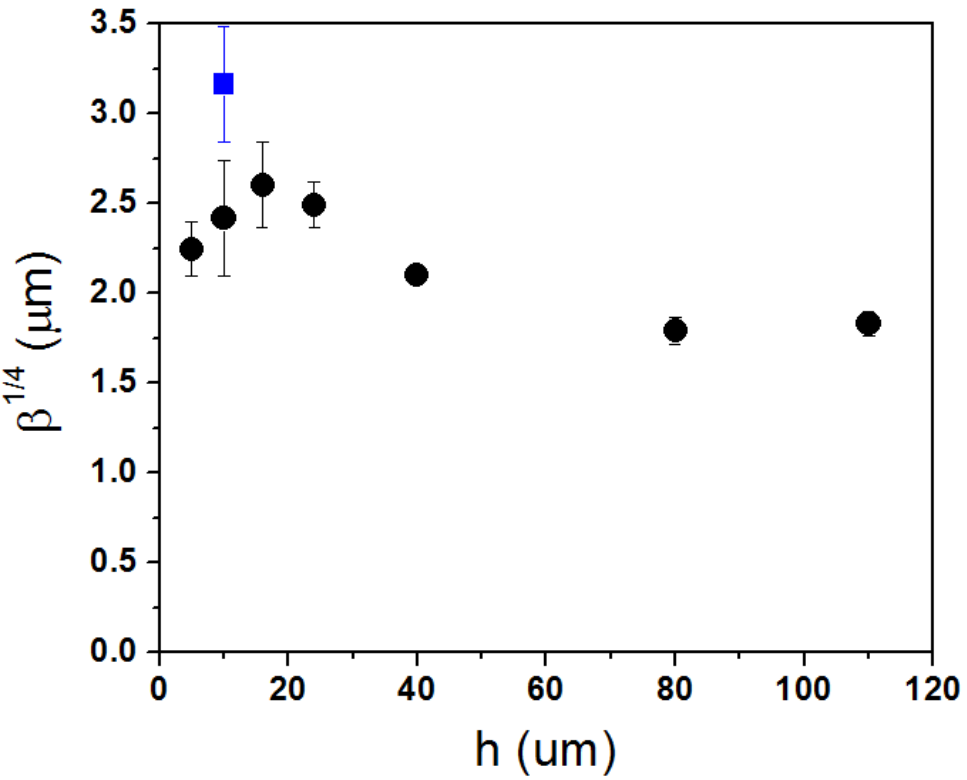

Figure I.2.6: Effect of the confinement in the $\beta^{1/4}$ value. Experiment performed in MMA at pH 6.9, using 2 μm diameter passive particles. Blue symbol, represents the value obtained from Wu and Libchaber experiment (2000).

Mesquita, 1991; Lobry and Ostrowsky, 1996) about the observed Brownian motion of passive particles in a confinement problem . It can be noticed that our experimental results are in concordance with the results obtained by Lobry and Ostrowsky.

After quantifying the effect of the wall on Brownian motion, I decided to study the influence of Bacterial activity on Brownian motion activation in such confined environments. To this purpose, I performed measurements at different bacterial concentrations and the various confinement heights reported in Fig. I.2.5. For all experiments in this configuration, the values of β were computed. Fig. I.2.6 shows how the length $\Lambda = \beta^{1/4}$ varies with the chamber height h. This result shows that the momentum transfer to the liquid is more efficient when the system is confined, reaching a maximum around 15 μm.

An interesting observation can be deduced from Wu and Libchaber's previous results. In their experiment, they observed an increase of the passive tracer diffusivity from 0 to 120 $\mu m^2/s$ when the bacterial concentration increases from 0 to

$6 \times 10^{10} Bacterias/cm^3$ (See Fig. 4 in Wu and Lischaber, 2000). In this work the mean velocity is approximately 20 $\mu m/s$, given a active flux varying from 0 to 1.2 $Bacteria/\mu m^2/s$. With these values we can infer the slope $\beta = \Delta D/\Delta J_x$ which yields a value of $\beta = 100\mu^4 = (3.16\mu m)^{1/4}$. Let us remind that Wu and Libchaber are working in a $10\mu m$ thin film which represents hydrodynamic boundary conditions different from our solid surfaces confinement. Nevertheless, we see that in terms of Λ both our results still come very close. However, quantitatively, the value of Wu and Libchaber is 30% higher, I would be interesting to see if this difference could be rationalized on the base of hydrodynamics interactions and boundary conditions.

I.2.3 Artificial Swimmers

In recent years, a vivid interest has emerged around the study of synthetic micromotors and auto-propelled artificial swimmers (Paxton *et al.* (2004), Dreyfus *et al.* (2005), Wheat *et al.* (2010) and, also Palacci *et al.* (2010) and refs. inside). A practical way to reach the autonomous motion of microscopic or colloidal objects is to use "Janus" properties of the surface such as bimetallic Au/Pt rods (Paxton *et al.*, 2004) or spheres (Wheat *et al.*, 2010).

In collaboration with Pr Mallouk, we used platinum/gold (Pt/Au) bimetallic rods synthesized in his group. In Pr Mallouk´s laboratory, Paxton *et al.* had shown in 2004 that suspended in an hydrogen peroxide solution, the rods display an autonomous motion quite mimetic of micro-organism motility. For micron size rods, velocities comparable to flagellated organism were reported. At the time, they proposed a mechanism to understand the motion linked to a tension gradient through the interface that is dynamically re-established by the reaction when the rode moves through the medium. In 2006, a new series of experiments were performed using Pt/Au inter digitated microelectrodes (Paxton *et al*, 2006). The thrust involves the oxidation reaction catalyzed by the Pt and the reduction in the Au that can be expressed as:

$$Pt : H_2O_2 \rightarrow O_2 + 2H^+ + 2e^-$$
$$Au : H_2O_2 + 2H^+ + 2e^- \rightarrow 2H_2O$$

This reaction requires an electron flow from platinum to gold. After the confirmation of the electrochemical decomposition in the microelectrodes, a relation between axial

velocity of the rod and the current density was found. Wang *et al* (2006) studied the decomposition of hydrogen peroxide in the combination of several metals and, by means of determining the potential of the bimetallic rod, they could predict the direction of motion.

Recently, a more complete and clear picture of all the mechanisms at work to produce autonomous motion was proposed by of Moran *et al* (2010) through a theoretical model (and experimental data). They show that the propulsion mechanism of Au/Pt rods is a consequence of a reaction-induced autoelectrophoresis. In the model, the motion is driven by electrical body forces (generates by concentration of the charged species) and a corresponding counter-hydrodynamic flow around the particle.

In this section, I present results obtained with such self-propelled Au/Pt rods of dimension 1,8 μm in length and 0,4 μm in diameter. A schematic representation of these rods and a field emission scanning electron image are shown in the fig. I.2.7. In comparison to bacteria, it can be noticed that they are very similar in size to the *E. Coli* cell body (1.9 μm long, 0.8 μm diameter) without taking into account the flagella (15 μm long for *E. Coli*). Note also that the mode of propulsion is intrinsically different from the on with flagella. Rods also have a much higher density ($17 g/ml$)

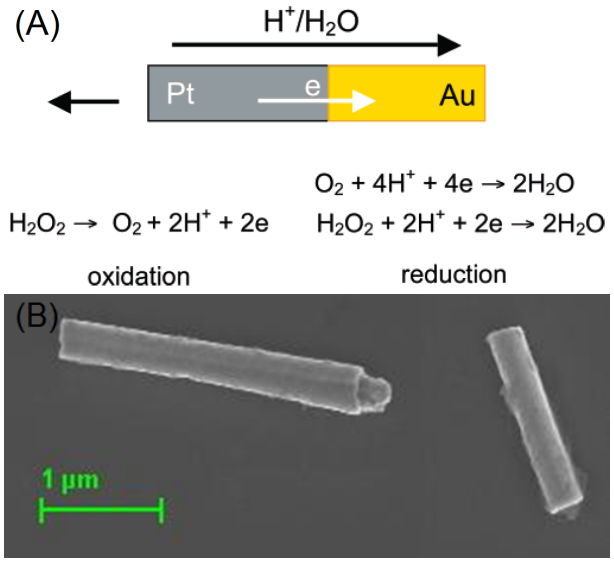

Figure I.2.7: (A). Scheme of Au/Pt rod, indicating where the reduction-oxidation takes place. In the two reduction-redaction ends, the four-electron reduction of oxygen to water is dominant in comparison to the hydrogen peroxide reduction (Wang *et al*, 2006). (B). Field emission scanning electron microscopy of bimetallic rods used in the experiment.

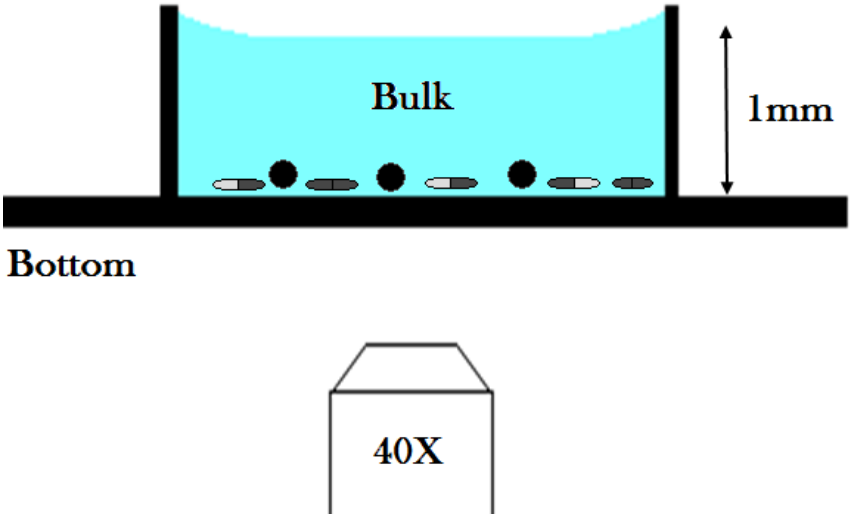

Figure I.2.8: Scheme of the setup used in the Au/Pt rod experiments. An open chamber was used in order to release the formation of bubbles. The videos were taken close to the bottom of the chamber as in the bacterial experiment

and sediment on the bottom surface. In the presence of $1\% - 10\%$ hydrogen peroxide, these particles propel in the axial direction towards the platinum side.

The experiments were conducted in a manner very similar to those involving *E. Coli* and described in the previous section. We use mixtures of passive and active rods, both of the same shape, in order to mimic distributions of diffusive/active swimmers. The activity of the fluid is monitored using passive tracers [1 μm (Dynal-MyOne, $1,8 g/ml$) or 2 μm (Beckman-Coulter, $1,027 g/ml$)]. The mixture of active and passive rods as well as the tracers are observed in an open chamber (i.e. without the upper wall, see Fig. I.2.8). This allow the oxygen micro-bubbles produced by the reaction to escape from the chamber.

The concentration of H_2O_2 was varied, as well as the concentration of active rods [$n = 3 - 20 \times 10^6 rods/ml$]. In all cases, all the particles in the suspension were localized at the bottom of the chamber due to sedimentation. Short videos (20 s duration at 20 $frames/s$) were used to track rods motion and long videos (40 s duration at 10 $frames/s$) were used to quantify the diffusion of the passive tracers. Note that the inactive rods mimicking the diffusive swimmers are made of gold only. Mixtures of both types were prepared keeping constant the total number of rods at the surface.

After applying a tracking processes to the images and a discrimination between

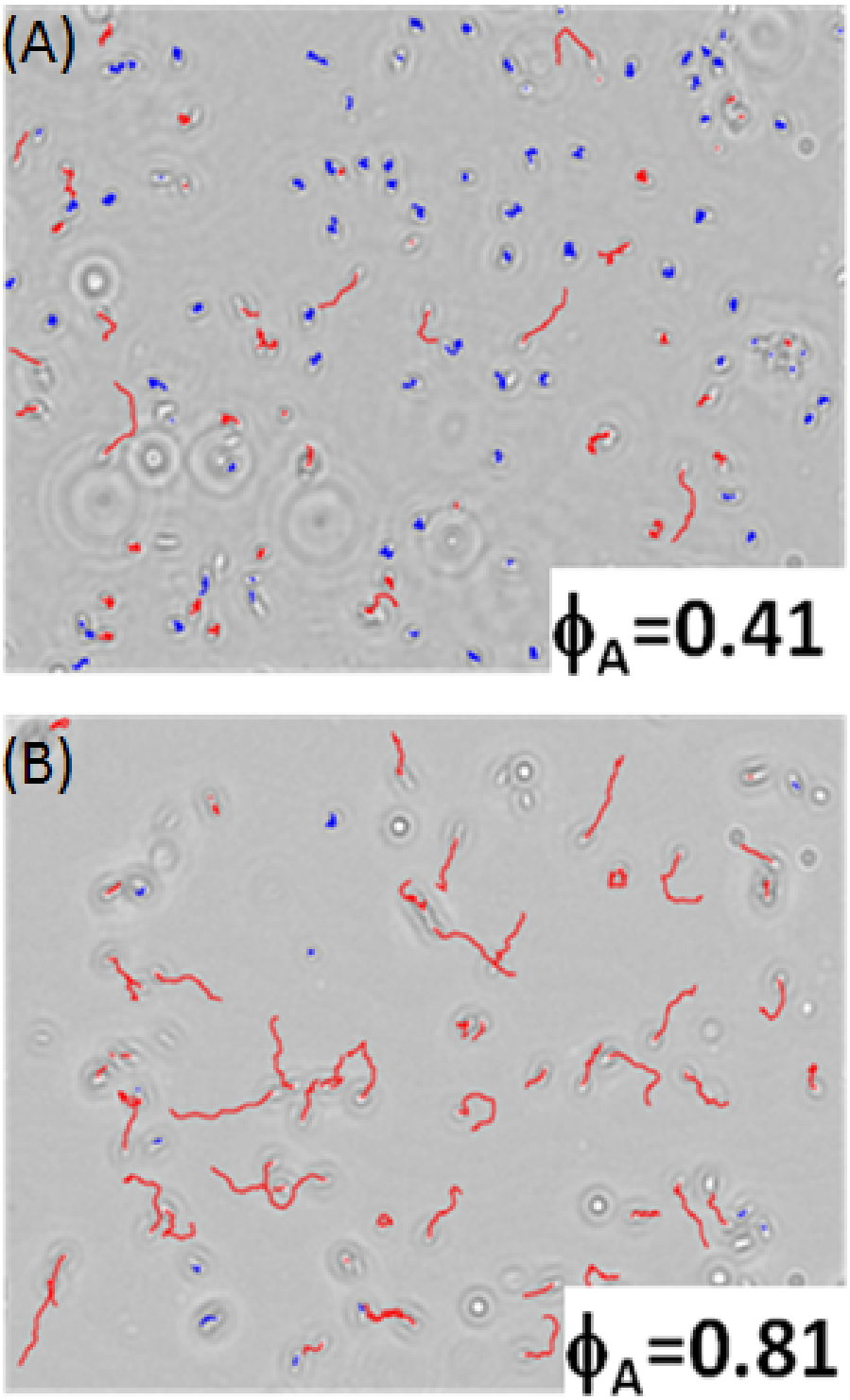

Figure I.2.9: Two experiment using a mixture of Au rods and Au/Pt rods, given two different values of ϕ_A.

"active" and "diffusive" rods, in exactly the same way as described for bacteria, I com-

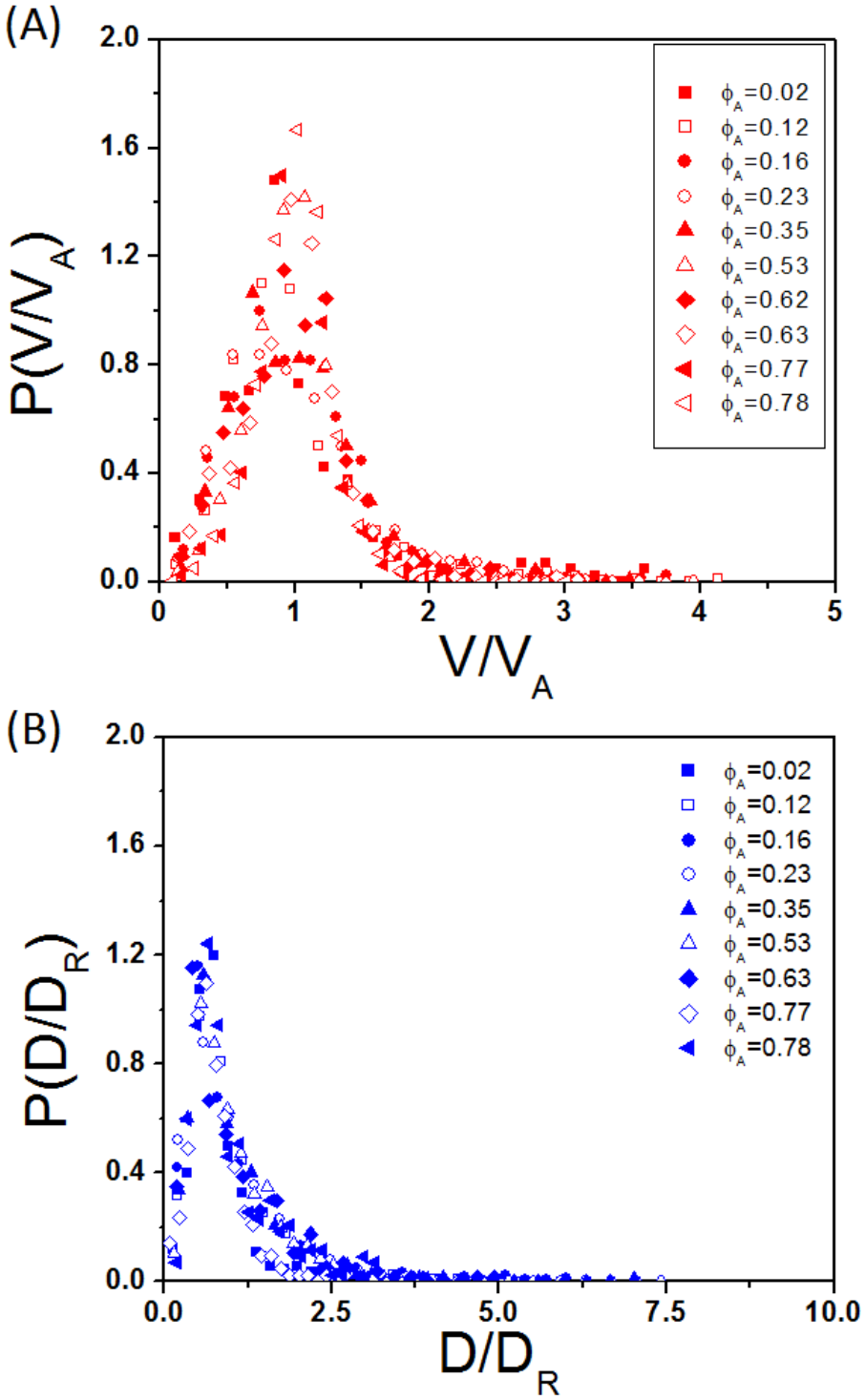

Figure I.2.10: (A) Velocity distribution of active rods at different ϕ_A using Au-rods . Half heigth width range from 0.87 to 1.12 and (B) Diffusion Distribution for random rods. Half heigth width range from 0.61 to 0.63

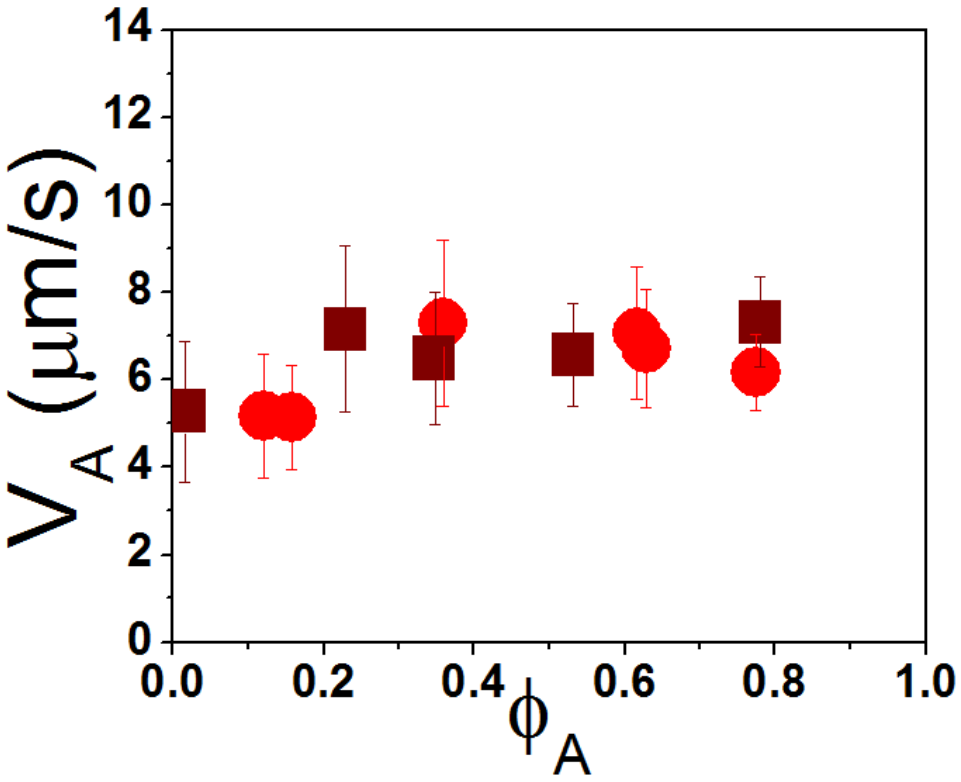

Figure I.2.11: Display the relation between the mean velocity of active swimmer V_A and active fraction ϕ_A. Au-Pt rods with varying proportions of inactive Au rods. Squares and circles represent tracer of 2 and 1 μm diameters

puted for each experiment a fraction ϕ_A of active swimmers and the corresponding density n_A. Note also that for a pure suspension of bimetallic rods the fraction that actually moves on the surface is not 100 %. Fig I.2.9 shows two examples with two different values of ϕ_A. Once the trajectories were computed and classified, the velocity distribution can be obtained for the active population as well as the diffusion coefficients distribution for the random one. Fig. I.2.10 illustrates both distributions. It can be noticed that the velocity distribution differs slightly from the one obtained for active bacteria, if we consider the half heigth width (ranging from 0.87 to 1.12 for rods and from 0.9 to 0.95 for bacteria) . However, the diffusion distributions for inactive rods have shapes similar to the ones found for random bacteria, here the half heigth width goes from 0.61 to 0.63 in the artificial case, and from 0.62 to 0.61 in the bacterial case.

On Fig. I.2.11, I display the relation between the mean velocity V_A and the active fraction ϕ_A. The velocity does not show a dependence which seems to indicate that

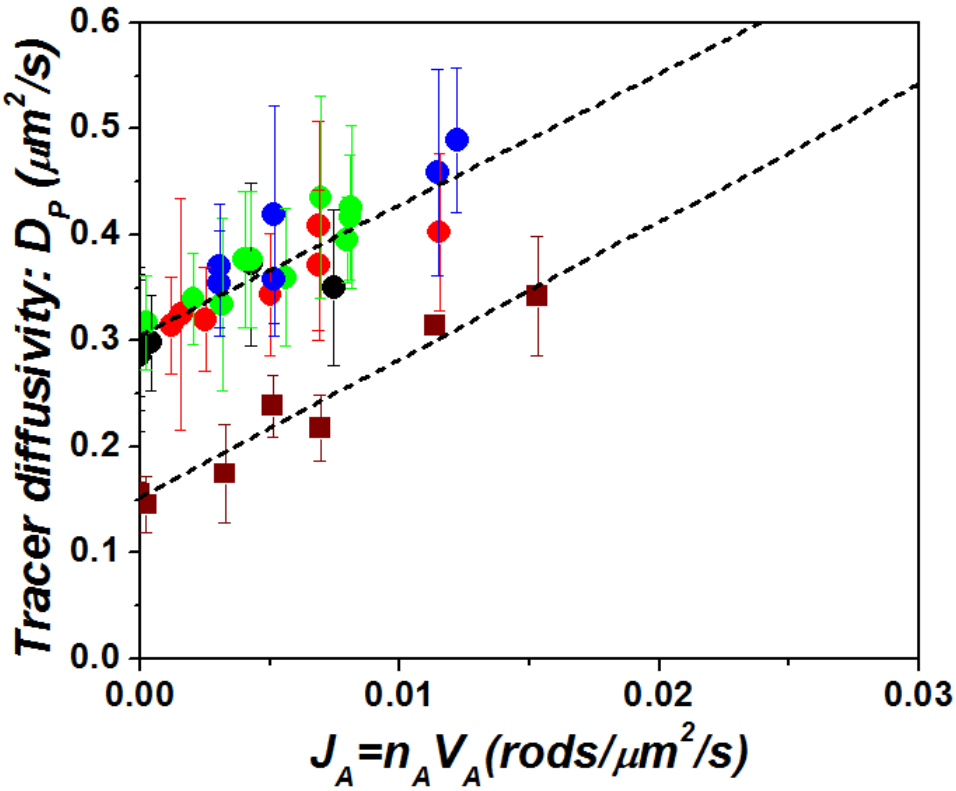

Figure I.2.12: Enhance diffusion in suspensions of Au-Pt rods: green, blue, and black circles correspond to various H_2O_2 concentrations (from 2.5%*to*20%). The dashed lines are linear fits and the error bars are standard deviations

we still operate in the low swimmer concentration regime. Also here, the passive particles diffusion was calculated and it was possible to relate this value to the active flux.

Fig. I.2.12 shows the relation between the bead diffusion and the product of the mean velocity and the active concentration of rods. Like in previous experiments, the data collapse onto a line characterized by the equation I.2.3. I found that the parameter $\alpha = 0.7 \pm 0.05$, is close to what was found for both buoyant $d = 1\mu m$ and $d = 2\mu m$ latex spheres. The prefactor β computed for active rods seems to be identical for both tracer sizes and equal to $13 \pm 0.7\mu m^4$ which gives $\Lambda = 1.9\mu m \pm 0.1$. This value appears to be higher if one compares with the result of non-buoyant suspension $\Lambda = 1.5\mu m \pm 0.1$ but closer to the case of buoyant suspensions $\Lambda = 1.8\mu m \pm 0.1$.

Part II

Swimmers in a flux

II.1

Active viscosity of E. Coli suspensions

As described in the introduction, the effect of micro-organisms motility in a suspension under shear, may change strongly the effective viscosity of the suspension. One experiment on viscous relaxation of a *Bacillus Subtillis* suspensions, trapped in a thin film, probed a significant viscosity reduction with concentration: a sign of the activity of the pusher-like swimmers. However, there is no direct proof that such an effect would exist in the bulk and no direct measurement of the full rheology relations as done for puller-like swimmers (Rafaï *et al.*, 2010). This is the reason why we designed a system to measure the viscosity of a wild type *E. Coli* suspension in the dilute and semi-dilute limits using a micro-fluidic device build as a Y-shape micro-channel. We adapted the system initially proposed by Guillot *et al.* (2006) suited to compare the viscosities of two liquids at low shear. In this chapter, I will describe the device and show preliminary tests on a suspension of latex spheres and also suspensions of dead and alive *E. Coli* bacteria. This part of the thesis was done in collaboration with Jérémie Gachelin as a part of his Master's thesis, he is now continuing his PhD in the group, pursuing the study of the rheology of active suspensions.

II.1.1 Operation principles

The rheometric device proposed by Guillot *et al.* (2006) is a Y-shape micro-channel that we adapted to measure the relative viscosity between different suspensions and the suspending fluid. In one arm, one injects the suspension and in the other arm, the suspending fluid. Both fluids are injected at the same flow rate (see figure II.1.1). From the position of the interface between the pure fluid and the suspension, one may extract the suspension relative viscosity.

For a thin rectangular channel, i.e. in the limit where the height of the channel is small with respect to its width, the Hele-Shaw relations between flux and pressure gradient are valid:

$$Q = \frac{1}{12}\frac{wh}{\eta}\frac{\partial P(x)}{\partial x} \tag{II.1.1}$$

where Q is the flow, η is the fluid viscosity, w and h are the channel width and height, respectively, P the pressure in the fluid and x the coordinate along the length of the channel.

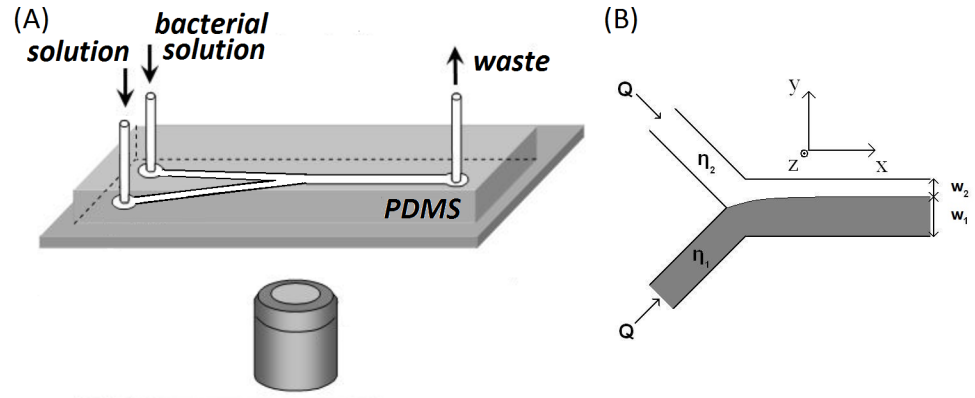

Figure II.1.1: Experimental setup. (A) Used Y-shape microchannel and the microscope position in the setup. (B) Definition of the main quantities and the reference system.

If we consider that the velocity profile is flat along the width (i.e. the y direction), we can applied the Hele-shaw equation II.1.1 to the section corresponding to each fluid labeled by 1 and 2:

$$\begin{cases} Q_1 = \dfrac{1}{12}\dfrac{w_1 h}{\eta_1}\dfrac{\partial P_1(x)}{\partial x}, \\ Q_2 = \dfrac{1}{12}\dfrac{w_2 h}{\eta_2}\dfrac{\partial P_2(x)}{\partial x}. \end{cases} \tag{II.1.2}$$

When the fluxes are equal i.e. $Q_1 = Q_2$, the pressure will reach an equilibrium for a steady interface position and then :

$$\frac{\eta_1}{\eta_2} = \frac{w_1}{w_2}. \tag{II.1.3}$$

Also the mean shear rate can be computed using the relation for the velocity gradient in a Poiseuille flow obtaining:

$$< \dot{\gamma} >= \frac{3Q}{h^2 d} \tag{II.1.4}$$

Therefore, from measurements of the interface position between both fluids at a given the flow rate, one has the possibility to estimate in a simple way, the rheogram, i.e. an effective relation between viscosity and shear rate. Of course the analysis is

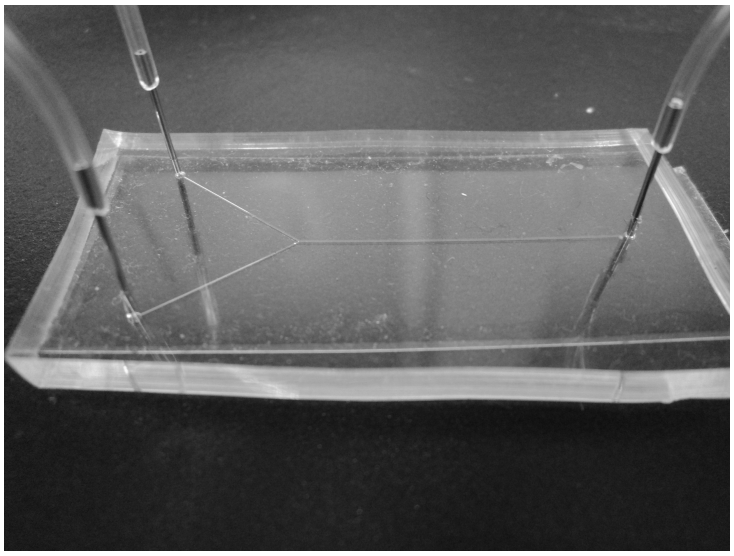

Figure II.1.2: Photograph of the channel. In this figure, the three connections are shown. The micro-channel is connected to the syringe pump (connectors in the left) and to the waste (right) through flexible tubes.

done here for a simple Newtonian fluid. For a Non-newtonian fluid, one would have to take into account the modifications in the flow profiles due to the more complex constitutive relations. However in the following, I will not go to this level of refinement. I just want to establish as a first step, the applicability of the method to a bacterial suspension and bring evidences for the anomalous character of the effective viscosity due to the presence of active pusher-like swimmers.

II.1.2 Methodology and Protocol

II.1.2.1 Experimental Setup

The microchannel (shown in fig.II.1.1) was fabricated in the Gulliver laboratory of the ESPCI in PDMS by soft lithography. The fabrication technique is describe in Appendix C. A photography of the channel is shown in fig. II.1.2.

Each branch of the channel is connected to a 50 μl *Hamilton* syringe. The imposed flow is controlled using a *nemSYS* pump. The flow rate varies from 0.5 to 100 nl/s. During the connection procedure and the channel filling, precautions have to be taken

in order to avoid bubble generation. The channel output is connected to a waste container. It is important that the tip of the corresponding tube is submerged, otherwise a drop can be formed altering the pressure in the channel.

The channel thickness is $h = 100\ \mu m$. The main channel width is $W = 600\ \mu m$ and the inlet branches have widths of $W/2$. The dimensions of the channel were chosen such as to achieve shear rates between 0.5 and 100 s^{-1}. The microfluidic device is put on the observation stage of the *Zeiss-Observer* microscope and the channel observed at a 2.5X magnification objective (AN of 0.07), hence providing an extended vision of the channel.

Note that, this rheometric setup has a decisive advantage to measure a viscosity ratio and thus is well adapted to suspensions where the relative viscosity between the suspending fluid and the suspension is the central issue. In principle, no limitation exists on the absolute viscosity values contrasting with classical rheometry where low-shear measurements are often problematic. Here, a small viscosity differences can be obtained when the interface position can be measured with accuracy. However, this method has some limitations. Special care has to be taken when both branches are supplied at a same constant flow Q. That was done in practice using the high-quality *nemSYS* pump that pushes two-syringes at the same time and imposes in principle an identical pushing velocity.

However as described in the following, we also checked explicitly that the results were symmetric with respect to the interchange of both the syringes and the channel inlets. A final limitation comes from the fact that we have two miscible fluids, so we have to make sure that no significant mixing occurs and that the interface remains of a limited thickness before a steady state is reached. We then discarded very low flow measurement as we checked that the interface was ill defined.

This viscometer was used to investigate the rheology of different fluids: passive particles colloids, as well as dead and alive bacteria suspensions. To avoid sedimentation, both the particle and the liquid densities were matched.

Finally, it is important to clean the channel after every measurement is done. By starting with detergent, the cleaning has to be continued with alcohol, and finished by rising the channel with distilled water. Cleaning can be improved by sonication before the rinsing.

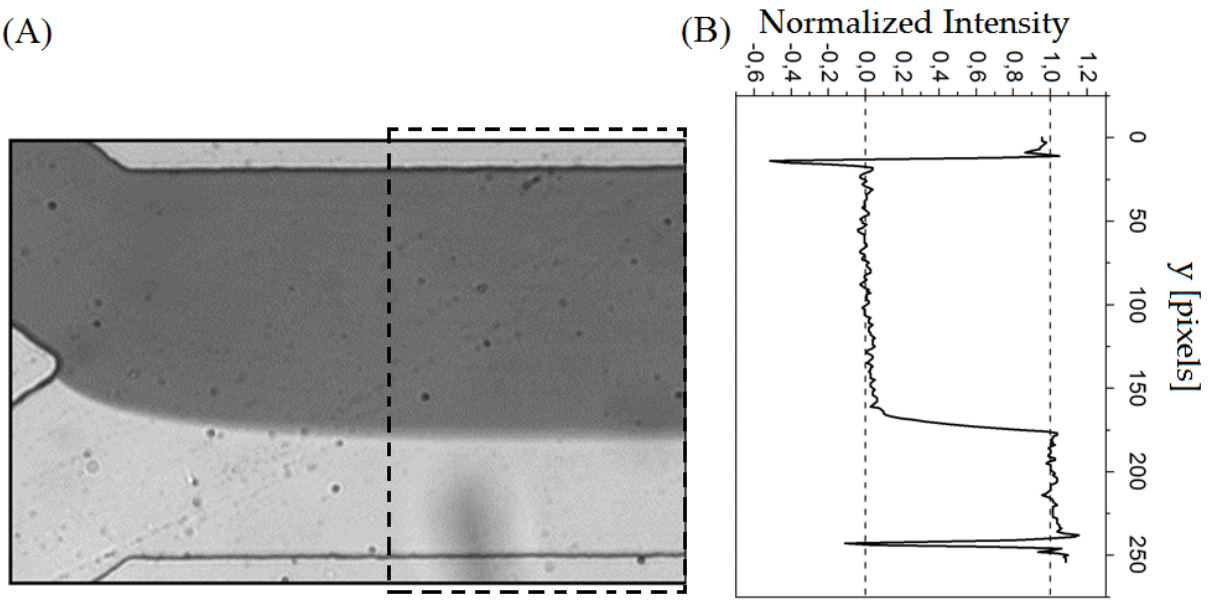

Figure II.1.3: Interface determination. (A) Typical image to be analyzed. Definition of the region of interest. (B) Normalized Intensity profile that will be used to fit with a erf function.

For a given experiment, measurements were made after the system reaches a steady state. The observation time to record the images depends on the flow velocity. The chosen criterion is that the liquid travels the double of the distance of the visualization field.

II.1.2.2 Image Analysis

The first step in the image analysis is to obtain an average of the image sequences. In order to reduce intensity fluctuations 120 images are averaged to establish the mean profile. Fig. II.1.3.(A) shows a typical average image to be analyzed. This procedure is important when the volume fraction of the solution is low, in order to gain signal since the contrast between the fluids is weak.

A program developed in Matlab automatizes the recognition procedure of the interface between the fluids. As indicated in figure II.1.3.(A) the routine allows the user to select a region of interest far away from the junction. An average intensity profile is computed on the x direction. Intensities are converted to concentrations through a logarithm, following the Beer-Lambert law. The profile is normalized between 0 and

1 using representative values of the maximum and minimum concentrations within the channel, at both sides of the interface (averages were made over 50 pixels on the image). Figure II.1.3.(B) displays the obtained concentration profile. Negative peaks in the profile are identified as the channel borders. An error function $erf(\frac{y-y_o}{\sigma})$ is used to fit the profile. From this, the position of the interface is given by y_o and the σ parameter is the interface width coming from the mixing process at the interface. w_1 and w_2, are calculated from the estimation made for the vertical position of the channel borders and y_o. Once the interface position is obtained, equation II.1.3 allows to calculate the viscosity ratio for the shear rate and volume fraction (ϕ), used in the experiment.

II.1.3 Quality test of the channel

To validate the use of a given micro-channel as a viscometer, different control experiments were performed. The objective here is to test the symmetry of the flow resulting from the quality of the microfluidic cell as well as the quality of the syringes. For this purpose, we performed 4 experiments with the same fluid interchanging both the

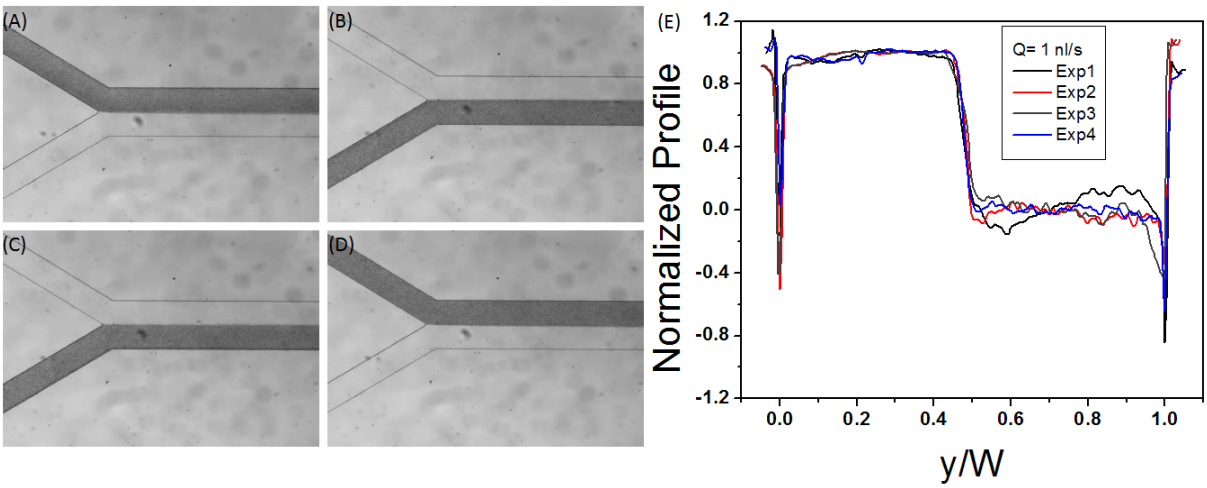

Figure II.1.4: Tested setup configurations (syringes and connections). The flow was set to 1 nl/s. (A) Syringe 1 with particles suspension connected to the upper input. (B) Syringe 1 with particles suspension connected the lower input. (C) Syringe 1 with the pure solution is connected in lower input. (D) Syringe 1 with pure solution connected to the upper input. (E) Measured intensity profiles.

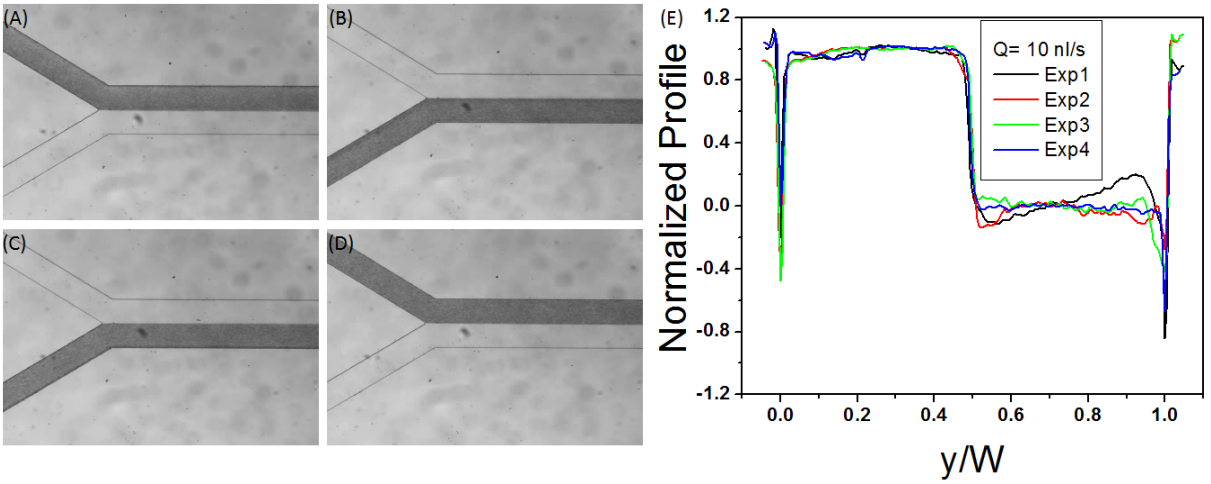

Figure II.1.5: Tested setup configurations (syringes and connections). The flow was set to 10 nl/s. (A) Syringe 1 with particles suspension connected to the upper input. (B) Syringe 1 with particles suspension connected the lower input. (C) Syringe 1 with the pure solution is connected in lower input. (D) Syringe1 with pure solution connected to the upper input. (E) Measured intensity profiles.

syringes and the inlet branches. In the left part of the figure II.1.4, pictures of the experiments are shown. Branches filled with a suspension of passive particle (particles + water-glycerol mixture (8:2)) appear in dark. Brighter branches indicate the presence of water-glycerol only. On the right, the corresponding intensity profiles are presented in fig.II.1.4.(E). During the experiment shown in fig.II.1.4.(A), syringes labeled 1 and 2 were connected to the upper and lower branch of the channel,respectively. During a second experiment (Fig.II.1.4.(B)), syringe 1 was connected to the lower branch and syringe 2 was connected to the upper one. For the experiments illustrated in figs.II.1.4.(C) and (D) the roles of the syringes were interchanged. For the experiments the flow was set to 1 nl/s. These experiments were repeated using a flow of 10 nl/s, schemes and results are presented in figure II.1.5.

All the profiles show a result independent of the chosen setup configuration, the measurements are consistent and reproducible. All channels used in the following (and the syringes) had to pass this test to be validated them for rheometric measurements.

II.1.4 Experimental results

In the following paragraphs, I present and discuss the rheological measurements made by using the tested micro-channel as a viscometer. Subsection II.1.4.1, shows the results obtained for suspensions of passive micro-beads, and subsections II.1.4.2 and II.1.4.3 analyze the measurements made for dead and living bacteria, respectively.

II.1.4.1 Passive Particles

Measurements were made using 1 μm diameter latex beads (Sigma Aldrich Fluoro-Mac, $\rho = 1.025 g/cm^3$), in order to verify the sensitivity of the device on a particulate fluid that we know Newtonian. At low volume fractions, the suspension viscosity obeys the Einstein's relation : $\eta = \eta_0(1 + 2.5\phi)$, where η_0 is the suspending fluid viscosity and ϕ the particle volume fraction. The fluid used was a water-glycerol (8:2) mixture, prepared in such a way that it matches the particles density to avoid sedimentation. As previously described, one branch of the channel was the solution input, and the other one was filled with the particle solution. Given a volume fraction, the flow was varied from 0.5 to 100 nl/s to modify the shear rate in the range of interest.

As a preliminary step to measure the viscosity ratio, we described the thickening of the interface during the flow. We define the transport time t_{tr} as:

$$t_{tr} = \frac{whx}{2Q} \tag{II.1.5}$$

where Q represents the flow rate, W is the total width after the junction, h is the channel height and, x is the horizontal distance from the branches junction. Measurements show that σ^2 increases with the transport time until it reaches a saturation level. However, a linear behavior is observed for times shorter than 20 sec, which means $Q > 2nl/s$.

On fig. II.1.6.(A), I display the quadratic width σ^2 as a function of the transport time t_{tr}, for a volume fraction equal to 1.2 (%). Figure II.1.6.(B) shows the results

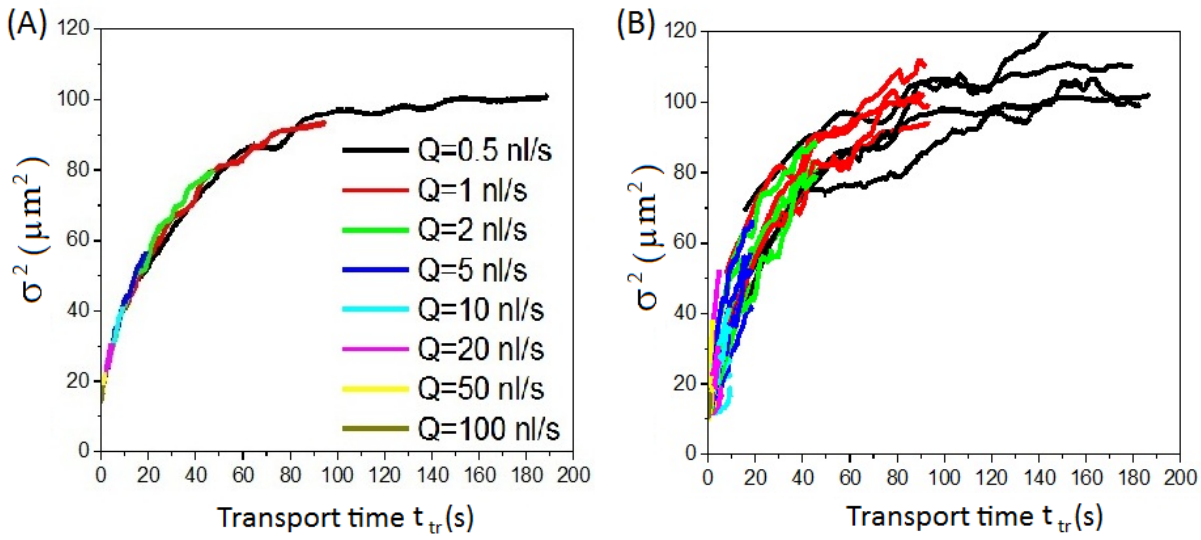

Figure II.1.6: (A). Quadratic width σ^2 as function of the transport time t_{tr} for a volume fraction equal to 1.2 (%). Different applied flows (shear rates) are considered. (B). σ^2 as function of t_{tr} for volume fraction equal to: 0.1, 0.3, 0.9, and 1.2. Different colors represent different flows.

.

obtained for all the explored volume fractions (0.1, 0.3, 0.9, and 1.2%). It can be noted that all the curves seem to collapse onto a single one.

If it were a diffusion process due to hydrodynamic dispersion the relation between σ^2 and t_{tr} should be linear, but the graphs present a saturation of the width (red and black curves), that we do not fully understand.

In a conventional rheological measurement, the information is presented plotting the shear stress as a function of the shear rate for the liquid of interest. However here, we have a Newtonian suspension and then, to estimate the relative viscosity, we define a relative shear stress Σ_r that we plot as a function of the shear rate. The relative viscosity is obtained by the slope of a linear fit (going through zero). The relative shear stress is :

$$\Sigma_r = \frac{\eta}{\eta_o}\dot{\gamma} \tag{II.1.6}$$

where η/η_o is the relative viscosity and $\dot{\gamma}$ is the mean shear stress. Figure II.1.7.(A) shows the measurements made at different volume fractions ranging from 0.1% to 1.2%.

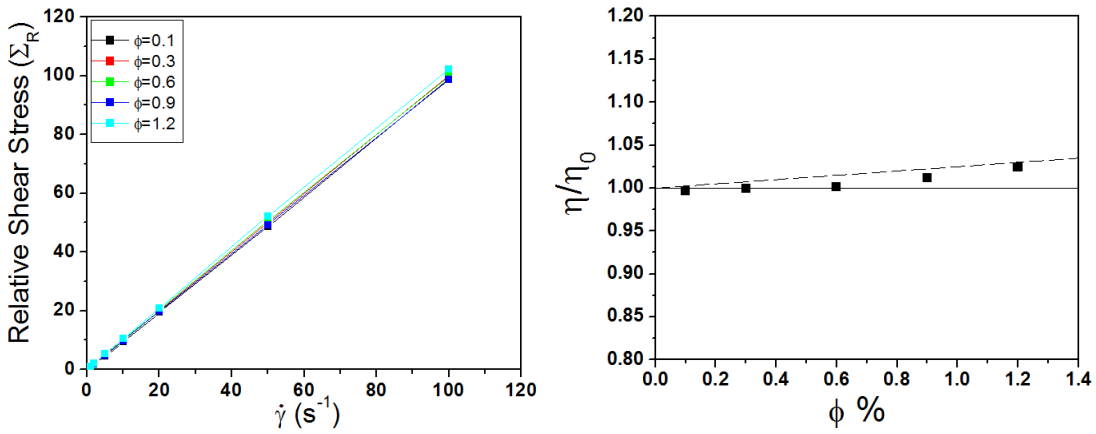

Figure II.1.7: (A). Relative shear stress (Σ_r) as a function of the mean shear rate ($\dot{\gamma}$), measured for different volume fraction of passive particles in non-buoyant condition. (B). Relative viscosity as function of the volumetric fraction. Dash line: Einstein relation.

Figure II.1.7.(B) presents the corresponding relative viscosities as a function of volume fraction. The results show that the relative viscosity increases with ϕ. I displayed on the graph, the Einstein relation ($\eta/\eta_o = 1 + 2.5\,\phi$). The measurements are consistent at $\phi = 1.2\%$ but also show a limit of sensitivity of the method at lower concentration. So we estimate the accuracy of the method to be of the order of 3%.

II.1.4.2 Bacterial Suspension: Dead Bacteria

For the following measurements, the passive tracers were replaced by dead bacteria and the suspending fluid the MMA-Percoll solution. Several volume fractions were tested. The bacteria were killed without producing cell lysis, following the protocol described in Appendix A. As shown in Fig. II.1.3, beyond the branches junction, the area occupied by the bacterial solution increases until it is stabilized at a maximum value. It remains constant for the following 100 pixels, measured over the image, in the x direction. Further away, diffusive processes start to be more important. The region where the interface remains stable, is used to measure the relative viscosity.

As in the previous subsection, the rheology of the suspensions is presented by plotting the relative shear stress as a function of the shear rate. Fig. II.1.8 illustrates the measurements for a bacterial volume fraction of 4.8 %.

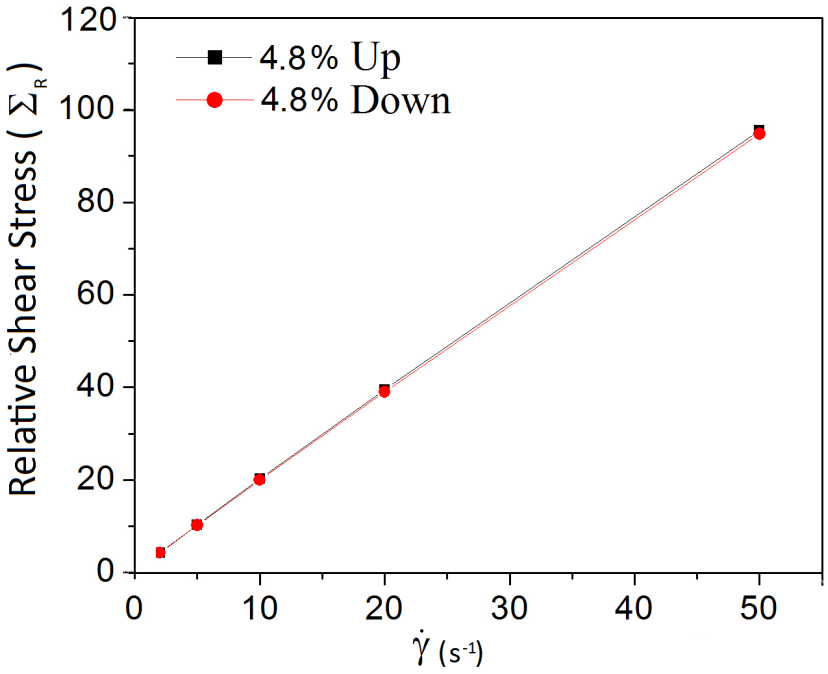

Figure II.1.8: Relative shear stress (Σ_r) as a function of the mean shear rate ($\dot{\gamma}$) for concentration of death bacteria of $\phi = 4.8\%$.

As before, from the slope obtained by a linear fit of the data, the relative viscosity was computed for bacterial volume fractions ranging between 1% and 6.8%. Results are shown in Fig. II.1.9.

The effective viscosity for dead bacteria shows a significant increase at volume fractions larger than few percent. This might be due to their elongated character and in particular, to the presence of flagella that might play a significant role in the rheology when the semi-dilute limit is reached.

II.1.4.3 Bacterial Suspension: Living Bacteria

Rheometric measurements were made with living bacteria swimming in an isodense suspension (mixture MMA/percoll) at different concentrations. The Fig. II.1.10 shows the averaged images for three experiments performed at different flow values, keeping the volume fraction at 0.35 %. From top to bottom, the low values are: 0.2, 1 and 10 nl/s. The dark zones on each channel image correspond to the suspending fluid (MMA-Percoll) and the bright ones, to the bacterial suspension. For the smaller shear

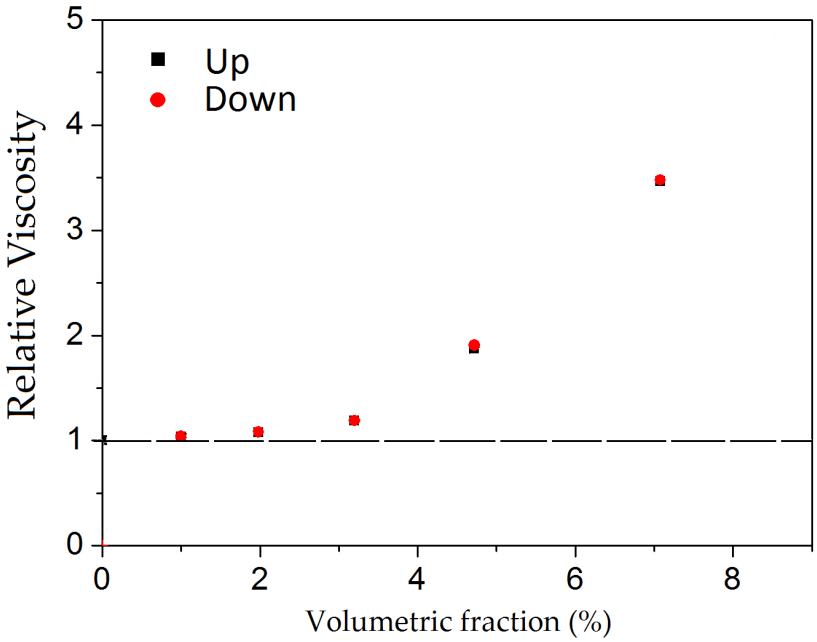

Figure II.1.9: Relative viscosity as a function of volume fractions using dead bacteria (circles and squares).

rate $\dot{\gamma}$ it can be noted that the area occupied by the bacterial solution is smaller than the one corresponding to the MMA-Percoll solution (see Fig. II.1.10.(A)). This is a direct proof that the effective viscosity of the bacteria suspension can be smaller than the viscosity of the suspending fluid. The tendency is reversed at higher flow rates (see Fig. II.1.10.(B) and (C)).

For each relative position of the interface, the relative viscosity is extracted and Fig. II.1.11.(A) shows the dependency of the relative viscosity as a function of the mean shear rate, at different volume fractions. Fig II.1.11.(B) shows the variation of the relative viscosity as a function of the volume fraction for different mean shear rates.

Clearly the rheology measured for the suspensions of living bacteria is different from the rheology found for the dead ones. The effective viscosity reflects a non Newtonian behavior as its variation is quite non-monotonic for volume fractions ranging from 3.510^{-3} up to 2510^{-3}. At low volume fractions and low shear rates, a decreasing of η_r to values smaller than one is observed, which is a crucial signature for the activity effect as predicted in 2009 by Haines *et al.* and Saintillan (2010), for dilute suspensions. However, the observed non-monotonous behavior of the viscosity (dis-

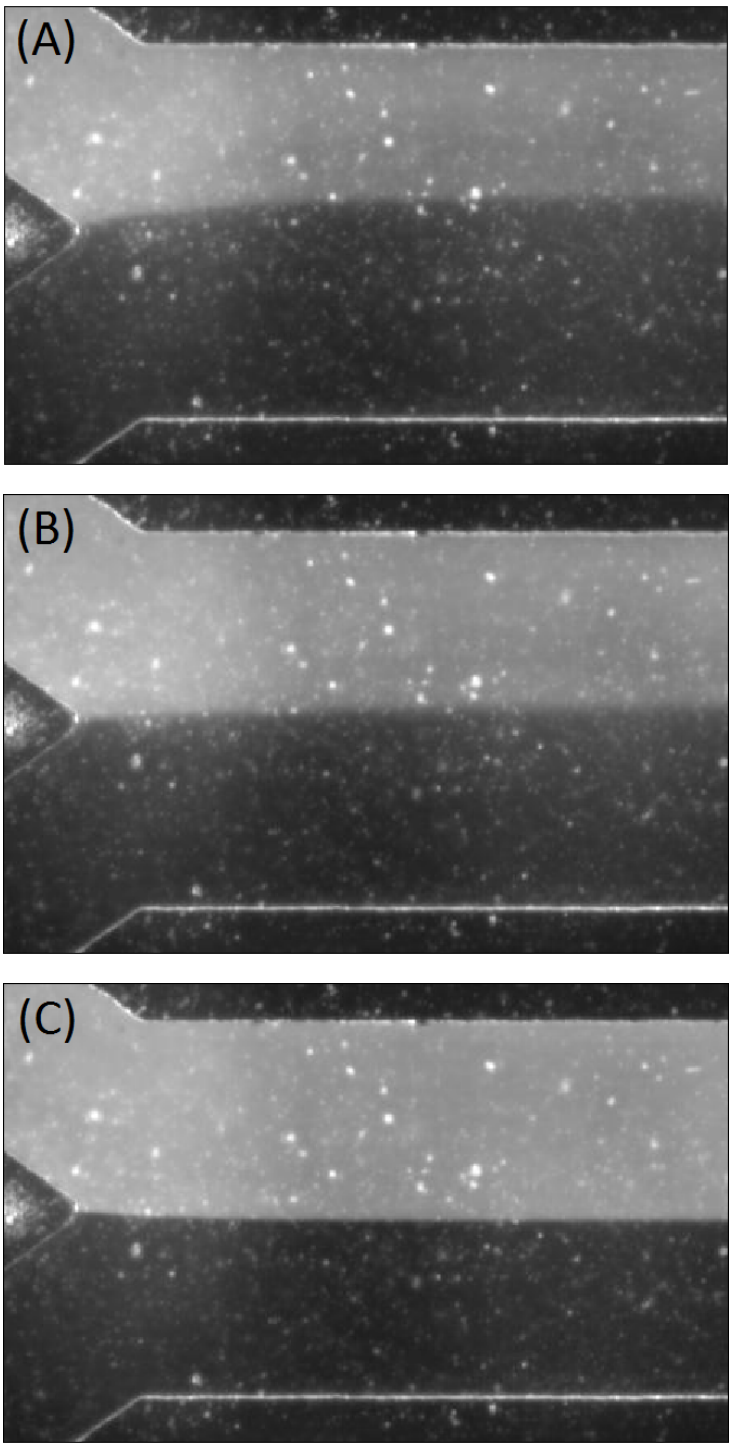

Figure II.1.10: Average images for three different shear rates: (A) 0.2 s^{-1}, (B) 1 s^{-1}, and (C) 10 s^{-1} using alive bacterial suspension keeping the volume fraction at 0.35 %.

playing a maximum) is closer to what Saintillan (2010) obtained in the dilute limit for a theoretical calculation using a slender body representation of the bacteria. The max-

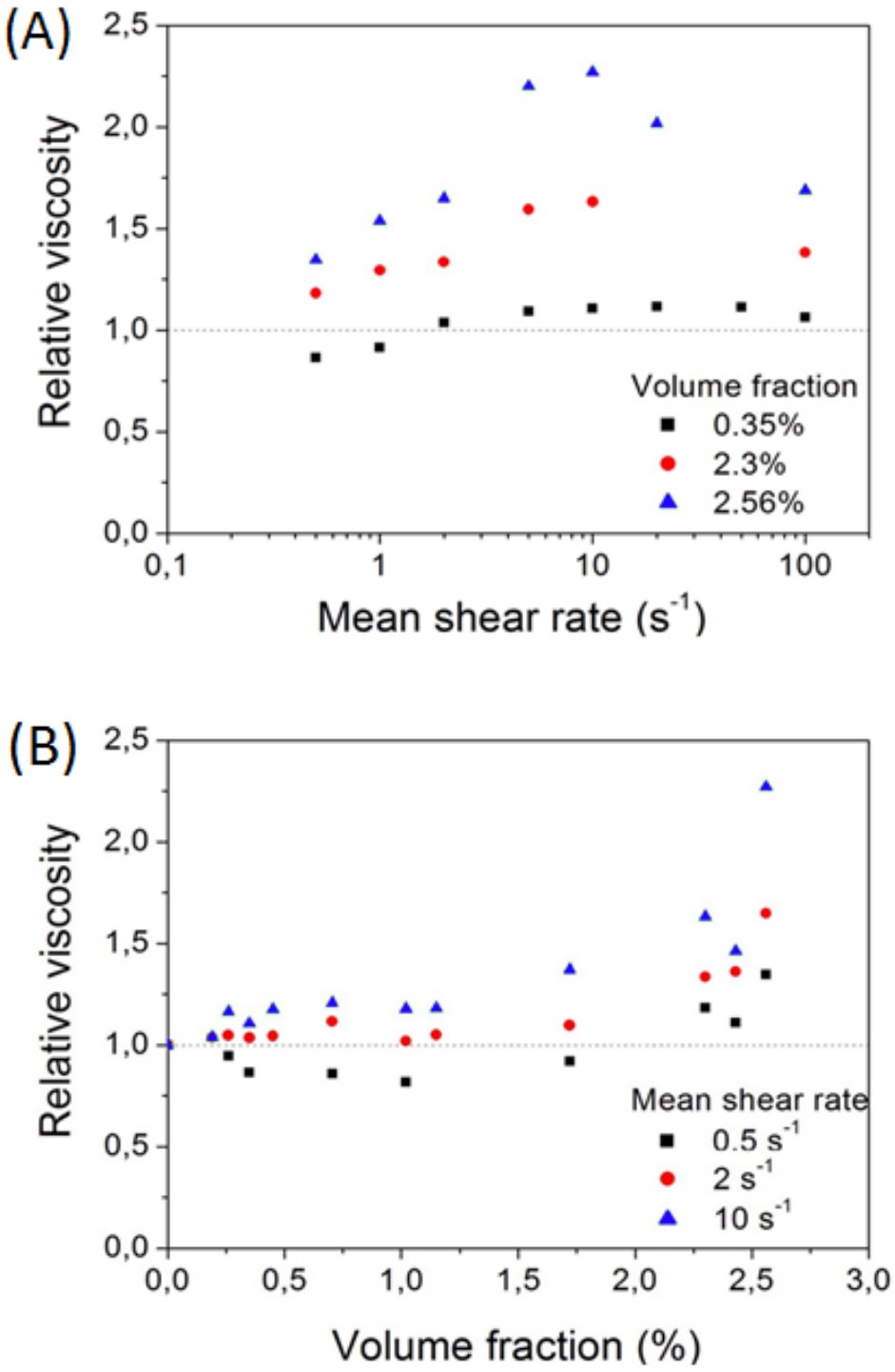

Figure II.1.11: Rheology measurement for living bacteria suspensions. (A) Relative viscosity as function of the mean shear rate for different volume fraction. (B) Relative viscosity as function of volume fraction for different mean shear rate.

imum occurs at a shear rate of 10 s^{-1} and it is quite independent of the concentration. This value is typically the inverse of the swimming time (the swimming time, is the time needed for a bacterium to swim his own length). A non monotonous variation of viscosity with volume fraction is also detected as observed by *Ryan et al.* (2011) in simulations of active pushers in the semi dilute limit.

II.2

Anomalous dispersion of a confined bacterial flow

The following part of this thesis was made in collaboration with Dr. Ernesto Altshuler's group from the University of La Habana in Cuba at the occasion of his sabbatical at the PMMH in 2010-2011. This section presents a study where a bacterial suspension of *E. Coli* is transported through a micro-fluidic channel holding a constriction in its middle (the funnel). Using this simple but archetypal geometry, I will address the question of the influence of geometry and confinement, on the dispersion and transport properties of bacteria in a flow.

II.2.1 Methodology and Protocols

II.2.1.1 The micro-fluidic funnel

A sketch of the experimental device is displayed in fig II.2.1.(A). The widths of the channel and the funnel are $w = 200\ \mu m$ and $w_f = 40\ \mu m$, respectively. The length of the funnel is $L_f = 200\ \mu m$. Importantly, here, the height of the channel was chosen to be $h = 20\ \mu m$ (same for the funnel), a distance of about 10 times over the bacterium body length or 3 times its total length including the flagella bundle. At a typical swimming velocity, it needs a couple of second for the micro-organism to travel vertically

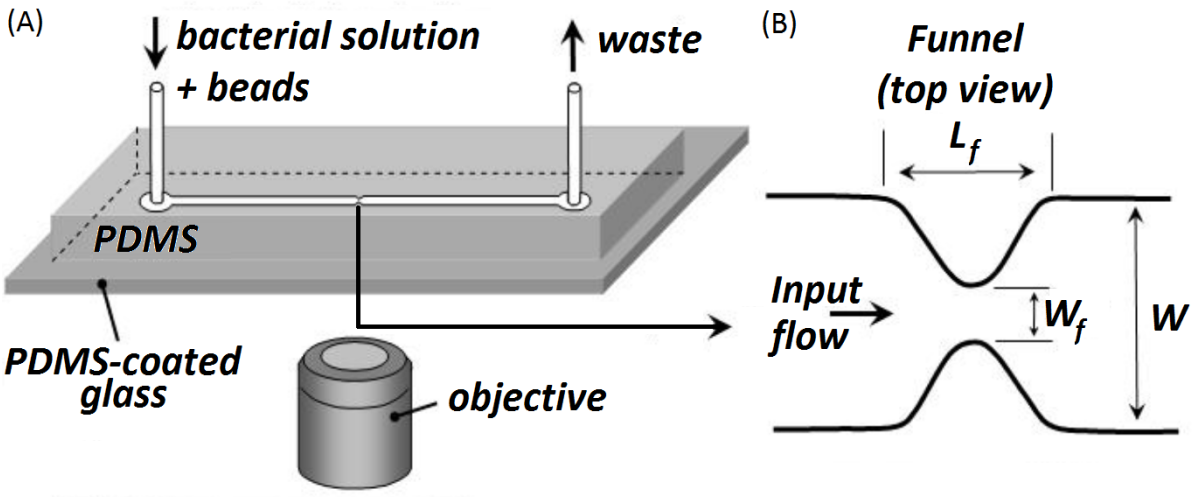

Figure II.2.1: Scheme of the experimental setup. (A) Shows the configuration of channel, input/output connection and the its configuration respect to the microscope. (B) Specification of main funnel dimension. W_f and L_f: width and length of the funnel. W: channel width.

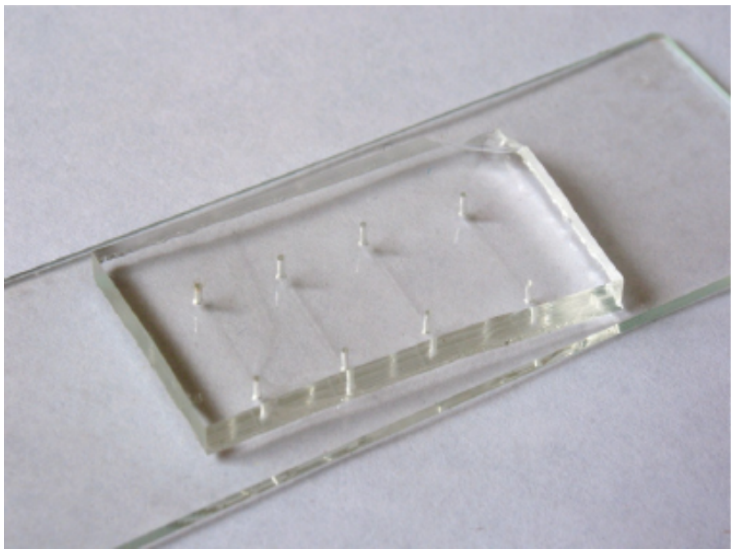

Figure II.2.2: Photography of the microchannel developed by soft Lithography.

from one surface to the other. So we have a situation where the surfaces will play a crucial and possibly dominant role with respect to the bulk transport properties, this is what we describe as "confinement". The total length of the funnel is $L = 15mm$.

The channel was built in PDMS using soft lithography technique (See appendix C). The inlet and the outlet are inox tubes of 1 mm outer diameter connected to flexible polymeric tubes. The glass substrate supporting the device was covered with a 27.8 μm thick PDMS coating. As a result, the ceiling, walls, and floor are made of the same material. Figure II.2.2 shows the photography of the channel used in the experiment.

II.2.1.2 Experimental setup and procedure

The bacteria suspension is prepared using the protocol described in Appendix A. In this case, I used the minimal motility media (MMA) at pH 7 with polyvinylpirrolidone (PVP), which prevent bacteria from sticking to the wall so they achieve close to the surface a velocity with a mean value around 15 $\mu m/s$. The *E. Coli* suspension is poured in a reservoir connected to the channel input. The output is connected to the waste. At this stage it is important to avoid the formation of bubbles that can perturb the flow in the channel. Once the previous step is completed, the reservoir is stuck on a Z-stage mover with a micrometric resolution. The speed flow of bacteria suspension is imposed by gravity i.e. by varying the distance between the upper level of liquid in

the reservoir and in the waste. The difficulty with this method is that the flow value is not precisely known (only estimated) for a given experiment. This is the reason why latex beads of 2 μm in diameter (Beckman-Coulter, density $\rho = 1.027 g/ml$) were added to the solution as passive tracers. This allows to quantify the flow analyzing the images at a later stage. In order to have a better control on the flow, note that the *nemSYS* pump and syringes were previously tested as described in the previous part. But in our case, where the flow range was going from 0 to 0.2 nl/s, our pump (as any commercial pump to our knowledge) cannot insure a stable flow. Therefore, the mean low velocities reported in this work are measured by monitoring and averaging the bead velocities in the mid horizontal plane when passing though the center of the funnel, along the symmetry axis of the channel. The following series of measurements were performed for both living and dead bacteria at the same mean concentration of $4 \pm 0.5 \times 10^8$ bact/ml.

The flowing suspensions were observed from below using the same inverted microscope (*Zeiss-Obzerver*) used in the other experiments, but in that case two magnifications were used (40X or 20X). In the experiments performed in this part, a phase contrast image technique is used. Under this condition, when a bacterium is set in focus, the cell body generally appears as a dark area surrounded with a white halo (Xie *et al.*, 2009). The digital camera *PixeLINK* is used for image acquisition. The visualization field is $600 \times 800 pixels^2$ for the 40X magnification and $1280 \times 1024 pixels^2$ for the 20X magnification (the rescaling relation for each magnification is 0.16 μm and 0.32 μm per pixel, respectively).

Once a steady flow is established, as revealed by the latex particles traveling in the center of the channel,videos are recorded at 20 $images/s$ (using 40X) during 20 s. Once one video is registered, the Z-position of the bacterial suspension reservoir is modified and the procedure is repeated again. Importantly, I noticed, when the objective focus plane was set at the bottom or the top wall of the channel, due to its relatively small height, all bacteria could be visualized at once. As described previously, bacteria that are below the focal plane are dark, on the contrary bright ones are above. Using this imaging trick , the two population could be analyzed separately. From the video recordings two parameters were defined: the mean flow velocity, using the passive tracers and the bacteria positions to compute the local concentrations.

From the tracking of the spheres, the corresponding mean flow velocity value in

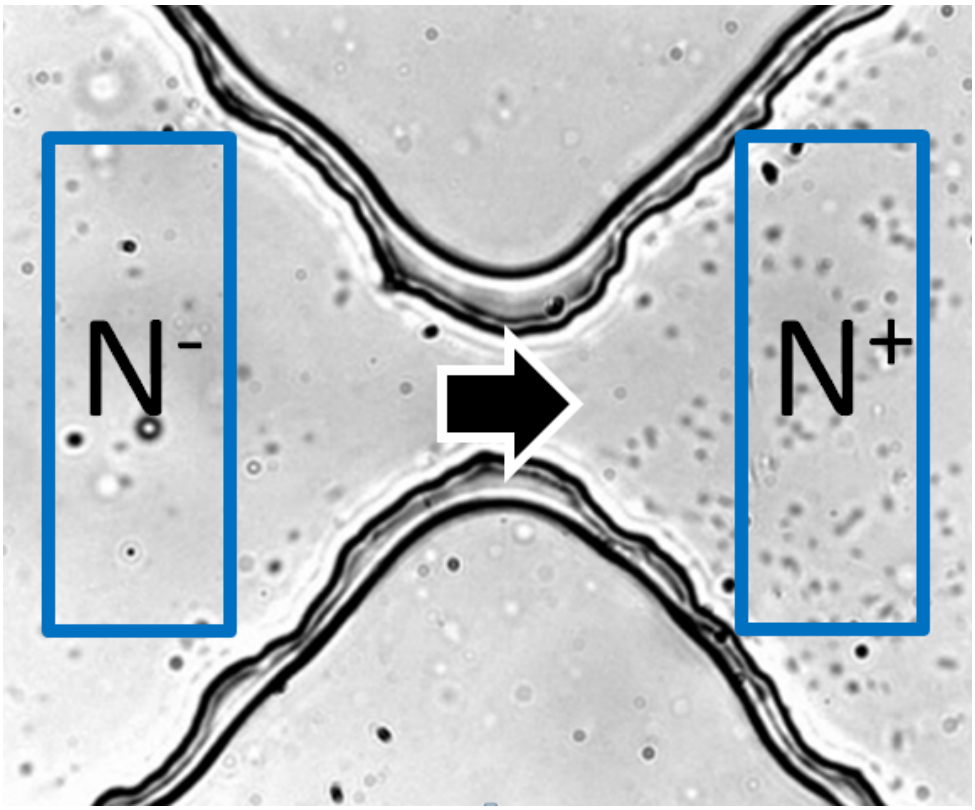

Figure II.2.3: Definition of the areas at both sides of the constriction. The arrow indicates the direction of the flow. N^- and N^+ represent the number of bacteria before and after the funnel (following the direction of the flow).

the constriction was computed and then used to compute the mean flow velocity V_x far from the funnel, multiplying its value by the ratio W_c/W. The bacteria detection and the eventual tracking are done using the techniques already described in the previous parts.

II.2.2 Experimental results

II.2.2.1 Flow induced symmetry breaking

In this first series of experiments, I will show that at low flow rate and in the presence of a constriction, one may observe a non intuitive symmetry breaking effect in the sense that bacteria accumulate past the funnel. After establishing a steady flow, the

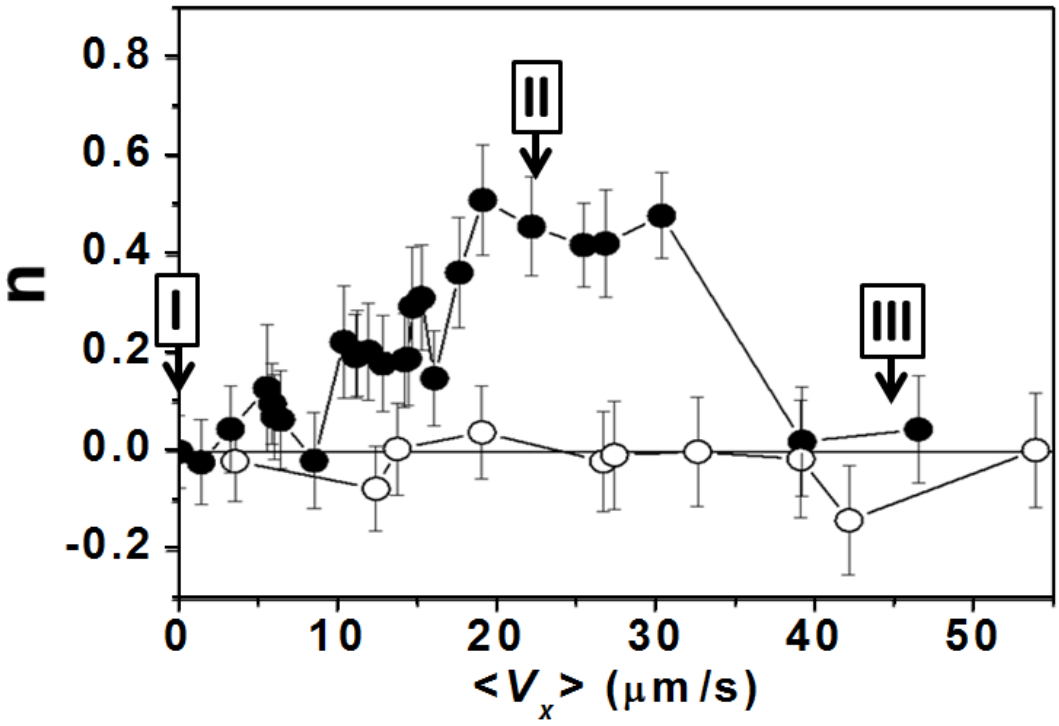

Figure II.2.4: Flow-controlled symmetry breaking in the concentration of *E. Coli.* Breaking parameter n as a function of the mean flow velocity $< V_x >$. Error bars correspond to standard deviation. Dark symbols are for living bacteria and empty symbols are for dead bacteria.

bacteria were counted inside two rectangular regions placed symmetrically on both sides of the funnel: N^- to the left and N^+ to the right (Fig.II.2.3). These measurements are made at a 40X magnification. Each area has 20 μm width and 60 μm height. It must be noted that here the "bulk" number of bacteria is counted. Those moving near the lateral walls of the cell are not considered at this stage (their effects will be discussed in the next section). The mean number of bacteria in each of the previously defined regions, are counted from 20 second videos (400 images). To quantify the difference in the bacteria concentrations on both sides of the funnel, a symmetry breaking parameter n is defined as follows:

$$n = \frac{N_+ - N_-}{N_+ + N_-} \tag{II.2.1}$$

Figure II.2.4 shows the symmetry breaking parameter n as a function of the mean velocity V_x. For suspensions of dead bacteria, n is about zero, regardless of flow velocity. In the case of living bacteria, no difference is observed on both sides at zero

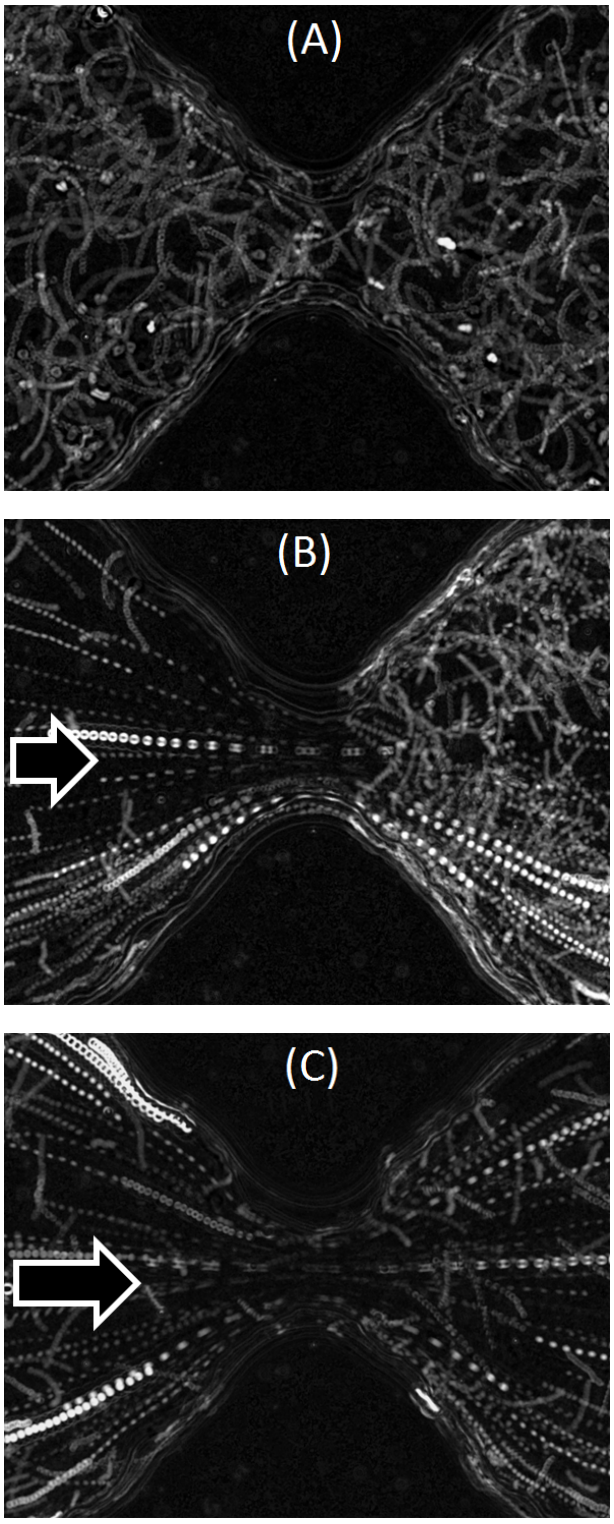

Figure II.2.5: Trajectory tracks of 1 second duration at different mean fluid velocities. (A) Living bacteria at zero flow (point I in Fig. II.2.4, (B) Living bacteria at $< V_x >= 22\ \mu m/s$ (point II in Fig. II.2.4, and (C) Living bacteria at $< V_x >= 45\ \mu m/s$ (point III in Fig. II.2.4. Note that some trajectories associated to the beads are observed as bigger circular spots in (B) and (C). All non-zero flows are from left to right as it indicated by the arrow.

flow rate. However, for a certain range of flow, the number of bacteria detected past the funnel is higher than before the funnel. Starting from zero flow, the symmetry breaking parameter increases up to approximately $n = 0.6$ as the mean flow velocity increases from zero to 20 $\mu m/s$. Then, n reaches a plateau and finally decays to zero quite abruptly around a mean flow velocity 40 $\mu m/s$. Note that n reaches its maximum value at a velocity around 20-30 $\mu m/s$ a value comparable to the mean bacteria swimming velocity.

To identify the effect of the flow on the swimming trajectories, I show on fig. II.2.5, the accumulation of 20 successive pictures taken in the surrounding of the constriction in order to visualize the bacteria tracks during a time-lag of 1 second. On figure II.2.5.(A), are displayed the tracks at zero flow. In this picture, bacteria describe essentially circular trajectories. The same kind of behavior was observed and discussed in the experiments reported in the first part of this thesis, which means that most of them swim close to the top/bottom surface. A mean swimming velocity around 15 ± 4 $\mu m/s$ can be estimated from these trajectories. In figure II.2.5.(B), the tracks for a moderate flow ($< V_x >= 22$ $\mu m/s$) are displayed. The corresponding value of the symmetry breaking parameter is $n = 0.6$. This figure illustrates the fact that the trajectories of the bacteria before and after the funnel are not the same. Before, they follow the flow lines but after, one observe much more circular trajectories. Figure II.2.5.(C) shows that the symmetry is restored at hight flow (in this case $< V_x >= 45$ $\mu m/s$) and the trajectories on both sides look more like flow lines.

II.2.2.2 Effect of flow reversal on symmetry breaking

At this point, any anomaly in the channel shape could be responsible for the symmetry breaking. To rule out this hypothesis, a second series of experiments was performed to test the reversibility of the effect and to obtain the characteristic timescale needed to build the symmetry breaking. First the bacteria concentration at the right of the funnel is established, with a flow of the order of 20 $\mu m/s$ (this mean that the flow goes from left to right). Then, the flux direction is reversed until its final magnitude reaches the initial one. This procedure was repeated in the opposite way, i. e., the direction of the flow was from right to left (more bacteria in the left side) and then, the flow is inverted. The symmetry breaking parameter, $n(t)$ was computed

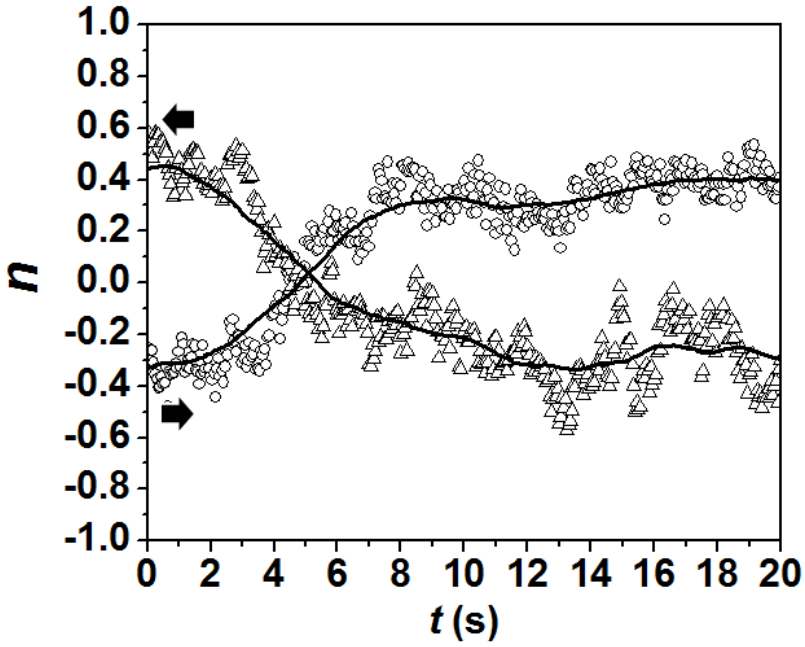

Figure II.2.6: Time evolution of $n(t)$ at $< Vx >= 20\ \mu m/s$ as the flux direction is suddenly reversed from left to right (triangles) and then right to left (circle); $t = 0\ s$ represents the onset of flow inversion; see arrows pointing in the flow direction. Points and continuous lines correspond respectively to experimental values and adjacent-average smoothing.

during the concentration readjustment process. Fig.II.2.6 displays the corresponding $n(t)$ for these two cases. In this picture, the zero-times are chosen in both cases at the end of the flow inversion process. Typically, the time for "population inversion" is about $\tau_{inv} \sim 7.5\ s$ corresponding roughly to the time scale for a swimmer to move to a lateral wall from the center of the channel. Figure II.2.7 (A), (B) and (C) show 1 second snapshot for $t = 0$, 5 and 20 seconds when the flow goes from left to right. Fig. II.2.7 (D), (E) and (F) illustrates the opposite case.

II.2.2.3 Evidence of long range anomalous dispersion

Next, I show results on the spatial range of concentration increase induced by the symmetry breaking effect. After establishing a constant flux of 30 $\mu m/s$ for few minutes, series of seven spatially overlapping videos were performed, starting at the funnel region and then, moving to the right along the channel up to a distance of 2500 μm. Each video was taken with a 20x magnification for 8 seconds (taken at 12.5 $images/s$).

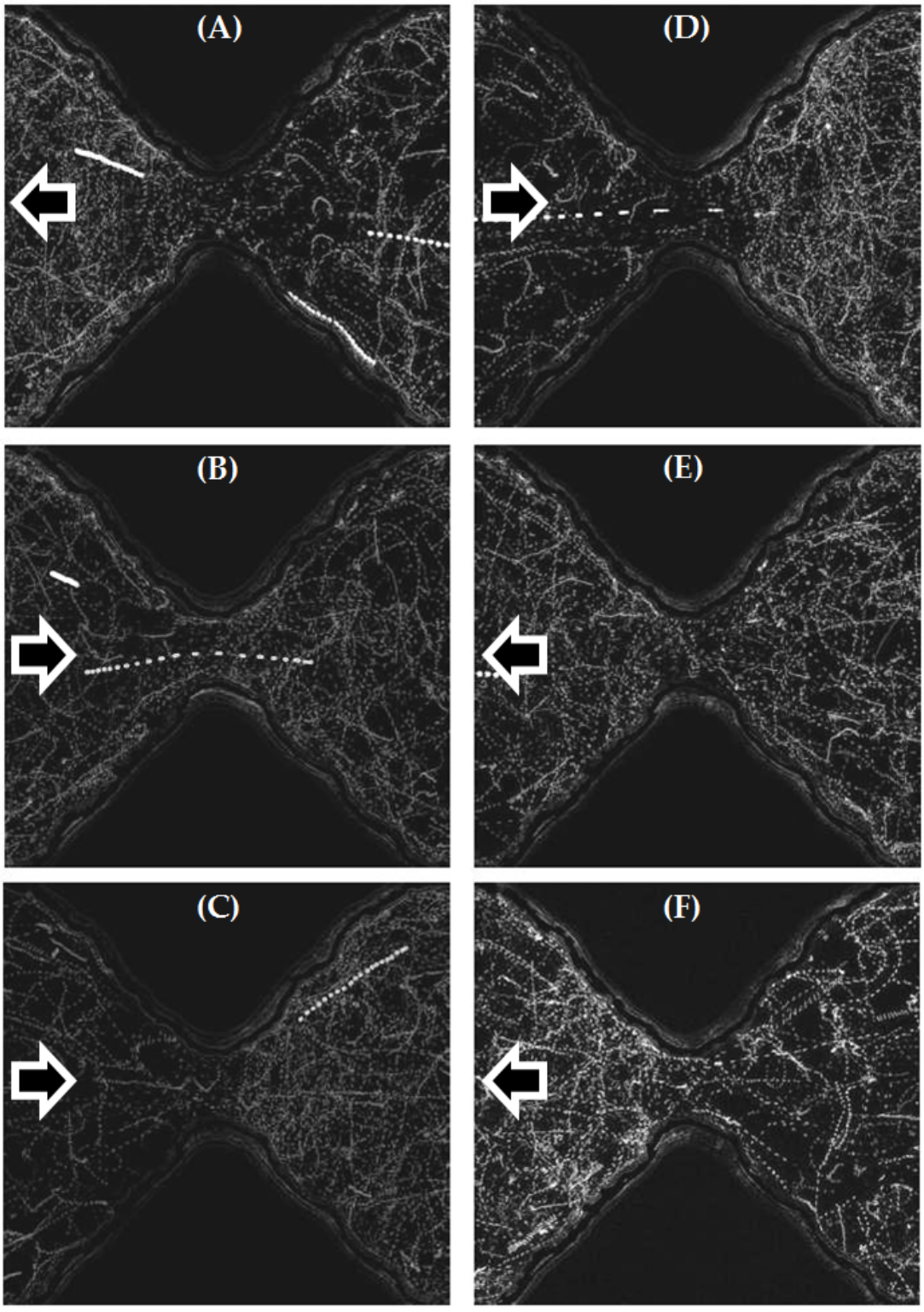

Figure II.2.7: Different moments in the flow reversibility, three snapshot of 1 s duration at different time, A) $t = 0$ s, B) $t = 5$ s and, C)$t = 20$ s when flow goes form right to left and then is inverted (left). Three snapshot inverting the flow in the other direction, i. e., when flow goes from left to right and then is inverted (right), D) $t = 0$ s, E) $t = 5$ s and, F)$t = 20$ s.

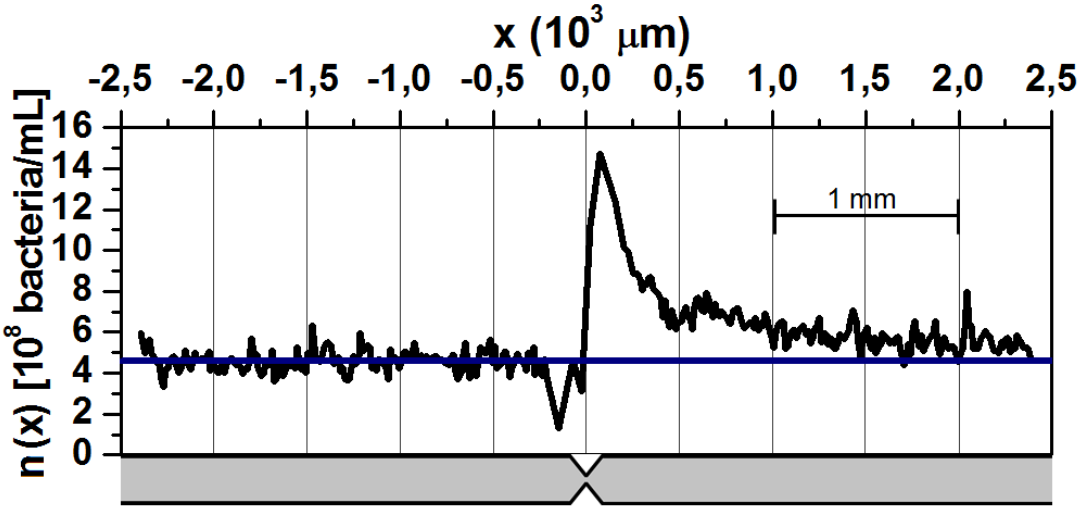

Figure II.2.8: Concentration profile $n(x)$ for a mean flow velocity $< V_x >= 30\mu m/s$. The black line n(x) corresponds to the mean bacterial concentration measured along the flow. The red line is a fit that will be explained below. The sketch underneath corresponds to a top-view geometry of the channel at the same X-scale. Note the change of scale compared to the previous figures.

Then, we returned to the funnel, took a second series of videos, performing a "traveling" to the left down to -2500 μm. Thereafter, the time average bacteria density $n(x)$ was computed within thin vertical stripes to cover a range of 5000 μm along the flow direction.

The resulting concentration profile $n(x)$ is displayed on figure II.2.8. Before the funnel, we see a constant concentration of around 5×10^8 $bacteria/ml$ which suddenly decreases to less than 2×10^8 $bacteria/ml$ at approximately -150 μm left from the geometrical center of the funnel. Then, a sharp increase in concentration takes place at the center of the funnel, reaching an absolute maximum of more than 14×10^8 $bacteria/ml$ at approximately 70 μm from the center of the funnel. This figure shows the long-range character of density increase that still persists few millimeters past the funnel (an order of magnitude larger than the funnel scale). At a distance of 2.5 mm from the funnel, the average concentration is still slightly higher than its value at the left side of the funnel by roughly 1×10^8 $bacteria/ml$. This is what we call the "anomalous dispersion effect" which seems to be triggered by presence of the central constriction.

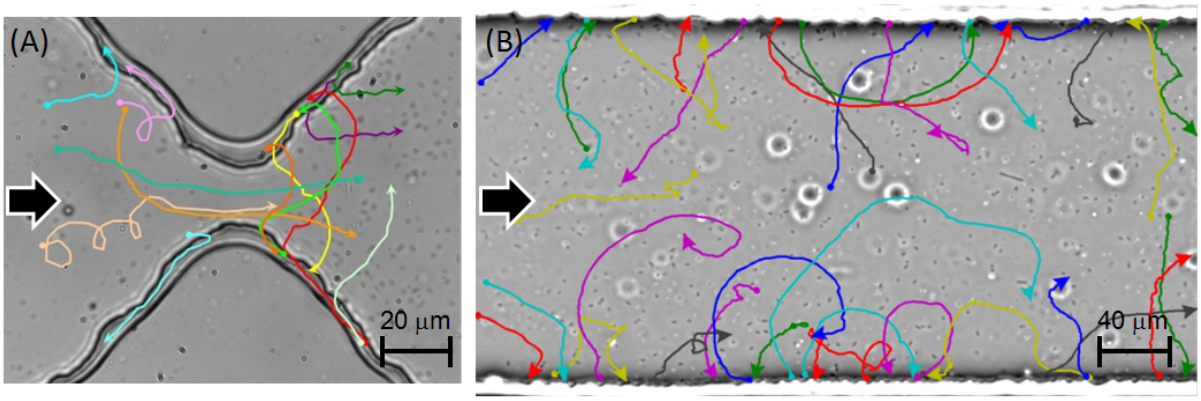

Figure II.2.9: Hand tracking trajectories. (A) A picture of the funnel area superposed with 10 trajectories tracked manually for a few seconds each, for a mean flow of 30 mum/s (flow direction indicated by a black arrow). (B) Trajectories in the same conditions, very far from the funnel ($x = 1.7 - 2.1\ mm$), showing side wall attachment and detachment effects.

II.2.2.4 Qualitative scenario for symmetry breaking

In order to understand the causes for the flow induced symmetry breaking, we outline here several "microscopic"' elementary mechanisms that could be at the origin of the anomalous macroscopic dispersion effect.

- First, in these confined conditions, most bacteria are located in the close vicinity of the boundaries. Direct visualization of several trajectories show that many of them can be quite insensitive to the direction of applied shear provided that it is not too large. We visualized under mean flow velocity of 30 $\mu m/s$ many bacteria trajectories in a direction opposite to the flow (see Fig. II.2.9.(A) and (B)). This surprising result was already outlined by Hill *et al.* (2007) for a bacteria suspension in an Hele-Shaw cell. This effect does not exactly contribute to the symmetry breaking but it may amplify the anomalous dispersion effect.

- Second, a close visualization of the lateral boundaries identifies a counter-flow traffic of bacteria moving at the left/right surface (also mentioned by Hill *et al.* (2007)). Note that due to fabrication imperfections it was difficult for us to visualize precisely bacteria swimming at the left/right walls and provide a quantitative description of the effect. The imperfections can be visualized on Fig.II.2.3. Importantly, the "ondulations" do not correspond to a roughnesses at the side walls. They are caused by imperfect corner junctions between the top/bottom and left/right walls. There is

so far not clear explanation of the effect but Hill *et al.* (2007) provide a qualitative scenario as they claim that when a bacterium hits the side walls, due to the action of shear, the body and the flagella get oriented downstream and consequently, the bacterium turns upstream. This is an important issue since it provides a mechanisms which brings back bacteria from the regions downstream to the upstream regions. However, it still does not provide a reason for symmetry breaking due to the presence of the funnel.

- Third, visualizing the bacteria trajectories in the funnel region see Fig. II.2.9.(A), one can clearly see a very different behavior on both sides of the constriction. Bacteria moving back-flow and trapped at the left/right walls, when they arrive in the vicinity of the maximal constriction get redirected in the flow. This is certainly due to a local increase of the hydrodynamic shear. Also bacteria moving on the top/bottom surfaces on this side of the contrition, get easily "captured" by the left/right walls and the previous described scenario repeats. Therefore the dwelling time past the junction increase compared to the dwelling time before the junction and the symmetry is broken. This results as an increase of the density difference on both parts of the funnel.

II.2.2.5 Trapping/untrapping at the lateral walls

As described in the previous section, the transfer of bacteria to the lateral walls is a central contribution to the symmetry breaking effect. So now we focus on a quantitative description of this effect. Let us first consider an heuristic scenario. Once the funnel is passed, if one bacterium reaches one of the sides walls, it moves back-flow until it reaches the constriction to be recycled in the flow. Then, for a constant input of bacteria, the bacteria concentration close to the funnel would increase boundlessly and the concentration far from the funnel would decrease to zero since, through the dispersion processes, any bacterium would get a finite probability to hit one the side walls. In this extreme scenario, the left/right trapping is considered as "perfect". However, if there is a finite probability of untrapping due to hydrodynamic shear or to thermal fluctuations, one would reach on both sides and far from funnel, a steady concentration of bacteria. If the untrapping probability is not too large, this scenario would yield all the qualitative features identified experimentally such as symmetry

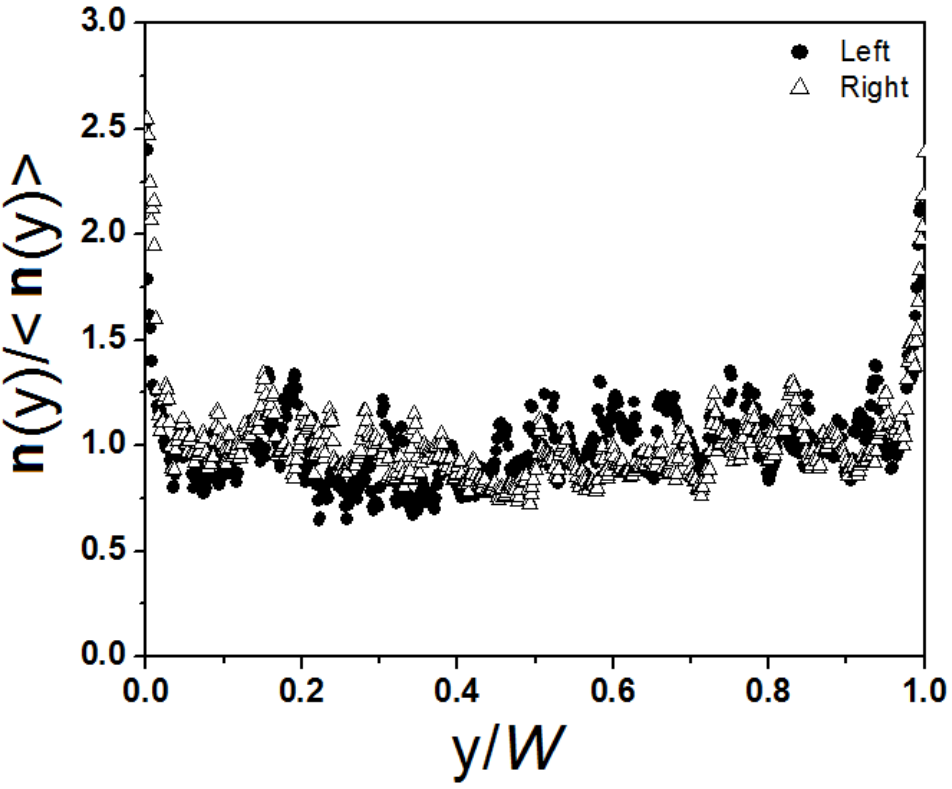

Figure II.2.10: Transverse bacterial concentration as function of y. Dark circles represent the profile measured between -2.1 and -1.7 mm and white triangles the result obtained between 1.7 to 2.1 mm. $< n(y) >= 4.25 \times 10^8\ Bact/ml$ and $< nC(y) >= 5.5 \times 10^8\ Bact/ml$, represent the mean concentration at the left and the right of the funnel, respectively.

breaking and concentration increase in the vicinity of the funnel. With this idea in mind, we measured properties of the bacteria transfer in the transverse direction.

First, I computed the transversal bacteria concentration profiles n(y), far from the constriction i.e. between 1.7 and 2.1 mm away from the funnel and on both sides. It can be noticed on Fig. II.2.10 that both profiles are similar, but with slightly different mean concentration ($< n(y) >= 4.25 \times 10^8 Bacteria/ml$ and $< n(y) >= 5.5 \times 10^8 Bacteria/ml$ before and after the constriction, respectively). One can observe a concentration increase at the lateral walls, but on a range of few microns. This is likely to be an effect similar to the hydrodynamic trapping effect as described in the first chapter. This measurement shows that far from the funnel, one has a quasi balanced flux of bacteria going in and out of the side walls. On figure II.2.9.(B), I display several bacteria trajectories detaching and reattaching from the sides walls. Note that some of them also travel upstream.

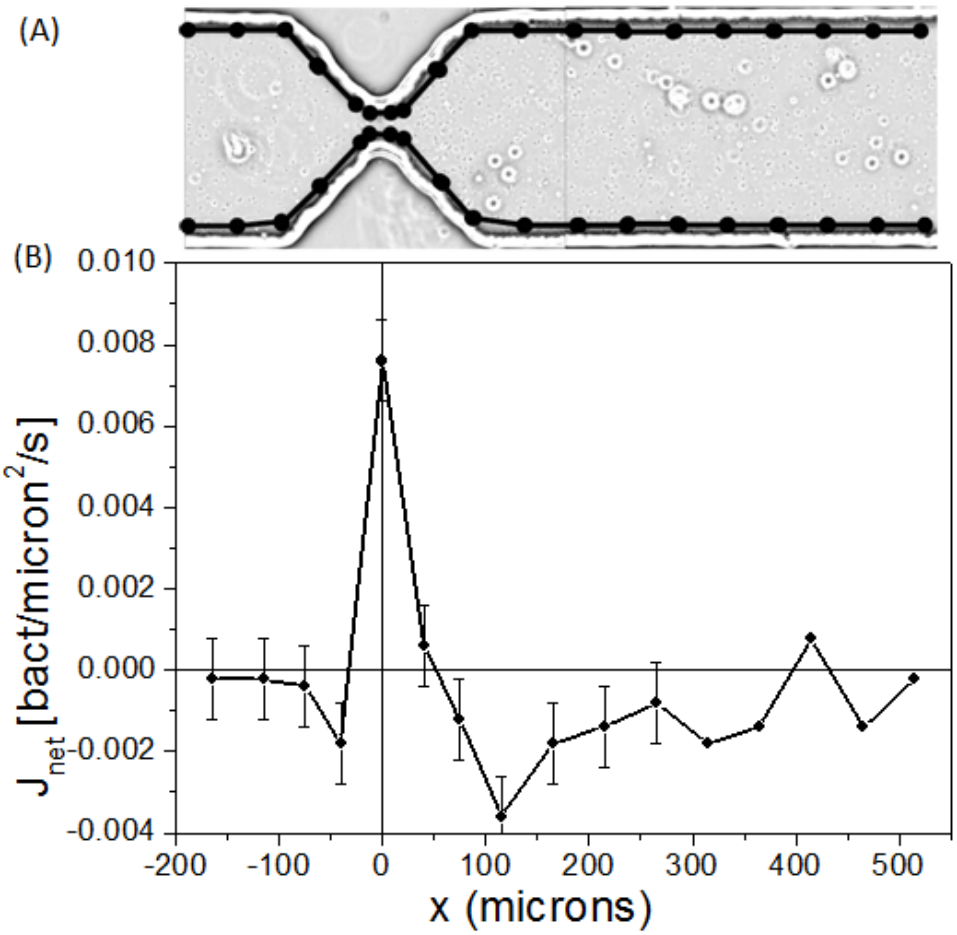

Figure II.2.11: Bacterial flows from and to the lateral walls. (A) Sketch of the segments defined near the lateral walls: the upper and lower walls of the channel used to count the flows of bacteria crossing them from and to the walls. Each segment is of approximately 50 μm-length (except in the central part of the bridge, where they are shorter). (B) Plot of the *net* number of bacteria crossing the segments from/to the walls. The green line is just the sum of the upper and lower walls (for clarity, error bars are displayed only , and roughly correspond to miscounting 5 bacteria every 5 seconds). When $J(x) > 0$, bacterial desorption dominates, when $J(x) < 0$ absorption dominates, and when $J(x) = 0$, the processes compensate each other. At distances bigger than 2000 μm to the right, the net flow is zero.

To quantify the contribution of the lateral walls to the bacteria transport and the dispersion properties, the flux of bacteria going towards and outwards the lateral (left/right) walls was measured. For a flow velocity $< V_x >= 25\ \mu m/s$, the number of bacteria crossing segments of length 50 μm located parallel and near the walls, was counted during 5 s. Figure (II.2.11) displays the net flux $J(x)$ i.e. the local flux transverse to the flow along the x direction either on the right of the left side. Note

that the sign convention on $J(x)$ is such that a positive value means more bacteria moving from the wall to the channel center. After a peak of desorption near the funnel (qualitatively described above), absorption at the walls dominates on the right part of the funnel over a distance of approximately 500 μm. Then, at long distances (2000 μm), $J(x)$ reaches a value close to zero. Within the experimental uncertainties, it means that a quasi-steady regime is obtained which is consistent with the previous measurement of an homogeneous bacteria concentration in the transverse direction.

The striking part of this result is the long range "memory" effect of the transverse flux. Passed the funnel and over long distances, the lateral boundaries still shows a dominant adsorption effect. This can be viewed as a non-local response of the transport process in response to the constriction since the local hydrodynamic flow fields in the channel are likely to be the same 100 microns after the constriction and 2 millimeters away! Note finally that this non local effect is not necessarily due to the left/right walls only but a contribution of all the surfaces including the top/bottom ones on the bacteria trajectories.

General Conclusion

In the research presented in this thesis, I provide two examples showing how active bacteria suspended in a fluid, transfer their momentum through the liquids and change the standard constitutive macroscopic relations of micro-size particles suspensions.

Brownian activation

The first example is concerned with the Brownian motion of a passive sphere of diameter d in a viscous fluid. For thermal fluids, the diffusive motion caused by thermal fluctuations is characterized, close to equilibrium by Einstein's relation which is a fluctuation-dissipation theorem : $D_B = k_B T/3\eta d$, relating diffusivity D to viscosity η through thermal energy : $k_B T$.

In the present work, I investigated how this relation is modified by the presence of active swimmers and I focused on the activation close to a solid boundary.

The central result is that I measured under many different conditions, the passive tracers diffusivity D_P and I have shown that it is linearly related to what I defined as an "active flux": $J_A = n_A V_A$, where n_A is the density of active swimmers close to the walls and V_A their mean velocity. The relation can be written:

$$D_P = D_P^B + \beta J_A \tag{2}$$

Where D_P^B is the Brownian diffusivity close to a boundary i.e. a fraction of the Brownian diffusivity in the bulk, which depends on the actual mean approach of the tracer to the wall. The proportionality factor is the fourth power of a length: $\beta = \Lambda^4$. I measured the value of Λ in many different conditions, changing the nature of the swimmer (*E.Coli* bacteria or active bimetallic rod), the concentration of active swimmers, their mean velocity. Note I also investigated suspending media of different viscosities and buoyancy with respect to the microparticles. In all cases I found that this length was between 1.5 and 2 μm, a typical microswimmer size. Looking closer at its dependence, I found that this length has a tendency to increase with confinement coming either from buoyancy effects, which get by sedimentation the particles closer

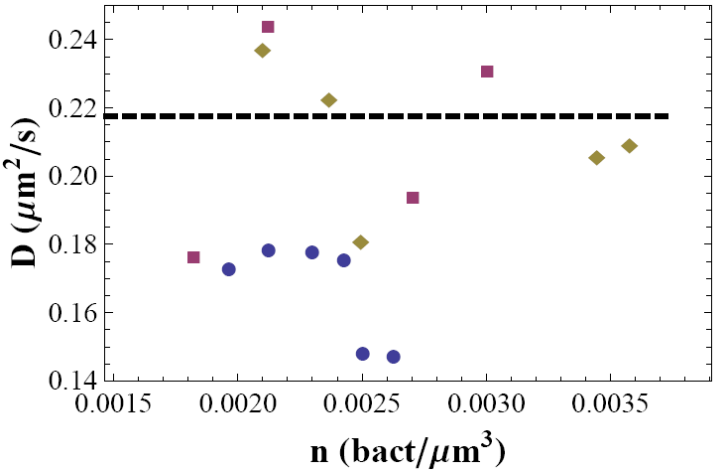

Figure 1: Constant diffusion measured in the bulk for 2 μm passive tracers in non-buoyant condition as a function of bacteria density n.

to the wall, or due to the influence of a second wall on the top. I also found re-analyzing their data, that the results of Wu and Libchaber (2000) for *E. Coli* trapped in a thin film are compatible with my results.

Now a question is to understand to which extend this result remains valid for a population of active swimmer in the bulk (i.e. far from the boundaries). There are two experimental results that seem to go in this direction, first the enhancement of diffusivity measured by Leptos *et al.* (2009) for the unicellular algae *Chlamydomonas*. They find a linear behavior with swimmer density and if I compute from their data the effective corresponding length Λ, I find $\Lambda = 5.46 \pm 0.66 \mu m$ for a 10 μm micro-organism diameter size. A second set of measurements was done by Wilson *et al.*(2011), using a low-k light scattering measurement under the microscope, they could obtain a diffusion enhancement of "passive" bacteria suspended in the bulk. They also found a linear relationship with density. If I cast their result in our frame-work I obtain a length $\Lambda = 2.28 \pm 0.05$, for *E. Coli* bacteria size.

On my side, I also performed experiments where I followed tracers far from the wall in the non-buoyant medium. However, in spite of the fact, I measured a concentration of bacteria in the vicinity of the focal plane, I observed no diffusivity enhancement! This seems to be in contradiction with the previous results, except if all the "active swimmers" after a while were to be found close to the walls. Note that the experiments were performed after approximately 10 min after the chamber was placed on the stage of the microscope and thus the active swimmers had plenty of

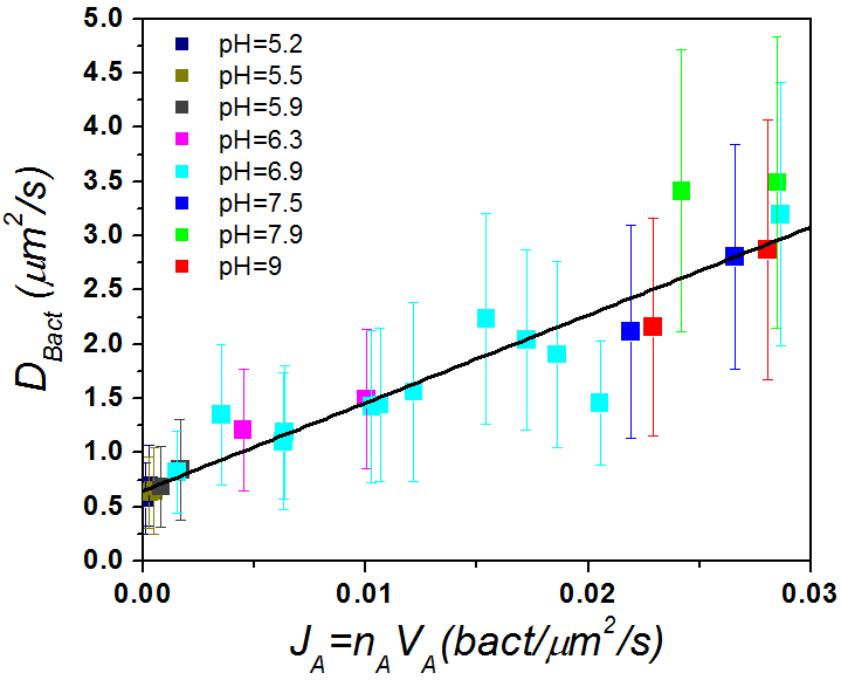

Figure 2: Enhancement of random bacteria diffusion under the effect of active bacteria close to the wall, in buoyant condition. Black line represent a linear fit where the slope $\beta = 81 \pm 5.4$ correspond to a $\Lambda = 3 \pm 0.8$. The mean number of bacteria in the visualization field was $< N >= 300$.

time to get trapped at the boundaries. Indeed, a decisive step in my work was that I could separate the random swimmers which do not participate to activation, from the active swimmer which contributed to the diffusion enhancement. Due to tracking difficulties in 3D, such a separation was not possible for the bulk measurements.

Finally, to "close the loop" and make contact with the work of Wilson *et al.* (2011) in the bulk, it would be interesting to see if the inactive swimmers undergo also a diffusion enhancement. This result is quite preliminary since this question was not at the focus of my thesis. However preliminary data seem to indicate that it is so. Fig. 2 displays results obtained for a buoyant MMA solution where the mean diffusivity of the random bacteria was extracted and plotted versus the active diffusivity. The effective diffusivity enhancement is quite large ($\Lambda = 3 \pm 0.8$).

From a conceptual point of view, the reason for the simple picture underlined by equation (2) remains to be understood. My measurements seem to indicate that the concentrations used in this experimental investigation is low enough so that I always remain in the low density limit. It also means that interactions between the active

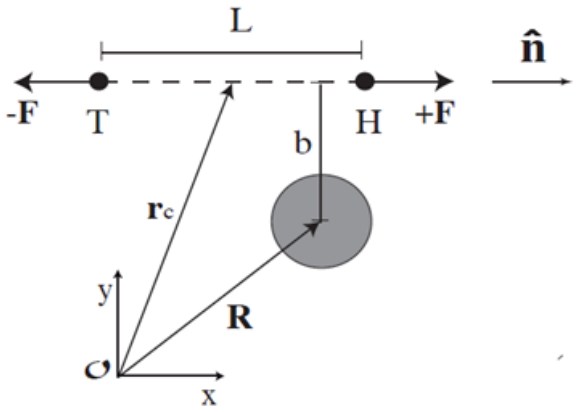

Figure 3: Dipolar model of a swimmer interacting with a particle, where H and T represent the head and the tail of the bacterial model, and b is the impact parameter.

suspension and the tracer can be viewed as a decomposition of elementary scattering interactions between a bacterium and a tracer. From this simple idea, the linear relation between diffusivity enhancement and so called "active flux" comes naturally. This is the kinetic theory picture.

To rationalize this idea from an hydrodynamic point of view, Jocelyn Dunstan in her Master's thesis(Dunstan (2010)) in Pr Soto's group, did a theoretical hydrodynamic calculation on a model, where the swimmer is modeled as a force dipolar interacting with a sphere (see fig. 3). The trajectory undertaken by the sphere, from the interaction with the dipole coming from infinity and moving to infinity, does not completely close. This is at the origin of the irreversible diffusive motion. Thus, summing on all the possible scattering interactions, she obtains the mean cross section and thus could compute a diffusivity enhancement proportional to the bacteria concentration multiplied by its velocity (i.e. the active flux). At the leading order, the tracer size does not play any role. Moreover, computing the order of magnitude for "realistic" parameters, she found a β value much to small compared to experimental data. It would be interesting to see if a more sophisticated swimmer model as the one we described in the first section, would improve the agreement with the experimental values.

Finally, a natural extension of this work would be to investigate higher bacterial densities in order to see if more complex hydrodynamic interactions and possibly collective bacterial motion may change the activation picture.

Active viscosity and Anomalous dispersion

In the experiment presented in the second part, two studies of bacteria flowing in a microchannel device were presented.

In the first one, by using a micro-fluidic channel rheometer, we have measured the effective viscosity in the bulk produced by pusher-type suspensions of *E. Coli*. We measured its dependence with concentration and established the variation with shear rate. At low shear and moderate concentrations we found evidence of a non Newtonian behavior of the relative viscosity. It reaches a maximum value, placed at a frequency of 10 Hz comparable to the inverse of the swimming time, almost independently of the concentration. This effect on the viscosity of active swimmer has been predicted by Haines (2009)*et al.* and Saintillan (2010), for dilute suspensions. Our results show a clear agreement in the low concentration limit with the model presented by Saintillan, as far as the qualitative shape of $\eta(\dot{\gamma})$ is concerned.

In the future it would be interesting to take advantage of the microfuidic device to directly identify organization of bacteria swimming in a flow. This might be an important question in the semidilute limit and it can help to make a contact with numerical simulation and theory (Ryan *et al.*, 2011).

In the second set of experiments, we have shown that an active suspension of *E. Coli* passing through a microfluidic channel with a funnel-like constriction, displays anomalous dispersion properties due to confinement. For mean flow velocities, typically smaller than the mean swimming velocity, the bacteria concentration shows a strong density increase passed the funnel. The reconcentration effect decays over large distances along the flow. The effect disappears at high flow rates. By a detailed microscopic analysis of the bacteria trajectories, I show that the symmetry breaking is caused by an interplay between surface interactions promoting bacteria motion up flow or across the flow and the constriction provoking a preferential reinjection of the upstream going bacteria, just before crossing the funnel. These combined actions of the surface and the channel geometry increase significantly the retention of bacteria in the vicinity of the funnel. The reconcentration effect will remain until viscous shear is large enough to "erode" the bacteria from the surface and reduce their dwelling time on the surfaces. Also this "non local" effect due to the channel geometry opens many

question on the description of suspension transfer in porous or tortuous materials. This is certainly an issue that can be analyzed using more complex microfluidic channel. From a practical point of view. This experiment opens the possibility to control the bacterial concentration in micro-fluidic channels by simply tuning the flow of the suspending fluid and the pore geometry.

To continue this study , it will be necessary to directly probe the spatial distribution of bacteria in the channel as well as their velocity distribution in order to address the question of anomalous statistical properties coming from hydrodynamic interactions. Moreover, the construction of an active tracking device will allow a direct test of the hypothesis at work either in the theory or in the numerical simulations modeling the swimming behavior of bacteria in a shear flow.

Appendix

Appendix A: Bacteria growth and working suspensions

In this Appendix, I will describe how the samples were prepared. To begin with, I will present the two media used in this study. The main one: Minimal Motility Medium (MMA) and its mixture with Percoll in order to obtain isobuoyant medium to suspend either latex beads or bacteria or their mixture. then, bacteria cultivation as well as beads and chamber preparation will be described.

Working Media

a) Minimal Motility Media (MMA)

MMA was prepared as followed: Stock solutions (1 M NaH_2PO_4,and 1M K_2HPO4) were mixed to generate phosphate buffers at a given pH (from 5;5 to 8). The stock phosphate buffers were diluted to a final concentration of 10 mM in the presence of 0.1mM K-EDTA that favors motility. (Adler and Templeton (1967) , and Adler (1973)); 20mM Sodium Lactate as an energy source ,in some cases 1% glucose was added to prevent the effects of miss-oxygenation. Potassium acetate (34mM) was also present in order to obtain bacteria with swimming velocities sensitive to pH (Minamino *et al.* (2003)). In the same way, we prepared MMA-Percoll suspensions by adding various proportion of Percoll to a concentrated stock solution of MMA pH 6,9(5x) as to obtain in fine the same salt concentration as in pure MMA.

In order to characterize the viscosity of pure MMA solutions at various pH, an Anton Paar Physica MCR Rheometer was used. For each solution, the shear rate was varied from 10 to $100s^{-1}$, and 20 points were measured. The procedure was repeated three times. Fig. 1 shows the shear stress as function of the shear rate for MMA at pH6, 6.9, and 8 in comparison to the values obtained with distilled water. It can be noticed that the presence of the various component in MMA nor the pH have an effect on its viscosity.

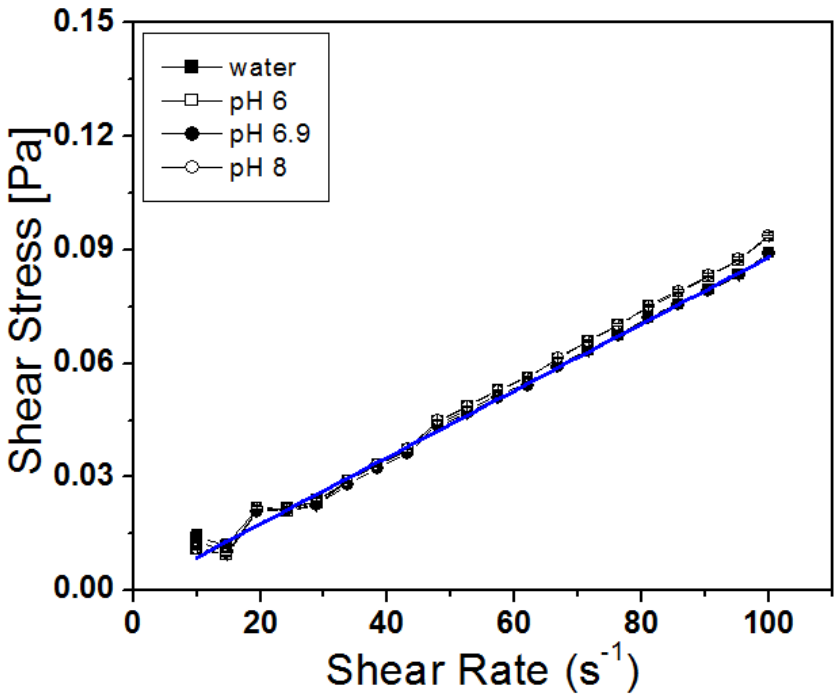

Figure 1: Shear Stress as function of the Shear Rate for Minimal Motility Medium at different pH, in comparison with the distilled water measurement (0.88 *mPas*). Error bars represent standard deviation from the three determinations.

b) Mixture of MMA and Percoll

The same was repeated with MMA-Percoll suspensions (1/1) but a different result was obtained. Percoll is a silica colloid extensively studied by Laurent *et al.* (1980).

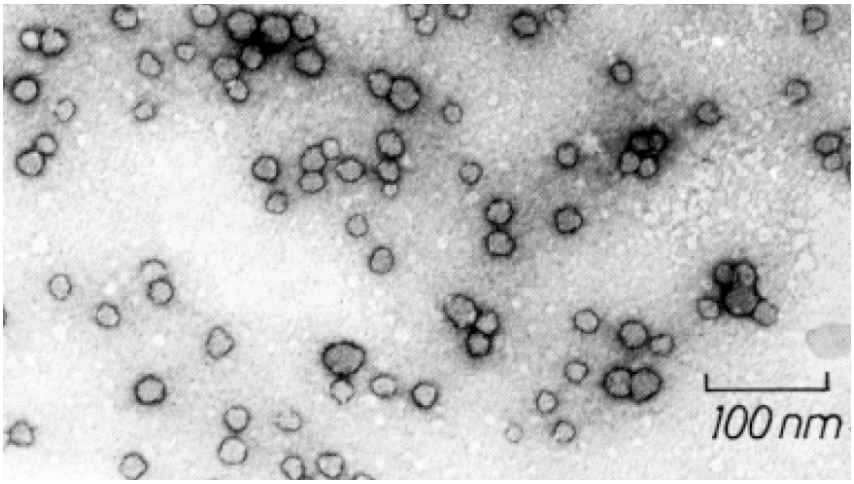

Figure 2: Electron microscope image of Percoll particles.

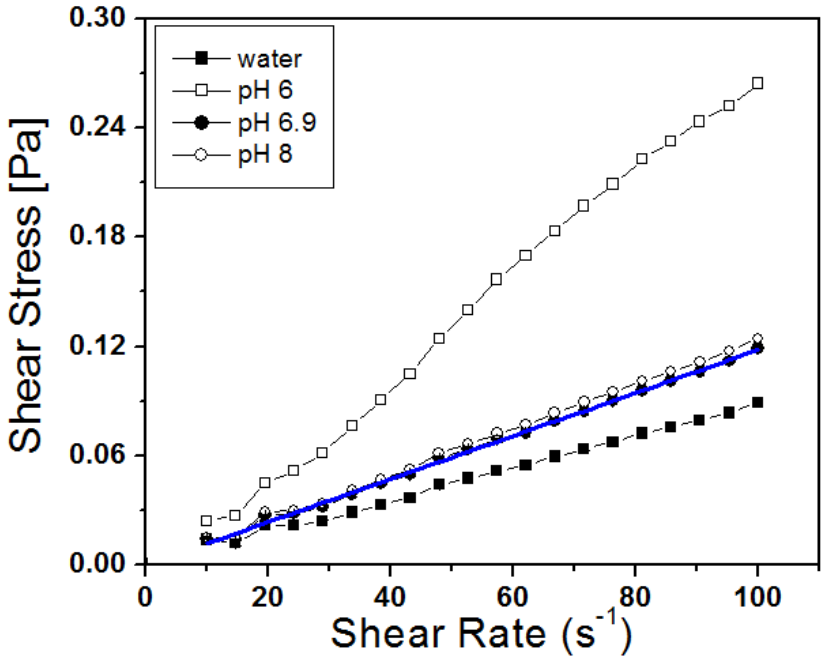

Figure 3: Shear Stress as function of the Shear Rate for the mixture of MMA-Percoll at different pH, compared to distilled water ($\nu = 0.88mPas$). Error bars represent standard deviation from the three determinations. Blue line represents a fit for the data obtained for pH 6.9 ($\nu = 1.18mPas$)

In the Fig 2, an electron micrograph of this colloid in suspension is shown. The silica appears as poly-dispersed particles with sizes ranging between 15 to 30 nm and a mean particle diameter of 21-22 nm. (See Percoll: Methodology and Applications, Amersham Biosciences AB 2001)

The rheology of the MMA/Percoll suspension (1/1) was studied. Fig. 3 shows the dependency of the stress rate as function of the shear rate at different pH (6, 6.9 and 8). It can be noticed that the presence of Percoll modifies the relation between the shear stress and the shear rate when compared to distilled water. In addition, the viscosity of the suspension changes with pH. Thus, when Percoll/MMA suspension was used the pH (6.9) was carefully controlled. As a consequence of the effect of pH on the viscosity of Percoll/MMa suspensions, in experiments where bacteria swimming velocity was controlled by pH no Percoll was present.

Bacteria

Wild-type *E. Coli* (ATCC 11105) were grown overnight in rich medium LB (Luria broth). The next day, part of this culture was diluted (100 times) in LB allowing logarithmic growth to restart. Several protocols were performed in other to obtain swimming bacteria with maximal velocity. Some authors, say that the maximum velocity is reached in the mid-exponential phase of the growth curve (Staropoli and Alon, 2000) whereas others, and also our observation, found that new born bacteria from the post exponential phase run faster (Amsler *et al*, 1993 and Prüβ and Matsumura, 1997). Thus once an optical density of 0.6 was reached (measured with spectrometer from Hitachi), bacteria suspension was washed twice by centrifugation in MMA to eliminate all LB traces and finally resuspended in MMA solution (pH 7) for at least an hour, allowing bacteria division to end as to obtain a population enriched with 1N bacteria, also called “baby cells”. In some cases, the “baby cells" were sorted by low speed centrifugation. The optical density of the resulting suspension was measured to determine the bacteria concentration and samples with given bacteria concentrations were prepared by sequential dilutions. When bacteria suspensions were introduced in micro-chamber Poly-Vinyl-Pyrrolidone (PVP) at 0.005% was added to the suspension to avoid stickiness.

Beads preparation

To study the effect of bacterial activity on the diffusivity of passive tracers, latex beads of 1 or 2 micron diameter (Beckman-Coulter, density ρ=1.027 g/ml) were added to the suspensions. These spherical particles come in an aqueous medium containing surfactant that was eliminated by 3 successive centrifugations in MMA. Finally they were resuspended in MMA containing 0.005% PVP.

Chamber preparation

The sample is placed in a chamber made out of two horizontal microscope coverslips separated by coverslip (N^0 0.085 to 0.13 mm thick) as spacers. As shown in Fig. **??**

the typical chamber height is 110 micrometer. To avoid the stickiness, coverslips were previously coated with Ethanolic PVP (20 mg/ml PVP in pure ethanol at -20mg/ml) and dried.

Appendix B: Programs for the image analysis

In this Appendix, I will describe the method I used to identify and differentiate passive tracers from active swimmers and the program I developed for the particle and swimmers tracking.

a) Passive Tracers recognition

To improve the contrast of the latex beads images over the background, the gray scale is inverted. As a second step, the analyzed image is filtered using a *band-pass filter* (from ImageJ toolbox), described online at: `http://rsbweb.nih.gov/ij/plugins/fft-filter.html`. The used macro has two important input parameters, defined as:

- Filter Large Structures Down to S_{max} pixels (allowing shading correction, by removing background inhomogeneities).
- Filter Small Structures Up to S_{min} pixels (to smooth the bacteria images, any objects with a size smaller than the tracer are strongly attenuated).

From a preliminar analysis, we found that acceptable filtering is achieved on the images of interest by setting $S_{max} = 40$ and $S_{min} = 5$.

A *Gaussian Blur Filter* was also applied to the images. The filter is part of the ImageJ toolbox and it is described online at `http://rsbweb.nih.gov`. It convolutes the image with a normalized Gaussian function, where the σ_{BF} parameter represents the radial distance were the intensity decreases to $\exp(\hat{} - 0.5)$. Considering the bead's sizes, the $\sigma_B F$ parameter was set to 4. A second smoothing effect on the image is achieved after this step.

b) Bacteria recognition

A similar process was used for bacteria. When bacteria are close to the surface they appear as bright objects in the image. To facilitate the analysis we had to increase the

contrast of the bright objects over the background. The image processing starts by using the *band-pass filter*, as described above but by setting $S_{max} = 10$ and $S_{min} = 0$. The postprocessing continues by appyling the ImageJ *Unsharp Mask filter* described at `http://rsbweb.nih.gov`. This filter brings out details in the images. As first stage on this filtering, a blurred copy of the image is generated after defining a blurring distance (σ_M). Such an image is substracted to the original one as a second step. Since this operation results in the background removing, this stage is similar to apply a high-pass filter on the image. On the second stage, the obtained image is multiplied by a weight coeficient (W_M) ranging between 0 and 1, after what it is added to the original image producing a sharper final image. This parameter determines the strength of filtering. As a final stage, a *Gaussian Blur filter* as described above is applied. To enhace levels of maximal intensity. σ_M, W_M and $\sigma_B F$ were chosen as 5, 0.7 and 2 respectively. As a last stage of the image postprocessing, intensity normalization is performed on the image by rescaling the grey levels to uniform the intensity mean value of all the analyzed images. This uniform value is arbitrary chosen by the user.

The next step of the image analysis is to determine the particles positions. To achieve it, the macro scans each image to detect the highest level of intensity by searching in a kernel of $3x3$ pixels all over the image. A bilinear interpolation is performed to find the position of the maximum (Press *et al.*, 1992).

Finally, the macro generates an output text file that contains the intensity, the x and y position and the corresponding frame number of each detected object. This file is used as input to a tracking program.

Particle Tracking

Once the particle positions are detected, the next step consists of linking the different points to construct the trajectories. For this purpose, a tracking program in C++ developed by Thierry Darnige is used. On one hand, this program needs the position file generated by the macro developed in ImageJ and, on the other hand, the specification of several parameters.

- sizeTrackMin: this is a length cut-off, i.e., minimum trajectory length to take into account.

- distmin: this value represents the minimal searching radio, and it has to be less than the size of the particle. This value was set in zero.
- distmax: this is the maximum radius of searching, and it is related to particle velocity. If this value is low compared to the displacement of the particle, the trajectory could be truncated because the program does not find the following point in the trajectory. If this value is hight compared to the "step size" of the particle, the program will confuse different particles assuming that is the same object. It can be noticed that this parameter will depend on particle displacement and acquisition frequency.

Once the program has been run, a tracking file with all the trajectories is generated. Moreover, a second file is created including only trajectories larger than the length cut-off parameter (sizeTrackMin).

From this point, the information is ready to be analyzed depending on the particles to be studied.

Appendix C: Channels Fabrication

The construction of microchannel using polidimethylsiloxane (PDMS) requests several steps that will be described in this appendix.

Mask preparation

The first step for the construction of any microchannel using soft lithograph method starts by designing the mask that contains the desired pattern (Xia and Whitesides, 1998). The drawing can be made in a CAD program (for example, Autocad or CleWin), using a scale 1:1. The fig. 4 shows the design of two masks developed to obtain channels with different patterns. The next step is to print the design on a transparent sheet of polymer with a commercial image setter (we used the service of SELBA S.A. Hight Precision Photolithography. Structures $> 6\mu m$ need a solution of 50800 dpi). In the mask, the transparent parts will be transfered to the wafer and will form the relieve.

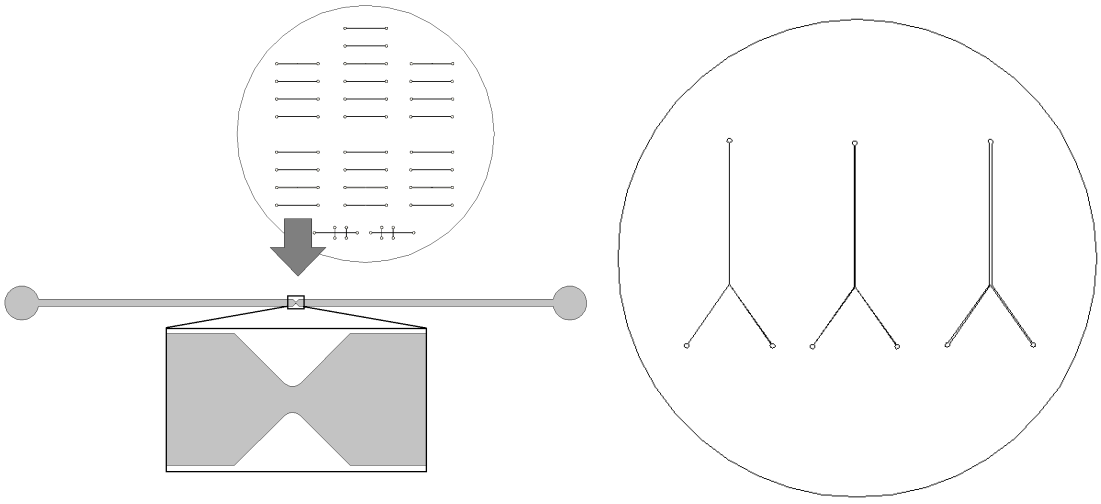

Figure 4: Mask developed for the fabrication of the microchannel with a constriction (left) and Y-shape channel (right)

Soft Lithography

In the process the resin SU-8 MicroChem is used. For each thickness there is a type of resin. For example, if the height of the chamber is 100 μm, the SU-8 2100 must be used. In the following, a detailing procedure is shown.

1. Clean the wafer with isopropanol, toluene or alcohol. This step is not performed if the wafer is new. The shining part has to be up.

2. A Spin-coater is used to obtain the desired height, and it has to be programed following the angular velocity ω scheme shown by fig. 5.

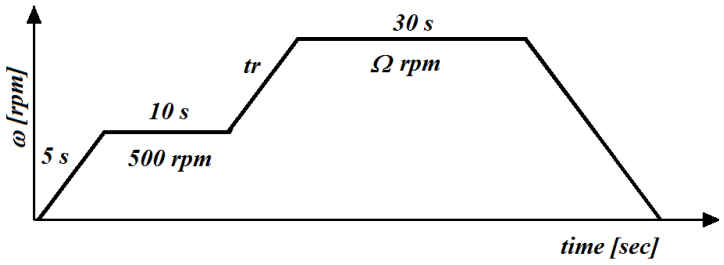

Figure 5: Spin coating time diagram

The selection of the angular velocity Ω is taken from the graph on the data sheet of the resin. With the height, we choose the resin. Then, we look in a graph that relates the height with the angular velocity in rpm, this value can modify by the temperature.

$$ac = 300rpm/sec$$
$$tr = (\Omega - 500)/300rpm$$

3. Put the wafer, and then put the resin. Cover the Spin-Coater. Run the program

4. Initialize the timer for the soft bake (at 65 °C and 95 °C).

5. Put the wafer in 65 °C during the time showed in the data sheet.

6. Sequentially, put the wafer in 95 °C (time in data sheet)

7. Let the wafer cool down for 5 min to room temperature.

8. UV Exposure Before this process: Clean the glass in the UV MJB4 machine. Cut the mask in a square way. Put the vacuum in the metal part. Place the glass and glue the mask to the glass. Place metal-glass-mask in the machine. (Don't forget the lever). We have to use a wafer sample that is in a Petri box. In the software, select the soft contact bottom. In this procedure, we move the knob until the program say that it touches. Then we go down until the program say that it is ok. From here, we turn until we have the required thickness. One 360 ° rotation is equal to 170 micrometers. 1/60 = 17 μm. The filter is putted in this case the I (365 nm) Place the wafer after the step 7. After it has been placed, expose to UV. Exposure time: See table in the data sheet and introduce this parameter in the program.

9. Bake the wafer in 65 °C (time in data sheet)

10. Bake the wafer in 95 °C (time in data sheet)

11. Cool down

12. Put the wafer in Developper SU 8. The part that was not exposed will be removed. We have to shake the solution until the trace disappears.

13. Rinse with isopropanol; if there is a trace of non exposure resin a white part will appear. Use a garbage recipient for this.

14. Dry with compressed air.

15. Verify the height with any dispositive to measure the profile of the mold (for example, DEKTAK profilometer).

We can mention that all these parameters depend on the resin used and the thickness of the relief. Fig. 6 shows an example of a wafer obtained for the Y-shape channel.

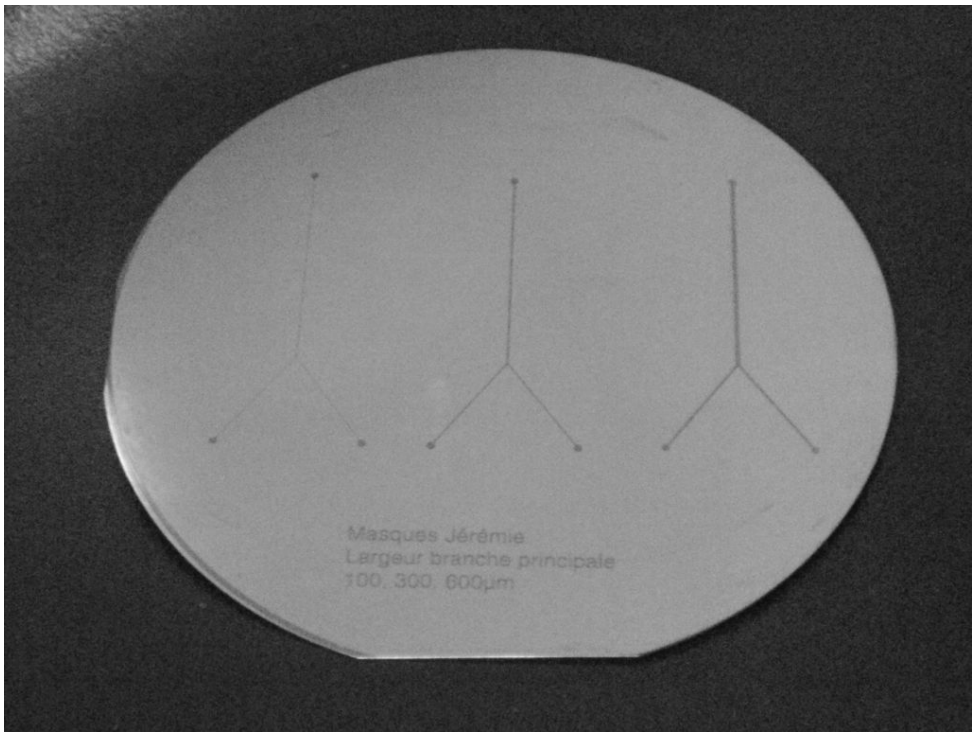

Figure 6: Stamp, wafer or mold for the Y-Shape channel

PDMS fabrication

After the stamp, wafer or mold is ready, the fabrication of the microchannel can start. The PDMS is made from a mixture of resin and the cross-linking agent (proportion 10:1, respectively). The mingle procedure generates a lot of bubbles, which, at a first stage will be eliminated using a centrifuge. Then the mixture is poured over the wafer that is inside of a little recipient made of aluminum paper. Next, to eliminate the bubbles, it is placed in a vacuum pump, for 30 min to 1 hr. Once the bubbles are

gone, the wafer-PDMS is placed in the oven at 70 ° C for 2 hr. After this the PDMS is solid and can be cut and the holes for the connection can be made.

In order to have the same type of walls in the channel, a coverslip is coated with a thin film of PDMS. In this case we used an spin coated to have a film of 27.8 μm. The coverslip is also baked in the oven.

The next step is to glue the PDMS onto the coated coverslip. Both surfaces are exposed to plasma during 30 seconds. This operation forms the radicals on the surface that will allow the gluing. Both surfaces are then put together to form the covalent junctions (attention needs to be pay that there are not bubbles between the surfaces). Lastly, the channel goes into the oven at 0 ° C for a couple of hours.

Bibliography

[1] Amsler C. D., Cho M., and Matsumura P. Multiple factors underlying the maximum motility of *Escherichia coli* as cultures enter post-exponential growth. *J. Bacteriol.*, 175, pp. 6238–6244, 1993.

[2] Archer C. T., Kim J. F., Jeong H., Park J. H., Vickers C. E., Lee S. Y., and Nielsen L. K. The genome sequence of e. coli w (atcc 9637): comparative genome analysis and an improved genome-scale reconstruction of *E. coli*. *BMC Genomics*, 12, pp. 9, 2011.

[3] Baskaran A. and Marchetti M. C. Statistical mechanics and hydrodynamics of bacterial suspensions. *Proc. Natl. Acad. Sci.*, 106, pp. 15567–15572, 2009.

[4] Berg H. C. Constraints on models for the flagellar rotary motor. *Phil. Trans. R. Soc. Lond. B*, 355, pp. 491–501, 2000.

[5] Berg H. C. The rotary motor of bacterial flagella. *Annu. Rev. Biochem.*, 72, pp. 19–54, 2003.

[6] Berg H. C. E. coli *in motion*. Springer-Verlag, New-York, 2004.

[7] Berg H. C. and Brown D.A. Chemotaxis in *Escherichia coli* analysed by three-dimensional tracking. *Nature*, 239, pp. 500–504, 1972.

[8] Berke A. P., Turner L., Berg H. C., and Lauga E. Hydrodynamic attraction of swimming microorganisms by surfaces. *Phys. Rev. Lett.*, 101, pp. 038102, 2008.

[9] Brenner H. The slow motion of a sphere through a viscous fluid towards a plane surface. *Chem. Eng. Sci.*, 16, pp. 242–251, 1961.

[10] Chen D. T. N., Lau A.W. C., Hough L. A., Islam M. F., Goulian M., Lubensky T. C., and Yodh A. G. Fluctuations and rheology in active bacterial suspensions. *Phys. Rev. Lett.*, 99, pp. 148302, 2007.

[11] Cheung C., Hwang Y. H., Wu X-l., and Choi H. J. Diffusion of particles in free-standing liquid films. *Phys. Rev. Lett.*, 76, pp. 2531–2534, 1996.

[12] Di Leonardo R., Dell'Arciprete D., Angelani L., and Iebba V. Swimming with an image. *Phys. Rev. Lett.*, 106, pp. 038101, 2011.

[13] DiLuzio W. R., Turner L., Mayer M., Garstecki P., Weibel D. B., Berg H. C., and Whitesides G. M. *Escherichia coli* swim on the right-hand side. *Nature*, 435, pp. 1271, 2005.

[14] Dombrowski C., Cisneros L., Chatkaew S., Goldstein R. E., and Kessler J. O. Self-concentration and large-scale coherence in bacterial dynamics. *Phys. Rev. Lett.*, 93, pp. 098103–1, 2004.

[15] Drescher K., Dunkel J., Cisneros L. H., Ganguly S., and Goldstein R. E. Fluid dynamics and noise in bacterial cell-cell and cell-surface scattering. *Proc. Natl. Acad. Sci.*, 108, pp. 10940–5, 2011.

[16] Dreyfus R., Baudry J., Roper M. L., Fermigier M., Stone H. A., and Bibette J. Microscopic artificial swimmers. *Nature*, 437, pp. 862, 2005.

[17] Dunstan J. *Modelo Hidrodinámico de bacterias interactuando con superficies y particulas micrométricas.* Tesis de Licenciatura, Departamento de Física, FCFM - Universidad de Chile, 2010.

[18] Dunstan J., Miño G., Clément E., and Soto R. A two-sphere model for bacteria swimming near solid surfaces. *Phys. Fluids*, 24, pp. 011901, 2012.

[19] Eisenbach M. Bacterial chemotaxis. *Encyclopedia of Life Science*, 2001.

[20] Feitosa M. I. M. and Mesquita O. N. Wall-drag effect on diffusion of colloidal particles near surfaces: A photon correlation study. *Phys. Rev. A*, 44, pp. 6677–6685, 1991.

[21] Gaffney E.A., Gadêlha H., Smith D.J., Blake J.R., and Kirkman-Brown J.C. Mammalian sperm motility: Observation and theory. *Annu. Rev. Fluid Mech.*, 43, pp. 501, 2011.

[22] Galajda P., Keymer J., Chaikin P., and Austin R. A wall of funnels concentrates swimming bacteria. *J. of Bact*, 189, pp. 8704, 2007.

[23] Goldman A. J., Cox R. G., and Brenner H. Slow viscous motion of a sphere parallel to a plane wall-i. motion through a quiescent fluid. *Chem. Eng. Sci.*, 22, pp. 637, 1967.

[24] Golestanian R. and Ajdari A. Analytic results for the three-sphere swimmer at low reynolds number. *Phys. Rev. E*, 77, pp. 036308, 2008.

[25] Gray J. and Hancock G. J. The propulsion of sea-urchin spermatozoa. *J. Exp. Biol.*, 32, pp. 802–814, 1955.

[26] Grègoire G. and Chatè H. Onset of collective and cohesive motion. *Phys. Rev. Lett.*, 92, pp. 025702–1, 2004.

[27] Guillot P., Panizza P., Salmon J.-P., Joanicot M., Colin A., Bruneau C.-H., and Colin T. Viscosimeter on a microfuidic chip. *Langmuir*, 22, pp. 6438–6445, 2006.

[28] Gyrya V., Aranson I. S., Berlyand L. V., and Karpeev D. A model of hidrodinamic interaction between swimming bacteria. *Bull. Math. Biol.*, 72, pp. 148, 2010.

[29] Haines B. M., Sokolov A., Aranson I. S., Berlyand L., and Karpeev D. A. Three-dimensional model for the effective viscosity of bacterial suspensions. *Phys. Rev. E*, 80, pp. 041922, 2009.

[30] Hernandez-Ortiz J. P., Stoltz C. G., and Graham M. D. Transport and collective dynamics in suspensions of confined swimming particles. *Phys. Rev. Lett.*, 95, pp. 204501, 2005.

[31] Hill J., Kalkanci O., McMurry J. L., and Koser H. Hydrodynamic surface interactions enable *Escherichia coli* to seek efficient routes to swim upstream. *Phys. Rev. Lett.*, 98, pp. 068101, 2007.

[32] Holmqvist P., Dhont J. K. G., and Lang P. R. Anisotropy of brownian motion caused only by hydrodynamic interaction with a wall. *Phys. Rev. E*, 74, pp. 021402, 2006.

[33] Huang P. and Breuer K. S. Direct measurement of anisotropic near-wall hindered diffusion using total internal reflection velocimetry. *Phys. Rev. E*, 76, pp. 046307, 2007.

[34] Hulme S. E., DiLuzio W. R., Shevkoplyas S. S., Turner L., Mayer H. C., M. Berg, and Whitesides G. M. Using ratchets and sorters to fractionate motile cells of escherichia coli by length. *Lab Chip*, 8, pp. 1888–1895, 2008.

[35] Koch D.L. and Subramanian G. Collective hydrodynamics of swimming microorganisms: Living fluids. *Ann. Rev. Fluid Mech.*, 43, pp. 637–659, 2011.

[36] Lauga E., DiLuzio W. R., Whitesides G. M., and Stone H. A. Swimming in circles: Motion of bacteria near solid boundaries. *Biophysical Journal*, 90, pp. 400–412, 2006.

[37] Lauga E. and Powers T. R. The hydrodynamics of swimming microorganisms. *Rep. Prog. Phys*, 72, pp. 096601, 2009.

[38] Laurent T. C., Ogston A. G., Pertoft H., and Carlsson B. Physical chemical characterization of percoll. ii. size and interaction of colloidal particles. *Journal of Colloid and Interface Science*, 76, pp. 133–141, 1980.

[39] Laurent T. C., Pertoft H., and Nordli O. Physical chemical characterization of percoll. i. particle weight of the colloid. *Journal of Colloid and Interface Science*, 76, pp. 124–132, 1980.

[40] Leptos K. C., Guasto J. S., Gollub J. P., Pesci A. I., and Goldstein R. E. Dynamics of enhanced tracer diffusion in suspensions of swimming eukaryotic microorganisms. *Phys. Rev. Lett.*, 103, pp. 198103, 2009.

[41] Li G., Tam L.-K., and Tang J. X. Amplified effect of brownian motion in bacterial near-surface swimming. *Proc. Natl. Acad. Sci.*, 105, pp. 18355–18359, 2008.

[42] Lobry L. and Ostrowsky N. Diffusion of brownian particles trapped between two walls: Theory and dynamic-light-scattering measurements. *Phys. Rev. B*, 53, pp. 12050, 1996.

[43] Lowe G., Meister M., and Berg H. C. Rapid rotation of flagellar bundles in swimming bacteria. *Nature*, 325, pp. 637–640, 1987.

[44] Minamino T., Imae Y., Oosawa F., Kobayashi Y., and Oosawa K. Effect of intracellular ph on rotational speed of bacterial flagellar motors. *J Bacteriol.*, 185, pp. 1190–1194, 2003.

[45] Moran J. L., Wheat P. M., and Posner J. D. Locomotion of electrocatalytic nanomotors due to reaction induced charge auto-electrophoresis. *Phys. Rev. E*, 81, pp. 065302, 2010.

[46] Palacci J., Abècassis B., Cottin-Bizonne C., Ybert C., and Bocquet L. Colloidal motility and pattern formation under rectified diffusiophoresis. *Phys. Rev. Lett.*, 104, pp. 138302, 2010.

[47] Palacci J., Cottin-Bizonne C., Ybert C., and Bocquet L. Sedimentation and effective temperature of active colloidal suspensions. *Phys. Rev. Lett.*, 105, pp. 088304, 2010.

[48] Paxton W. F., Baker P. T., Kline T. R., Wang Y., Mallouk T. E., and Sen A. Catalytically induced electrokinetics for motors and micropumps. *J. Am. Chem. Soc.*, 128, pp. 14881–8, 2006.

[49] Paxton W. F., Kistler K. C., Olmeda C. C., Sen A., St. Angelo S. K., Cao Y., Mallouk T. E., Lammert P. E., and Crespi V. H. Catalytic nanomotors: Autonomous movement of striped nanorods. *J. Am. Chem. Soc.*, 126, pp. 13424–13431, 2004.

[50] Press W. H., Teukolsky S. A., Vetterling W. T., and Flannery B. P. *Numerical Recipes in C: The Art of Scientific Computing*. Cambridge University Press, 1992.

[51] Prüβ B. M. and Matsumura P. Cell cycle regulation of flagellar genes. *J Bacteriol.*, 179, pp. 5602–5604, 1997.

[52] Purcell E.M. Life at low reynolds number. *Am. J. Phys.*, 45, pp. 3, 1977.

[53] Rafaï S., Jibuti L., and Peyla P. Effective viscosity of microswimmer suspensions. *Phys. Rev. Lett.*, 104, pp. 098102, 2010.

[54] Ramia M., Tullock D. L., and Phan-Thien N. The role of hydrodynamic interaction in the locomotion of microorganisms. *Biophys.*, 65, pp. 755, 1993.

[55] Ringo D. L. Flagellar motion and fine structure of the flagellar apparatus in chlamydomonas. *J Cell Biol.*, 33, pp. 543–571, 1967.

[56] Ryan S. D., Haines B. M., Berlyand L., Ziebert F., and Aranson I. S. Viscosity of bacterial suspensions: Hydrodynamic interactions and self-induced noise. *Phys. Rev. E.*, 83, pp. 050904, 2011.

[57] Saintillan D. The dilute rheology of swimming suspensions: A simple kinetic model. *Exp. Mech.*, 50, pp. 1275, 2010.

[58] Saintillan D. and Shelley M. J. Orientational order and instabilities in suspensions of self-locomoting rods. *Phys. Rev. Lett.*, 99, pp. 058102, 2007.

[59] Sokolov A. and Aranson I. S. Reduction of viscosity in suspension of swimming bacteria. *Phys. Rev. Lett.*, 103, pp. 148101, 2009.

[60] Staropoli J. F. and Alon U. Computerized analysis of chemotaxis at different stages of bacterial growth. *Biophys J.*, 78, pp. 513–519, 2000.

[61] Wang Y., Hernandez R. M., Bartlett D. J., Bingham J. M., Kline T. R., Sen A., and Mallouk T. E. Bipolar electrochemical mechanism for the propulsion of catalytic nanomotors in hydrogen peroxide solutions. *Langmuir*, 22, pp. 10451–10456, 2006.

[62] Wheat P. M., Marine N. A., Moran J. L., and Posner J. D. Rapid fabrication of bimetallic spherical motors. *Langmuir*, 26, pp. 13052–13055, 2010.

[63] Wilson L. G., Martinez V. A., Schwarz-Linek J., Tailleur J., Bryant G., Pusey P. N., and Poon W. C. K. Differential dynamic microscopy of bacterial motility. *Phys. Rev. Lett.*, 106, pp. 018101, 2011.

[64] Wu X.-L. and Libchaber A. Particle diffusion in a quasi-two-dimensional bacterial bath. *Phys. Rev. Lett.*, 84, pp. 3017, 2000.

[65] Xia Y. and Whitesides G. M. Soft lithography. *Angew. Chem. Int. Ed.*, 37, pp. 550–575, 1998.

[66] Xie J., Khan S., and Shah M. Automatic tracking of *Escherichia coli* in phase-contrast microscopy video. *IEEE Trans. Biomed. Eng.*, 56, pp. 390, 2009.

Enhanced Diffusion due to Active Swimmers at a Solid Surface

Gastón Miño,[1] Thomas E. Mallouk,[2] Thierry Darnige,[1] Mauricio Hoyos,[1] Jeremi Dauchet,[1] Jocelyn Dunstan,[3] Rodrigo Soto,[3] Yang Wang,[2] Annie Rousselet,[1] and Eric Clement[1]

[1]*PMMH, ESPCI, CNRS (UMR 7636) and Université Paris 6 and Paris 7, 10 rue Vauquelin, 75005 Paris, France*
[2]*Department of Chemistry, The Pennsylvania State University, University Park, Pennsylvania, USA*
[3]*Departmento de Física, FCFM, Universidad de Chile, Santiago, Chile*

(Received 1 September 2010; published 25 January 2011)

We consider two systems of active swimmers moving close to a solid surface, one being a living population of wild-type *E. coli* and the other being an assembly of self-propelled Au-Pt rods. In both situations, we have identified two different types of motion at the surface and evaluated the fraction of the population that displayed ballistic trajectories (active swimmers) with respect to those showing random-like behavior. We studied the effect of this complex swimming activity on the diffusivity of passive tracers also present at the surface. We found that the tracer diffusivity is enhanced with respect to standard Brownian motion and increases linearly with the activity of the fluid, defined as the product of the fraction of active swimmers and their mean velocity. This result can be understood in terms of series of elementary encounters between the active swimmers and the tracers.

DOI: 10.1103/PhysRevLett.106.048102 PACS numbers: 87.17.Jj, 05.40.−a, 47.63.Gd, 47.63.mf

Since the pioneering work of Wu and Libchaber [1], considerable efforts have been made to understand hydrodynamic properties of active suspensions. Generally speaking, this is the name borne by fluids laden with self-swimming entities such as bacteria [2–5], algae [6,7], or collections of active artificial swimmers [8]. Assemblies of microscopic motors dispersed in a fluid display emergent properties that differ strongly from passive suspensions. The momentum and energy transfer balances as well the constitutive transport properties are deeply modified by the momentum sources distributed in the bulk [2,9]. Some of these anomalous properties have already been identified, such as active diffusivity [1,2], anomalous viscous response [7,10], active transport, and mixing [11], as well as the possibility to use fluctuations to extract work [12]. The presence of living and apparently gregarious entities also offers the possibility to move collectively and organize at the mesoscopic or macroscopic level in the form of flocks and herds [9,13]. Similar collective effects were also identified in suspensions of self-propelled inorganic particles [14]. In the bulk, swimming bacteria with flagella such as *E. coli* create in the far field limit a force-dipole velocity field, and, consequently, experience a hydrodynamic attraction toward surfaces [15]. Then, it has been observed that *E. coli* smooth out their run-and-tumble movement and spend long times parallel to the surface undergoing circular motion as a consequence of the torque-free condition [16,17]. When the concentration becomes large, the *E. coli* population eventually associates collectively to form a biofilm. Even in the low concentration limit, the quantitative analysis of the near surface motion increases tremendously in complexity, a reason being the close field hydrodynamic forces that become prevalent and require a complex treatment of the lubrication hydrodynamic fields. However, even in this frame of description, it remains unclear whether the motion close to the surface is hydrodynamically stable and if the presence of thermal noise is essential to account for the bacterium dwelling time at a surface [18]. Beyond the hydrodynamic interactions, more complex ingredients may come into play, such as surface interaction potentials (electrostatic or van der Waals) [19] or more refined details of the bacterium physiology such as swimming speed variations and desynchronization during bacteria cell cycle [20,21]. From the perspective of providing a fully consistent treatment of active hydrodynamics, with important applications for understanding bacterial transfer in biological microvessels, microfluidic devices, or the formation of biofilms, a reliable description of fluid activity in the vicinity of a solid surface is strongly needed. In this Letter, to tackle this open and timely question, we compared the behavior of two kinds of active micrometric swimmers: wild-type *E. coli* K-12 and artificial self-propelling rods [8], with completely different propulsion mechanisms. In both cases, we monitor the swimmers' motions and their ability to activate, beyond Brownian motion, passive tracers, hence characterizing the active momentum transfer to the fluid.

Following the experimental procedure described in Ref. [15], wild-type *E. coli* K-12 were grown overnight in rich medium (Luria broth). After washing, they were transferred into MMAP, a motility medium supplemented with K-acetate (0.34 m*M*) and polyvinyl pyrolidone (PVP, 0.005%). They were incubated for at least an hour in that medium and, in some cases, so-called ''baby cells'' were selected by centrifugation and resuspended in MMAP. To avoid bacterial sedimentation (isodense conditions), Percoll was mixed with MMAP (1 vol/1 vol). We checked

that under these conditions, the suspending fluid was still Newtonian (viscosity $\eta = 1.28 \times 10^{-3}$ Pa s at 22 °C). The overall concentration of bacteria was controlled such as to prepare suspensions between 10^9 and 10^{10} bacteria/ml. To study the effect of bacterial activity on the diffusivity of passive tracers, latex beads of 1 or 2 μm diameter (Beckman-Coulter, density $\rho = 1.027$ g/ml) were added to the suspensions. Experiments were performed in 110 μm thick chambers, built with two horizontal microscope cover slips separated by a glass spacer. To avoid sticking, cover slips were coated with PVP. The biological sample consisted in a drop of liquid (20 μl) placed between the two slides. The suspension was observed under an inverted microscope (Zeiss-Observer, Z1-magnification 40 ×) connected to a digital camera. The observation field ΔV was 96×128 μm^2 and 5 μm in depth. In a first series of experiments, we measured the bacterial density profile through the entire height of the chamber. We obtained profiles similar to the ones published by Berke and coworkers [15], namely, a flat density in the bulk and a strong density increase near the surfaces. However, the wild-type *E. coli* we used was significantly less attracted by the surfaces (2.5 times increase in density within 10 μm of the surface) than a mutant *E. coli* strain that does not display tumbling motion [16,17]. Another series of experiments was performed with bimetallic Au-Pt self-propelled rods (length 1.2 μm and diameter 0.4 μm) that are very similar in size to the *E. coli* cell body (1–2 μm long, 0.8 μm diameter) but have no flagella (15 μm long for *E. coli*) [see insets in Figs. 1(c) and 1(f)]. They also have a much higher density ($\rho = 17$ g/ml). In the presence of 1%–10% hydrogen peroxide, these particles are propelled in the axial direction towards the platinum end by the catalytic decomposition of the peroxide fuel [8]. Recent experiments and simulations are consistent with self-electrophoresis as the dominant propulsion mechanism [22,23]. Here, the mode of propulsion is intrinsically different from the flagellar one. The experiments were conducted in a similar fashion to those involving *E. coli*, but in an open chamber (without the upper wall), in order to allow the oxygen bubbles produced in the reaction to escape from the cell. The concentration of H_2O_2 was varied, as well as the concentration of active rods [$n = (3\text{–}20) \times 10^6$ rods/ml]. We also used passive tracers [1 μm (Dynal-MyOne, $\rho = 1.8$ g/ml) or 2 μm (Beckman-Coulter, $\rho = 1.027$ g/ml)] to follow the Au-Pt rod fluid activation. In all cases, all the particles in the suspension were localized at the bottom of the chamber due to sedimentation. Short videos (20 s duration at 20 frames/s) were used to track both bacterial and self-propelled rods motion.

In the following, we only focus on bacteria and rods moving close to the surface (less than 5 μm). In both cases, we observed that not all swimmers display similar trajectories. This was expected, as for wild-type bacteria, the run or tumble dynamics may depend strongly on the microenvironment or on the position in the cell cycle. For Au-Pt rods, this is also consistent with previous

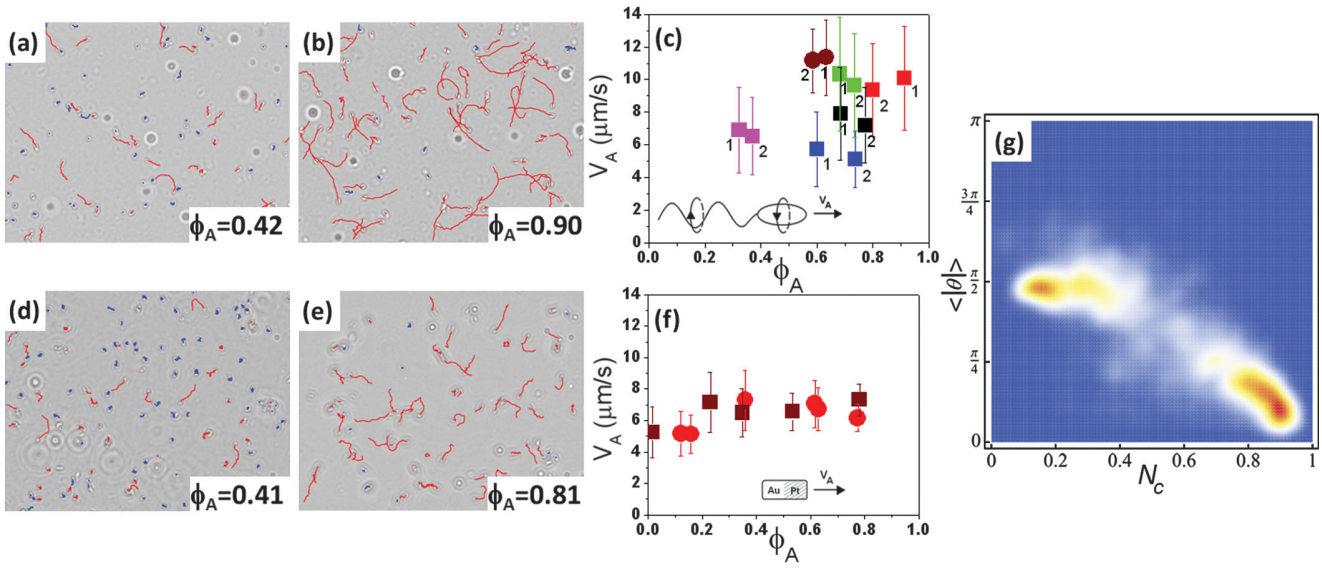

FIG. 1 (color). Identification of the swimmer populations by tracking active swimmers (red tracks) and random swimmers (blue tracks), ϕ_A is the corresponding fraction of active swimmers. Panels (a),(b),(g) correspond to *E. coli* see inset in (c)] and panels (d),(e) correspond to Au-Pt rods [see inset in (f)]. The round black circles in (a),(b) are 2 μm latex beads; the white small circles in (d),(e) are 1 μm Dynal beads. Panels (c),(f) display the relation between the active swimmer's mean velocity V_A and ϕ_A. In (c) are 6 independent experiments with *E. coli*: 1N cells (brown, red, and green), mixture of 1N and 2N cells (black), and 2N cells (pink, blue). Labels (1) and (2) are for $\langle N \rangle = 100$ and $\langle N \rangle = 200$ cells in the observation field, respectively. (f) Au-Pt rods with varying proportions of inactive Au rods (2 independent experiments). (g) density probability of the observed bacterial tracks in the $(N_c, \langle|\theta|\rangle)$ space. The color map goes from blue for vanishing probability to red for high probability. Two clusters are identified, centered at (0.9, 0.3) and (0.17, $\pi/2$), corresponding, respectively, to the active and random swimmers.

observations that, even within a single batch, electrochemically grown rods have a range of catalytic activity [8]. We developed a tracking program to analyze the short videos and obtained tracks for each swimmer present in the field. We identified two major types of motion: a ballistic and a random one [see Figs. 1(a), 1(b), 1(d), and 1(e)], and the swimmers that follow these motions are called "active" swimmers and "random" swimmers, respectively. To discriminate all the tracks systematically, two parameters were defined. The first parameter $\langle|\theta|\rangle$ is the mean angle between two successive steps. For example, $\langle|\theta|\rangle = 0$ for straight trajectories and $\langle|\theta|\rangle = \pi/2$ for a purely random walk. The second discriminating parameter is based on the minimal circle diameter L that encompasses a given trajectory of duration T. For an acquisition time δt (1/20 s) and a mean step size δr, the number $N_c = \frac{L\delta t}{T\delta r}$ is computed. When N_c is close to 1, the trajectory is associated with a straight line, whereas when N_c is small, its value points to diffusive motion. Therefore, each track is associated with these two numbers, and in the $(N_c, \langle|\theta|\rangle)$ parameter space we could identify two clusters that clearly differentiated the active and random swimmers [see Fig. 1(g)]. Nevertheless, for very small or interrupted trajectories, the separation procedure remained ambiguous, so we systematically discarded tracks shorter than 10 steps. In the case of artificial swimmers, we also managed to control *a priori* the fraction of active swimmers by adding inactive rods (made only of gold) and keeping the total number of rods at the surface constant. According to the trajectory classification, a fraction ϕ_A of active swimmers was determined. Thus, for a mean number $\langle N\rangle$ of swimmers, identified in the field of vision, we define a density of "active swimmers" as $n_A = \phi_A\langle N\rangle/\Delta V$. In Fig. 1, we display tracks during a time lag $\tau = 1.5$ s, for two populations of swimmers [1(a) and 1(b), bacteria, and 1(d) and 1(e), Au-Pt rods], having different ϕ_A [1(a) and 1(d), small active fraction, and 1(b) and 1(e), high active fraction]. In Figs. 1(c) and 1(f), we present the mean velocities of active swimmers V_A as a function of their fraction ϕ_A, for different experiments with bacteria and active rods. In the case of the bacterial suspension, we also tried several synchronization protocols to select bacteria, at different positions in the cell cycle, showing different swimming characteristics. We were able to produce "baby-bacteria" populations (1N short cells, 1.12 μm long) which were found to have a ϕ_A larger than the more mature bacteria populations (2N long cells, 2.5 μm long). We took advantage of this difference to look at the influence of ϕ_A on V_A in bacterial suspensions. In Fig. 1(c) we display 6 independent experiments performed with populations having a majority of 1N cells (brown, red, and green), a mixture of 1N and 2N cells (black), a majority of 2N cells (pink, blue). For each sample, ϕ_A was taken from suspensions showing an average of 100 or 200 bacteria in the observation field [represented by (1) and (2) in Fig. 1(c), respectively]. ϕ_A shows little influence on V_A, but V_A could be different according to bacteria position within the cell cycle. In the case of the Au-Pt rods, Fig. 1(f) does not show a stronger dependence of V_A on ϕ_A. This low dependence on ϕ_A is due to the low swimmer concentration of the suspension, where no collective behavior is observed.

In the following, we will relate the motion of the passive tracers to the number of active swimmers and their mean velocity. Passive tracer trajectories were analyzed (about 10 tracks in a 300-image video at 1 frames/s for bacteria and 40 s sequences at 8 frames/s for Au-Pt rods). No significant stickiness between the spheres and the swimmers was observed, and those rare cases were eliminated. From these tracks, the mean passive tracer diffusion coefficient D_P was extracted consistently using two independent methods. The first one applied mean square displacements at long times (diffusive regime [1]) of individual particles; the second one used particles as pairs in order to eliminate residual drift. In Fig. 2 the passive tracer diffusivities are displayed for all the experiments presented in Figs. 1(c) and 1(f). D_P values are displayed as a function of $J_A = n_A V_A$, which we call the "activity flux." For experiments performed with the same tracer size, we observe a collapse of all data onto a linear curve:

$$D_P = D_P^B + \beta J_A, \tag{1}$$

where D_P^B is the Brownian diffusivity of the latex particles in the vicinity of the surface, in the absence of swimmers. Note that, due to lubrication forces, this value is smaller than the Brownian diffusivity expected in the bulk ($D_B = k_B T/3\pi\eta d$) and, for the parallel motion, they are related by $D_P^B = \alpha D_B$, where $\alpha < 1$ is the parallel drag correction factor [24–26]. The α factor depends on the bead distance to the surface, vanishing at contact and going asymptotically to one at large distances. The beads are not at a fixed distance to the surface, but they are distributed according to Boltzmann's factor $\exp(-m^* gz/k_B T)$, where m^* is the

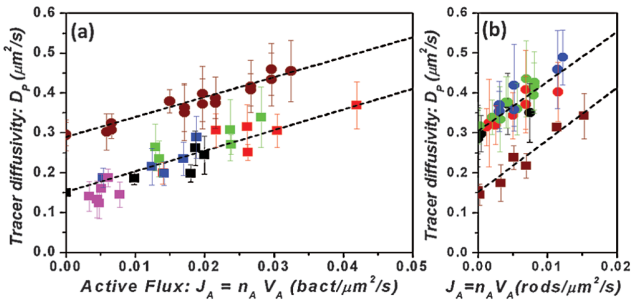

FIG. 2 (color). Enhanced diffusivity D_P of passive tracers as a function of J_A. Squares and circles represent tracer of 2 and 1 μm diameters, respectively. Panel (a) corresponds to the bacterial suspensions. Each color represents an experiment performed over a range of bacterial dilution. Panel (b) corresponds to suspensions of Au-Pt rods: green, blue, and black circles correspond to various H_2O_2 concentrations (from 2.5% to 20%). The dashed lines are linear fits and the error bars are standard deviations (the rest of the colors defined in Fig. 1 and text).

buoyant mass. Therefore, α must be averaged with this factor. In the active rods experiments we obtained $\alpha = 0.7$ both for the buoyant $d = 1\ \mu$m and $d = 2\ \mu$m latex spheres, values that agree with the theoretical prediction given above ($\alpha = 0.64$ for $d = 1\ \mu$m and $\alpha = 0.74$ for $d = 2\ \mu$m). In the experiments with bacteria, the suspended beads are almost isodense, but they sediment anyway. The experimental fit gives $\alpha = 0.85$. This value allows us to infer the density mismatch $\Delta\rho = 0.008$ g/ml, which is consistent with the experimental preparation. The collapse holds also for bacterial populations at different maturation stages (1N, 2N, or unsynchronized mixtures). From dimensional analysis of expression (1), it can be seen that the prefactor β is a length to the fourth power. It varies from 5 $\mu m^4 = (1.5\ \mu m)^4$ for bacteria to 13 $\mu m^4 = (1.9\ \mu m)^4$ for active rods, but seems to be almost independent of the passive tracer size. Close to the plates the hydrodynamic perturbations created by the swimmers decay as the inverse cube of the distance, faster than in the bulk [27]. Therefore, at low concentrations, the enhanced diffusivity in (1), proportional to n_A and V_A, can be understood as a result of a series of elementary encounters between active swimmers and the tracers: the number of encounters per unit time is proportional to $n_A V_A$. On the other hand, low Reynolds dynamics points out that the tracer displacement at each encounter is independent of the swimmer velocity and depends only on geometrical factors: the impact parameter, the swimmer dimensions, and weakly on the tracer size through the Faxén correction of passive transport [28,29]. The β factor comes out from averaging the tracer's displacements, but its computation is difficult because it requires a correct modeling of the near field interactions between the swimmer and the tracer, taking into account the detailed swimmer geometry and the effect of the surface.

In conclusion, we have characterized active momentum transfer close to solid surface for two active suspensions (wild-type bacteria and artificial self-propelled swimmers). The effect was measured using the diffusion enhancement of a passive tracer. In spite of the *a priori* complexity of the hydrodynamics and essential differences in the propulsion modes, we demonstrated that the effect emerges quantitatively in a similar way. The resulting diffusion coefficient is the sum of the Brownian contribution near the wall and an active part, proportional to the product of the density of active swimmers and their mean velocity at the surface. The proportionality factor, scaling as the 4th power of a micron size length, encompasses the details of momentum transfer for each swimmer and is found to be weakly (if at all) sensitive to the probe diameter. Importantly, discriminating between so-called "active" and "random" swimmers was crucial for predicting the induced transport phenomenon, and we have developed a protocol to make such a distinction. The functional dependence of the enhanced diffusivity is explained in terms of successive interactions between a single swimmer and the tracer, each one producing a net displacement. Our results justify the pursuit of a quantitative determination of such encounters based on simple hydrodynamic models [28].

We thank D. Grier for discussions on the tracking programs, financial support from PGDG Foundation, the Alfa-SCAT program, Sesame Ile-de-France, Fondecyt Grants No. 1061112, No. 1100100, Anillo Grant No. ACT127, No. ECOS C07E08, and NSF No. 0820404.

[1] X.-L. Wu and A. Libchaber, Phys. Rev. Lett. **84**, 3017 (2000).
[2] D. T. N. Chen *et al.*, Phys. Rev. Lett. **99**, 148302 (2007).
[3] D. Saintillan and M. J. Shelley, Phys. Rev. Lett. **99**, 058102 (2007); Phys. Rev. Lett. **100**, 178103 (2008).
[4] Y. Hatwalne *et al.*, Phys. Rev. Lett. **92**, 118101 (2004).
[5] C. Dombrowski *et al.*, Phys. Rev. Lett. **93**, 098103 (2004).
[6] K. C. Leptos *et al.*, Phys. Rev. Lett. **103**, 198103 (2009).
[7] S. Rafaï, L. Jibuti, and P. Peyla, Phys. Rev. Lett. **104**, 098102 (2010).
[8] W. F. Paxton *et al.*, J. Am. Chem. Soc. **126**, 13 424 (2004).
[9] R. A. Simha and S. Ramaswamy, Phys. Rev. Lett. **89**, 058101 (2002).
[10] A. Sokolov and I. S. Aranson, Phys. Rev. Lett. **103**, 148101 (2009); B. Haines *et al.*, Phys. Rev. E **80**, 041922 (2009).
[11] N. Darnton *et al.*, Biophys. J. **86**, 1863 (2004).
[12] A. Sokolov *et al.*, Proc. Natl. Acad. Sci. U.S.A. **107**, 969 (2009), andreferences therein.
[13] G. Gregoire, H. Chate, and Y. Tu, Phys. Rev. E **64**, 011902 (2001).
[14] M. Ibele, T. E. Mallouk, and A. Sen, Angew. Chem., Int. Ed. **48**, 3308 (2009).
[15] A. P. Berke *et al.*, Phys. Rev. Lett. **101**, 038102 (2008).
[16] E. Lauga *et al.*, Biophys. J. **90**, 400 (2006).
[17] P. D. Frymier *et al.*, Proc. Natl. Acad. Sci. U.S.A. **92**, 6195 (1995).
[18] G. Li, L.-K. Tam, and J. X. Tang, Proc. Natl. Acad. Sci. U.S.A. **105**, 18 355 (2008).
[19] M. A. S. Vigeant and R. M. Ford, Appl. Environ. Microbiol. **63**, 3474 (1997).
[20] B. M. Prüß and P. Matsumura, J. Bacteriol. **179**, 5602 (1997).
[21] R. Allman, T. Schjerven, and E. Boye, J. Bacteriol. **173**, 7970 (1991).
[22] Y. Wang *et al.*, Langmuir **22**, 10 451 (2006).
[23] J. L. Moran, P. M. Wheat, and J. D. Posner, Phys. Rev. E **81**, 065302 (2010).
[24] H. Brenner, Chem. Eng. Sci. **16**, 242 (1961); A. J. Goldman, R. G. Cox, and H. Brenner, Chem. Eng. Sci. **22**, 637 (1967).
[25] P. Holmqvist, J. K. G. Dhont, and P. R. Lang, Phys. Rev. E **74**, 021402 (2006).
[26] P. Huang and K. S. Breuer, Phys. Rev. E **76**, 046307 (2007).
[27] J. R. Blake and A. T. Chwang, J. Eng. Math. **8**, 23 (1974).
[28] J. Dunstan, M.Sc. thesis, Universidad de Chile, 2010; J. Dunstan *et al.* (to be published).
[29] J. Happel and H. Brenner, *Low Reynolds Number Hydrodynamics: With Special Applications to Particulate Media* (Kluwer, The Hague, 1983).

A two-sphere model for bacteria swimming near solid surfaces

Jocelyn Dunstan,[1] Gastón Miño,[2] Eric Clement,[2] and Rodrigo Soto[1]
[1]*Departamento de Física, FCFM, Universidad de Chile, Santiago, Chile*
[2]*PMMH-ESPCI, UMR 7636 CNRS-ESPCI-Université Paris 6 and Paris 7, 10 rue Vauquelin, 75005 Paris, France*

(Received 23 May 2011; accepted 16 December 2011; published online 27 January 2012)

We present a simple model for bacteria like *Escherichia coli* swimming near solid surfaces. It consists of two spheres of different radii connected by a dragless rod. The effect of the flagella is taken into account by imposing a force on the tail sphere and opposite torques exerted by the rod over the spheres. The hydrodynamic forces and torques on the spheres are computed by considering separately the interaction of a single sphere with the surface and with the flow produced by the other sphere. Numerically, we solve the linear system which contains the geometrical constraints and the force-free and torque-free conditions. The dynamics of this swimmer near a solid boundary is very rich, showing three different behaviors depending on the initial conditions: (1) swimming in circles in contact with the wall, (2) swimming in circles at a finite distance from the wall, and (3) swimming away from it. Furthermore, the order of magnitude of the radius of curvature for the circular motion is in the range $8 - 50\mu$m, close to values observed experimentally. © *2012 American Institute of Physics*. [doi:10.1063/1.3676245]

I. INTRODUCTION

In recent decades, interest in the dynamics of self-propelled organisms such as bacteria, fish, and birds has increased enormously. This can be explained, first, by interest in the physics behind the phenomena, for which tools from continuum mechanics are used to describe the motion of single swimmers as well as from statistical physics to deduce collective behaviors due to their mutual interactions. Besides, study of how this locomotion affects biological processes such as human reproduction or bacterial infection remains fundamental.[1] Finally, development of applications in which artificial swimmers could perform specific tasks in microfluidic devices is certainly an area of intense research.[2]

A particular kind of self-propelled organisms are bacteria. Considering their micrometer scale and typical propulsion velocities, they are in the low-Reynolds-number regime, in which inertial effects are negligible in comparison with viscous ones. Therefore, the dynamics of the fluid is governed by the Stokes equation and immersed objects by the force-free and torque-free conditions.[3] In this category, the bacterium *Escherichia coli* (*E. coli*) has been intensively studied, and much is known about its genetics, biological processes, and motility.[4] The body cell is about 1 μm in width and 2–5 μm in length, and around 70% of it is water. Its propulsion is due to rotary motors connected to around six filaments of approximately 15 μm in length, which emerge from different points of the cell. When these filaments rotate counterclockwise, seen from behind, they form a bundle and the bacterium swims in an approximately straight line at about 20 μm/s.[5] This is called the *run* mode. If one or more filaments start to rotate in the opposite direction, the bundle (flagella) unravels, and the bacterium can change its direction, which is known as a *tumble*. The alternation of these modes creates a three-dimensional random walk.[5]

In addition, when *E.coli* swims near a non-slip surface, it describes clockwise circles when is viewed from above. In 1995, Frymier *et al.*[6] reported a three-dimensional tracking of the movement of two kind of *E.coli*: wild type and a smooth-swimming mutants, which are unable to perform the tumbling motion described above. In the first case, the bacteria describe circular segments but they leave the surface after a tumbling. Conversely, the smooth-swimming cells

swim for a much longer time along the surface. An explanation for this circular motion was given by Lauga *et al*. from the fact that the head and the flagella rotate in opposite directions, which together with a stronger drag near a wall, produce a net force directed to the centre of the circle.[7]

An extremely interesting question is how these living entities can modify the mass, momentum, and energy transport properties in a suspension. Since the pioneering work of Wu and Libchaber,[8] considerable efforts have been made to understand this issue. Recently, Miño *et al*.[9] observed that, near to a solid boundary, a suspension of *E. coli* increases the diffusion coefficient of passive tracers by a factor proportional to the *active flux*, i.e., the concentration of active bacteria multiplied by their mean velocity.

In the literature, there are various models for *E. coli* with diverse levels of complexity; for example, Ramia *et al*.[10] simulated *E. coli* as a sphere joined to a single helicoidal flagellum, and the velocity field near the surface was obtained using the boundary element method. In that work, the radius of curvature was about 10 μm, and it was reported a tendency for the bacterium to crash into the wall, i.e., it approaches the solid surface until it touches it, with the tail pointing up, at which point it stops. A different approach was made by Lauga *et al*.,[7] who used the same bacterium geometry, but to obtain its trajectory near the surface, they calculated the resistance matrix for the swimmer. It is important to note that in their work, the distance to the wall was fixed, not allowing vertical motion, which is an interesting point since the radius of curvature depends strongly on the distance to the wall. In 2008, it was reported by Li *et al*.,[11] using fluorescence microscopy, that this gap is only tens of nanometers. Finally, it is important to mention the work of Gyrya *et al*.,[12] in which *E. coli* was modeled using two spheres joined to a point of force by a dragless rod (a similar model was introduced previously by Hernandez-Ortiz *et al*.[13]). There, the velocity field was obtained in the bulk for an isolated swimmer as well as for a pair of them. This latter approach inspired our work aiming to build a simple model for a bacterium using spheres, like in Gyrya *et al*., but adding the interaction with the surface and rotation of the spheres, which is necessary to reproduce circular motion near the surface. Construction of a minimal model of a bacterium that can perform this motion near a surface is the central aim of this work.

The present work is organized as follows: in Sec. II, the point-force model for bacteria is described, and the corresponding problem close to a solid boundary is discussed. Then, in Sec. III, our finite-size model is presented, obtaining its velocity in the bulk and the geometrical parameters of the model are fixed. The problem of this swimmer near a surface is treated in Sec. IV, where the formalism of resistance tensors is introduced. After that in Sec. V, the results from numerical simulations are presented. Different types of motion are obtained, depending on the initial conditions. Finally, conclusions are presented in Sec. VI.

II. BACTERIUM AS TWO POINT FORCES INTERACTING WITH A SOLID BOUNDARY

At large distances, a pusher bacterium such as *E. coli* creates a velocity field perturbation that can be described as that produced by a force dipole. Using this model, Berke *et al*.[14] showed that a pusher swimmer experiences an attraction toward surfaces in the form of a negative vertical velocity. Moreover, the swimmer orientation is affected by the presence of the surface, adopting a stable equilibrium orientation parallel to the surface.[14] However, the dipolar model fails to provide an appropriate description of the swimmer–surface interaction, as we show in the next paragraphs, due to the dominant finite-size effects from the swimmer. In particular, these effects regularize the apparently divergent vertical velocity obtained when the swimmer approaches the surface.[14]

Using the model described in detail in Sec. III, in which the swimmer has a finite size, it is possible to compute the limit of point forces. Considering two point forces of intensities f_0, separated at a distance L, analytic expressions can be obtained using the images system.[15] If the distance from the swimmer to the surface is h (Fig. 1) and its orientation is parallel to the surface, the vertical velocity is given by

$$V_z = -\frac{3f_0 L h^3}{2\pi\eta(L^2 + 4h^2)^{5/2}}, \tag{1}$$

where η is the dynamic viscosity of the fluid.

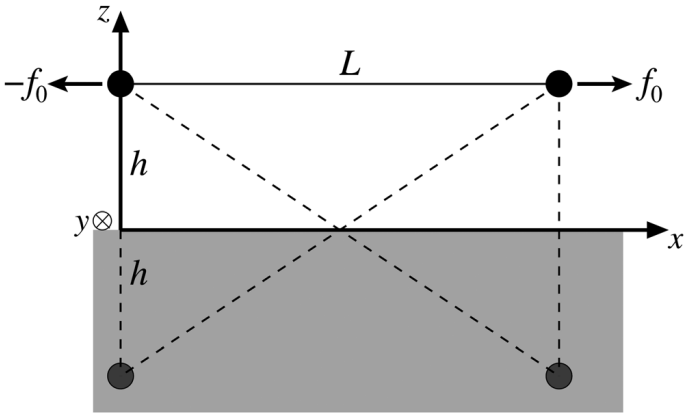

FIG. 1. A two-point-force model for a bacterium near a wall. The interaction with the wall is obtained using the image method proposed by Blake and Chwang.[15] The arrows represent the forces exerted by the point forces on the fluid for a pusher bacterium. Dashed lines represent the interactions due to the image forces.

For a dipole of vanishing size ($L \to 0$) and fixed force dipole of strength $p = f_0 L$, the vertical velocity matches the result of Berke *et al.*, which diverges when $h \to 0$. Note that limits do not commute and the velocity divergence is only obtained when the limit in L is taken before the limit in h. However, when L is finite, the velocity is regularized for all distances and vanishing for $h \to 0$. Furthermore, the angular velocity vanishes as predicted by Berke *et al.*[14] The factor $(L^2 + 4h^2)^{1/2}$ corresponds to the cross distance between one sphere and the image of the other. Therefore, the attraction to the wall is due to the two-sphere interaction through the surface. In fact, it can be easily verified that the field created by the image of a point force moving in the x direction does not have a vertical velocity or angular velocity at the position of the point force itself and therefore cannot lead to an attraction toward or repulsion from the surface.

It must be remarked that the point particle approximation is not accurate, as it predicts a vanishing vertical velocity when the height of the force dipole vanishes ($h \to 0$), while the bacterium should stop its vertical motion when its body reaches the surface. Near-field corrections, obtained from the lubrication-theory approximation, should be used to describe the swimmer motion accurately. The model described in Sec. III considers this approximation, and in Sec. V, the full swimming dynamics is described.

III. THE TWO-SPHERE MODEL

The bacterium is modeled as two spheres, denoted by H (head) and T (tail), with radii a_H and a_T, respectively, and connected by a dragless rod of length L (Fig. 2). The positions of the spheres are $\mathbf{r}_H$ and $\mathbf{r}_T$, and the unit vector along the swimmer is defined as

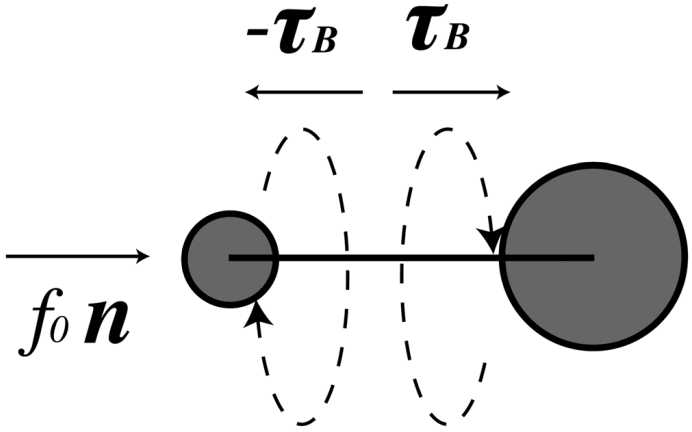

FIG. 2. Two-sphere model for bacteria: two spheres of different radii connected by a dragless rod, which exerts equal and opposite torques $\pm\boldsymbol{\tau}_B$. Over the T-sphere, a *propulsion force* $f_0\hat{\mathbf{n}}$ is applied by the fluid to mimic the effect of the rotating flagella.

$\widehat{\mathbf{n}} = (\mathbf{r}_H - \mathbf{r}_T)/|\mathbf{r}_H - \mathbf{r}_T| = (\mathbf{r}_H - \mathbf{r}_T)/L$. To mimic the effect of the rotary motors in *E. coli*, the rod applies equal and opposite torques $\pm\boldsymbol{\tau}_B = \pm\tau_0\widehat{\mathbf{n}}$ on the spheres, with positive sign for H. The T-sphere represents the bacterium flagella, and in the present model, its rotation is not directly related to the propulsion; rather it is considered as an extra *propulsion force* $f_0\widehat{\mathbf{n}}$ applied by the fluid at the sphere center. The rotation of the spheres along the swimmer axis and the interaction with the solid surface are the main differences from the *dumbbell* models proposed before.[12,13]

Due to the micrometer scale of the swimmer, the total force and torque acting on each sphere are zero. Making explicit the separation between forces and torques applied by the fluid (hydro) and those applied by the rod,

$$\mathbf{F}_H = \mathbf{F}_H^{\text{hydro}} + \mathbf{F}^{\text{int}} = 0, \tag{2}$$

$$\mathbf{F}_T = \mathbf{F}_T^{\text{hydro}} - \mathbf{F}^{\text{int}} = 0, \tag{3}$$

$$\boldsymbol{\tau}_H = \boldsymbol{\tau}_H^{\text{hydro}} + \boldsymbol{\tau}_B = 0, \tag{4}$$

$$\boldsymbol{\tau}_T = \boldsymbol{\tau}_T^{\text{hydro}} - \boldsymbol{\tau}_B = 0, \tag{5}$$

where $\mathbf{F}^{\text{int}}$ is the internal force exerted by the rod. The hydrodynamic forces and torques are those over smooth spheres with the nonslip boundary condition (for example the Stokes drag in the case of spheres in the bulk). The exception is the T-sphere where, to mimic the propulsion effect of the rotating flagella, an additional propulsion force $f_0\widehat{\mathbf{n}}$ is added to $\mathbf{F}_H^{\text{hydro}}$. From Eqs. (4) and (5),

$$(\boldsymbol{\tau}_H - \boldsymbol{\tau}_T)\cdot\widehat{\mathbf{n}} = (\boldsymbol{\tau}_H^{\text{hydro}} - \boldsymbol{\tau}_T^{\text{hydro}})\cdot\widehat{\mathbf{n}} + 2\boldsymbol{\tau}_B\cdot\widehat{\mathbf{n}} = 0. \tag{6}$$

The torque intensity $\tau_0 = \boldsymbol{\tau}_B\cdot\widehat{\mathbf{n}}$ has been measured for *E. coli*, obtaining values of the order of 1 pN μm ($\tau_0 = 1.26$ pN μm in Ref. 16, value that we use in the present article).

From the geometrical constraints of the swimmer, the angular velocities of the spheres, perpendicular to the swimmer axis, must be equal (denoted by Ω_B), and since the rod is rigid in these directions,

$$(\Omega_H - \Omega_T)\times\widehat{\mathbf{n}} = \mathbf{0}. \tag{7}$$

Besides, the linear velocities of the spheres are related by

$$\mathbf{U}_H = \mathbf{U}_T + L\widehat{\mathbf{n}}\times\Omega_B, \tag{8}$$

where $\mathbf{U}_H$ ($\mathbf{U}_T$) and Ω_H (Ω_T) are the linear and angular velocity of the sphere H (T).

A. Swimmer in the bulk

In the bulk, neglecting the Faxén corrections,[3] the hydrodynamic forces and torques on the spheres are given by

$$\mathbf{F}_H^{\text{hydro}} = -6\pi\eta a_H\left[\mathbf{U}_H - \mathbf{u}^H(\mathbf{r}_H)\right], \tag{9}$$

$$\mathbf{F}_T^{\text{hydro}} = -6\pi\eta a_T\left[\mathbf{U}_T - \mathbf{u}^T(\mathbf{r}_T)\right] + f_0\widehat{\mathbf{n}}, \tag{10}$$

$$\boldsymbol{\tau}_H^{\text{hydro}} = -8\pi\eta a_H^3\left[\Omega_H - \frac{1}{2}\nabla\times\mathbf{u}^H(\mathbf{r}_H)\right], \tag{11}$$

$$\boldsymbol{\tau}_T^{\text{hydro}} = -8\pi\eta a_T^3\left[\Omega_T - \frac{1}{2}\nabla\times\mathbf{u}^T(\mathbf{r}_T)\right]. \tag{12}$$

These expressions consider the far-field approximation, that is, when the separation between the spheres is large in comparison with the radius. The neglected contributions are of order $\mathcal{O}(a^2/L^2)$. Here $\mathbf{u}^H(\mathbf{r}_H)$ is the velocity of the fluid at the position of the center of sphere H but calculated in its absence (the same being valid for sphere T). Being more specific, if the swimmer is isolated, the field produced by the two spheres in the far-field approximation is

$$\mathbf{u}(\mathbf{r}) = -\mathbb{G}(\mathbf{r}-\mathbf{r}_H)\cdot\mathbf{F}_H^{\text{hydro}} - \mathbb{G}(\mathbf{r}-\mathbf{r}_T)\cdot\mathbf{F}_T^{\text{hydro}}, \tag{13}$$

where $\mathbb{G}(\mathbf{r})$ is the Oseen tensor defined as $\mathbb{G}(\mathbf{r}) = \frac{1}{8\pi\eta|\mathbf{r}|}\left(\mathbb{I} + \frac{\mathbf{r}\mathbf{r}^T}{|\mathbf{r}|^2}\right)$ with $\mathbb{I}$ the unit tensor. Again, the Faxén corrections $\mathcal{O}(a^2/L^2)$ haven been neglected. Note that $\mathbf{F}^{\text{hydro}}$ are forces applied by the fluid. Hence, the fields $\mathbf{u}^H(\mathbf{r})$ and $\mathbf{u}^T(\mathbf{r})$ are

$$\mathbf{u}^H(\mathbf{r}) = \mathbf{u}(\mathbf{r}) + \mathbb{G}(\mathbf{r}-\mathbf{r}_H)\cdot\mathbf{F}_H^{\text{hydro}}, \tag{14}$$

$$\mathbf{u}^T(\mathbf{r}) = \mathbf{u}(\mathbf{r}) + \mathbb{G}(\mathbf{r}-\mathbf{r}_T)\cdot\mathbf{F}_T^{\text{hydro}}. \tag{15}$$

To obtain the velocity of the swimmer in the bulk, like in Ref. 12, we replace Eqs. (14) and (15) in Eqs. (9)–(12), and with the zero-force and zero-torque conditions together with the geometrical constraints, we obtain

$$\mathbf{U}_H = \mathbf{U}_T = \frac{2L-3a_H}{12\pi\eta[L(a_H+a_T)-3a_Ha_T]}f_0\hat{\mathbf{n}} = \mathrm{U}_0\hat{\mathbf{n}}, \tag{16}$$

$$\Omega_H = \frac{L^3-a_H^3}{8\pi\eta a_H^3L^3}\boldsymbol{\tau}_0\widehat{\mathbf{n}}, \tag{17}$$

$$\Omega_T = \frac{a_T^3-L^3}{8\pi\eta a_T^3L^3}\boldsymbol{\tau}_0\widehat{\mathbf{n}}. \tag{18}$$

Thus, the linear velocity is proportional to the propulsion force, with a constant of proportionality depending on the swimmer geometry. Similarly, the angular velocities of the spheres are along the swimmer axis (i.e., it swims in a straight line), with magnitude proportional to the imposed torque along the axis, depending also on the relation between the geometrical parameters a_H, a_T, and L. Since the torques applied by the rod have opposite sign, the H-sphere rotates in clockwise direction while the T-sphere rotates counterclockwise, both as seen from behind the swimmer.

B. Choice of geometrical parameters

The geometrical parameters of the model a_H, a_T, and L were chosen in the following way: the head sphere was related to the cell body using the *equivalent sphere* concept.[7,17] Following Lauga *et al.*, an equivalent sphere having the same viscous resistance as a prolate ellipsoid moving along its axis of symmetry has radius

$$a = \frac{4w}{3}\left(\frac{2\phi^2-1}{(\phi^2-1)^{3/2}}\ln\left(\frac{\phi+\sqrt{\phi^2-1}}{\phi-\sqrt{\phi^2-1}}\right) - \frac{2\phi}{\phi^2-1}\right)^{-1}, \tag{19}$$

where w is the width and ϕ is the aspect ratio of the ellipsoid. In the case of *E. coli*, the radius of the equivalent sphere varies from 0.89 to 1.07 μm.[7] We therefore fix $a_H = 1\mu$m.

Recent experiments have shown that, when the flow field around an *E. coli* bacterium is measured, the separation of the associated force dipole is on the order of 2 μm.[18] With this information, we fix the separation between the spheres at $L = 2\,\mu$m.

We took the radius of the tail sphere as $a_{T=}0.5\,\mu$m. This choice is rather arbitrary, since this model is a great simplification of *E. coli* and a direct comparison is not possible. Other values give qualitatively similar results.

Finally, Eq. (16) allows one to fix f_0 for a given geometry by knowing the experimental value obtained in Ref. 5, $U_0 = 20\,\mu$m/s. Using the values above, $f_0 = 1.13$ pN.

IV. TWO-SPHERE SWIMMER IN THE PRESENCE OF A SOLID BOUNDARY

When the swimmer is near to a solid boundary, there is a complex hydrodynamic interaction with the wall. One possible approach to calculate this interaction is to use the image method proposed by Blake and Chwang,[15] i.e., to consider the bacterium as two equal and opposite point

forces and point torques. Since this is a far-field approximation, and the swimmer can be very close to (namely touching) the wall, we will introduce corrections given by the Faxén formula[19] and lubrication theory.[20]

Using the resistance matrix formalism, which is based on the linearity of the Stokes equations, the hydrodynamic forces and torques on the spheres that compose the swimmer are given by the relation

$$\begin{pmatrix} \mathbf{F}_H^{\text{hydro}} \\ \boldsymbol{\tau}_H^{\text{hydro}} \\ \hline \mathbf{F}_T^{\text{hydro}} \\ \boldsymbol{\tau}_T^{\text{hydro}} \end{pmatrix} = \left(\begin{array}{c|c} \mathcal{R}_H & \mathcal{R}_{HT} \\ \hline \mathcal{R}_{TH} & \mathcal{R}_T \end{array}\right) \begin{pmatrix} \mathbf{U}_H \\ \boldsymbol{\Omega}_H \\ \hline \mathbf{U}_T \\ \boldsymbol{\Omega}_T \end{pmatrix} + \begin{pmatrix} 0 \\ 0 \\ \hline f_0 \widehat{\mathbf{n}} \\ 0 \end{pmatrix}, \tag{20}$$

where the 6×6 matrices $\mathcal{R}_H$ and $\mathcal{R}_T$ give the interaction of each sphere with the wall, and $\mathcal{R}_{HT}$ and $\mathcal{R}_{TH}$ are the couplings between them considering the wall. These matrices already take into account the Faxén and lubrication corrections. In the article of Swan and Brady,[19] expressions for these matrices are given in the case of spheres of the same radius in the far-field approximation; the generalization to spheres of different radii is rather complicated. This approach, however, is too rigid, because if two or more swimmers are considered, the size of the resistance matrix grows accordingly and even more so the complication of the computation of its elements.

As a simplification to this approach, we compute the interaction of the swimmer with the wall as the complete interaction of each sphere with the boundary (considering the far- and near-field contributions), while the coupling between the spheres is obtained from the interaction with the *external flow* produced by the other sphere. For example, for the H-sphere,

$$\begin{bmatrix} \mathbf{F}_H^{\text{hydro}} \\ \boldsymbol{\tau}_H^{\text{hydro}} \end{bmatrix} = \begin{bmatrix} \mathcal{R}_H^{FU} & \mathcal{R}_H^{F\Omega} \\ \mathcal{R}_H^{\tau U} & \mathcal{R}_H^{\tau\Omega} \end{bmatrix} \begin{bmatrix} \mathbf{U}_H \\ \boldsymbol{\Omega}_H \end{bmatrix} + \begin{bmatrix} \mathcal{R}_H^{FU^\infty} & \mathcal{R}_H^{F\Omega^\infty} \\ \mathcal{R}_H^{\tau U^\infty} & \mathcal{R}_H^{\tau\Omega^\infty} \end{bmatrix} \begin{bmatrix} \mathbf{U}_H^\infty \\ \boldsymbol{\Omega}_H^\infty \end{bmatrix}, \tag{21}$$

where the matrix elements $\mathcal{R}$ are the 3×3 resistance tensors, and $(\mathbf{U}_H^\infty, \boldsymbol{\Omega}_H^\infty)$ correspond to the fluid velocity and fluid angular velocity at the position of the H-sphere due to the presence of the T-sphere. This approach has the benefit of being simple enough to extend to the case of many swimmers or other passive objects or to include an imposed flow. The associated velocity fields are introduced in the $(\mathbf{U}^\infty, \boldsymbol{\Omega}^\infty)$ terms. This approximation is valid when the two spheres are sufficiently separated and no close field interactions are present. As a consequence, the corrections are of order $\mathcal{O}(a^2/L^2)$.

The hydrodynamic coupling between the spheres is obtained by computing the flow produced by each of them and evaluating it at the position of the other sphere. In the presence of a plane wall, the Oseen tensor is modified by image terms. The image set of a force monopole is not simply an opposite force as in electrostatics but also includes a force quadrupole and a mass source dipole; the combination of these together with the original force monopole produces the flow that satisfies the nonslip boundary condition at the wall.[15] In the case of a sphere close to the plane, the flow should be modified to include the Faxén correction of the spheres and the lubrication flows. In the present model, we will neglect the Faxén corrections, as they contribute subdominant terms. Thus, the flow produced by the H-sphere (that applies a force $\mathbf{F}$ and a torque τ over the fluid), evaluated at $\mathbf{r}_1 = (x_1, y_1, z_1)$, is

$$\begin{aligned} [\mathbf{u}(\mathbf{r}_1)]_i = \frac{F_j}{8\pi\eta} \Bigg[& \left(\frac{\delta_{ij}}{r} + \frac{r_i r_j}{r^3}\right) - \left(\frac{\delta_{ij}}{\bar{r}} + \frac{\bar{r}_i \bar{r}_j}{\bar{r}^3}\right) \\ & + 2h(\delta_{j1}\delta_{1k} + \delta_{j2}\delta_{2k} - \delta_{j3}\delta_{3k}) \frac{\partial}{\partial \bar{r}_k} \left\{ \frac{h\bar{r}_i}{\bar{r}^3} - \left(\frac{\delta_{i3}}{\bar{r}} + \frac{\bar{r}_i \bar{r}_3}{\bar{r}^3}\right) \right\} \Bigg] \\ & + \frac{1}{8\pi\eta} \Bigg[\frac{\varepsilon_{ijk}\tau_j r_k}{r^3} - \frac{\varepsilon_{ijk}\tau_j \bar{r}_k}{\bar{r}^3} + 2h\varepsilon_{kj3}\tau_j \left(\frac{\delta_{ik}}{\bar{r}^3} - \frac{3\bar{r}_i \bar{r}_k}{\bar{r}^5}\right) \\ & + 6\varepsilon_{kj3} \frac{\tau_j \bar{r}_i \bar{r}_k \bar{r}_3}{\bar{r}^5} \Bigg], \end{aligned} \tag{22}$$

where $\mathbf{y} = \{y_1, y_2, h\}$ is the position of the force point, $\mathbf{r} = \{x_1 - y_1, x_2 - y_2, x_3 - h\}$ is the vector from the singularity to the observation point, and $\bar{\mathbf{r}} = \{x_1 - y_1, x_2 - y_2, x_3 + h\}$ is the vector from the position of the image to the observation point. In the coordinate axes, x and y are the planar directions and z is the perpendicular direction to the plane, as shown in Fig. 1.

Considering the symmetries and the linearity of the flow at low Reynolds number, the resistance tensors have the following general expressions for a single sphere:

$$\mathcal{R}^{FU} = \begin{bmatrix} R_{\parallel}^{FU} & 0 & 0 \\ 0 & R_{\parallel}^{FU} & 0 \\ 0 & 0 & R_{\perp}^{FU} \end{bmatrix}, \tag{23}$$

$$\mathcal{R}^{\tau\Omega} = \begin{bmatrix} R_{\parallel}^{\tau\Omega} & 0 & 0 \\ 0 & R_{\parallel}^{\tau\Omega} & 0 \\ 0 & 0 & R_{\perp}^{\tau\Omega} \end{bmatrix}, \tag{24}$$

$$\mathcal{R}^{\tau U} = \left(\mathcal{R}^{F\Omega}\right)^T = \begin{bmatrix} 0 & R_{xy}^{\tau U} & 0 \\ -R_{xy}^{\tau U} & 0 & 0 \\ 0 & 0 & \end{bmatrix}, \tag{25}$$

and similarly for the tensors that couple with the velocity field, $\mathcal{R}^{FU^\infty}$, $\mathcal{R}^{F\Omega^\infty}$, $\mathcal{R}^{\tau U^\infty}$, and $\mathcal{R}^{\tau\Omega^\infty}$.

In the bulk, the resistance tensors take the asymptotic values

$$\mathcal{R}^{FU} = -\mathcal{R}^{FU^\infty} = -6\pi\eta a\mathbb{I}, \mathcal{R}^{\tau\Omega} = -\mathcal{R}^{\tau\Omega^\infty} = -8\pi\eta a^3\mathbb{I},$$

$$\mathcal{R}^{\tau U} = \mathcal{R}^{\tau U^\infty} = \mathcal{R}^{F\Omega} = \mathcal{R}^{F\Omega^\infty} = 0,$$

where a is the radius of the corresponding sphere. Together with the geometrical constraints, these produce the bulk results (16)–(18).

To obtain each term in the resistance tensors for a sphere in the presence of a planar wall, we take advantage of the linearity of the Stokes equation. In fact, it is possible to consider separately the cases of a sphere moving and rotating in a quiescent fluid and that of a stationary sphere in an ambient fluid. The first case allows $\mathcal{R}^{FU}$, $\mathcal{R}^{F\Omega}$, $\mathcal{R}^{\tau U}$, and $\mathcal{R}^{\tau\Omega}$ to be computed, and the second case is used to obtain $\mathcal{R}^{FU^\infty}$, $\mathcal{R}^{F\Omega^\infty}$, $\mathcal{R}^{\tau U^\infty}$, and $\mathcal{R}^{\tau\Omega^\infty}$.

A. Translational and rotational motion of a sphere in the presence of a plane wall in a fluid at rest at infinity

In the far-field limit, the resistance for a sphere of radius a translating parallel and perpendicular to a wall, with its center located at distance h from the wall (Fig. 3), is[19]

$$\frac{\mathcal{R}_{\parallel}^{FU}}{6\pi\eta a}|_{h\gg a} = -\left[1 - \frac{9}{16}\left(\frac{a}{h}\right) + \frac{1}{8}\left(\frac{a}{h}\right)^3\right]^{-1},$$

$$\frac{\mathcal{R}_{\perp}^{FU}}{6\pi\eta a}|_{h\gg a} = -\left[1 - \frac{9}{8}\left(\frac{a}{h}\right) + \frac{1}{2}\left(\frac{a}{h}\right)^3\right]^{-1}. \tag{26}$$

Furthermore, due to the presence of the solid boundary, there is a coupling between the translation and the torque

$$\frac{\mathcal{R}_{xy}^{F\Omega}}{6\pi\eta a^2}|_{h\gg a} = -\frac{\mathcal{R}_{yx}^{F\Omega}}{6\pi\eta a^2}|_{h\gg a} = \frac{1}{8}\left(\frac{a}{h}\right)^4, \tag{27}$$

where $\mathcal{R}^{F\Omega} = [\mathcal{R}^{\tau U}]^T$ (see Ref. 3 for a description of the general properties of the resistance matrix). Similarly, the resistance experienced by a sphere rotating parallel and perpendicular to a wall in the far-field approximation is[19]

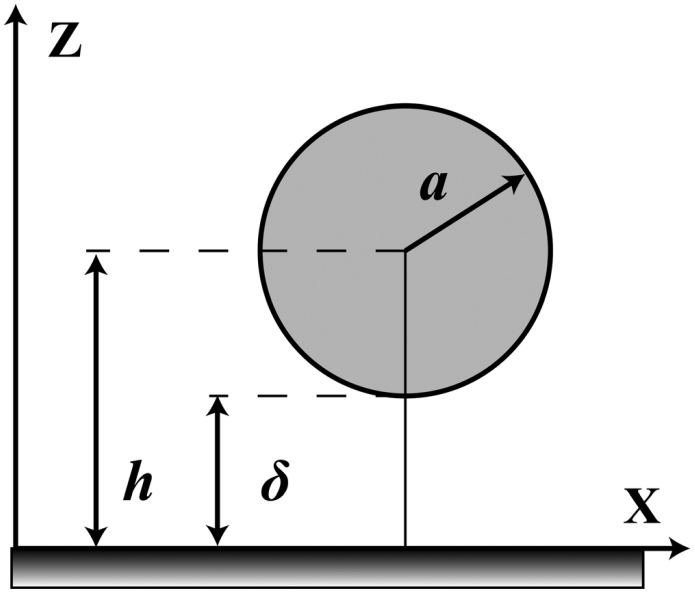

FIG. 3. Sketch of the quantities used to compute the resistance tensors. The surface is in the x–y plane, the sphere radius is a, h is the distance from the sphere center to the plate, and $\delta = (h - a)$ is the gap.

$$\frac{\mathcal{R}_{\parallel}^{\tau\Omega}}{8\pi\eta a^3}|_{h\gg a} = -\left[1 - \frac{5}{16}\left(\frac{a}{h}\right)^3\right]^{-1},$$
$$\frac{\mathcal{R}_{\perp}^{\tau\Omega}}{8\pi\eta a^3}|_{h\gg a} = -\left[1 - \frac{1}{8}\left(\frac{a}{h}\right)^3\right]^{-1}. \tag{28}$$

On the other hand, when the sphere is close to the plane [that is, when the gap distance is much smaller than the sphere size, $\delta = (h - a) \ll a$], the asymptotic lubrication theory must be used. Goldman *et al.*[20] obtained the following asymptotic expressions:

$$\frac{\mathcal{R}_{\parallel}^{FU}}{6\pi\eta a}|_{h\to a} = \frac{8}{15}\ln\left(\frac{\delta}{a}\right) - 0.9588,$$
$$\frac{\mathcal{R}_{xy}^{F\Omega}}{6\pi\eta a^2}|_{h\to a} = -\frac{2}{15}\ln\left(\frac{\delta}{a}\right) - 0.2526,$$
$$\frac{\mathcal{R}_{\parallel}^{\tau\Omega}}{8\pi\eta a^3}|_{h\to a} = \frac{2}{5}\ln\left(\frac{\delta}{a}\right) - 0.3817. \tag{29}$$

We propose global interpolation formulas, valid in both limits, with the following generic form

$$[a_0 + b_0 x]\log\left(\frac{x-1}{x}\right) + c_0 + d_0\frac{1}{x} + e_0\frac{1}{x^2} + f_0\frac{1}{x^3}, \tag{30}$$

where $x \equiv h/a$ is the normalized distance from the center of the sphere. The coefficients of the interpolation are fixed to match the two asymptotic expressions up to the known orders in each case. For example, for $\mathcal{R}_{\parallel}^{FU}$, the expression is

$$\frac{\mathcal{R}_{\parallel}^{FU}}{6\pi\eta a} = \left(1.5296 - 0.9963\frac{h}{a}\right)\log\left(\frac{h-a}{h}\right) - 1.9963,$$
$$+ 0.4689\left(\frac{a}{h}\right) + 0.4327\left(\frac{a}{h}\right)^2 + 0.1358\left(\frac{a}{h}\right)^3. \tag{31}$$

The expressions of the global fits in the other cases are given in Appendix.

On the other hand, for a sphere moving perpendicular to the wall, we use the resistance obtained by Bevan and Prieve[21] as a regression of the exact solution given by Brenner[22]

$$\frac{\mathcal{R}_{\perp}^{FU}}{6\pi\eta a} = -\frac{2+9\left(\frac{\delta}{a}\right)+6\left(\frac{\delta}{a}\right)^2}{2\left(\frac{\delta}{a}\right)+6\left(\frac{\delta}{a}\right)^2}. \tag{32}$$

It is remarkable that this expression is valid for both short and long distances from the wall. Finally, rotation perpendicular to the wall has been rarely treated in the literature; in the work of Lee and Leal,[23] the Stokes equation is solved for a sphere moving and translating in the presence of a wall. The expressions for the resistances are given in terms of infinite series. In particular,

$$\frac{\mathcal{R}_{\perp}^{\tau\Omega}}{8\pi\eta a^3} = -\frac{\sinh^2\eta_0}{\sqrt{2}}\sum_{n=1}^{\infty} n(n+1)\frac{2\sqrt{2}ce^{(n+1/2)\eta_0}}{\sinh[(n+1/2)\eta_0]}, \tag{33}$$

where $\eta_0 = -\text{arccosh}(x)$ and $c = \sqrt{x^2-1}$, with $x = h/a$. For small gaps, this expression goes as $\mathcal{R}_{\perp}^{\tau\Omega} = 8\pi\eta a^3[1.202 + 0.414(x-1)\log(x-1)]$. A global interpolation between this limit and the expression (28) is proposed in the form

$$\left[a_0(x-1)+b_0\frac{(x-1)^2}{x}\right]\log\left(\frac{x-1}{x}\right)+c_0+d_0\frac{1}{x}+e_0\frac{1}{x^2}+f_0\frac{1}{x^3}, \tag{34}$$

and the coefficients are given in Appendix.

B. Immobilized sphere in an ambient flow

In the work of Goldman *et al*. that considers a shear flow passing around an immobilized sphere,[20] it was found that the shear flow induces forces and torques. The associated resistances approach finite values when the sphere is in contact with the wall

$$\frac{\mathcal{R}_{\parallel}^{FU^\infty}}{6\pi\eta a}|_{h\to a} = 1.7005\,\frac{\mathcal{R}_{\parallel}^{\tau U^\infty}}{8\pi\eta a^3}|_{h\to a} = 0.9440. \tag{35}$$

As in the case of a sphere in the bulk, for large distances, the resistances are the same as for a sphere translating and rotating in a quiescent fluid but with opposite sign

$$\frac{\mathcal{R}_{\parallel}^{FU^\infty}}{6\pi\eta a}|_{h\gg a} = 1+\frac{9}{16}\left(\frac{a}{h}\right) \quad \frac{\mathcal{R}_{\parallel}^{\tau U^\infty}}{8\pi\eta a^3}|_{h\gg a} = 1-\frac{3}{16}\left(\frac{a}{h}\right). \tag{36}$$

The global interpolation between both limits is given in Appendix.

On the other hand, when the flux is perpendicular to the wall, there is no known expression for the lubrication approximation. For simplicity, we assume that, as for $\mathcal{R}_{\parallel}^{FU^\infty}$ and $\mathcal{R}_{\parallel}^{\tau U^\infty}$, this resistance does not diverge when $\delta \to 0$. Therefore, we use the expression for large distances of a sphere moving perpendicular in a rest fluid, with the opposite sign, i.e.,

$$\frac{\mathcal{R}_{\perp}^{FU^\infty}}{6\pi\eta a}|_{h\gg a} = 1+\frac{9}{8}\left(\frac{a}{h}\right) \quad \frac{\mathcal{R}_{\perp}^{\tau\Omega^\infty}}{8\pi\eta a^3}|_{h\gg a} = 1+\frac{1}{8}\left(\frac{a}{h}\right)^3. \tag{37}$$

Finally, there remains the coupling between force and rotation (and equivalently torque and translation) due to this external flow. In Ref. 20, these coupling were not considered, because the imposed flow was a simple linear shear flow characterized by a single parameter, the shear rate. Hence the local velocity $\mathbf{U}^\infty$ is proportional to the local angular velocity $\boldsymbol{\Omega}^\infty$. We have extended this to consider external flows that may not be linear and that are characterized by the local velocity and angular velocity, independently. A condition for consistency is that, in the case of linear flows, the known result should be recovered. For simplicity, and without any other information, we neglect these couplings.

V. RESULTS

A. Stable swimming in contact with the surface

At each time step, the linear system of equations for the linear and angular velocities is solved numerically. The associated matrix depends on the orientation and vertical position of the swimmer, becoming singular when any of the spheres touches the wall. The swimmer motion, that is its position and orientation as a function of time, is obtained using a fourth order Runge-Kutta method with adaptive time step.

For a wide range of geometrical parameters ($0.5\ \mu\text{m} < a_H < 2\ \mu\text{m}$, $0.2\mu\text{m} < a_T < 1\mu\text{m}$, and $1\mu\text{m} < L < 4\ \mu\text{m}$), including those in Sec. III B, the dynamics of our model is as follows. If the swimmer is initially pointing toward the surface, it approaches the surface in almost a straight line until it is very close to it, at which point it slows down and orients such that both spheres almost touch the surface (close but not exactly parallel to the surface because of the difference in radii). Then, the complete swimmer is attracted to the surface until it touches it in finite time. At this stage, the swimmer stops any motion (translation and rotation) in a stable state except for eventual numerical errors if the time step is not small enough. This motion is similar to that previously reported for other models: when the initial conditions of the swimmer are prepared such that it reaches the surface, it crashes into the surface and stops moving.[10] In our model, the swimmer stops with both spheres touching the surface.

The stopping process can be understood because the resistance tensors diverge when the spheres touch the surface. Therefore, the finite propulsion force and rod torque cannot produce motion. However, the nature and character of the divergence of the different tensors is different, requiring deeper analysis. The vertical resistance $\mathcal{R}_{\perp}^{FU}$ (Eq. (32)) diverges strongly as $1/\delta$. This divergence is necessary to avoid penetration of the body into the surface and it is always present, quite independently of the precise geometrical shape of the swimmer. On the other hand, the parallel resistance $\mathcal{R}_{\parallel}^{FU}$ (Eq. (31)) has a soft divergence as $\log(\delta)$, which is only noticeable when the sphere is extremely close to (namely, in contact with) the surface. However, before becoming divergent, in real swimmers, the roughness at the nanoscale regularizes this resistance.[24] The same happens for all resistances with the exception of $\mathcal{R}_{\perp}^{FU}$. Therefore, the resistances are naturally regularized at the nanometer scale, and eventually electrochemical forces enter into play, also avoiding that the spheres touch the surface.[11]

To keep the model at a hydrodynamic level, without including extra forces, the vertical resistance $\mathcal{R}_{\perp}^{FU}$ is modified such that it diverges at a small but finite value of δ; therefore, the vertical movement is stopped before the other resistances diverge. Specifically, instead of Eq. (32), we take

$$\frac{\mathcal{R}_{\perp}^{FU}}{6\pi\eta a} = -\frac{2+9\left(\frac{\delta^*}{a}\right)+6\left(\frac{\delta^*}{a}\right)^2}{2\left(\frac{\delta^*}{a}\right)+6\left(\frac{\delta^*}{a}\right)^2}, \tag{38}$$

where $\delta^* = (\delta - \epsilon)$ and the gap size is chosen as $\epsilon = 0.01 a_H = 10$ nm. This value agrees with the swimming distance of some tens of nanometers measured by Li *et al.*, which is consistent with the prediction of the stable position including the Derjaguin–Landau–Verwey–Overbeek (DLVO) potential.[11]

With this regularization scheme, the swimmer can perform stable motion in contact with the surface, as described in Sec. V B.

B. Swimming modes for fixed parameters

Depending on the initial condition, characterized by the initial height of the sphere H, $z(0)$, and the initial orientation with respect to the surface $\alpha(0)$ (Fig. 4(a)), the swimmer shows different asymptotic behaviors. Three different behaviors were identified: (I) swimming in circles in contact with the plate, (II) swimming parallel to the plate at a finite distance, and (III) swimming away from the surface. Figure 4(b) presents a phase diagram of the initial conditions that lead to these final regimes, which are schematically presented in Fig. 4(c). Animations of these three regimes can be seen in Fig. 4(c).

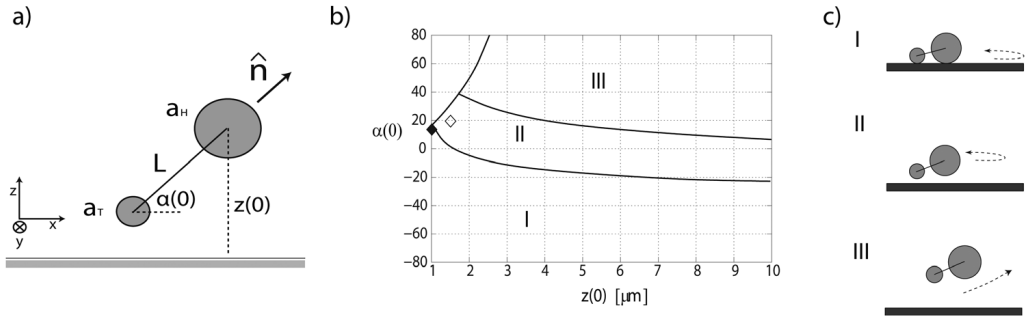

FIG. 4. (a) Initial condition for the swimmer: the orientational angle with respect to the surface is $\alpha(0)$, and the position of the center of sphere H is $z(0)$. The geometrical parameters are $a_H = 1$ μm, $a_T = 0.5$ μm, $L = 2$ μm, and the gas size is set to $\varepsilon = 0.01$ μm. (b) Phase diagram of the initial conditions. Three situations are observed: (I) swimming in circles in contact with the wall, (II) swimming parallel to the wall at a finite distance, and (III) swimming away from the wall. The final states for regimes I and II are indicated by a symbol. The upper left corner is forbidden by the condition that the T sphere must be above the surface. (c) Sketch of the three final regimes. Enhanced online with videos obtained with the following conditions: (I) bacterium starting at $z_0 = 4$ μm and $\alpha_0 = -30$ (3D view (enhanced online) [URL: http//dx.doi.org/10.1063/1.3676245.1] and x-z projection) [URL: http//dx.doi.org/10.1063/1.3676245.2], (II) bacterium starting at $z_0 = 4$ μm and $\alpha_0 = 0$ [URL: http//dx.doi.org/10.1063/1.3676245.3], and (III) bacterium starting at $z_0 = 4$ μm and $\alpha_0 = 30°$ [URL: http//dx.doi.org/10.1063/1.3676245.4].

1. Swimming in circles touching the surface

When the swimmer is initially close to the surface and pointing towards it (negative angle α), it approaches the surface, orients such that both spheres almost touch the surface, and swims in circles. This state is stable, and the swimmer remains in this state almost in contact with the surface thanks to the regularization described in Sec. V A. All initial conditions in region I of the phase diagram end in the same final state, characterized by $z_H - R_H = z_T - R_T = \epsilon$. Consequently, the final orientation, which depends on the swimmer geometry, is given by $\alpha = 14°$. The swimmer velocity is $V_{\text{circle}} = 9.8\mu$m/s, and the radius of curvature $R_C = 15.8\mu$m. Experiments show a wide dispersion of velocities and radius of curvature of *E. coli* swimming in contact with a solid surface.[7,25] The computed values for this model fall within the observed experimental ranges.

2. Swimming in circles at a finite distance

When the initial orientation angles are higher than in the former regime, while still not being too large, the swimmer ends up in a stable state, moving parallel to the surface at a finite distance. The final configuration is given by $z_H = 1.51\mu$m, $z_T = 0.84$ μm, and orientation with respect to the surface $\alpha = 19^{\circ}$. Due to the distance to the wall, the hydrodynamic interaction with it is strong, and the radius of curvature of this state is $R_C = 12.9$ μm while the swimming velocity is that of the bulk $V_{\text{parallel}} = 20$ μm/s. All the initial conditions in region II of the phase diagram end in the same state. This regime has not been identified in experiments as a different regime from the previous one. Possibly because the radii of curvature are similar and the distance to the wall is not easy to measure.

3. Swimming away from the surface

Finally, if the swimmer starts with orientations even larger than those of the previous regime, it will swim away from the surface. It must be remarked that, if $z(0)$ is large, even if the initial angle is negative, the reorientation produced by the interaction with the wall can be strong enough to take it away (not shown in the phase diagram of Fig. 4). The final states in this regime are not unique and depend on the initial condition.

C. Sensitivity on the gap distance

In Sec V A, it was argued the need of a small gap, ϵ, that would take into account the roughness at the nanometer scale and its value was fixed to $\epsilon = 10$ nm. The motion in the bulk and the

swimming mode parallel to the surface are insensitive to this parameter choice not like the circular motion in contact with the surface. It is found that when changing the gap in the range 4 nm $<\epsilon<$ 20 nm, the radius of curvature and the circular velocity vary in the range $8\,\mu\text{m} < R_C < 50\,\mu\text{m}$ and $8.6\,\mu\text{m/s} < V_{\text{circle}} < 10.8\,\mu\text{m/s}$, respectively. This sensitivity on the value of ε could be responsible of the wide dispersion of velocities and radius of curvature observed in experiments,[6,25] due to the diversity in the nanometric roughness of the bacteria.

VI. CONCLUSIONS

A simple model for a swimmer at zero Reynolds number has been built, consisting of two spheres of different radii joined by a dragless rod. The model aims to reproduce the swimming of a pusher bacteria like *E. coli* near solid surfaces. The hydrodynamic forces and torques on each sphere are computed taking into account the full interaction with the surface using the complete resistance matrix. The hydrodynamic interaction between the spheres is treated approximately by considering the force and torque over a sphere under the flow produced by the other. The rod imposes opposite torques on the spheres making them rotate in opposite directions. Finally, the propulsion is obtained by adding an extra hydrodynamic force on one sphere (the tail) as to mimic the effect of the rotary flagella of *E. coli*. The dimensions of the spheres and their separation are fixed according to experimental results of the size of *E. coli*, its velocity in the bulk, and its effective force dipole.

When pure hydrodynamic interactions of perfect spheres are used, if the swimmer is set to approach the surface, it reaches the surface in finite time with both spheres in contact with it. At this point, the swimmer stops moving due to the divergence of the hydrodynamic resistances. Appealing to the existence of nanometric roughness of the body cell or electrochemical forces with the surfaces, the resistances are regularized at the nanometric scale obtaining finite velocities when it swims close to the surface.

The swimmer shows three different behaviors depending on the initial condition. If the swimmer is close to the surface pointing toward it, it approaches the surface and orients in such a way as to have both spheres touching the surface. Once reached this state, the swimmer performs a circular motion at constant speed with a radius of curvature in the range $8 - 50\,\mu\text{m}$, depending on the value used to regularize the resistances, which is in the range of the experimental observations. In the present model, the swimmer remains in this state forever. It is expected that surface roughness, thermal noise, velocity agitations, or the tumbling mechanism can allow the swimmer to exit the wall region. A second regime is obtained when the swimmer starts at higher altitudes. In this case, it approaches the surface without touching it and swimming in circles parallel to the surface with a gap of approximately a half of micron. The trajectory is also circular with a similar radius of curvature but larger velocity. To our knowledge, this regime has not been identified experimentally. Finally, if the swimmer is initially far enough, it will reorient as to move away from the surface.

ACKNOWLEDGMENTS

This research is supported by Fondecyt 1100100, Anillo ACT 127, and ECOS C07E07 grants. E.C. thanks the SESAME-Ile de France program for support.

APPENDIX: FITS FOR THE RESISTANCE TENSORS

Using the notation shown in Fig. 3, the normalized distance to the wall is defined as $x = h/a$, the gap distance is $\delta = (h - a)$, and the minimum distance that the swimmer can approach to the wall is ϵ. Global fits are built such that the appropriate series when $\delta \ll a$ and when $x \gg 1$ reproduce the known asymptotic expansions (see discussion in Sec. IV). There is not global bounding error of the fits, but we expect that the interpolating procedure produce uniformly convergent expressions if more known terms were added in both limits. The resulting resistances for a sphere moving in a quiescent fluid and for a sphere immobilized in an ambient fluid are the following.

1. Global fits for a sphere translating and rotating in a quiescent ambient fluid

$$\frac{\mathcal{R}_{\parallel}^{FU}}{6\pi\eta a} = (2.5295 - 1.9963x)\log\left(\frac{x-1}{x}\right) - 2.9963 + 0.9689\frac{1}{x} + 0.5993\frac{1}{x^2} + 0.4691\frac{1}{x^3}, \quad \text{(A1)}$$

$$\frac{\mathcal{R}_{\perp}^{FU}}{6\pi\eta a} = -\left[2 + 9\left(\frac{\delta-\epsilon}{a}\right) + 6\left(\frac{\delta-\epsilon}{a}\right)^2\right] \Big/ \left[2\left(\frac{\delta-\epsilon}{a}\right) + 6\left(\frac{\delta-\epsilon}{a}\right)^2\right], \quad \text{(A2)}$$

$$\frac{\mathcal{R}_{xy}^{F\Omega}}{6\pi\eta a^2} = (0.3657 - 0.4991x)\log\left(\frac{x-1}{x}\right) - 0.4991 + 0.1162\frac{1}{x} + 0.0165\frac{1}{x^2} - 0.0028\frac{1}{x^3} + 0.1166\frac{1}{x^4}, \quad \text{(A3)}$$

$$\frac{\mathcal{R}_{\parallel}^{\tau\Omega}}{8\pi\eta a^3} = (-0.3898 + 0.7898x)\log\left(\frac{x-1}{x}\right) - 0.2101 + 0.0050\frac{1}{x} + 0.0683\frac{1}{x^2} - 0.2449\frac{1}{x^3}, \quad \text{(A4)}$$

$$\frac{\mathcal{R}_{\perp}^{\tau\Omega}}{8\pi\eta a^3} = -\left(0.414(x-1) + 0.318\frac{(x-1)^2}{x}\right)\log\left(\frac{x-1}{x}\right) - 1.732 + 0.684\frac{1}{x} - 0.037\frac{1}{x^2} - 0.117\frac{1}{x^3}. \quad \text{(A5)}$$

2. Global fits for a sphere immobilized in an ambient fluid

$$\frac{\mathcal{R}_{\parallel}^{FU^{\infty}}}{6\pi\eta a} = 1 + \frac{9}{16}\left(\frac{a}{h}\right) + 0.1375\left(\frac{a}{h}\right)^2, \quad \text{(A6)}$$

$$\frac{\mathcal{R}_{\perp}^{FU^{\infty}}}{6\pi\eta a} = 1 + \frac{9}{8}\left(\frac{a}{h}\right), \quad \text{(A7)}$$

$$\frac{\mathcal{R}_{\parallel}^{\tau\Omega^{\infty}}}{8\pi\eta a^3} = 1 - \frac{3}{16}\left(\frac{a}{h}\right)^3 + 0.1315\left(\frac{a}{h}\right)^4, \quad \text{(A8)}$$

$$\frac{\mathcal{R}_{\perp}^{\tau\Omega^{\infty}}}{8\pi\eta a^3} = 1 + \frac{1}{8}\left(\frac{a}{h}\right)^3, \quad \text{(A9)}$$

$$\mathcal{R}^{F\Omega^{\infty}} = \mathcal{R}^{\tau U^{\infty}} = 0. \quad \text{(A10)}$$

[1]S. Suarez and A. Pacey, "Sperm transport in the female reproductive tract," Human Reprod. Update **12**, 23 (2006); G. L. Cooper, A. L. Schiller, and C. C. Hopkins, "Possible role of capillary action in pathogenesis of experimental catheter-associated dermal tunnel infections," J. Clin. Microbiol. **26**, 8 (1988); G. Harkes, J. Dankert, and J. Feijen, "Bacterial migration along solid surfaces," Appl. Environ. Microbiol. **58**, 1500 (1992); E. A. Gaffney, H. Gadêlha, D. J. Smith, J. R. Blake, and J. C. Kirkman-Brown, "Mammalian Sperm Motility: Observation and Theory," Annu. Rev. Fluid Mech. **43**, 501 (2011).

[2]A. Sokolov, M. M. Apodaca, B. A. Grzybowski, and I. S. Aranson, "Swimming bacteria power microscopic gears," Proc. Natl. Acad. Sci. U.S.A. **107**, 969 (2009); R. Di Leonardo, L. Angelani, D. Dell'Arciprete, G. Ruocco, V. Iebba, S. Schippa, M. P. Conte, F. Mecarini, F. De Angelis, and E. Di Fabrizio, "Bacterial ratchet motors," Proc. Natl. Acad. Sci. U.S.A. **107**, 9541 (2010).

[3]S. Kim and S. J. Karilla, *Microhydrodynamics: Principles and Selected Applications* (Dover, New York, 2005).

[4]H. C. Berg, *E. coli in Motion* (Springer, New York, 2004).

[5]H. C. Berg, *Random Walks in Biology* (Princeton University Press, Princeton, NJ, 1993).

[6]P. D. Frymier, R. M. Ford, H. C. Berg, and P. T. Cummings, "Three-dimensional tracking of motile bacteria near a solid planar surface," Proc. Natl. Acad. Sci. U.S.A. **92**, 6199 (1995).

[7]E. Lauga, W. R. DiLuzio, G. M. Whitesides, and H. A. Stones, "Swimming in circles: Motion of bacteria near solid boundaries," Biophys. J. **90**, 400 (2006).

[8]X.-L. Wu and A. Libchaber, "Particle diffusion in a quasi-two-dimensional bacterial bath," Phys. Rev. Lett. **84**, 3017 (2000).

[9]G. Miño, T. E. Mallouk, T. Darnige, M. Hoyos, J. Dauchet, J. Dunstan, R. Soto, Y. Wang, A. Rousselet, and E. Clement, "Enhanced diffusion due to active swimmers at a solid surface," Phys. Rev. Lett. **106**, 048102 (2011).

[10]M. Ramia, D. L. Tullock, and N. Phan-Thien, "The role of hydrodynamic interaction in the locomotion of microorganisms," Biophys. J. **65**, 755 (1993).

[11]G. Li, L.-K. Tam, and J. X. Tang, "Amplified effect of Brownian motion in bacterial near-surface swimming," Proc. Natl. Acad. Sci. U.S.A. **105**, 18355 (2008).
[12]V. Gyrya, I. S. Aranson, L. V. Berlyand, and D. Karpeev, "A model of hydrodynamic interaction between swimming bacteria," Bull. Math. Biol. **72**, 148 (2010).
[13]J. Hernandez-Ortiz, C. Stoltz, and M. Graham, "Transport and collective dynamics in suspensions of confined swimming particles," Phys. Rev. Lett. **95**, 204501 (2005).
[14]A. P. Berke, L. Turner, H. C. Berg, and E. Lauga, "Hydrodynamic attraction of swimming microorganisms by surfaces," Phys. Rev. Lett. **101**, 038102 (2008).
[15]J. R. Blake and A. T. Chwang, "Fundamental singularities of viscous flow," J. Eng. Math. **8**, 23 (1974).
[16]S. W. Reid, M. C. Leake, J. H. Chandler, C. J. Lo, J. P. Artimage, and R. M. Berry, "The maximum number of torque-generating units in the flagellar motor of Escherichia coli is at least 11," Proc. Natl. Acad. Sci. U.S.A. **103**, 8066 (1993).
[17]J. Happel and H. Brenner, *Low Reynolds Number Hydrodynamics with Special Applications to Particulate Media* (Prentice Hall, Englewood Cliffs, NJ, 1965).
[18]K. Drescher, J. Dunkel, L. H. Cisneros, S. Ganguly, and R. E. Goldstein, "Fluid dynamics and noise in bacterial cell-cell and cell-surface scattering," Proc. Natl. Acad. Sci. U.S.A. **108**, 10940 (2011).
[19]J. W. Swan and J. F. Brady, "Simulation of hydrodynamically interacting particles near a no-slip boundary," Phys. Fluids **19**, 113306 (2007).
[20]A. J. Goldman, R. G. Cox, and H. Brenner, "Slow viscous motion of a sphere parallel to a plane wall-II," Chem. Eng. Sci. **22**, 653 (1967).
[21]M. A. Bevan and D. C. Prieve, "Hindered diffusion of colloidal particles very near to a wall: Revisited," J. Chem. Phys. **113**, 1228 (2000).
[22]H. Brenner, "The slow motion of a sphere through a viscous fluid towards a plane surface," Chem. Eng. Sci. **16**, 241 (1961).
[23]S. H. Lee and L. G. Leal, "Motion of a sphere in the presence of a plane interface. Part 2. An exact solution in bipolar co-ordinates," J. Fluid Mech. **98**, 193 (1980).
[24]F. R. Da Cunha and E. J. Hinch, "Shear-induced dispersion in a dilute suspension of rough spheres," J. Fluid Mech. **309**, 211 (1996).
[25]G. Miño, personal communication (2011).

Flow-controlled densification and anomalous dispersion of *E. coli* through a constriction

E. Altshuler[1,2,3], G. Miño[1], C. Pérez-Penichet[2], L. del Río[2], A. Lindner[1], A. Rousselet[1], and E. Clément[1,*]

Received Xth XXXXXXXXXX 20XX, Accepted Xth XXXXXXXXX 20XX
First published on the web Xth XXXXXXXXXX 200X
DOI: 10.1039/b000000x

Dispersion and migration of bacteria under flow in tortuous and confined structures such as porous or fractured materials, is related to a large spectrum of practical interests, but is still poorly understood. Here, we address the question of transport and dispersion of an E-coli suspension flowing though a micro-fluidic channel with a funnel-like constriction in its center. We show a counter-intuitive symmetry breaking of the bacteria concentration, which increases significantly past the funnel. This concentration enhancement persists over large distances from the funnel and disappears at large flow rate values. We map our results onto a one dimensional convection/diffusion equation predicting quantitatively the experimental results, without free parameters, when a conservative non-local source term is introduced. This last term, measured experimentally, represents a long range memory effect due to the unbalance of wall adsorption and desorption processes past the constriction. Our model experiment points on the generic importance of considering such constriction effects in the description of transport properties of active matter in porous media. It also opens the possibility to control the concentration of bacteria suspensions in micro-fluidic channels by simply tuning the flow intensity or direction.

From the hydrodynamics point of view, assemblies of microscopic swimmers such as bacteria dispersed in a fluid, display constitutive properties differing strongly from those of passive suspensions [1–3], Momentum transport equations and constitutive relations, are deeply modified by the presence of these autonomous swimmers dispersed in the fluid. New and surprising effects were reported such as activated Brownian motion [4–6], anomalous viscosity [7,8], mixing enhancement [9], bio-convection [10] or work extraction from fluctuations [11] . Along those lines, the fundamental question of hydrodynamic dispersion of bacteria suspended in a fluid, remains an issue that has not received yet a fully satisfactory treatment. This difficult question is closely linked to many practical issues related to bio-contamination in porous rocks, in biological micro-vessels or through medical catheters. Methods of analysis used to describe bacterial transport consist essentially of macroscopic convection/diffusion equations in association with adsorption/desorption terms describing retention effects by the surfaces. However, in spite of the fact that many fitting parameters can be used to match the dispersion curves, systematic inconsistencies were reported between experiment and modeling [12] and may lead to further phenomenological refinements including, for example, straining effect as in the colloidal filtration problem which would occur at the smallest pores and at the grain-grain junction [13]. Consequently, there is a strong and timely need to identify precisely, the many processes at work contributing to the transport of bacteria in a confined environment, including those directly related to the micro-organism swimming capability.

In this work we will use suspensions of *E. coli*, a microorganism that can move at low Reynolds number in aqueous media at speeds of about 20 microns per second. The *E. coli* mode of propulsion is rather well understood [14]. This 2 μm body-length swimmer produces a thrust due to the counterclockwise rotation of an helical bundle of 10 μm length flagella. In the bulk, for the wild-type strain, the motion is made of straight "runs" interrupted every few seconds by a sudden change of direction (or "tumble") [15]. The tumbling rate is triggered by chemotaxy i.e. complex intracellular biochemical cascades triggering the flagella rotation in relation with fine strategies for finding nutriments [16]. In the vicinity of a solid boundary, the swimming picture drastically changes [17–19]. Lubrication forces acting on the counter-rotating body, lead generically to circular trajectories. Experimental measurements and hydrodynamic studies suggest that solid boundaries also act as "traps" [20]. The bacteria stay at the surface for long time and this persistent motion induces a strong increase of concentration at the walls [21]. The recent use of microfluidic

[1] PMMH, UMR 7636 CNRS-ESPCI-Universités Paris 6 and 7, 10, rue Vauquelin - 75231 Paris Cedex 5, France
[2] "Henri Poincaré" Group of Complex Systems and Superconductivity Laboratory, Physics Faculty-IMRE, University of Havana, 10400 Havana, Cuba
[3] Centre for Advanced Study, Norwegian Academy of Sciences and Letters, NO-0271, Oslo, Norway
[*] corresponding author : eric.clement@espci.fr

tools has revolutionized the way microorganisms motility can be approached experimentally. The fabrication of microscopic scale channels of different forms, enabling observations of high spatial and temporal resolution, allows crucial tests of many fundamental hypotheses on transport properties. Furthermore, such channel can directly be used to enhance selection of target species depending on their motile character. For bacteria suspensions such tools have recently been used to describe spontaneous densification induced by wall shape asymmetry[22,23], upstream trajectories in the presence of flow[24] or chemotactic response in well controlled chemical gradients[25].

In the present work, we will use microfluidic channels to visualize the effect of a funnel like constriction on the bacterial transport in a flow. This geometry can be seen as a situation encountered generically in many porous structures at the pore necks. For appropriate flow conditions, a strong concentration enhancement of active bacteria is observed past the funnel, opposite to observations for complex flows containing "inactive" particles[26]. We discuss our results in the light of elementary mechanisms of interaction between the swimming bacteria and the walls. To render quantitatively the dispersion curves, we propose an advection-diffusion equation containing an effective long range source term that is directly related to the specific swimming properties of the bacteria at the walls.

1 Experimental set-up

The bacterial suspension is a wild-type strain of *E. coli* W (ATCC 11105[27]) prepared in a "minimal motility medium", as follows. Wild type *E. coli* W, ATCC 11105 were grown overnight in a rich culture medium (LB). From this sample 40 μL of bacteria were diluted in 8 mL of LB. They were incubated for at least five hours to obtain a maximal activity[28]. After washing, they were transferred into Minimal Motility Media MMA[29](10 mM NaH_2PO_4, 10 mM K_2HPO_4, 0.1 mM EDTA, and 20 mM Sodium Lactate), supplemented with K-acetate (0.34 mM) and polyvinyl pyrolidone (PVP: 0.005%). The overall concentration of bacteria was kept at $4\pm0.5\times 10^8$ bact/mL. We checked that the suspending fluid was Newtonian (viscosity $\eta = 0.88$ *mPa s* at 25°C). All experiments were performed at a fixed temperature $T = 25°C$. The minimal motility medium is a controlled environment where bacteria can swim but do not replicate and where the influence of chemotaxis or aerotaxis driving the bacterial motion is limited. We also use, for comparison, suspensions of dead-bacteria obtained under identical conditions but killed using ethanol at 80%.

The bacteria suspension is flown by gravity overpressure through a microfluidic channel of total length $L = 15mm$ made in PDMS by standard soft-lithography technique (see Fig.1(a)). The channels were fabricated onto glass covered by a 28μm-thick PDMS coating to avoid sticking of the bacteria. The inlet and the outlet are inox tubes of 1-mm outer diameter connected to flexible plastic tubes. The rectangular section has a width $W = 200\ \mu m$ and a depth $h = 20\ \mu m$ and the channel contains, in its middle, a symmetric constriction over a distance $L_f = 200\ \mu m$ and reaching a minimum width $W_f = 40\ \mu m$ (see Fig. 1(a)). On Fig. 1(b), we show a bottom view of the channel in the vicinity of the constriction.

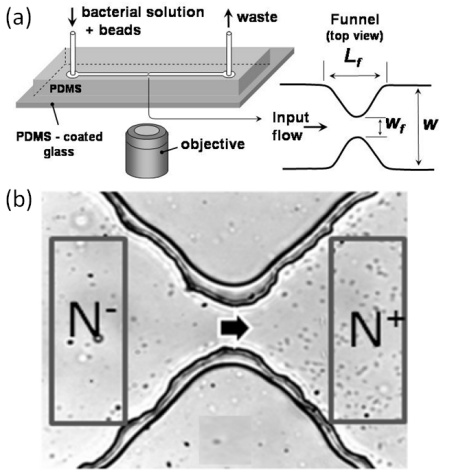

Fig. 1 (a). Sketch of the microfluidic channel fixed on a glass plate. On the right side, zoom on the funnel geometry viewed from the top; the dimensions are $L_f = 200\mu m$, $W_f = 40\mu m$ and $W = 200\mu m$ (b). Visualization of the symmetry breaking effect at the funnel for an active *E. coli* suspension for $< V_x >= 25\mu m/s$. The image includes the two symmetric rectangular domains where the number of bacteria N^- and N^+ are computed. The thick arrow corresponds to the flow direction.

The flowing suspensions were observed from below using an inverted microscope (Zeiss-Observer, Z1-magnification 40x or 20x). A digital camera PixeLINK PL-A741-E was used for image acquisition, (600×800 pix^2 and 1280×1024 pix^2) capturing videos at a frame rate of 20 and 12.5 frame/s, depending if the magnification used was 40X or 20X. Due to the relatively small height of the channel, all bacteria could be visualized along the vertical axis at a fixed position of the objective lens. For counting bacteria, the background of each video was digitally homogenized and "binarized" with appropriate thresholds to reveal all the individuals.

As can be seen on the snapshot shown on figure 1(b), at the junction between the lateral walls and the top and bottom surface there is a small apparent bulge. The lateral wall is straight over most of the channel height. However, the bulge at the junction corner makes the visualization of the bacteria motion very close to the *lateral* walls (typically at a 5 μm distance), difficult. These bacteria will not be considered in the first part of the paper and their role will be discussed later.

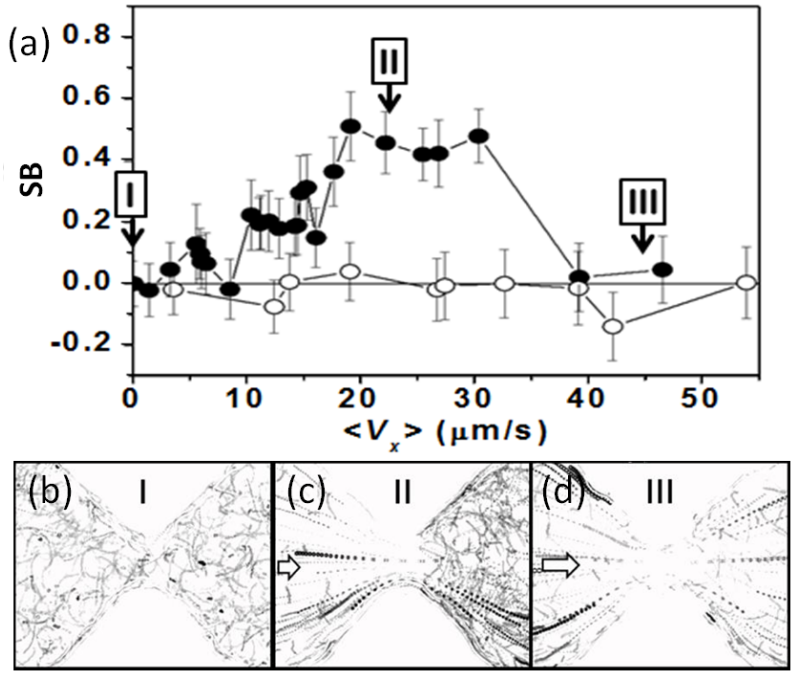

Fig. 2 Flow-controlled symmetry breaking in the concentration of *E. coli*. (a) *SB* as a function of the mean flow velocity $< V_x >$. Error bars correspond to RMS fluctuations. Dark symbols are for living bacteria and empty symbols are for dead bacteria. Trajectories obtained by snapshots accumulation over 1 *s* (20 frames) for three mean flow velocities (b) $< Vx >= 0\mu m/s$, (c) $< Vx >= 25\mu m/s$ and (d) $< Vx >= 50\mu m/s$. The corresponding roman numbers I, II, III are displayed on (a). Note that trajectories corresponding to the beads appear as big circular spots in (C) and (D). Flows are from left to right as indicated by the arrows.

Polystyrene beads of diameter $d = 2\ \mu m$ were dispersed in the suspension to serve as flow tracers. For a given overpressure, the average flow velocity $< V_x >$ was estimated by averaging the tracer velocities detected in the constriction and multiplying its value by the ratio W_c/W. In principle, if one assumes a random distribution of passive tracers in the flow, this measurement provides a reasonable estimation of the mean flow velocity.

2 Flow induced symmetry breaking

We use bacteria suspensions prepared with a concentration $n = 4\ \pm 0.5 \times 10^8 bact/mL$. Fig. 1(b) displays a snapshot obtained at a mean flow velocity $V = 25\mu m/s$ were an accumulation of bacteria is clearly observed on the right side of the funnel. To quantify this effect the bacteria were counted inside two rectangular regions placed symmetrically on both sides of the funnel: N^- on the left and N^+ on the right (counting was done over 20 *s* with an acquisition frequency of 20 frames/s). We quantify the difference in bacteria concentration on both sides of the funnel by defining a symmetry breaking parameter :

$$SB = \frac{N^+ - N^-}{N^+ + N^-} \quad (1)$$

On Fig.2(a), we display *SB* as a function of the mean flow velocity $< V_x >$ both for living and dead bacteria. In the case of living bacteria, starting from zero flow, the symmetry breaking parameter increases roughly linearly up to approximately $SB = 0.6$ as the mean flow velocity increases from zero to 20 $\mu m/s$. Then, *SB* reaches a plateau and finally decays to zero quite abruptly around a mean flow velocity 40 $\mu m/s$. Note that *SB* reaches its maximum value at a velocity around 20-30 μm/s, a value comparable to the mean bacteria velocity measured in the absence of flow ($V_b = 15 \pm 5\mu m/s$). For suspensions of dead bacteria, the amount of individuals in the control regions before and after the constriction, were identical, regardless of the flow velocity (see Fig.2(a) hollow circles). This shows that the symmetry breaking effect is directly related to the active character of the suspension. On Figs 2.(b), (c) and (d), we show that the symmetry breaking is also associated with a change in the trajectory shapes. On these figures, we display the tracks of bacteria and tracer particles obtained by superimposing snapshots acquired over 1 *s* (20 frames). At zero flow (Fig.2(b)), the trajectory shapes are

clearly curved and mostly circular which is a signature that on both sides of the funnel the bacteria dwell preferentially at the top/bottom wall. The situation changes drastically when the symmetry breaking is established. On Fig.2(c), corresponding to the symmetry breaking plateau ($< V_x >= 25\ \mu m/s$), one can clearly observe asymmetry in the trajectory shapes before and after the funnel. Before the funnel, bacteria are convected mostly passively by the flow with trajectories identical to the latex particles appearing as thick tracks on the figures. However, passed the funnel, the bacteria trajectories are much more curved showing a net tendency to swim very close to the upper and lower boundaries. Finally, at high speeds ($< V_x >= 50\ \mu m/s$), most trajectories follow the stream lines as passive particles do (see Fig.2(d)).

The symmetry breaking of the concentration profile can be controlled by changing not only the intensity, but the *direction* of the imposed flux. For example, starting with a flux of $< V_x >= 25\ \mu m/s$ from left to right, we get a symmetry breaking parameter $SB \approx 0.6$ (higher concentration of bacteria at the right of the funnel). If we then suddenly reverse the direction of the flow to $< V_x >= -25\ \mu m/s$, a value $SB \approx -0.6$ is reached within less than 10 seconds (i.e., the higher concentration has moved to the left of the funnel; see videoS1 and figureS1 in SIText). The process can be repeated several times with no obvious memory effects.

Next, we study the spatial range of concentration increase induced by the symmetry breaking. After establishing a constant flux of 30 μm/s during few minutes, we performed a series of 14 spatially overlapping videos spanning a 5000 μm range along the channel, symmetrical around the constriction. Each video was taken at a $20X$ magnification and lasted 8 seconds (taken at 12.5 $frames/s$). From these movies, the time averaged bacteria density $n(x)$ along the flow was computed (the stripe width used for density measurements was $\Delta x = 5\mu m$). On Fig.3, we display the density profile $n(x)$. Before the funnel, the concentration is constant, around 5×10^8 $bact/ml$ and suddenly decreases to less than $1\times10^8 bact/ml$ at approximately -150μm left from the geometrical center of the funnel. Then, a sharp increase in concentration occurs at the center of the funnel, reaching 14×10^8 $bact/ml$ at approximately 70μm from the funnel center. This measurement shows not only the huge concentration amplification resulting from the flow constriction but also the long-range effect since the bacteria densification persists several millimeters passed the funnel i.e. a distance larger by one order of magnitude than the funnel. length L_f. Note that at a distance of 2.5 mm to the right of the funnel, the average concentration is still slightly higher than its value at the left side of the funnel.

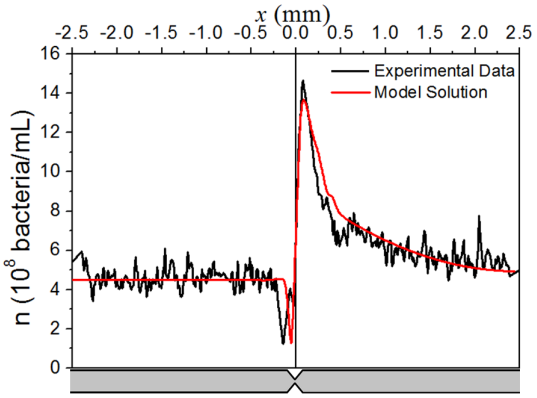

Fig. 3 Spatial extension of the symmetry breaking effect. The black line corresponds to the mean bacterial concentration measured along the flow $n(x)$. The red line is the solution of the 1-D advection-diffusion model as explained in the text. The sketch underneath corresponds to a top-view geometry of the channel at the same X-scale. Note the change of scale compared to the previous figures.

3 A micro-macro view of the transport properties

To understand the mechanisms leading to this symmetry breaking and the corresponding long range density enhancement effect, we visualize and analyze the bacteria trajectories to infer qualitatively and quantitatively the salient features influencing the macroscopic transport properties of the suspension. In this part, we consider a flow velocity of $< V_x >= 30\mu\ m/s$, corresponding to the symmetry breaking plateau.

First, we study the situation far away from the funnel. On Fig.4(a), we display a snapshot of the channel far from the constriction. We superimpose on this picture, as colored lines, 30 individual bacteria trajectories (each taken over 8 s). The corresponding arrow on each line, points to the forward direction of motion. This representation leads to several crucial remarks. We observe that a significant fraction of the trajectories are upstream. This upstream motion was already noticed by Hill *et al.*[24] in a straight channel of constant width. Second, many of these trajectories correspond to an "adsorption" or a "desorption" process with respect to the *lateral* left/right walls. Far from the wall it seems that rates of adsorption and desorption are almost identical. To show this balance of desorption and adsorption, we measured directly the number of bacteria crossing a plane parallel to the side walls at a distance of $10\mu m$ from the wall during $8s$. We deduced from these measurements, that either far before or after the funnel, the mean lateral flux $J(x) = J^+(x) - J^-(x)$ is almost zero. Note that we define $J^+(x)$ as the flux of bacteria going from the side walls (left or right) to the bulk and $J^-(x)$ as the flux of

bacteria going from the bulk to the side walls. We obtained $J^+(x) \approx J^-(x) \approx 0.0028\ bact/\mu\, m^2/s$. We also measured the bacteria density profile across the channel width on the left and on the right sides of the funnel. The profiles $n(y)$ are displayed on Fig.4(b) and the flux equilibration is consistent with the flatness of the profile.

From these profiles one can also see that there is an important bacteria population very near the lateral walls (see transverse profile on Fig.4(b)) and noticed an important upstream traffic of bacteria in this region. We show in supplementary information a movie that illustrates the adsorption/desorption effect of bacteria at the lateral walls (see videoS2) and also a spatial-temporal diagram of a line along the lateral walls (see figure S2 in SIText), showing streaks corresponding to an upstream velocity around $-15\ \mu m/s$. To quantify the mean transport properties due to the flow, we tracked 280 bacteria trajectories far from the funnel (on both sides) during $\tau = 4\ s$. The corresponding displacements Δ_x along the flow were computed. On Fig. 4(c), the corresponding distribution $P(\Delta_x)$ is displayed. From the mean value $\overline{\delta X} = 14\mu m$ and the average quadratic deviation from the mean $\overline{\sigma_x^2} = 1040\mu m^2$, we obtain a mean transport velocity far from the funnel $u_0 = \overline{\delta X}/\tau = 3.5\mu\, m/s$ and the corresponding dispersion coefficient along the flow $D = \overline{\sigma_x^2}/2\tau = 130\mu\ m^2/s$. The mean transport velocity is almost one order of magnitude smaller that the mean flow velocity. Importantly, we have checked that the time scale $\tau = 4\ s$ is appropriate to compute the emerging macroscopic quantities. On Fig.4.(d), we display the mean longitudinal velocity autocorrelations $C_{xx}(s)$ for a time lag s : $C_{xx}(s) = <\overline{V_x^b(t+s)V_x^b(t)}>_b - \overline{<V_x^b(t)>^2}_b$. Note the double average: a time average along each track, and a second average over the 280 bacteria trajectories. The error bars correspond to the RMS deviation for the different trajectories. The "instantaneous" bacteria velocity along the track $V_x^b(t)$ was computed with a time scale resolution $\delta t = 0.08s$. For a time lag of $s = 4\ s$, the autocorrelation has reached - within experimental uncertainties- a zero value which means that computing the mean transport properties using the time scale $\tau = 4\ s$ is meaningful.

Thereafter, we look at the region close to the funnel. To characterize the adsorption/desorption effects at the lateral walls, we computed the average fluxes $J(x) = J^+(x) - J^-(x)$, in a region around the funnel i.e. for $-150\mu m < x < 500\mu m$ (see Fig.5(a)). The values $J(x)$ are displayed on Fig.5(b). Note that, as explained above, positive values mean net "desorption" and negative values mean net "adsorption". We observe a strong peak of desorption at the funnel constriction, followed by a slightly increased adsorption in the region downstream of the funnel. This effect persists over a large distance and the equilibrium value of $J = 0$ is not yet reached after 500 microns. More qualitatively, the symmetry breaking in the vicinity of the constriction can be illustrated by following several typical trajectories of the bacteria. On Fig.5(c), we display a snapshot of the funnel area and superimpose on the figure, some trajectories as in Fig.4(a). We see that the bacteria moving counterflow at the lateral walls and approaching the constriction will undergo "forced" desorption, most likely due the increase of viscous shear stress, and will be recycled into the flow. We also noticed that many trajectories after this desorption process are significantly curved, indicating a preferential position at the bottom/top walls (consistently with (Fig.2(c)). These bacteria will eventually hit the lateral boundary and move again up-stream to the funnel area. This cyclic persistent motion will induce an important sojourn time at the right, in the vicinity of the constriction, and a local increase of the density as shown on Fig.3. So far, we ignore the typical dwelling time assumed by our *E. coli* at the lateral walls for a given flow rate . Note that without flow, a value was obtained by Drescher *et al.*[21] and it could be as long as 1 *min*, which should represent an upper bound for our situation. For a typical bacteria velocity around $15\mu m/s$ at the lateral walls (corroborated by the spatio-temporal diagram displayed in supplementary documents), this would lead to a typical traveling length without desorption of $900\mu m$ maximum. This length is of the same magnitude as the distance over which the adsoption/desorption fluxes are found to be unbalanced (Fig.5(b)), which is consistent with the idea of premature desorption at the constriction which explains the symmetry breaking.

4 Anomalous dispersion

Now, to provide a quantitative picture of the influence of a funnel-like structure on the transport and the dispersion properties of a bacterial suspension, we map the problem onto a simple one dimensional advection-diffusion equation taken at steady-state :

$$-D\frac{d^2n(x)}{dx^2} + \frac{d}{dx}[u_a(x)n(x)] = S(x) \qquad (2)$$

where $n(x)$ is the volume concentration of bacteria, $u_a(x)$ is their mean advection velocity along the flow, D is an effective longitudinal dispersion coefficient and $S(x)$ is a conservative bulk source/sink term coming from the lateral wall contributions. The source-sink term is defined as $S(x) = J(x)/w(x)$, where $w(x)$ is the channel width at position x. Since the total number of bacteria must be conserved, the condition $\int S(x)dx = 0$ must be fulfilled (the integration taking place along the whole channel).

To pursue the analysis quantitatively, we now assume that the mean bacteria velocity is proportional to the local flow velocity, which gives a relation between the local advection

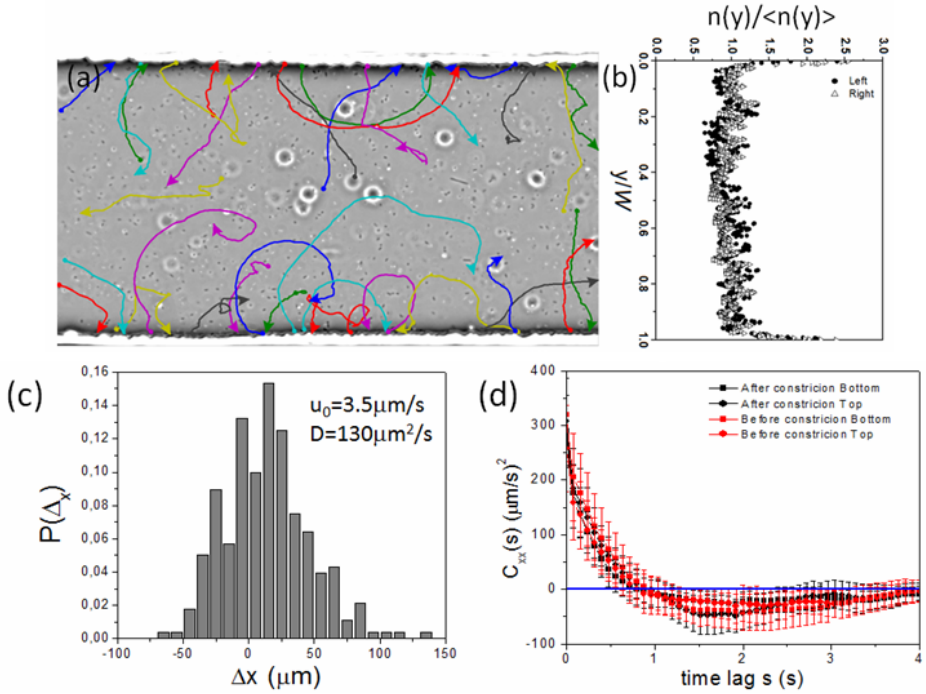

Fig. 4 (a) Bacteria trajectories superimposed to a snapshot far from the funnel ($x = 1.7 - 2.1mm$), showing side wall adsorption and desorption effects. (b) Transverse bacteria concentration as function of vertical position y. Dark circles and empty triangles represent the profile measured between -1.7 and $2.1mm$ and between 1.7 and $2.1mm$, respectively. $< n(y) >= 4.25 \times 10^8 bact/mL$ and $< n(y) >= 5.5 \times 10^8 bact/mL$, represent the mean concentration before and after the funnel, respectively. (c) Mean displacement distribution $P(\Delta x)$. The statistics is taken over 280 trajectories. (d) Longitudinal velocity autocorrelation C_{xx} as a function of the time lag s (see text for definition).

velocity and u_0, the mean advection velocity far from the funnel: $u_a(x) = \frac{W}{w(x)} u_0$. If $S(x)$ is known, only two parameters remain to be introduced in equation 2: u_0 and D. Provided the values computed previously from the distribution of the longitudinal displacements (see Fig. 4.(c)): $u_0 = 3.5\mu\ m/s$, $D = 130\mu\ m^2/s$, and the experimental values for $S(x)$ from the $J(x)$ measurement (see Fig. 5.(b)), the equation can be integrated numerically with the boundary conditions at $x = -\infty$, $n(-\infty) = 4.5 \times 10^8\ bact/ml$ and $dn/dx(-\infty) = 0$. The result is displayed on Fig.3 (red curve). We observe a good agreement with the experimental determination of the density along the flow which means that we have identified the necessary parameters to describe the transport and dispersion of bacteria in this micro-channel.

5 Conclusion

We have shown experimentally that a suspension of *E. coli* passing through a micro-fluidic channel with a funnel-like constriction displays anomalous dispersion properties, which allows ro control a bacterial concentration profile just by manipulating the flow intensity or its direction.

A crucial element here is the presence of bacterial motion at the walls, which features may differ significantly in magnitude and even in direction from the mean bacterial motion in the bulk. As a consequence, the typical sojourn times can be extremely long with respect to the bulk transport time for the channel dimensions. This has direct consequences on the spatial distribution of bacteria under flow and could impact more generally our vision of bacterial transport in porous and in confined media. Due to large hydrodynamic stresses, the presence of a constriction is forcing locally the desorption of the bacteria moving at the wall and then modifies the balance of adsorption/desorption processes in the down stream direction over large distances. The phenomenon we have reported here is essentially due to the active character of the suspension and cannot be assimilated to the straining effects described when filtering colloidal suspensions .We have shown that taking into account this non local process as a conservative bulk source term, we can reproduce without free fitting parameters, the mean concentration distribution of the bacteria along the channel.

In the future, it seems important to quantify the sojourn time and the motion of the bacteria at the walls under flow, as a

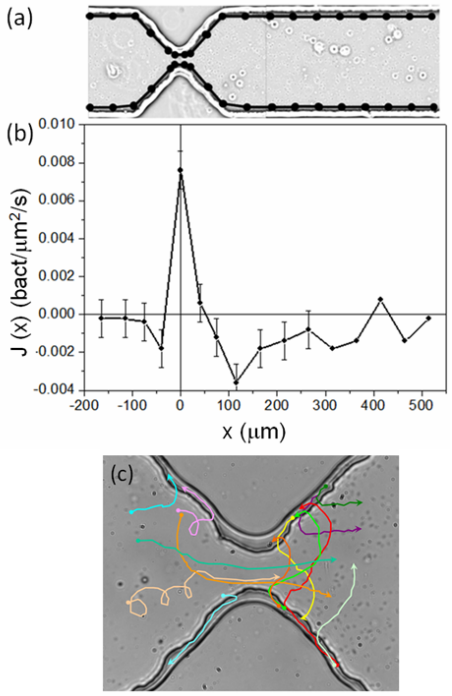

Fig. 5 (a) Snapshot of the funnel area on which are superposed the segments used to count number of bacteria crossing in and out the lateral walls in order to defined the transverse fluxes. Each segment is of approximately 50μm -length (except in the constriction area where they are shorter). (b) Plot of the transverse flux $J(x)$) corresponding to number of bacteria crossing the segments in/out of the walls per unit time. Note that when $J(x) > 0$, bacteria desorption dominates and when $J(x) < 0$, absorption dominates. At distances bigger than 2000 μm to the right, the net flow is zero. (c) Zoom on the funnel area with 10 trajectories handtracked during 4 seconds. The mean flow is $25\mu m/s$.

function of the geometry of the micro-fluidic channel. Our results also open the possibility to control hydrodynamically the concentration and delivery of motile bacteria depending on their activity, but this will be the subject of a future report.

6 Acknowledgments

E.A. and G.M have contributed equally to this work as far as data collection, analysis and final discussion are concerned and thus should share formally the first author position in the authors list.

We thank H. Berthet, F. Monti and M. Hoyos for help in the microchannels fabrication, J. C. Carrillo help on tracking and O. Ramos and I. Galperin for useful discussions. We acknowledge financial support from the Pierre-Gilles de Gennes Foundation, Sesame Ile-de-France and the ESPCI for a Joliot-Curie invited chair.

References

1 A.Baskarana and M.C.Marchetti, Statistical mechanics and hydrodynamics of bacterial suspensions, PNAS **106**, 15567 (2009).

2 D.L. Koch and G Subramanian, Collective hydrodynamics of swimming micro-organisms: Living fluids, Ann. Rev. Fluid Mech., 43, 637 - 659 (2011).

3 M.F. Copeland and D.B. Weibel, Bacterial swarming: a model system for studying dynamic self-assembly, Soft Matter 5, 1174-1187 (2009).

4 X.-L. Wu and A. Libchaber, Particle Diffusion in a Quasi-Two-Dimensional Bacterial Bath, Phys. Rev. Lett. **84**, 3017 (2000).

5 G. Miño, T. E. Mallouk, T. Darnigue, M. Hoyos, J. Dauchet, J. Dunstan, R. Soto, Y. Wang, A. Rousselet and E. Clément, Enhanced Diffusion due to Active Swimmers at a Solid Surface, Phys. Rev. Lett. **106**, 048102 (2011).

6 J. Dunkel, V. B. Putz, I. M. Zaid and J. M. Yeomans, Swimmer-tracer scattering at low Reynolds number, Soft Matter,6, 4268-4276, , (2010).

7 A. Sokolov and Aranson I., Reduction of Viscosity in Suspension of Swimming Bacteria, Phys. Rev. Lett 103, 148101 (2009). D.Saintillan, The dilute rheology of swimming suspensions, Model Exp. Mech., 50, 1275 (2010).

8 S. Rafaï, L. Jibuti, and P. Peyla, Effective viscosity of microswimmer suspensions, Phys. Rev. Lett. **104**, 098102 (2010).

9 M.J. Kim and K.S.Breuer, Controlled mixing in microfluidic systems using bacterial chemotaxis, Analytical Chemistry **79** 955 (2007).

10 C. Dombrowski, L. Cisneros, S. Chatkew, R. E. Goldstein, J. O. Kressler, Self-concentration and large-scale coherence in bacterial dynamics, Phys. Rev. Lett. **93**, 098103(2004).

11 Sokolov et al. PNAS **107**, 969 (2009); Di Leonardo et al. PNAS **107** 9541 (2010).

12 G. M. Hornberger, A. L. Mills, and J. S. Herman, Bacterial transport in porous media: evaluation of a model using laboratory observations, Water Resources Research **28**, 915-938 (1992).

13 S.A. Bradford, J. Simunek and S. L. Walker, Transport and straining of E. coli O157:H7 in saturated porous media, Water Resources Research. **42**, W12S12 (2006).

14 H. C. Berg *E. coli in Motion* (Verlag, New York, 2004).

15 N. C. Darnton, L. Turner, S. Rojevsky, H. C. Berg, On torque and tumbling in swimming Escherichia coli, *J. Bacteriology*, **189**, 1756 (2007).

16 E. Korobkova, T. Emonet, J. M. G. Vilar, T. S. Shimizu, P. Cluzel, From molecular noise to behavioral variability in a single bacterium, Nature **428**, 574 (2004).
17 P. D. Frymier et al., 3-Dimensional tracking of motile bacteria near a solid planar surface, Proc. Natl. Acad. Sci. U.S.A. 92, 6195 (1995).
18 E. Lauga, W. R. DiLuzio, G. M. Whitesides, H. A. Stone, Biophys. J. Swimming in Circles: Motion of Bacteria near Solid Boundaries **90**, 400 (2006).
19 S. van Teeffelen , U. Zimmermann and H. Loswen, Clockwise-directional circle swimmer moves counter-clockwise in Petri dish- and ring-like confinements, Soft Matter,5, 4510-4519 (2009).
20 G. Li, and J. X. Tang, Accumulation of Microswimmers near a Surface Mediated by Collision and Rotational Brownian Motion Phys.Rev.lett 103, 078101 (2009).
21 K. Drescher, J. Dunkel, L. H. Cisneros, S. Ganguly, R. E. Goldstein , Fluid dynamics and noise in bacterial cell-cell and cell-surface scattering PNAS **108**, 10940 (2011).
22 P. Galajda, J. Kleymer,, P. Chaikin, R. Austin, A wall of funnels concentrates swimming bacteria, J. Bacteriol. **189**, 8704 (2007).
23 E. Hulme, W. R. DiLuizio, S. S. Shevkoplyas, C. Turner, M. Mayer, H. C. Berg, G. M. Whitesides, Using ratchets and sorters to fractionate motile cells of Escherichia coli by length LabChip, **8**, 1888 (2008).
24 J. Hill, O. Kalkanci, J. L. McMurry, H. Koser, Hydrodynamic surface interactions enable Escherichia coli to seek efficient routes to swim upstream, Phys. Rev. Lett. **98**, 068101 (2007).
25 T. Ahmed and R. Stocker, Experimental verification of the behavioral foundation of bacterial transport parameters using microfluidics, Biophysical Journal. **95**, 4481-4493 (2008).
26 D. Genovese and J. Sprakel, Crystallization and intermittent dynamics in constricted microfluidic flows of dense suspensions, Soft Matter. **7**, 3889-3896 (2011).
27 C. T. Archer, J. F. Kim, H. Jeong, J. H. Park, C. E. Vickers, S. Y. Lee, L. K. Nielsen. The genome sequence of E. coli W (ATCC 9637): comparative genome analysis and an improved genome-scale reconstruction of E. coli, BMC Genomics, **12**:9 (2011).
28 B.M. Prüβ, P. Matsumura, Cell cycle regulation of flagellar genes, J. Bacteriol. **179**, 5602 (1997).
29 T. Minamino, Y. Imae, F. Oosawa, Y. Kobayashi, and K. Oosawa, Effect of Intracellular pH on Rotational Speed of Bacterial Flagellar Motors, Journal of Bacteriology, **185**, 1190-1194 (2003).

Induced Diffusion of Tracers in a Bacterial Suspension: Theory and Experiments

G. L. MIÑO[1], J. DUNSTAN[2,3], A. ROUSSELET[1], E. CLÉMENT[1], AND R. SOTO[2] †

[1]PMMH-ESPCI, UMR 7636 CNRS-ESPCI-Université Paris 6 and Paris 7, 10 rue Vauquelin, 75005 Paris, France

[2]Departamento de Física, FCFM, Universidad de Chile, Casilla 487-3, Santiago, Chile

[3]Department of Applied Mathematics and Theoretical Physics, University of Cambridge, Wilberforce Road, Cambridge CB3 0WA, UK

(Received ?; revised ?; accepted ?. - To be entered by editorial office)

The induced diffusion of tracers in a bacterial suspension is studied theoretically and experimentally at low bacterial concentrations. Considering the swimmer-tracer hydrodynamic interactions at low-Reynolds number and using a kinetic theory approach, it is shown that the induced diffusion coefficient is proportional to the swimmer concentration, their mean velocity and a coefficient β, as observed experimentally. The coefficient β scales as the tracer-swimmer cross section times the mean square displacement produced by single scatterings. The displacements depend on the swimmer propulsion forces. Considering simple swimmer models (acting on the fluid as two monopoles or as a force dipole) it is shown that β increases for decreasing swimming efficiencies. Close to solid surfaces the swimming efficiency degrades and, consequently, the induced diffusion increase. Experiments on W wild-type *Escherichia coli* in a Hele-Shaw cell under buoyant conditions are performed to measure the induced diffusion on tracers near surfaces. The modification of the suspension pH vary the swimmers' velocity in a wide range allowing to extract the β coefficient with precision. It is found that the solid surfaces modify the induced diffusion: decreasing the confinement height of the cell, β increases by a factor 4. The theoretical model reproduces this increase although there are quantitative differences, probably attributed to the simplicity of the swimmer models.

Key words: bacterial suspension, confinement, passive particle diffusion.

1. Introduction

An active suspension is a fluid containing autonomous swimmers such a bacteria, algae or artificial self-propelled entities. In general, the presence of active swimmers changes the mechanical picture usually considered for passive suspension problems. When an organism swims, it interacts with the surrounding medium (i. e., the suspending fluid, other swimmers in the fluid and also the boundaries of the system). Consequently, balances of momentum and energy as well as the constitutive transport properties, are deeply modified by the momentum sources distributed in the bulk. When a microscopic cell swims in a fluid, usually viscous forces dominates the inertial terms, which is evidenced if we compare these two magnitudes by computing the Reynolds number $\mathrm{Re} = \frac{\rho V L}{\eta}$,

† Email address for correspondence: rsoto@dfi.uchile.cl

where V is a typical velocity, L a typical length, and ρ and η are the density and the dynamic viscosity of the fluid, respectively. Swimmers, such as bacteria, with a typical length of $1\,\mu$m, and a propulsion velocity $V = 20\,\mu$m/s moving in water ($\rho = 1\,\mathrm{g/cm^3}$ and $\eta = 10^{-2}\,\mathrm{g/cm{\cdot}s}$), leads to a Reynolds number in the order of 10^{-5} (Purcell 1977). Under these conditions, autonomic propulsion is assured only if the time reversibility is broken during the motion (Purcell 1977; Golestanian & Ajdari 2008).

Since the swimming motion has no inertia, the total force and torque exerted by the swimmer on the fluid vanish. Therefore, the leading long range hydrodynamic flow produced by a single swimmer should be governed at most by a dipole force. As a consequence, depending on the dipole polarity, many micro-organisms can be classified under two categories: "pushers" and "pullers", depending if the dipole is tensile or contractile, respectively (Hernandez-Ortiz *et al.* 2005; Saintillan & Shelley 2007; Baskaran & Marchetti 2009). From this point of view, *Escherichia coli* or *Bacillus subtilis* can be classified as pushers and algae such as *Chlamydomonas reinhardtii* as pullers.

Escherichia coli (*E. coli*) represents a good example of self-propelled swimmer. This widely studied bacterium will represent the active component in the solution studied in this work. *E. coli* is a cylindrical cell with hemispherical endcaps, with $1\,\mu$m diameter and $2\,\mu$m length (Berg 2000*b*, 2004). The motion is the consequence of the rotation of several helicoidal flagella, where each flagellum is linked to the cell membrane by a nanoscale motor. When all the motors turn in a counterclockwise (CCW) direction, the flagella rotates in a bundle and this pushes the cell steadily forward (what is called "run"). When the motor rotation switches to clockwise (CW), the cell can change direction (known as a "tumble" process). The mean run interval is typically 1 s, whereas the mean tumble time is around 0.1 s. The ratio between tumble and run depends upon the chemotactic signals (Berg 2000*a*). Due to the drag anisotropy on the helicoidal flagella, its rotation produces a net force that pushes the fluid backward, while the head pushes the fluid in the opposite direction (Purcell 1977; Lauga & Powers 2009). As consequence of the fluid incompressibility, the fluid is pulled toward the centre of the *E. coli* body, creating two toroidal vortices around it.

The induced motion of the fluid produced by swimming microorganisms can be measured indirectly by observing the induced motion of tracers dispersed in the fluid. The seminal work addressing the effect of active suspension on the enhancement of passive tracers diffusivity, was presented by Wu & Libchaber (2000). They conducted an interesting experiment: wild-type *E. coli* as well as 4.5 and $10\,\mu$m diameter particles were trapped in a thin film (see Wu & Libchaber 2000, figures 2 and 3). When looking at the passive tracers, they found the presence of superdiffusion for $t < t_c$ and normal diffusion for $t > t_c$, where t_c is a characteristic time representing the lifetime of coherent structures in the sample. They also studied the influence of the bacterial concentration in the diffusion of $10\,\mu$m diameter particles, showing the diffusion of these particles increases linearly with the bacterial concentration. They suggested that this effect could be related to the spontaneous formation of swirls in the bacterial bath. In 2009, Leptos *et al.* studied the enhancement of tracers diffusion into an aqueous medium, for a puller type swimmer. They used *Chlamydomonas reinhardtii* as the active component of the solution and $2\,\mu$m diameter beads as passive tracers. Their observation was performed far from the wall and they show a linear increase of the tracers diffusion with the volume fraction ϕ. They found that the effective diffusivity D_{eff} for the passive tracers can be written as $D_{\mathrm{eff}} = D_B + \alpha\phi$, where D_B is the Brownian diffusion value in the bulk (without swimmers) and, α can be defined (from dimensional analysis) as $\alpha = U^2\tau = Ul$ (where U, τ and l represent a characteristic advective velocity, encounter time, and advective length, respectively). In a recent work presented by Wilson *et al.* (2011), Differential Dy-

namic Microscopy (DDM) was applied to characterised the bacterial motion in *E. coli* suspensions. They show that the diffusion of non-motile bacteria is enhanced with the active fraction, given by the proportion of active swimmers, also establishing a linear relationship between these two quantities.

In 2011, we presented results obtained for passive particles near a solid surface in a bacterial suspension of density n under non-buoyant conditions (Miño *et al.* 2011). We were able to distinguish two kind of bacterial motion: bacteria that exert a random motion and those that move in ballistic way, called active swimmers. From this separation of populations sorted according to their motion, one can define a fraction of active swimmers ϕ_A, and their mean velocity V_A. To characterise the activity at the surface we define the "active flux" $J_A = n_A V_A$, where $n_A = n\phi_A$ is the active concentration. Systematic experiments varying the bacteria concentration were done for two tracer sizes and in each case the mean diffusion of the passive tracer D_P was obtained. Interestingly all data seem to group on a straight line

$$D_P = D_P^B + \beta J_A, \tag{1.1}$$

where D_P^B is the Brownian diffusivity close the wall in the absence of bacteria. The parameter β represents the slope that can be determined experimentally by a linear fit. A dimensional analysis of the equation (1.1) yields that this pre-factor is a length to the power 4.

In the present work we present a kinetic theory analysis considering the swimmer-tracer hydrodynamic interactions, that explains the observed dependence of D_P on V_A and n_A, and provide an expression for β. When a tracer is placed in the suspension, the swimmer-tracer scattering produce a net displacement that, as a consequence of the low-Reynolds number hydrodynamics as will be demonstrated in Sec. 2, is independent on the swimmer velocity. In kinetic theory, the diffusion coefficient can be computed as the collision frequency times the net displacement squared. On the other hand, the collision frequency is proportional to the swimmer concentration, their mean speed and the cross section. Putting all together, results in an expression like (1.1). The β coefficient scales, then, as the cross section times the average displacement squared. As a result of the analysis, it turns out that an enhancement of the induced diffusion can be obtained near solid surfaces, calculations that are performed in Sec. 3. Controlled experiments near solid surfaces, in which bacterial batches with different swimming speeds are prepared, are described in Sec. 4 showing the predicted enhancement of the diffusion near the solid surface and under confinement. The numerical comparison show good qualitative agreement. Finally, conclusions are presented in Sec. 5.

2. Induced diffusion in the bulk

Self-propelled objects agitate the fluid when they swim and, therefore, a passive object placed nearby will be transported by the fluid. At low Reynolds number, the transport is passive with no inertial delay. The experiments described in the Introduction and the new ones described in Sec. 4 show that, at low volume fraction, the induced diffusion is proportional to the swimmer concentration. This result implies that it should be possible to understand the induced diffusion as the additive effect of the interaction of the tracer with individual swimmers. Swimmer-swimmer interactions or the collective motion of the swimmers would lead to higher order contributions in the concentration to the induced diffusion. The hydrodynamic interaction of passive tracers with a single swimmer was studied in detail by Dunkel *et al.* (2010). They showed that in the scattering process, the

tracer trajectories are loop-shaped, almost closed, with small total displacements. Here we consider the effect of these scattering processes in the induced diffusion of the tracers.

Two simple swimmer models will be considered in order to compute the induced diffusion on passive objects. At low Reynolds number, swimmers have no inertia and the net force and torque acting on them vanish. As a first approximation, a swimmer can be modelled as a force dipole. The second, more refined, model consists of two force monopoles separated by a finite distance, representing the head and tail of the swimmer.

The Stokes equations allow to obtain the fluid velocity at a point $\mathbf{r}$ produced by a force monopole $\mathbf{F}$ located at $\mathbf{r}'$

$$u_i(\mathbf{r}) = J_{ij}(\mathbf{r}' - \mathbf{r})F_j, \tag{2.1}$$

where i and j indicate the Cartesian coordinates, J is the Ossen tensor

$$J_{ij}(\mathbf{r}) = \frac{1}{8\pi\eta}\widehat{J}_{ij}(\mathbf{r}) = \frac{1}{8\pi\eta}\frac{1}{r}\left(\delta_{ij} + \frac{r_i r_j}{r^2}\right), \tag{2.2}$$

δ_{ij} is the Kronecker symbol, η is the fluid viscosity and the Einstein summation notation is used throughout the text (Happel & Brenner 1965; Kim & Karilla 2005). Thanks to the linearity of the Stokes equations, the velocity field produced by a force distribution is simple obtained by summing the different contributions to the fluid velocity. Then, two monopoles located at $\mathbf{r}_B \pm a\,\widehat{\mathbf{n}}/2$ (that is, centred at $\mathbf{r}_B$ and separated by a in the direction $\widehat{\mathbf{n}}$) produce a velocity field

$$u_i(\mathbf{r}) = \left[J_{ij}(\mathbf{r}_B + a\,\widehat{\mathbf{n}}/2 - \mathbf{r}) - J_{ij}(\mathbf{r}_B - a\,\widehat{\mathbf{n}}/2 - \mathbf{r})\right] F_j, \tag{2.3}$$

that in the dipolar limit reduces to

$$u_i(\mathbf{r}) = J_{ij,k}(\mathbf{r}_B - \mathbf{r})aF_j n_k, \tag{2.4}$$

where $J_{ij,k}$ is the gradient of the Oseen tensor in the direction k

$$J_{ij,k}(\mathbf{r}) = -\frac{1}{8\pi\eta}\left(\frac{\delta_{ij}r_k - \delta_{ik}r_j - \delta_{jk}r_i}{r^3} + 3\frac{r_i r_j r_k}{r^5}\right). \tag{2.5}$$

When a passive tracer is placed in the vicinity of a swimmer, it will move with a velocity equals to the fluid velocity at its centre, corrected by the Faxén contribution (Happel & Brenner 1965; Kim & Karilla 2005). This Faxén correction is proportional to the tracer radius squared and the Laplacian of the fluid velocity. In the experiments reported in Miño *et al.* (2011) the induced diffusivity does not present dependence on the tracer size for particle diameters of 1μm and 2μm, showing that in this regime the particle displacements are dominated by the fluid velocity at their center and the Faxén correction is subdominant. Accordingly, in what follows we will consider point-like tracers and the Faxén correction will be neglected. If precise calculations were needed, this correction should be added when the tracer and the swimmer are close, in which case the velocity field changes rapidly, but if this would be the case, also a more refined swimmer model would be necessary. Then, the instantaneous tracer velocity is the fluid velocity at its position given either by (2.3) or (2.4). The tracer motion can be made non-dimensional by the following choice of dimensions: lengths are scaled by the swimmer size a, $\widetilde{r} = r/a$, and dimensionless time $\widetilde{t}$ is defined in terms of the swimmer velocity V_B by $\widetilde{t} = ta/V_B$. The resulting tracer equation of motion is

$$\frac{d\widetilde{r}_i}{d\widetilde{t}} = \gamma^{-1}G_i(\widetilde{\mathbf{r}}_B - \widetilde{\mathbf{r}}), \tag{2.6}$$

where the dimensionless parameter

$$\gamma = 8\pi V_B a\eta/F \tag{2.7}$$

is a measure of the swimming efficiency and

$$G_i^{\text{monopoles}}(\mathbf{x}) = \left[\widehat{J}_{ij}(\mathbf{x}+\widehat{\mathbf{n}}/2) - \widehat{J}_{ij}(\mathbf{x}-\widehat{\mathbf{n}}/2)\right] n_j \tag{2.8}$$

$$G_i^{\text{dipole}}(\mathbf{x}) = \widehat{J}_{ij,k}(\mathbf{x}) n_j n_k. \tag{2.9}$$

We have assumed, as it is usually the case, that the direction of the force is parallel to $\widehat{\mathbf{n}}$, with $\mathbf{F} = F\widehat{\mathbf{n}}$. Therefore, F and γ are positive (negative) for pushers (pullers).

It is worth noticing that the swimming efficiency γ depends on the geometry of the swimmer but it does not depend directly on the fluid viscosity or the activity of the swimmer (e.g. the flagella rotation speed for *E. coli*). Indeed, if the swimmer increases its activity, by the linearity of the Stokes equations, it will swim more rapidly keeping γ unchanged. Also, if the activity is fixed, and the swimmer is placed in a more viscous fluid, its swimming velocity will decrease and γ is not modified. In the case of *E. coli* in water, using the typical velocity of $V_b = 20\,\mu$m/s (Berg 2004), the measured dipole distance $a = 2\,\mu$m (Drescher *et al.* 2011), and a fitted value $F = 1.13\,$pN, calculated by Dunstan *et al.* (2012) using a two-sphere model, it gives an efficiency of $\gamma_{E.coli} = 0.89$. The swimming efficiency changes, however, close to fixed solid surfaces where, for a fixed force, the swimmer moves slower than in the bulk. This issue will be exploited in Sect. 3 as it will be shown to increase the induced diffusion. There is, finally, the possibility that dynamically the swimmer changes its efficiency when moving in a more viscous fluid. Indeed, it has been reported that increasing the viscosity, some bacteria swim faster, effect that is explained by a modification of the flagella geometry due to a balance of elastic and viscous stresses (Shneider & Doetsch 1974; Atsumi *et al.* 1996; Chattopadhyay *et al.* 2006). To simplify the analysis and because we have no evidence that there are conformational changes in our experiments, we will assume that the geometry remains fixed.

To integrate Eq. (2.6) the swimmer motion must be specified. As the dipolar interaction decays at large distances, the swimmer motion can be assumed to be in a straight line, with constant speed, during all the scattering process. That is, we neglect the circular motion bacteria perform near surfaces and, consistently, the torque dipole created by the rotation of the head and flagella are neglected as well. Finally, we neglect tumbling during the scattering process. As usual when describing scattering processes, the swimmer trajectory is parametrized by the direction of motion $\widehat{\mathbf{n}}$, the dimensionless impact parameter $\widetilde{b} = b/a$ and the azimuthal angle θ, that define completely the vector $\widetilde{\mathbf{b}}$ that goes from the initial position of the tracer to the point of minimal approach of the swimmer trajectory (see Fig. 1). Then, the full swimmer trajectory in dimensionless units is parametrized by $\widetilde{\mathbf{r}}_B = \widetilde{t}\widehat{\mathbf{n}} + \widetilde{\mathbf{b}}$, with $-\infty < \widetilde{t} < \infty$, and the origin has been placed at the initial position of the tracer. Then, the tracer equation of motion reduces to

$$\frac{d\widetilde{r}_i}{d\widetilde{t}} = \gamma^{-1} G_i(t\widehat{\mathbf{n}} + \widetilde{\mathbf{b}} - \widetilde{\mathbf{x}}). \tag{2.10}$$

Figure 2 shows typical trajectories of tracers for both models. They show the loop-shape also described in Dunkel *et al.* (2010) for a different model. The net dimensionless displacement

$$\widetilde{\Delta}_i = \widetilde{r}_i(+\infty) - \widetilde{r}_i(-\infty) = \gamma^{-1} \int_{-\infty}^{\infty} d\widetilde{t}\, G_i(\widetilde{t}\widehat{\mathbf{n}} + \widetilde{\mathbf{b}} - \widetilde{\mathbf{r}}(\widetilde{t})) \tag{2.11}$$

is small, effect that can be understood when doing a formal expansion of the equation of

FIGURE 1. Parameters describing the scattering geometry between a swimmer (solid circle) and a tracer (open circle) in the bulk (Left) and close to a solid surface (Right). The swimmer moves in the $\hat{\mathbf{n}}$ direction (parallel to the surface when close to it). The vector $\mathbf{b}$ points from the initial position of the tracer to the position of minimal approach of the straight trajectory and its magnitude is b, the impact parameter. Close to a solid surface, the tracer initial height is z_T, the angle θ gives the horizontal displacement of the swimmer trajectory with respect to the initial position of the tracer and the height of the swimmer is z_B.

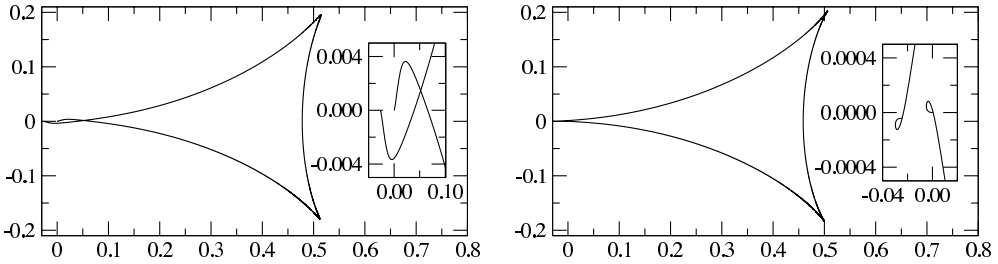

FIGURE 2. Tracer trajectory that starts at the origin produced by the scattering with a swimmer that moves along the x axis from left to right, above the tracer. The dimensionless impact parameter is $\widetilde{b} = 2$, the swimmer efficiency is $\gamma = 1$ and the swimmer model is that of two monopoles (Left) and one dipole (Right). The insets show a zoom near the origin to put in evidence the small displacements. In both cases, the tracer moves left and down.

motion for small tracer displacements

$$\widetilde{\Delta}_i = \gamma^{-1} \int_{-\infty}^{\infty} d\widetilde{t}\, G_i(\widetilde{t}\hat{\mathbf{n}} + \widetilde{\mathbf{b}}) - \gamma^{-2} \int_{-\infty}^{\infty} d\widetilde{t}_1\, G_{i,j}(\widetilde{t}_1\hat{\mathbf{n}} + \widetilde{\mathbf{b}}) \int_{-\infty}^{\widetilde{t}_1} d\widetilde{t}_2\, G_j(\widetilde{t}_2\hat{\mathbf{n}} + \widetilde{\mathbf{b}}) + \mathcal{O}(\gamma^{-3}).$$

It can be directly verified that the first integral in the expansion cancels both in the case of two monopoles or a dipole. Indeed, this integral corresponds to using the velocity field at a fixed position and, as a result of the head and tail pushing in opposite directions, the effect of the head and the tail cancel and the total induced displacement vanishes.

Then, the first contribution to net displacement is proportional to γ^{-2}. Figure 3 shows the net displacement computed by numerical integration of Eq. (2.10) for the two models and two values of b as a function of γ. The dependence $\Delta \sim \gamma^{-2}$ is obtained from $\gamma \gtrsim 0.5$ and not only in the asymptotic regime of large efficiencies. At smaller values of γ or small impact parameters, the displacements are large and the tracer approaches the swimmer to the core of the singularities, making predictions not to be trusted. In those cases, more refined swimmer models should be used. Note that the net displacement does not depend on the sign of γ at least in the dominant term. Therefore, there is no difference between pushers and pullers as far as the net displacement of tracers is concerned. We finally remind that the net displacement depends only on $\widetilde{b}$ and γ and is independent on the swimmer force or velocity.

Now, considering a tracer in a low concentration suspension of swimmers, the different scattering processes can be studied separately and the total tracer displacement results

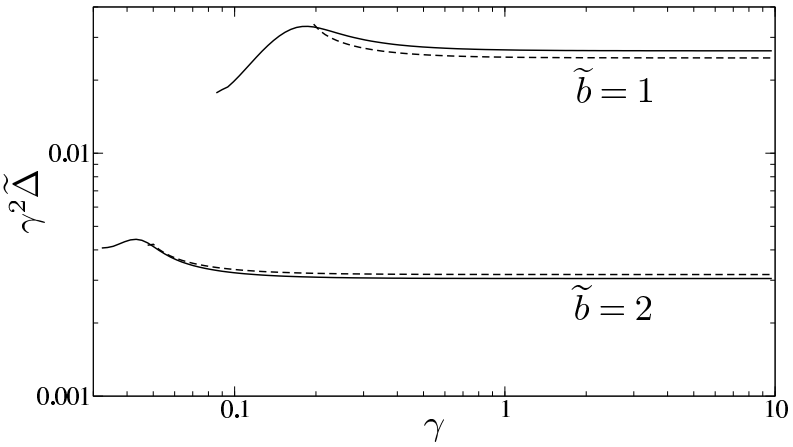

FIGURE 3. Net dimensionless displacements $\widetilde{\Delta}$ times γ^2 as a function of the swimmer efficiency γ for two impact parameters: $\widetilde{b} = 1$ and $\widetilde{b} = 2$. Two swimmer models are considerer: two monopoles (solid line) and a dipole (dashed line).

in the vectorial sum of the sequence of displacements. Let's call $\mathbf{\Delta}^{(n)}$ the displacement vector produced in the n-th encounter, then the mean square displacement up the n-th encounter is

$$\langle \Delta R^2 \rangle = \left\langle \left| \sum_{m \leqslant n} \mathbf{\Delta}^{(m)} \right|^2 \right\rangle . \tag{2.12}$$

Assuming that subsequent swimmers move in uncorrelated directions, the cross averages vanish, resulting in

$$\langle \Delta R^2 \rangle = \left\langle \sum_{m \leqslant n} \left| \mathbf{\Delta}^{(m)} \right|^2 \right\rangle = a^2 \left\langle \sum_{m \leqslant n} \widetilde{\Delta}^2 (\widetilde{b}^{(m)}, \gamma^{(m)}) \right\rangle , \tag{2.13}$$

where $\widetilde{b}^{(m)}$ and $\gamma^{(m)}$ describe the m-th encounter, and the a^2 factor appears when substituting $\Delta = a\widetilde{\Delta}$.

To compute the averages, we assume that swimmers are described by a distribution function f such that $f(\widehat{\mathbf{n}}, F, \gamma)\, d^2\widehat{\mathbf{n}}\, dF\, d\gamma$ is the number of swimmers per unit volume that swim along the direction $\widehat{\mathbf{n}}$, with a force F, and an efficiency γ. We assume that, in general, the swimmers in the suspension can have different efficiencies and can swim also at different velocities. The tracer induced diffusion coefficient equals one sixth the time derivative of the mean square displacement, averaged over the incoming flux of swimmers $V f(\widehat{\mathbf{n}}, F, \gamma)$ and the impact parameters

$$\begin{aligned} D &= \frac{1}{6} \frac{d}{dt} \langle \Delta R^2 \rangle = \frac{1}{6} \int \Delta^2(b, \gamma) f(\widehat{\mathbf{n}}, F, \gamma) V\, b\, db\, d\theta\, d^2\widehat{\mathbf{n}}\, dF\, d\gamma \\ &= \frac{a^4}{6} \int \widetilde{\Delta}^2(\widetilde{b}, \gamma) f(\widehat{\mathbf{n}}, F, \gamma) V\, \widetilde{b}\, d\widetilde{b}\, d\theta\, d^2\widehat{\mathbf{n}}\, dF\, d\gamma. \end{aligned} \tag{2.14}$$

If all swimmers have the same efficiency γ_0 the previous expression simplifies to

$$D = n \langle V \rangle \beta, \tag{2.15}$$

with

$$\beta = \frac{a^4}{6} \int \widetilde{\Delta}^2(\widetilde{b}, \gamma_0)\, \widetilde{b}\, d\widetilde{b}\, d\theta, \tag{2.16}$$

where $n = \int f(\widehat{\mathbf{n}}, F, \gamma)\, d^2\widehat{\mathbf{n}}\, dF\, d\gamma$ is the swimmer concentration and $\langle V \rangle$ is the average velocity in the swimmer sample. The coefficient β can be written as

$$\beta = \langle \Delta^2 \rangle \sigma / 6, \tag{2.17}$$

proportional to the product of the cross section σ and the average square displacement over this cross section, which has been shown to be typically small. Therefore $\beta^{1/4}$ should not be understood as a single length scale.

As has been noted above, the net displacement is roughly proportional to γ^{-2} and therefore the diffusion coefficient is proportional to γ^{-4}. More inefficient swimmers produce larger displacements and, therefore, larger diffusion coefficients. The rationale behind this is that at low Reynolds number, the flow field and the induced displacement are proportional to the swimmer force. On the other hand, the net displacement is proportional to the total interaction time, that is inversely proportional to the swimmer speed. Therefore, a slower swimmer, exerting the same force will induce larger displacements because the interaction time increases.

To compute numerically the coefficient β a cutoff distance, $b_{\min}$ should be included in the impact parameter: physically, swimmers have a transverse radius that impose a minimal impact parameter and, in the models (2.8) and (2.9), a minimal distance should be included to not approach the singularity core. Then, $\Delta(b)$ is computed by numerically integrating the differential equation (2.10) and the coefficient β is then obtained from Eq. (2.16). As the displacements are larger for smaller impact parameter, the final value of β depends singnificantly on $b_{\min}$ and a sensible election should be made.

In the case of *E. coli*, $\gamma = 0.89$, and the tracers do not reach the singularity cores for impact parameters larger than $\widetilde{b} = 0.75$ in the case of the swimmer modelled as two monopoles and $\widetilde{b} = 1.0$ in the case of the dipole model. These values, which are close to the bacterial radius, are chosen as the cutoff impact parameters. The resulting coefficients are $\beta^{\text{dipole}}/a^4 = 0.030$ ($\beta = 0.48\,\mu\text{m}$)^4 and $\beta^{\text{monopoles}}/a^4 = 0.088$ ($\beta^{\text{monopoles}} = 1.40\,\mu\text{m}$)^4, where $a = 2\,\mu$m has been used.

As it is discussed in Sec. 4, under our experimental methodology is not possible to extract a value for β in the bulk to compare with the theoretical predictions. On the other hand, analysis of the experimental results on *Chlamydomonas reinhardtii* by Leptos *et al.* (2009) allows to estimate $\beta^{\text{C.r. bulk}} = (5.5 \pm 0.7\,\mu\text{m})^4$. This value, however, cannot be compared with the predictions of the simple swimmer models described here, that do not consider the time dependence of the flow produced by this alga and the higher multipole moments needed to accurately describe the near flow (Drescher *et al.* 2010; Guasto *et al.* 2010).

3. Effect of a solid boundary

Near a solid boundary, swimmers decrease their swimming efficiency due to hydrodynamic hindrance. Lubrication forces and far-field images modify the drag coefficient parallel to the wall such that the swimming speed is

$$V_B = \alpha(z_B) V_{B0}, \tag{3.1}$$

where V_{B0} is the swimmer velocity in the bulk, z_B is the distance of the swimmer to the surface and α is the parallel drag correction factor, that vanishes when the swimmer gets

in contact with the surface and goes asymptotically to 1 at large distances (Brenner 1961; Goldman *et al.* 1967; Holmqvist *et al.* 2006; Huang & Breuer 2007). According to Eq. (2.7), the swimmer efficiency is modified by the drag with the wall as $\gamma(z_B) = \alpha(z_B)\gamma_0$, where γ_0 is the efficiency in the bulk. Therefore, close to a solid surface, the diffusion coefficient should increase by a factor α^{-4}.

There are, however, other effects that should be considered close to a surface that can either increase or decrease the diffusion coefficient. First, it is known that *E.coli* and other pusher swimmers are attracted to and trapped by solid surfaces, and swim parallel to them for long time (Ramia *et al.* 1993; Frymier *et al.* 1995; Lauga *et al.* 2006; Berke *et al.* 2008; Li *et al.* 2008; Dunstan *et al.* 2012). Therefore, we consider trajectories that are parallel to the surface at a fixed height z_B and with planar orientation $\widehat{\mathbf{n}}$. Also, the experimental setups in Hele-Shaw geometries allow to measure the in-plane diffusion coefficient and, therefore, only the parallel components of $\mathbf{\Delta}$ should be considered.

The second aspect to be taken into account is geometrical: close to a surface, the cross section is reduced as swimmers must be above the surface. In the limiting case of a tracer in contact with the surface, the cross section is reduced by one half. We also take into account that there is a finite transverse swimmer radius r_{0B}, such that if z_T is the initial height of the tracer, the swimmer height is $z_B = z_T + b\cos\theta$ (see Fig. 1). The condition $z_B > r_{0B}$ limits the integration region in the b-θ space in Eq. (2.14).

Finally, the presence of the planar surface modifies the flow profile induced by the force distribution. Using the image method, Blake & Chwang (1974) obtained the solution for a force monopole, taking into account the non-slip boundary condition, therefore modifying the bulk solution (2.1). First, the flow field is smaller because momentum is dissipated by the surface and, second, the flow field is non-isotropic anymore and depends explicitly on the distance of the source to the solid surface. The flow produced by a force $\mathbf{F}$ evaluated at $\mathbf{r}_1 = (x_1, y_1, z_1)$, is

$$u_i(\mathbf{x}) = \frac{1}{8\pi\eta}\left[\left(\frac{\delta_{ij}}{r} + \frac{r_i r_j}{r^3}\right) - \left(\frac{\delta_{ij}}{\bar{r}} + \frac{\bar{r}_i \bar{r}_j}{\bar{r}^3}\right) \right.$$
$$\left. +2h(\delta_{jx}\delta_{kx} + \delta_{jy}\delta_{ky} - \delta_{jz}\delta_{kz})\frac{\partial}{\partial \bar{r}_k}\left\{\frac{h\bar{r}_i}{\bar{r}^3} - \left(\frac{\delta_{iz}}{\bar{r}} + \frac{\bar{r}_i\bar{r}_z}{\bar{r}^3}\right)\right\}\right] F_j, \qquad (3.2)$$

where $\mathbf{r}_2 = \{x_2, y_2, h\}$ is the position of the force point, $\mathbf{r} = \{x_1 - x_2, y_1 - y_2, z_1 - h\}$ is the vector from the singularity to the observation point, and $\bar{\mathbf{r}} = \{x_1 - x_2, y_1 - y_2, z_1 + h\}$ is the vector from the position of the image to the observation point. In the coordinate axes we are using, x and y are the planar directions and z is the perpendicular direction to the plane. This expression, simplified after using that the force is parallel to the surface, allows to obtain the tracer equation for the dipole and two-monopole models.

To study the consequence of these additional effects due to the surface, the β coefficient will be first computed without considering the modification of the swimmer efficiency close to the surface. Again, the dominant contribution to the net displacement goes as γ^{-2}, but the numerical integration of the tracer equation of motion gives two new features. First, if the tracer is close to the surface, the non-slip boundary condition included in Eq. (3.2) implies small velocities and therefore small displacements. But, the presence of the surface breaks the symmetry of the flow and, as a result, the trajectories depart more from closed loops as the back-and-forth motion is not symmetric. As a result, the net displacement can increase at a finite distance from the wall and then decreases to approach the bulk values. Integrating over the allowed impact parameters and azimuthal angles the β coefficient is obtained, which shows a maximum for a finite tracer height (see Figure 4). This unexpected result, obtained even in absence of the enhanced displacement

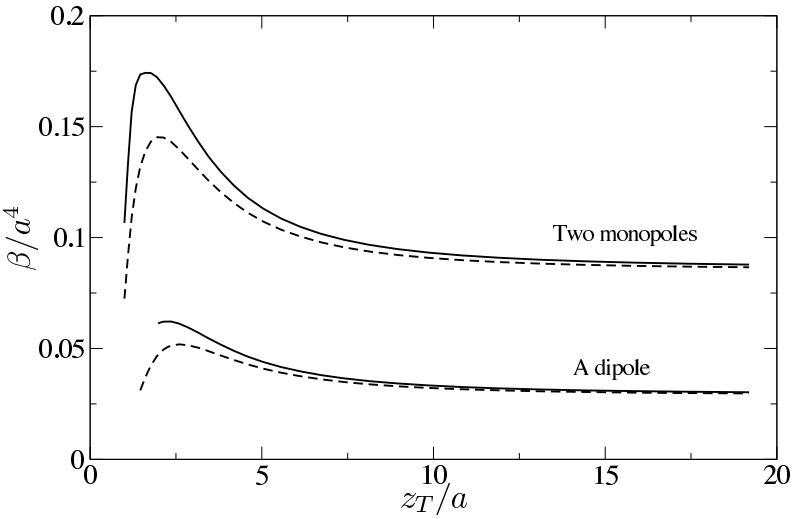

FIGURE 4. Effect of the tracer height, z_T, on the β value. Two swimmer models are considered: two monopoles and a dipole. The calculations are done considering the enhanced drag coefficient (solid line) or without it (dashed line). The numerical parameters are those that model the *E. coli*, that is, $a = 2\,\mu m$, $\gamma = 0.89$, $r_{0B}/a = 0.25$, and the cutoff impact parameter is $b_{\min}/a = 0.75$ for the two-monopole model and $b_{\min}/a = 1.0$ for the dipole model .

due to the swimmer inefficiency near walls shows that the perturbation of the loop-like trajectories compensates the other two effects near walls that tend to decrease the tracer displacement.

Finally, when the effect of the enhanced drag coefficient is included, the β coefficient also shows, with larger numerical values, first an increase of β with height, reaching a maximum value for a finite height, to further decrease for larger distances, approaching the bulk value. The results for both swimmer models are presented in Fig. 4 as a function of the tracer height z_T.

Considering the previously described numerical values to model the *E. coli* plus the bacterial radius of $r_{0B} = 0.5\,\mu$m, the maximal diffusivity is obtained when the tracer is located at a height $z_T \sim 4.7\,\mu$m. At this height β is increased by a factor 2 compared to the bulk value. That is, the induced diffusivity is doubled close to the surface. Both swimmer models, although producing qualitatively similar results, predict different values for β. In this respect, the two-monopole model [described by the singularity distribution in Eq. (2.8)] is more precise than the dipolar model as it gives a more detailed description of the near field (actually, as it was shown by Drescher *et al.* (2010) even three monopoles were necessary to describe in detail the near field produced by some microorganisms). Also, the two-monopole model allowed to use smaller cutoff values, implying larger displacements. In consequence, in what follows, we will concentrate only on the two-monopole model.

3.1. *Confinement by two solid walls*

Now we study the effect on induced diffusion in a confined geometry i.e. when the bacteria and the passive tracer are placed between two solid walls. This will correspond to a situation studied experimentally in the next chapter. The theoretical calculations are similar to the previous one. However they are slightly more involved because the image system for point forces between two parallel walls is complex, as the images reflect at the walls an infinite number of times, increasing the complexity of the image system

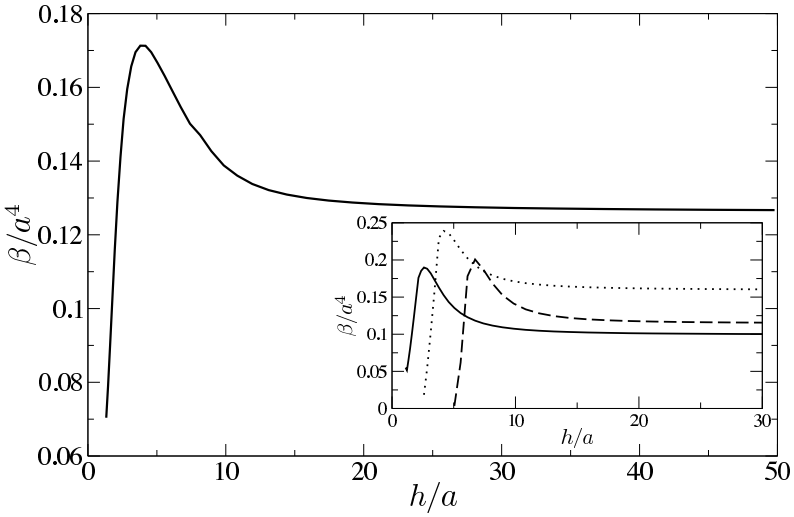

FIGURE 5. Effect of the confining height of the system h on the β value. The computations are done with the two-monopole model. The main figure shows the predicted values for a buoyant tracer averaged over the Boltzmann distribution of tracer heights. The inset shows the predicted values for fixed initial tracer heights: $z_T/a = 1$ (solid line), $z_T/a = 2.5$ (dotted line), and $z_T/a = 5$ (dashed line). The numerical parameters are those that model the *E. coli*, that is, $a = 2\,\mu m$, $\gamma = 0.89$, $r_{0B}/a = 0.25$, and the cutoff impact parameter $b_{\min}/a = 0.75$. To compute the Boltzmann averages, the mean tracer height is that of experiments $(k_B T/m^* g)/a = 1.85$.

at each reflection (Bhattacharya & Bławzdziewicz 2002). As a first approximation, we make only one reflection at each wall. That is, the image system presented in Eq. (3.2) is repeated for the top wall as well. The reflection on the top wall breaks the back-and-forth symmetry even more resulting in an increase of the net displacements compared to the case with just one surface.

The inset of Figure 5 shows the effect of the confinement height h on the β coefficient for different fixed tracer heights z_T. The main figure shows the effect of confinement averaged over the Boltzmann distribution of tracer heights with numerical values given by the experiments (details are given in Sec. 4). First, at short confinement heights, the induced diffusivity increases, reaching a maximum and later it decreases to reach the value of an unconfined system, subject only to the effect of the bottom surface. Both the maximum diffusivity and the height at which it is reached depend on the tracer height. In summary, it is predicted then that, close but not in contact to the solid surface, the induced diffusivity is enhanced under confinement in Hele-Shaw cells.

4. Experiments on enhanced diffusion

To test the theoretical predictions made previously, we performed series of experiments on passive tracers activated by swimming bacteria. The goal here is to test the validity of Eq. (1.1), varying the bacterial density and the mean velocity over a significant range. A crucial point in the previous report by Miño *et al.* (2011) was that a distinction has to be made between active swimmers performing ballistic trajectories and the non-active ones, displaying diffusive motion. Under these conditions, the effect of enhancement in the diffusion of passive tracers can be assessed quantitatively. In the bulk, because of the 3D motion, bacteria rapidly go out of focus, and there is not enough data to make the separation between the two populations. Consequently, we have restricted ourselves to

measure close to the surfaces where the separation between active and non-active bacteria can be made without ambiguity. Also, in the previous experiments, the dependence of the swimmer velocity on the diffusion coefficient was only investigated by taking bacteria at different stages of their life cycle i.e. the post division fast swimmers (1N cells) and the pre-division slow swimmers (2N cells). In this way, a factor 2 between the corresponding mean velocities was obtained. However, 1N and 2N populations have different shapes which from the previous theoretical analysis, can be a questionable issue since a change in shape would imply a change in the efficiency parameter γ. If there were a variability in γ then Eq. (1.1) is no longer valid and the diffusion coefficient is given instead by the more involved expression (2.14). Finally, the advantage of the present experiment is that by varying the swimming velocity, relation (1.1) can be studied more extensively.

Another question addressed in the theoretical sections is the influence of confinement, i.e. the presence of another surface limiting the height of the chamber. From the experiments it is possible to extract the effect of confinement in the Brownian diffusivity as well as in the enhanced diffusion due to the presence of bacteria.

The bacteria used here are Wild-type *E. coli* (ATCC 11105). They were grown and prepared following the protocol described in Appendix A.

Observation on the bacterial suspension was performed using a *Z1* inverted microscope from *Zeiss-Observer*. Images and videos were captured using a *Pixelink PL-A741-E* CCD digital camera, connected to and controlled by a computer which stores the images that will be post-processed. The CCD chip has a maximum resolution of 1024×1280 pixels^2 and can run at 10 frames/s full frame. To gain speed of acquisition, we reduced the visualisation field to 600×800 with a rate of 20 frames/s.

For experiments on induced diffusion, the principle is to follow the motion of passive particles in a bacterial suspension. A sketch of the chamber is shown in figure 7 (a). A 10 μl drop of the suspension containing the W wild-type *E. coli* bacteria (see Archer *et al.* 2011) and the tracer latex beads of diameter $d = 2\mu m$, were placed in a transparent chamber on the visualisation stage of the microscope. The chamber is made of two coverslips separated by a typical distance h, ranging between 5 and $110\mu m$ (see Appendix A for details).

As discussed previously our goal is to produce bacterial samples at different concentrations and with different mean swimming velocities. In the work presented by Minamino *et al.* (2003) the effect of pH in the motility of *E. coli* and *Samonella* motility was studied. They varied the pH between 5 and 7.8, showing that in the presence of potassium acetate, there is a significant variation of the swimming speed reaching a maximum at pH 7. Inspired by this result, we used a similar protocol to vary the velocity of the bacteria (see Appendix A). We obtained a mean velocity variation from 4 μm/s at low pH up to 20 μm/s at high pH, that is, an increase of the mean velocity by a factor 5 (see Fig. 6). However it is important to notice that the results presented in Miño *et al.* (2011) were obtained in non-buoyant condition using a 1:1 mixture of Minimal Motility Medium (MMA) and Percoll, a nanoparticles suspension (Laurent *et al.* 1980). We actually noticed that the viscosity of the MMA-Percoll mixture changes strongly with pH and forms a gel at low pH, therefore, we could not obtain a density matching between the solution and both the beads and the bacteria while keeping the viscosity fixed. Consequently, the experiments presented here were done with MMA only (without Percoll) and we tested by direct rheometric measurements that in all cases the fluid stays Newtonian. The pH variation does not affect the viscosity of the fluid with a value, at 25°C, close to the one of pure water (see Appendix A). In this context, the latex particles (density 1.03 g/cm^3) will sediment and stay preferentially close to the bottom wall. In figure 7(b), bacterial concentration profiles are shown in a situation where the chamber

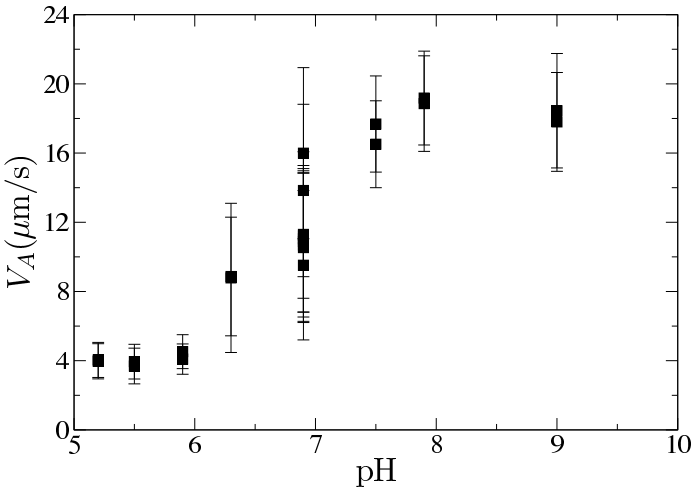

FIGURE 6. Effect of the pH in mean velocity V_A of the active population using MMA solution. Error bars represent standard deviations.

height is h = 110 μm in buoyant conditions. We observe an increase of concentration close to the bottom surface and the corresponding visualisation region is displayed in a rectangle on the same figure. Also an increase of the bacteria concentration near the top wall can be noticed, phenomenon that has been reported previously by Frymier *et al.* (1995); Lauga *et al.* (2006); Berke *et al.* (2008); Li *et al.* (2008), as a consequence of the trapping of bacteria at the surface by hydrodynamic interactions

Given the specific protocol explained in Appendix A, once the chamber is placed under the microscope, the steady distribution of bacteria in the vertical direction is reached very rapidly. The experiments start few minutes later in order to let the latex beads sediment. Figure 7(c) shows a snapshot of several latex beads among the bacteria close to the bottom surface and we superpose the corresponding tracks for 30 s. In Fig. 7(d) is shown an averaged quadratic displacement as a function of the time lag τ that the tracers are tracked, obtained at two different frame-rates of acquisition. This indicates that after 0.5 s , a diffusive motion is reached. The diffusion coefficients extracted by linear fit of the quadratic displacement versus time lag are obtained by analysing 300 images, taken at 1 frame per second. The time lags used for the fit are between 1-10 s. For all the data, the bacterial motion is analysed using 20 s videos at 20 images per second. The active bacteria concentration n_A is determined by characterising the tracks with the method described in Miño *et al.* (2011), using as indicators the mean persistence angle and the exploration radius. For each experiment, the mean bacteria velocity V_A is computed from the mean track length over the total visualisation time.

4.1. *Diffusivity enhancement close to the bottom surface*

In this first series of experiments the chamber height is maintained at its higher value of 110 μm. As described in detail in Appendix A, the change of pH changes the mean bacterial velocity V_A. Systematic measurements of the diffusion coefficient of tracers were made for suspensions prepared at pH 5.2, 5.5, 5.9, 6.3, 6.9, 7.5, 7.9 and 9. For each pH, the bacterial concentration was varied by preparing suspensions at different OD (Optical density) ranging from $OD = 0$ up to $OD = 1$. As discussed before, for each experiment, the corresponding values of the particle diffusivity D_P, the mean active bacterial velocity V_A and the mean active density n_A were measured. Figure 8 shows the relation between

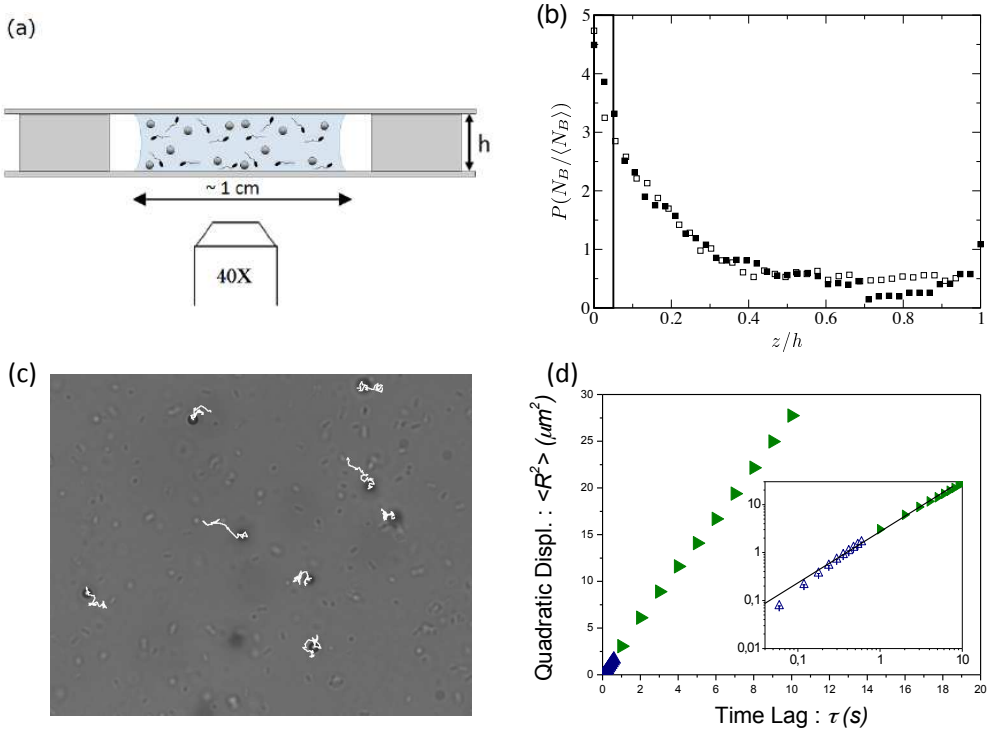

FIGURE 7. (a) Sketch showing a a lateral view of the chamber observed on the microscope. For these experiments a 40X objective (Aperture number AN 0.65) was used, given a visualisation field of $96 \times 128\,\mu\text{m}^2$. Observation are performed in the centre of the drop, far away from the drop border. (b) Distribution of bacteria as function of height in buoyancy solution (Minimal Motility Medium at pH 7) for two bacterial concentration n: 4.5×10^8bact/ml (solid squares) and 7×10^8bact/ml (empty squares), corresponding to optical densities OD 0.7 and 1, respectively. The cell height is $h = 110\,\mu$m. (c) picture of tracer trajectories. (d) quadratic displacement as a function of time lag at two temporal resolutions.

passive tracer diffusion D_P and the active flux $J_A = n_A V_A$. Different symbols represent different pH, except for the solid circles which correspond to the results presented by Miño *et al.* (2011). The data collapse on a straight line as it is proposed in Eq. (1.1) where the Brownian diffusivity near solid boundaries is

$$D_P^B = \alpha D_B = \frac{\alpha k_B T}{3\pi\eta d}. \tag{4.1}$$

Here, k_B is the Boltzmann constant, T is the absolute temperature, η the viscosity of the liquid, d the diameter of the particle and $\alpha < 1$ is the parallel drag correction factor introduced in (3.1). From the data presented in Fig. 8, the fitted value for α is 0.80 ± 0.08 and β is $13.0 \pm 0.7\,\mu\text{m}^4$, where the last one gives the influence of bacterial motion in the tracers diffusion.

Now, comparing with the values reported previously in a non-buoyant condition (Miño *et al.* 2011) the value α found for passive tracer of $2\,\mu$m was 0.74 ± 0.03, and for β was $5.0 \pm 0.4\,\mu\text{m}^4$. It can be noticed that for small heights β in a buoyant condition it is significantly higher than the one found for non-buoyant conditions. This result can be observed in Fig. 8, where the previous results in non-buoyant conditions (black circles) also are plotted.

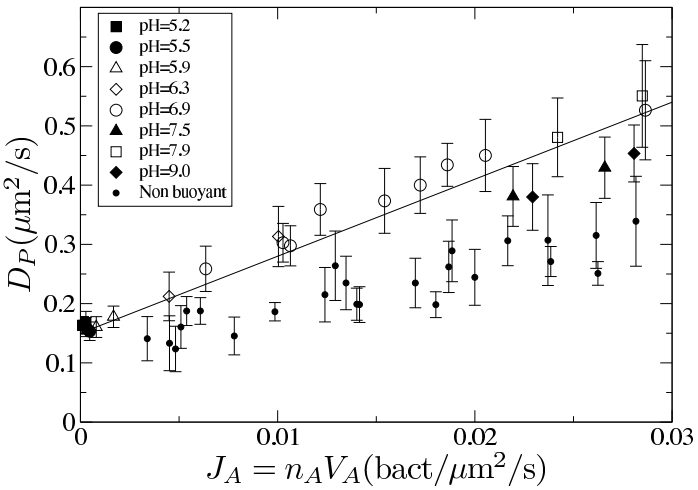

FIGURE 8. Enhanced diffusivity D_P of passive tracers as a function of J_A in buoyancy conditions. Squares represent tracer of $2\,\mu$m diameters. Each symbol represents an experiment performed with different pH. Black circles represent the result obtained under isodense (non-buoyant) condition for passive tracers of $2\,\mu$m diameter (see Miño *et al.* 2011).

To make a numerical comparison with the theoretical model, we must note that although the tracers are buoyant, they are not in contact with the surface due to thermal Brownian motion. In fact, the tracer heights are distributed according to the Boltzmann distribution $\rho \sim \exp(-m^* g z_T/k_B T)$, where m^* is the buoyant mass, with an average tracer height $k_B T/m^* g = 3.7\,\mu$m. Then, the β coefficients shown in Fig. 4 must be averaged over the tracers distribution, resulting in $\beta^{\mathrm{avg}} = 2.0\,\mu\mathrm{m}^4$ when the two-monopole model is used. The predicted numerical values are smaller than the observations. The difference could be attributed to the simplified swimmer models, which do not treat adequately the near field flows.

4.2. *Variation of active diffusivity with the confinement*

Now we explore the effect of varying the confinement height h between the top and the bottom walls. In these experiments, the pH value is maintained at $pH = 6.9$ and the OD is varied from 0 to 0.9. At each value of h, we extract by fitting linearly the relation between D_P and J_A, the Brownian diffusivity coefficient in the absence of bacteria (D_P^B) and the slope β representing the activation effect. The results for various confinement heights h are presented in Fig. 9. In the Inset, we plot the relative Brownian diffusivity D_P^B/D_B, where D_B is the theoretical thermal diffusion in the bulk. It can be noted that the value of D_P^B/D_B decreases when the separation between the two wall decreases, which is in good agreement with the experimental results presented by Lobry & Ostrowsky (1996), in which they measured the transverse Brownian motion of passive particles in a confined geometry. In the main figure we display the effect of confinement in the enhanced diffusion, given by the slope β in Eq. (1.1). β increases significantly when the upper wall is near to the bottom one, presenting a maximum at height $h \sim 8\,\mu$m. This maximum is approximately four times the value for unconfined system.

The observed enhancement in the diffusion under confinement is similar to the predicted effect in Sec. 3.1. To make a quantitative comparison, the β coefficients showed in the inset of Fig. 5 must be averaged over the tracer distribution, results that are displayed in Fig. 5. There is a remarkable similarity among the two curves. When decreasing the

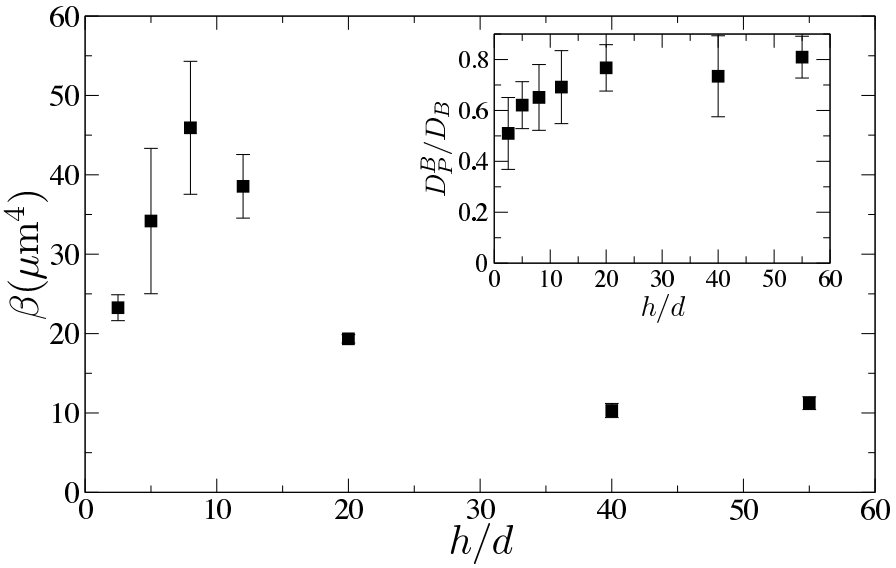

FIGURE 9. Effect of the confinement on the β value. Experiment was performed in MMA at pH 7, using 2 μm diameter passive particles. Inset: Effect of the confinement in the value α for 2 μm diameter passive tracers. D_P^B represent the diffusion of particles without bacteria and D_B the thermal diffusion in the bulk.

confining height, both show a maximum in β at a finite height to further decrease when the two plates are very close. The position of the maximum for the model, $h \sim 11\,\mu$m, is comparable with the experimental value. However, the predicted values and the observed enhancement are smaller than the experimental values. This quantitative discrepancy can be attributed to the simplicity of the swimmer models, the non-uniformities of the bacterial concentration near the surface and the approximation made to calculate the image system between two surfaces (see Sec. 3.1).

5. Conclusion and Discussion

Experimentally, in a mixture of swimmers and tracers, it has been observed that at low swimmer concentration, the agitation created by their movement produces an enhanced diffusive motion on the tracers, with a diffusion coefficient that grows linearly with the swimmer concentration. A kinetic theory explanation, that uses the properties of the hydrodynamic interactions at low Reynolds number, is given to this experimental observation. The successive displacements produced by uncorrelated swimmers produce a diffusive motion, with a diffusion coefficient that is proportional to the swimmer concentration, their mean velocity and a constant β that scales as the scattering cross section and the mean displacement squared in individual swimmer-tracer encounters. A dimensional analysis shows that the displacements grow for decreasing swimmer efficiencies, that is measured as the swimmer velocity times its size and the fluid viscosity, divided by the force of the swimmer. It results, then, that inefficient swimmers produce large tracer diffusion. The calculations are done for simple swimmer models described as a force dipole or two monopoles. More complex models can be used as well, leading to the same qualitative conclusions on the scaling of the diffusion coefficient with the bacterial concentration and mean velocity, although with different expressions for β. A separate

analysis, though, should be used in the case of swimmers that have time dependent strokes as is the case of *Chlamydomonas reinhardtii*.

The swimming efficiency is decreased near solid surfaces, where the modification of the viscous drag produces smaller swimming speeds. Near surfaces there are, however, other effects that lead to either an increase or decrease of the induced diffusion. Numerical calculations, considering all these effects, show that the induced diffusion is enhanced near solid surfaces and present a maximum at a finite distance form the wall.

To verify these results, experiments with *Escherichia coli* were performed in confined Hele-Shaw geometries. Changing the solution pH it was possible to modify substantially the swimming speed, and together with a variation in the bacterial concentration, it was possible to deduce the β coefficient from the measurements of the diffusion coefficient. Experiments were done under buoyant conditions and therefore surface effects are present. To test the predicted enhancement of tracer diffusion near surfaces, the confinement height was changed, finding that β increases by 4 times when the cell height is only $8\,\mu$m. There is a good qualitative agreement with the theoretical calculations, that predict, however, smaller increases.

It must be remarked that the swimmer models used to obtain the numerical predictions of β were very crude (a dipole of forces or two force monopoles) which are expected to describe correctly the fluid motion only at large distances. It is then remarkable that the numerical prediction give the correct order of magnitudes and the mean features produced by the solid surfaces. To obtain quantitative predictions, the same theoretical framework can be used but more accurate swimmer models should be considered, including higher multipole moments, to compute the tracer displacements.

We thank A. Honerkamp-Smith for valuable comments. This research is partially supported by Fondecyt 1100100, Anillo ACT 127, and ECOS C11E04 grants. J.D. thanks the support of a CONICYT grant (Becas Chile). G.M. and E.C. acknowledge the financial support of the the Pierre-Gilles de Gennes Foundation and the Sesame Ile-de-France "SMAC".

Appendix A. Bacteria growth and working suspensions

In this Appendix, we describe how the samples were prepared. We present the characterisation of the minimal Motility Medium (MMA) and the bacteria cultivation as well as the beads and chamber preparation.

A.1. *Minimal Motility Media (MMA)*

The choice of the ambient medium is always a difficult issue as it may strongly modify bacterial behaviour in terms of chemotaxis, ambient fluid viscosity or response to pH. In the literature, several protocols were designed to achieve different goals. For example, for *E. coli*, Berg & Brown (1972) defined an specific protocol to study the chemotactic effects of amino-acids in the bacterial response. A different protocol was chosen by Lowe *et al.* (1987) as they sought to change the viscosity of the suspending medium in order to study the rotation of flagella bundles with *Streptococcus*. Note that in general, the biological conditions impose a very narrow window of parameters and in practice it is always difficult to conduct experiments that change one parameter at a time as soon as a set of working conditions is established. In the present study, we consider a Minimal Motility Medium (MMA) as the swimming medium. The use of MMA has several advantages. First, it contains a sufficient amount of nutritional elements to preserve the bacterial metabolism, but cell division is strongly reduced, thus allowing control over density of the bacterial population and limiting the influence of chemotaxis. Second, this

medium enables adjustment of bacterial velocity by modifying the pH of the solution, acting directly on the molecular proton motor that activates the flagella rotation (see Minamino *et al.* 2003). A third advantage is that for different values of pH, the MMA solution remains Newtonian and it keeps physical properties similar to water as far as density and viscosity are concerned.

MMA was prepared as followed: stock solutions (1 M NaH_2PO_4 and 1M K_2HPO4) were mixed to generate phosphate buffers at a given pH (from 5.5 to 8). The stock phosphate buffers were diluted to a final concentration of 10 mM in the presence of 0.1 mM K-EDTA, which favours motility (Adler & Templeton 1967; Adler 1973) and 20 mM sodium lactate as an energy source. In some cases 1% glucose was added to prevent the effects of deoxygenation. Potassium acetate at 34 mM was also present in order to obtain bacteria with swimming velocities sensitive to pH (Minamino *et al.* 2003).

In order to characterise the viscosity of pure MMA solutions at various pH, an Anton Paar Physica MCR Rheometer was used. For each solution, the shear rate was varied from 10 to 100s^{-1}, and 20 points were measured at 25°C. The procedure was repeated three times. The pH variation does not affect the viscosity of the fluid which stays Newtonian with a value, at 25°C, close to the one of pure water .

A.2. *Bacteria cultivation*

Wild-type *E. coli* (ATCC 11105) were grown overnight at 25°C in rich medium LB (Luria broth). The next day, part of this culture was diluted 100 times in LB, allowing logarithmic growth to restart. Several protocols were performed in order to obtain swimming bacteria with maximal velocity. Some authors claim that the maximum velocity is reached in the mid-exponential phase of the growth curve (Staropoli & Alon 2000) whereas others, and also our observation, found that new born bacteria from the post exponential phase run faster (Amsler *et al.* 1993; Prüβ & Matsumura 1997). Thus once an optical density of 0.6 was reached (measured with spectrometer from Hitachi), the bacterial suspension was washed twice by centrifugation (500 rpm during 10 min) in MMA to eliminate all LB traces, and finally resuspended in MMA solution (pH 7) for at least an hour, allowing division to end, and obtaining a population enriched in 1N bacteria, also called "baby cells". In some cases, the "baby cells" were sorted by low speed centrifugation. The optical density of the resulting suspension was measured in order to prepare, by serial dilutions, samples of bacteria at different concentrations. Finally, when bacterial suspensions were introduced in the microchamber, Polyvinylpyrrolidone (PVP) at 0.005% was added to the suspension to avoid stickiness.

A.3. *Beads preparation*

To study the effect of bacterial activity on the diffusivity of passive tracers, latex beads of 2 micron diameter (Beckman-Coulter, density ρ=1.027 g/ml) were added to the suspensions. These spherical particles come in an aqueous medium containing surfactant that was eliminated by 3 successive centrifugations in MMA. Finally they were resuspended in MMA containing 0.005% PVP.

A.4. *Chamber preparation*

The chamber is made of two coverslips separated by a typical distance h. The largest distance $h = 110\,\mu$m is achieved by using two calibrated coverslips N°0 (0.085 to 0.13 mm thick) as spacers. For smaller confining heights, we use as spacer calibrated beads previously dispersed in the suspension. The action of capillary forces of the outer rim of the droplet will hold tight the bottom plate and the top coverslip at the right distance

from each others. In this way we can achieve confinement heights ranging between 5 and $110\mu m$.

Finally, to avoid the stickiness, coverslips were coated with ethanolic PVP (20 mg/ml of PVP in pure ethanol at 20 mg/ml) and dried.

REFERENCES

Adler, J. 1973 A method for measuring chemotaxis and use of the method to determine optimum conditions for chemotaxis by *Escherichia coli*. *J. Gen. Microbiol.* **74**, 77–91.

Adler, J. & Templeton, B. 1967 The effect of environmental conditions on the motility of *Escherichia coli*. *J. Gen. Microbiol.* **46**, 175–184.

Amsler, C. D., Cho, M. & Matsumura, P. 1993 Multiple factors underlying the maximum motility of *Escherichia coli* as cultures enter post-exponential growth. *J. Bacteriol.* **175**, 6238–6244.

Archer, C. T., Kim, J. F., Jeong, H., Park, J. H., Vickers, C. E., Lee, S. Y. & Nielsen, L. K. 2011 The genome sequence of e. coli w (atcc 9637): comparative genome analysis and an improved genome-scale reconstruction of *E. coli*. *BMC Genomics* **12**, 9.

Atsumi, T., Maekawa, Y., Yamada, T., Kawagishi, I., Imae, Y. & Homma, M. 1996 Effect of viscosity on swimming by the lateral and polar flagella of *Vibrio alginolyticus*. *J. of Bacteriology* **178**, 5024–5026.

Baskaran, A. & Marchetti, M. C. 2009 Statistical mechanics and hydrodynamics of bacterial suspensions. *Proc. Natl. Acad. Sci.* **106**, 15567–15572.

Berg, H. C. 2000*a* Constraints on models for the flagellar rotary motor. *Phil. Trans. R. Soc. Lond. B* **355**, 491–501.

Berg, H. C. 2000*b* Motile behavior of bacteria. *Phys. Today* **53**, 24.

Berg, H. C. 2004 E. coli *in motion*. Springer-Verlag, New-York.

Berg, H. C. & Brown, D.A. 1972 Chemotaxis in *Escherichia coli* analysed by three-dimensional tracking. *Nature* **239**, 500–504.

Berke, A. P., Turner, L., Berg, H. C. & Lauga, E. 2008 Hydrodynamic attraction of swimming microorganisms by surfaces. *Phys. Rev. Lett.* **101**, 038102.

Bhattacharya, S. & Bławzdziewicz, J. 2002 Image system for stokes-flow singularity between two parallel planar walls. *J. Math. Phys.* **43**, 5720.

Blake, J. R. & Chwang, A. T. 1974 Fundamental singularities of viscous flow. *J. Eng. Math.* **8**, 23.

Brenner, H. 1961 The slow motion of a sphere through a viscous fluid towards a plane surface. *Chem. Eng. Sci.* **16**, 242–251.

Chattopadhyay, S., Molddovan, R., Yeung, C. & Wu, X. L. 2006 Swimming efficiency of bacterium *Escherichia coli*. *Proc. Natl. Acad. Sci. U.S.A.* **103**, 13712–13717.

Drescher, K., Dunkel, J., Cisneros, L. H., Ganguly, S. & Goldstein, R. E. 2011 Fluid dynamics and noise in bacterial cell-cell and cell-surface scattering. *Proc. Natl. Acad. Sci. U.S.A.* **108**, 10940.

Drescher, K., Goldstein, R. E., Michel, N., Polin, M. & Tuval, I. 2010 Direct measurement of the flow field around swimming microorganisms. *Phys. Rev. Lett.* **105**, 168101.

Dunkel, J., Putz, V. B., Zaid, I. M. & Yeomans, J. M. 2010 Swimmer-tracer scattering at low reynolds number. *Soft Matt.* **6**, 4268.

Dunstan, J., Miño, G., Clément, E. & Soto, R. 2012 A two-sphere model for bacteria swimming near solid surfaces. *Phys. Fluids* **24**, 011901.

Frymier, P. D., Ford, R. M., Berg, H. C. & Cummings, P. T. 1995 Three-dimensional tracking of motile bacteria near a solid planar surface. *Proc. Natl. Acad. Sci. U.S.A.* **20**, 6195–6199.

Goldman, A. J., Cox, R. G. & Brenner, H. 1967 Slow viscous motion of a sphere parallel to a plane wall-i. motion through a quiescent fluid. *Chem. Eng. Sci.* **22**, 637.

Golestanian, R. & Ajdari, A. 2008 Analytic results for the three-sphere swimmer at low reynolds number. *Phys. Rev. E* **77**, 036308.

Guasto, J. S., Johnson, K. A. & Gollub, J. P. 2010 Oscillatory flows induced by microorganisms swimming in two dimensions. *Phys. Rev. Lett.* **105**, 168102.

Happel, J. & Brenner, H. 1965 *Low Reynolds Number Hydrodynamics with Special Applications to Particulate Media*. Prentice Hall, Englewood Cliffs, NJ.

Hernandez-Ortiz, J. P., Stoltz, C. G. & Graham, M. D. 2005 Transport and collective dynamics in suspensions of confined swimming particles. *Phys. Rev. Lett.* **95**, 204501.

Holmqvist, P., Dhont, J. K. G. & Lang, P. R. 2006 Anisotropy of brownian motion caused only by hydrodynamic interaction with a wall. *Phys. Rev. E* **74**, 021402.

Huang, P. & Breuer, K. S. 2007 Direct measurement of anisotropic near-wall hindered diffusion using total internal reflection velocimetry. *Phys. Rev. E* **76**, 046307.

Kim, S & Karilla, S. J. 2005 *Microhydrodynamics: Principles and Selected Applications*. Dover, New York.

Lauga, E., DiLuzio, W. R., Whitesides, G. M. & Stone, H. A. 2006 Swimming in circles: Motion of bacteria near solid boundaries. *Biophysical Journal* **90**, 400–412.

Lauga, E. & Powers, T. R. 2009 The hydrodynamics of swimming microorganisms. *Rep. Prog. Phys* **72**, 096601.

Laurent, T. C., Pertoft, H. & Nordli, O. 1980 Physical chemical characterization of percoll. i. particle weight of the colloid. *Journal of Colloid and Interface Science* **76**, 124–132.

Leptos, K. C., Guasto, J. S., Gollub, J. P., Pesci, A. I. & Goldstein, R. E. 2009 Dynamics of enhanced tracer diffusion in suspensions of swimming eukaryotic microorganisms. *Phys. Rev. Lett.* **103**, 198103.

Li, G., Tam, L.-K. & Tang, J. X. 2008 Amplified effect of brownian motion in bacterial near-surface swimming. *Proc. Natl. Acad. Sci.* **105**, 18355–18359.

Lobry, L. & Ostrowsky, N. 1996 Diffusion of brownian particles trapped between two walls: Theory and dynamic-light-scattering measurements. *Phys. Rev. B* **53**, 12050.

Lowe, G., Meister, M. & Berg, H. C. 1987 Rapid rotation of flagellar bundles in swimming bacteria. *Nature* **325**, 637–640.

Miño, G. L., Mallouk, T. E., Darnige, T., Hoyos, M., Dauchet, J., Dunstan, J, Soto, R., Wang, Y, Rousselet, A. & Clément, E. 2011 Enhanced diffusion due to active swimmers at a solid surface. *Phys. Rev. Lett.* **106**, 048102.

Minamino, T., Imae, Y., Oosawa, F., Kobayashi, Y. & Oosawa, K. 2003 Effect of intracellular ph on rotational speed of bacterial flagellar motors. *J Bacteriol.* **185**, 1190–1194.

Prüβ, B. M. & Matsumura, P. 1997 Cell cycle regulation of flagellar genes. *J Bacteriol.* **179**, 5602–5604.

Purcell, E.M. 1977 Life at low reynolds number. *Am. J. Phys.* **45**, 3.

Ramia, M., Tullock, D. L. & Phan-Thien, N. 1993 The role of hydrodynamic interaction in the locomotion of microorganisms. *Biophys.* **65**, 755.

Saintillan, D. & Shelley, M. J. 2007 Orientational order and instabilities in suspensions of self-locomoting rods. *Phys. Rev. Lett.* **99**, 058102.

Shneider, W. R. & Doetsch, R. N. 1974 Effect of viscosity on bacteial motility. *J. of Bacteriology* **117**, 696–701.

Staropoli, J. F. & Alon, U. 2000 Computerized analysis of chemotaxis at different stages of bacterial growth. *Biophys J.* **78**, 513–519.

Wilson, L. G., Martinez, V. A., Schwarz-Linek, J., Tailleur, J., Bryant, G., Pusey, P. N. & Poon, W. C. K. 2011 Differential dynamic microscopy of bacterial motility. *Phys. Rev. Lett.* **106**, 018101.

Wu, X.-L. & Libchaber, A. 2000 Particle diffusion in a quasi-two-dimensional bacterial bath. *Phys. Rev. Lett.* **84**, 3017.

Non-Newtonian viscosity of E-coli suspensions

Jérémie Gachelin, Gastón Miño, Hélène Berthet, Anke Lindner, Annie Rousselet and Éric Clément
PMMH-ESPCI, UMR 7636 CNRS-ESPCI-Universities Pierre et Marie Curie and Denis Diderot, 10 rue Vauquelin, 75005 Paris, France.
(Dated: October 9, 2012)

The viscosity of an active suspension of E-Coli bacteria is determined experimentally in the dilute and semi dilute regime using a Y shaped micro-fluidic channel. From the position of the interface between the pure suspending fluid and the suspension, we identify rheo-thickening and rheo-thinning regimes as well as situations at low shear rate where the viscosity of the bacteria suspension can be lower than the viscosity of the suspending fluid. In addition, bacteria concentration and velocity profiles in the bulk are directly measured in the micro-channel.

PACS numbers: 47.63.-b, 47.57.Qk, 47.57.E-

The fluid mechanics of microscopic swimmers in suspension have been widely studied in recent years. Bacteria [1, 2], algae [3, 4] or artificial swimmers [5] dispersed in a fluid display properties that differ strongly from those of passive suspensions [6]. The physical relationships governing momentum and energy transfer as well as constitutive equations vary drastically for these suspensions [7, 8]. Unique physical phenomena caused by the activity of swimmers were recently identified such as enhanced Brownian diffusivity [1, 8–10] uncommon viscosity [4, 12, 13], active transport and mixing [11] or the extraction of work from isothermal fluctuations [13, 16]. The presence of living and cooperative species may also induce collective motion and organization at the mesoscopic or macroscopic level [17, 18] impacting the constitutive relationships in the semi-diluted or dense regimes.

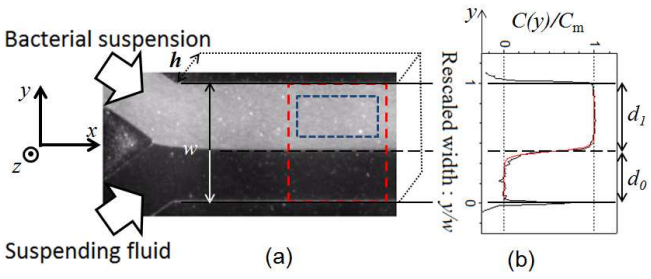

FIG. 1: Experimental set-up. (a) Time averaged image of the micro-channel ($W = 600$ µm) for $Q = 10$ nL/sec and volume fraction $\phi = 0.35\%$. The red and blue frames indicate the measurement areas. (b) Concentration profile $C(y)$ normalized by the maximal concentration C_M (black line) and error function fit used to determine the interface position (red line).

The E.Coli bacterium possesses a quite sophisticated propulsion apparatus consisting of a collection of flagella (7-10 μm length) organized in a bundle and rotating counter-clockwise [20]. In a fluid at rest, the wild-type strain used here has the ability to change direction by unwinding some flagella and moving them in order to alter its swimming direction (a tumble) approximately once every second [21]. In spite of the inherent complexity of the propulsion features, low Reynolds number hydrodynamics impose a long range flow field which can be modeled as an effective force dipole. Due to the thrust coming from the rear, E.coli are described as "pushers", hence defining a sign for the force dipole which has a crucial importance on the rheology of active suspensions [7]. For a dilute suspension of force dipoles, Haines et al [22] and Saintillan [24] derived an explicit relation relating viscosity and shear rate. They obtained an effective viscosity similar in form to the classical Einstein relation for dilute suspensions : $\eta = \eta_0(1 + K\phi)$ (η_0 being the suspending fluid viscosity and ϕ the volume fraction). These theories predict a negative value for the coefficient K for pushers at low shear rates, meaning the suspension can exhibit a lower viscosity than the suspending fluid. The theoretical assessment of shear viscosity relies on an assumed statistical representation of the orientations of the bacteria, captured by a Fokker-Plank equation and a kinematic model for the swimming trajectories [25, 26].

Despite the large number of theoretical studies, few experiments have been conducted. With *bacillus subtilis* (pushers) trapped in a soap film Sokolov et al.[12] have shown that a vorticity decay rate could be associated with a strong decrease of shear viscosity in the presence of bacteria. For algea (pullers), Rafai et al. [4] have shown that the effective viscosity measured in a classical rheometer is larger than the viscosity of the corresponding dead (passive) suspension. However, no measurements of the viscosity of a dilute suspension of pushers under controlled shear conditions exist to date. This is mainly due to the fact that one has to assess small viscosities near the viscosity of water at very small shear rates to probe the theoretical predictions. These parameters are typically outside of the resolution of a classical rotational rheometer and have thus made these measurements inaccessible. In this letter, we present the first measurements of the shear viscosity of a suspension

of pushers using a microfluidic device to overcome these difficulties and obtain the relative viscosity of an active suspension for a large range of shear rates and bacteria concentrations. Our set-up also allows direct visualization of the flow as well as the spatial distributions of bacteria in the flow.

The wild type *E. coli* W used here are prepared following the experimental procedure described in Ref. [9, 15]. The strain is grown overnight in rich medium (LB). After washing, it is transferred into MMA, a motility medium supplemented with K-acetate (0.34 mM) and polyvinyl pyrolidone (PVP: 0.005%). The sample is then incubated for at least one hour. To avoid bacteria sedimentation, Percoll is mixed with MMAP 1vol/1vol (isodense conditions). We verified that under these conditions, the suspending fluid is Newtonian (viscosity $\eta = 1.28 \times 10^{-3}$ Pa s at 22°C). All experiments are performed at a fixed temperature $T = 25°C$.

To obtain the shear viscosity, we adapted a microfluidic device [27] to compare the Newtonian viscosities of two liquids. The device is a Y-shape Hele-Shaw cell of height h, such that each branch receives a different fluid (resp fluid 0 of viscosity η_0 and fluid 1 of viscosity η_1 (see fig.1). Both flows are driven at an identical flow rate Q. In a Hele-Shaw approximation, the velocity profile in the z direction can be described by a parabolic flow profile and the dominant shear rate occurs in the z direction. Under these conditions and for a viscosity ratio near one, the position of the interface between both fluids at steady state i.e. d_1/d_0 is determined by the viscosity ratio η_1/η_0 [27]. Guillot *et al.* [27] have also used this approach for non-Newtonian fluids, where it corresponds to the measurement of an apparent viscosity. Here we will follow the same approach and will verify our method subsequanty. The suspension of bacteria is flown into one arm and the suspending Newtonian fluid into the other arm. The interface position is then measured at various flow rates Q. The experimental data is presented as a function of the maximum shear rate obtained by assuming a parabolic flow profile $\dot{\gamma}_M = (6Q)/(h^2 d_1)$ where d_1 is the lateral width occupied by the suspension. The relative viscosity $\eta_r =$ is then :

$$\eta_r = \frac{\eta_1}{\eta_0} = \frac{d_1}{d_0} \tag{1}$$

This micro-fluidic device has the advantage of measuring a viscosity ratio and provides very good resolution of the suspension viscosity independent of its absolute value or the applied shear rate. Special care has to be taken that both branches are fed at the same constant flow rate Q. We use a very high precision two-syringe pump from *nemeSYS* and a precision syringe (Hamilton Gastight 1805RN) of a very small volume ($50\mu L$) allowing to impose identical and very small flow rates (down to $Q = 0.5$ nL/sec) on both arms. Finally, the position of the sample region (indicated by the red rectangle on figure 1) is chosen in such a way as to be in steady state conditions (reached at a distance of approximately 600 μm from the junction of the inlet channels) while avoiding significant mixing.

The Y-shape channel was fabricated completely from PDMS using a soft-lithography technique. The channel thickness is $h = 100$ μm. The main channel width is $w = 600$ μm and the two inlet branches widths are $w/2$. Inlets are connected by 500 μm diameter tubes to the two-syringe pump. The total length of the main channel is $40mm$. Suspensions were prepared (see [9]) with a number of bacteria per unit volume n in the range $1.9\ 10^{12} L^{-1} < n < 25.6\ 10^{12} L^{-1}$. The volume fraction is estimated using the space occupied by the body of each bacteria $v_b = 1\ \mu m^3$ such that $\phi = n v_b$, yielding a range of $0.19 < \phi < 2.56\%$. Note that other definitions of the volume fraction, for example based on the length of the body or including the length of the flagella would lead to significantly higher volume fractions. The flowing suspension was observed using an inverted microscope (Zeiss-Observer, Z1) connected to a digital camera PixeLINK PL-A741-E ($1280\ X\ 1024 pix^2$) capturing videos at a frame rate of 22 images/s. Low magnification (2.5x) allowed an extended view of the channel (see Fig.1).

During an experiment we begin with an initial flow rate of $Q = 0.5$ 1 nL/sec, and then the input flow is increased step by step up to $Q = 100$ nL/sec. Note that we have verified for all experiments that identical results are obtained when subsequently decreasing the flow rate. In fig 1, the shape of the interface obtained by averaging over 120 successive images is displayed for the measurement area. To quantitatively determine the interface position, we measure the mean bacteria density across the channel width $\bar{n}(z)$ using the logarithm of the profile of the average intensity $C(y) = \ln(\langle I \rangle(y)/\langle I \rangle_0$ as a measure of the concentration, with $\langle I \rangle_0$ is the mean intensity in the absence of bacteria. The average is calculated in the x-direction over a distance of 600 μm (see red rectangle in fig.1). The concentration $C(y)$ is fitted with an error function erf(y) to obtain the interface position y_I. Once the interface position is determined, we extract the relative viscosity according to equation (1) and associate it with $\dot{\gamma}_M$.

Experimental observations are presented in fig. 2(a) displaying averaged images for flow rates of $Q = 0.5$ nL/sec, $Q = 2$ nL/sec and $Q = 10$ nL/sec for a suspension at a volume fraction of $\phi = 0.35\%$. When increasing the flow rate the interface position changes from a value above the mid-position to a value below the mid-position indicating a change in the suspension viscosity from greater then the viscosity of the suspending fluid to smaller. Quantitative measurements are given in fig.2(e) showing the relative viscosity η_r of the suspension as a function of the maximum shear rate for various concentrations $\phi = 0.19,\ 0.75,\ 2.3$ and 2.48 %. The er-

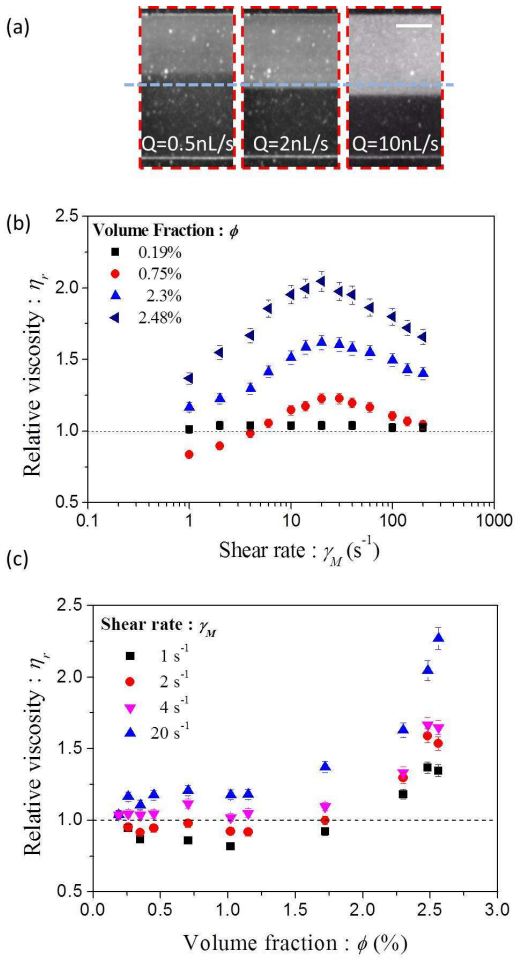

FIG. 2: Rheology curves. Fig (a) are 3 averaged pictures of the bilaminar flow for flow rates of $Q = 0.5\ nL/s$, $Q = 2\ nL/s$ and $Q = 10\ nL/s$ respectively for a $\phi = 0.35\%$ bacteria suspension. These images are averaged over 120 images at 22im/s and observed with a 2.5x magnification using phase contrast. The dotted line represents the mid-position in the channel width. The scale bar corresponds to 200 µm. (b) Relative viscosity versus mean shear rate at several volume fractions (c) Relative viscosity versus volume fraction at several shear rates. The errors bars are estimated using the detection error of the interface position.

ror bars are estimated using the uncertainty in determining the interface position and in marked contrast to classical rheology, the error does not increase for lower shear rates, once again demonstrating the strength of our micro-rheometer. For the lowest concentration the viscosity of the Newtonian suspending fluid is recovered for all shear rates validating our rheological device. For all other concentrations, the curves display the same qualitative behavior. At low shear rates, we observe shear thickening and at higher shear rates, shear thinning occurs. For all of these cases, the shear thinning and shear thickening character of the active suspensions are weak and power law indices n (using $\eta = K\dot{\gamma}^{(n-1)}$) close to one are found for both regimes for all concentrations. At all concentrations tested, a maximum viscosity is observed at a value around $\dot{\gamma}_M = 20s^{-1}$. The non-monotonic behavior as a function of shear-rate is in agreement with the results of Saintillan [24] obtained for slender bacteria. Note that the low shear rate plateau predicted by the theory could not be observed in our experiments due to practical limitations of our device (minimum flow rates 0.5 nL/sec). At low volume fractions and low shear rates, we observe a decrease of η_r below one which agrees with the theoretical predictions of Haines et al. [22] and Saintillan [24] of this striking effect. Figure 2(c) shows the relative viscosity as a function of the volume fraction ϕ at various shear rates $\dot{\gamma_M} = 1,\ 2,\ 4$ and $20\ s^{-1}$. A decrease in viscosity is observed for the small shear rates, followed by a sharp increase of viscosity for all shear rates, corresponding to a semi-dilute regime. In our case this regime is observed for concentrations above approximately 1%. Similar behavior was also observed by Sokolov et al.[12] using vortex decay in a suspension of Bacilus subtilis confined in a soap film and has been predicted by Ryan et al. [23] in their simulations.

So far we have measured the shear viscosity of the suspensions as a function of the maximum shear rate assuming a parabolic velocity profile. One of the advantages of our microfluidic device is that we can access the local velocity and bacteria concentration profiles as a function of the channel height directly. Bacteria moving in the flow were visualized with a high magnification objective (40x, phase contrast) allowing the position of the bacteria to be monitored at various heights z (field depth 3 μm). Videos were taken using a highspeed camera (Photron FastCam SA3, resolution 1024x1024pixels, shutter speed $(1/500s)$, frame rate $1/50s$ for $Q = 0.5, 1nL/s$ and $1/500s$ for $Q = 10nL/s$). To monitor the flow velocity, we suspended a very low concentration of $2\mu m$ density-matched latex beads as passive tracers (density $1.03g/cm^3$). Here we present selected results for the volume fraction $\phi = 0.75$ % at which the reduction of the relative viscosity below 1 is observed at three flow rates ($Q = 0.5, 1, 10$ nL/sec corresponding respectively to maximum shear rates $\dot{\gamma_M} = 1, 2, 20\ s^{-1}$. Videos were taken in a region situated in the middle between the interface and the side wall (see blue frame of fig. 1). To reduce the detection noise, a bacterium is retained only if it is detected on at least two consecutive frames. The flow velocities were computed for particles moving in the focal plane. In Fig. 3a) we see that the concentration profiles are similar in shape to those published previously by [15] in the absence of flow, i.e. a quasi-constant density and a strong density increase within $10\mu m$ of the wall, hence probing a trapping effect that persists over the range of shear rates explored. The calculated mean concentration is represented by the dashed line in fig. 3a and is in agreement with the measured bulk concentration. It is impor-

tant to note that the concentration profiles are identical for the various shear rates. The change in viscosity observed is therefore not due to a change in concentration within the microchannel. The velocity profiles $V_x(z)$ are displayed in Fig.(3b). Within the precision of our experimental setup, a deviation from a parabolic velocity profile is not observed justifying the approximation used for our analysis. Note also that this finding is in agreement with the weak shear thinning or shear thickening character of our suspensions, that predict only small changes in the velocity profile, not detectable in our experiments. For each flow rate the curves presented in fig. 3b) agree within 3% with the theoretical predictions for a rectangular cell of the aspect ratio of (1/6) [28].

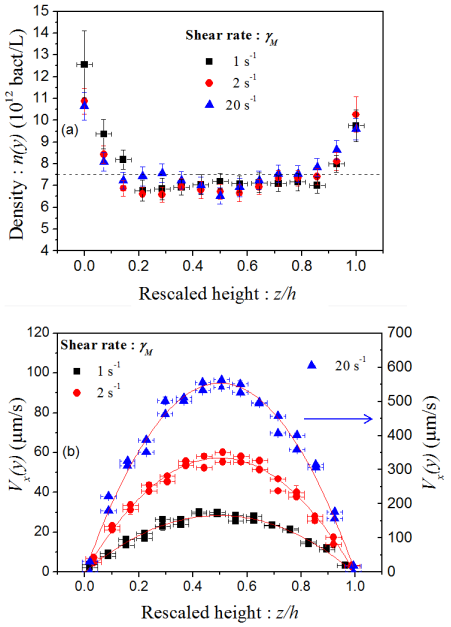

FIG. 3: Bulk profile measurements for a volume fraction $\phi = 0.75$ % and shear rates $\dot{\gamma_M} = 1, 2, 20\ s^{-1}$. (a) Bacteria density profile $n(z)$. The horizontal dashed line represents the mean density: $\bar{n} = 7.5\text{bact}/L$. (b) Velocity profile of passive tracers $V_x(z)$.

In conclusion, using a micro-fluidic device, we have measured for the first time the effective shear viscosity of a suspension of "pushers" (E-coli bacteria) over a large range of shear rates$(1 - 200\ s^{-1})$ under controlled shear conditions in the dilute and semi-dilute regime. We confirmed an important prediction for the rheology of pushers: the active viscosity can be lower than the viscosity of the suspending fluid at low shear rates [7, 22, 24]. In the dilute as well as in the semi-dilute regime, we observed a shear-thickening behavior at lower shear rates followed by a shear-thinning regime at higher shear rates. The viscosity maximum is observed at a shear rate on the order of the inverse of the time a bacterium needs to swim over a distance of its own size and this value seems independent of the bacteria concentration. These results are consistent with the theoretical calculation of Saintillan [24]. Direct measurements of the bacteria concentrations and flow velocities confirm that the bacteria distribution remains homogeneous and the parabolic flow profile is not significantly modified by the weak non-Newtonian character of the active fluid. This last result validates the use of the Newtonian approximations for the extraction of our viscosity measurements. In the semi-dilute regime (here for volume fractions greater than 1%), we observe a strong increase of the viscosity consistent with numerical simulations by Ryan et al.[23]. Our results represent the first experimental validation of the non-Newtonian rheology of an active suspension of pushers under controlled shear conditions.

Acknowledgment. We acknowledge the financial support of the Pierre-Gilles de Gennes Foundation and the SESAME Ile-de-France research grant :" Milieux actifs et stimulables". We thank Profs R.Soto, D.Saintillan, I.Aronson and M. Alves for enlightening scientific discussions and C. Davis for a careful reading of the manuscript.

[1] X.-L. Wu et al., Phys. Rev. Lett. **84**, 3017 (2000).
[2] C. Dombrowski *et al.*, Phys. Rev. Lett. **93**, 098103(2004).
[3] K.C. Leptos *et al.*, Phys. Rev. Lett. **103**, 198103 (2009).
[4] S. Rafaï, L. Jibuti, and P. Peyla, Phys. Rev. Lett. **104**, 098102 (2010).
[5] W.F. Paxton *et al.*, J. Am. Chem. Soc. **126**, 13431 (2004).
[6] A.Baskarana et al., PNAS **106**, 15567 (2009), Koch D.L. et al., Ann. Rev. Fluid Mech., 43, 637 - 659 (2011)
[7] Y. Hatwalne *et al.*, Phys. Rev. Lett **92**, 118101 (2004).
[8] D.T.N. Chen *et al.*, Phys. Rev. Lett. **99**, 148302 (2007).
[9] G. Mino et al., Phys.Rev.Lett **106**, 048102 (2011).
[10] P.T. Underhill et al. Phys. Rev. Lett. **100** 248101 (2008)
[11] M.J. Kim et al., Analytical Chemistry **79** 955 (2007).
[12] A. Sokolov et al., Phys. Rev. Lett. **103**, 148101 (2009),
[13] R. Di Leonardo *et al.*, PNAS **107**, 9541, (2010).
[14] N. Darnton *et al.*, Biophys. J. **86**, 1863 (2004).
[15] A.P. Berke et al., Phys. Rev. Lett. 101, 038102 (2008).
[16] A. Sokolov *et al.*, PNAS **107**, 969 (2010).
[17] G. Gregoire et al. Phys. Rev. E **64**, 011902 (2001).
[18] D.Saintillan et al. J.R. Soc. Interface 9, 571 (2012).
[19] Marcos, H.C. et al., PNAS, doi: 10.1073/pnas.1120955109 (2012).
[20] H. C. Berg *E. coli in Motion* (Verlag, New York, 2004).
[21] N. C. Darnton et al. J. Bacteriology, **189**, 1756 (2007).
[22] B. M. Haines et al., PR E 80, 041922 (2009)
[23] S. Ryan et al., Phys. Rev. E **83**, 050904 (2011).
[24] D. Saintillan, Model Exp. Mech. 50, 125 (2010).
[25] F. P. Bretherton, J. Fluid Mech., 14, 284 (1962), G.B. Jeffery. Proc. Roy. Soc. London A, 102, 161 (1922).

[26] Zöttl et al. Phys. Rev. Lett. 108, 218104 (2012)
[27] P. Guillot et al., Langmuir **22**, 6438-6445, (2006), Galambos et al. F. Int. Mech. Eng. Congr. Exp., Anaheim, CA 1998, P. Nghe, J. Non-Newtonian Fluid Mech., 165 (2012) 313-322
[28] F.M. White (2005) "Viscous fluid flow". McGraw-Hill.